Structure-borne sound transmission on frameworks of beams

Thesis submitted in accordance with the requirements of the University of Liverpool for the degree of Doctor of Philosophy

by

Xing Wang

July 2015

Abstract

Many engineering structures are built from frameworks of beams, particularly lightweight structures. For the purpose of noise control from airborne and structure-borne sources, it is useful to be able to predict vibration transmission across these frameworks. This thesis investigates the potential use of Advanced Statistical Energy Analysis (ASEA) to predict structure-borne sound transmission when the beams support multiple wave types due to wave conversion at the junction. In contrast to Statistical Energy Analysis (SEA), ASEA is able to account for high propagation losses and indirect coupling through the use of ray tracing.

SEA and ASEA were validated through comparison with measurements and numerical experiments with Finite Element Methods (FEM). When each beam supports at least two local modes for each wave type in the frequency band of interest and the modal overlap factor is at least 0.1, FEM and measurement data tend to have average values which form smooth curves such as those predicted by SEA and ASEA. It was shown that SEA and ASEA models could incorporate Euler-Bernoulli and Timoshenko theory by changing over from Euler-Bernoulli to Timoshenko group velocity when calculating the coupling loss factors. However, comparisons with measurements were not conclusive although there were indications that a suitable crossover frequency could be when Timoshenko and Euler-Bernoulli group velocities differ by at least 26%.

Agreement between FEM and ASEA indicates that it is appropriate to ignore phase effects in the ray tracing approach used with ASEA. This was particularly noteworthy for the three-bay and five-bay truss beams as these were perfectly periodic for which phase effects could be important. Results for an L-junction, a rectangular beam frame and a five-bay truss with relatively long beams and relatively high internal loss factors demonstrated that ASEA was able to incorporate high propagation losses. This was not possible with SEA. For a three-bay truss beam with relatively short beams ASEA showed close agreement with FEM and measurements confirming that there was significant indirect coupling rather than high propagation losses. There are indications from the five-bay truss beams that ASEA may no longer be accurate in predicting the response on beams that are at least three structural junctions away from the source beam, particularly when ASEA predicts high propagation losses on the receiving beam.

Acknowledgements

I would like to express my heartfelt gratitude to my first supervisor, Prof. Carl Hopkins, whose firm support and professional guidance throughout my four years' PhD career are invaluable. I feel honored and lucky to meet him and to be his student as he is so friendly.

I also owe special gratitude to my second supervisor, Dr Gary Seiffert. I would never forget his support and help in this project and the experimental work.

Many thanks go to Prof. Barry Gibbs and Prof. Kirill Horoshenkov for their specialist advices on this thesis.

I would also like to thank all the colleagues in the Acoustic Research Unit. In particular, I should thank Jianfei Yin for teaching me using the Abaqus and Python, Jianfei Yin and David Wilson for the help of ASEA algorithm, and Nuno Ferreira, Sang Hee Park and Hyoseon Jang for various topics.

I gratefully acknowledge the support from my teachers in the National University of Defense Technology, Changsha, China. Special thanks go to Prof. Jihong Wen and Dr. Dianlong Yu for leading me to the research of vibration and noise control and offering me the rare opportunity of further study abroad.

I am also grateful for the funding from China Scholarship Council and University of Liverpool's CSC scholarship funding.

Last but not least, I would like to thank my wife and parents for their love, understanding, tolerance, support and always being there waiting for me to come back.

Contents

List of Symbols

A	Area of cross-section (m^2)
B	Bending stiffness for beam (Nm^2)
c_g	Group velocity (m/s)
c_L	Longitudinal wave phase velocity (m/s)
c_T	Torsional wave phase velocity (m/s)
c_B	Bending wave phase velocity (m/s)
d_{mpf}	Mean free path for wave travel in one subsystem (m)
D_{ij}	Energy level difference between subsystem i and j
e_i	Modal energy (JHz)
E	Energy (J), Young's modulus (Pa)
$f_{B(thin)}$	Thin beam limit frequency (Hz)
F_L	Axial force due to longitudinal motion (N)
F_B	Shear force due to bending motion (N)
G	Shear modulus (Pa)
i	$\sqrt{-1}$
I	Moment of inertia across neutral surface (m^4)
J	Polar moment of inertia (m^4)

k_B, k_L, k_T	Wave number of bending, longitudinal and torsional waves (m^{-1})
K	Shear stiffness (N/rad)
L	Length of beam (m)
m_1'	Mass per unit length (kg/m)
M_r	Reduced modulus (Pa)
M_T	Moment due to torsional motion (Nm)
M_B	Moment due to bending motion (Nm)
n_B, n_L, n_T	Modal density of bending, longitudinal and torsional waves (Hz^{-1})
R	Transmission loss (dB)
r	Complex amplitude of the reflected wave at beam junction (-)
t	Complex amplitude of the transmitted wave at beam junction (-)
s_{dB}	Standard deviation
T	Torsional stiffness (kgm)
v_B	Velocity for bending vibration motion (m/s)
v_L	Velocity for longitudinal vibration motion (m/s)
W_{ij}	Power transmitted from subsystem i to j (W)
Y	Mobility (m/Ns)
Z	Driving point impedance (Ns/m)
ω	Angular frequency (rad/s)
ω_T	Velocity for torsional vibration motion (rad/s)

ω_{co}	Cut-off frequency for bending waves from Timoshenko theory (rad/s)
θ	Rotational displacement (rad)
γ	Angle due to shear deformation in Timoshenko theory (rad)
μ	Poisson's ratio (-)
κ	Shear stress distribution parameter (-)
κ'	Shear coefficient (-)
τ_{ij}	Transmission coefficient from beam *i* to beam *j* (-)
η_{ii}	Coupling loss factor from beam *i* to beam *j* (-)
Θ	Mass moment of inertial per unit length (kg)
ξ	Displacement for bending wave motion (m)
λ_B	Bending wavelength (m)
ρ	Density (kg/m^3)

FEM	Finite Element Method
SEA	Statistical Energy Analysis
ASEA	Advanced Statistical Energy Analysis
CLF	Coupling Loss Factor
ILF	Internal Loss Factor
B, L, T, N	Bending, Longitudinal, Torsional, Nearfield

List of Figures

List of Tables

1. Introduction

1.1 Background

Many engineering structures are constructed from frameworks of beams for which prediction models are needed to determine vibration transmission across these frameworks for noise control purposes. Such models are relevant to machinery that is directly connected to the beams as well as to lightweight structures where frameworks of beam support thin plates which form separating and/or flanking walls/floors that provide sound insulation.

For coupled beams that form a two-dimensional junction, four possible incident waves can be considered: Type A bending waves (defined here as having displacement in the same plane as the junction), Type B bending waves (defined here as having displacement perpendicular to the plane of the junction), longitudinal waves and torsional waves. For beams that are perpendicular to each other at the junction, excitation of Type A bending waves generates longitudinal waves at the junction, and excitation of Type B bending waves generates torsional waves at the junction. This thesis considers the following models: Bending waves only (B model), Bending and Longitudinal model (BL model) and Bending and Torsional wave model (BT model).

For prediction models of sound and structure-borne sound in the audio frequency range there are often sufficiently large numbers of modes that statistical approaches can be used, such as Statistical Energy Analysis (SEA) [1]. However for frameworks of beams the number of modes in one-third octave or octave bands is not as high as with plates and acoustic cavities. In addition, most frameworks of beams have a repeating pattern such that they form a periodic structure and SEA is not suited to prediction on perfectly periodic structures. Advanced SEA (ASEA) [2] has been shown to be able to incorporate features of structure-borne sound propagation such as indirect coupling and high propagation losses. In addition, ASEA has also been used to model bending wave transmission across a periodic ribbed plate [3]. Therefore this thesis investigates whether ASEA could be used to model frameworks of beams with multiple wave types.

1.2 Literature review

The choice of prediction model for vibration transmission across coupled beams partly depends on the wavelength in relation to the beam length and whether the framework of beams is periodic with a repeating unit cell.

1.2.1 Isolated junctions of beams

Much of the literature looks at isolated planar junctions formed by two, three or four beams connected at a single junction. For such junctions, the following wave models can be given: bending wave only (pinned junctions), longitudinal wave only model (collinear beam systems with longitudinal wave excitation), torsional wave only model (collinear beam systems with torsional wave excitation), bending and longitudinal wave model and bending and torsional wave model. The majority of studies have focused on the bending and longitudinal coupling model and the out-of-plane bending and torsional wave model on collinear discontinuity, non-collinear corner junction, L-junction, T-junction, X-junction and H-junction.

Assuming only bending (Euler-Bernoulli theory) and longitudinal waves on semi-infinite beams, Cremer [4] and Cremer *et al* [5] derived transmission coefficients from wave theory for an L-junction of beams (although with an incident longitudinal wave it was assumed that both beams had the same material properties). For T- and X-junctions, Cremer, Heckl and Ungar [5] stated the bending wave transmission coefficients around the corner and across the straight section of the junction, but not the transmission coefficients involving longitudinal wave motion. Cremer, Heckl and Petersson [6] gave a general derivation for an X-junction where all beams could have different material properties and different cross-sections. This approach was adapted to derive results for a T-junction. For these T- and X-junctions, asymptotic expressions were only given for bending wave transmission coefficients (i.e. not those involving longitudinal wave motion) and the graphed transmission coefficients gave no indication that some values can be frequency-dependent.

Lyapunov [7] studied the flexural wave transmission on an articulated joint that connected beams and plates with a blocking mass. Wave theory was developed and

compared with measurements which indicated a high degree of vibration isolation was possible.

Wang and Kinsman [8] used Timoshenko beam theory to study the dynamic response of a portal frame to show the free vibration and forced response.

Rosenhouse *et al* [9] used the wave theory and experimental work to study bending and longitudinal wave transmission on T-junction with a welded joint, screw-fastened joint and a joint with a rubber layer. For these types of junction there was close agreement between the theoretical and experimental mode shapes.

Under nearfield bending wave excitation, Mace [10] derived the reflection and transmission matrices for beam discontinuities and showed that in some cases it is necessary to consider the effect of nearfields.

Moor [11] extended previous studies on L-, T- and X-junctions to an isolated beam junction with arbitrary orientations. Analytical derivations in terms of impedance were carried out to calculate the reflection of and transmission coefficients of incident in-plane bending, longitudinal, out-of-plane bending and torsional wave excitation. All beams were assumed to be identical to simplify the derivations, but no experimental validation was carried out.

Horner and White derived transmission coefficients for three beams coupled together at a single junction [12] and for two non-collinear beams [13] both with variable angles between them. The equations quoted in the former paper that give transmission coefficients for bending wave excitation appear to be in error because when they are implemented, the sum of the transmission coefficients does not equal unit. Horner and White assumed the junction was a rigid mass whereas Leung and Pinnington [14,15] derived transmission coefficients for L-junctions with spring-dashpots incorporated in the junction.

Richard *et al* [16] studied the coupling of bending and longitudinal waves on a T-junction. Measurements showed good agreement with finite element method, indicating that power of bending and longitudinal waves can be separated when both exist in one beam.

Ouisse and Guyader [17] also studied the BL model of non-collinear beam junction with arbitrary angle using wave theory. This provided an explanation for hypersensitivity of vibration transmission when beams are connected at certain angles.

Jee-Hun Song and Suk-Yoon Hong [18] studied a BL model for a non-collinear beam junction with a spring and dashpot at the beam junction. This aimed to build a non-conservative modelling technique to predict vibration transmission in the mid- and high-frequency ranges.

Mei [19,20,21,22,23] applied Timoshenko beam theory to the study of bending and longitudinal wave coupling on a T-shaped, H-shaped and L-shaped beam junctions. For the L-junction and a portal beam frame, controllers that were dynamically identical to stiffness of spring attachments were introduced at the joint to control the bending, longitudinal and torsional motion. These studies highlighted the importance of using Timoshenko beam theory at high frequencies.

As well as wave theory, other forms of analysis have been considered for isolated beam junctions including Fourier technique, asymptotic modal analysis and the receptance method.

Lee and Kolsky [24] employed the Fourier technique to solve the longitudinal and bending pulse transmission between two non-collinear rods with arbitrary connection angle but assuming the same materials and cross-section. Timoshenko beam theory was adopted to describe the bending motion, and good agreements between measurements and analytical calculations were achieved. Atkins and Hunter [25] studied the L-junctions with right angle analytically and experimentally for comparison with Lee and Kolsky's work. Yong and Atkins [26,27] also used the Fourier technique to predict bending and longitudinal wave transmission on two non-collinear rods and a T-junction of rods. Timoshenko beam theory was used and was shown to be able to accurately describe the bending wave motion. Similar research can be found by Thomas [28].

Farage and Pan [29] adopted the receptance method in the study of power flow in planar coupled beam structures. A BL model was used for a non-collinear beam junction and X-junction and validated against a finite element model. Using the receptance approach,

Besharaa and Keane [30] also numerically studied the L-junction with the joint modelled by three sets of springs and dashpots.

The above literature concerned the BL model. For the BT model assuming only bending waves (Euler-Bernoulli theory) and torsional waves on semi-infinite beams, Heckl [31] derived the transmission coefficients from wave theory for frameworks of beams formed from T- and X-junctions, and Sablik [32] derived those for an L-junction. In both cases the junction that connects the beams is assumed to be massless with a rigid cross-section that does not support wave motion. Chi [33] used the modal theory (asymptotic modal analysis) on a BT model of X-junction. The results were compared with SEA predictions. As mentioned before, by using impedance in the derivation Moor [11] also calculated the out-of-plane bending and torsional wave transmission coefficients on L-, T and X-junctions but assuming all beams identical. The power evaluation equations for different kinds of wave types on beams were also given in terms of impedance. Tso and Norwood [34] produced a general derivation to calculate transmission coefficients for a three-dimensional junction of beams with arbitrary cross-section.

In terms of experimental validation of wave models, Kurtze *et al* [35], Hinsch [36] and Rosenhouse *et al* [37] validated the bending and longitudinal wave model from Cremer [5]. Extending the experimental validation to the bending and torsional wave model, Gibbs and Tattersall [38] showed agreement between measured and predicted level differences for an L-junction of square cross-section beams. In these experimental studies the bending wavelength was at least six times the beam thickness at the highest frequency under consideration; hence it was appropriate to consider only Euler-Bernoulli theory. Doyle and Kamle [39,40] captured time signals for bending waves incident on beam junctions. This indicated that Euler-Bernoulli theory was adequate but that Timoshenko theory was likely to be necessary at high frequencies. Troshin and Sanderson [41,42] examined energy flow on a T-junction of rectangular beams with two experimental methods: structural intensity technique based on finite-difference approximation and mobility energy flow technique. Feng, Liu and Nilsson [43] studied the effect of the overlap of joint on the vibration transmission loss based on measurements on a two collinear beam systems. Gautier *et al* [44,45] provided a measurement method in which the measured structural response is used to calculated the

far field scattering matrix. Thus the reflection and transmission coefficients of the bending and longitudinal wave motions were obtained on a collinear beam junction (beams with discontinuity). Muggleton and Mace [46] also measured beams with a discontinuity as well as a right-angled pipe. Bending and longitudinal wave transmission coefficients were calculated from measured data through an averaging procedure and compared with theoretical estimates. It was concluded that this measurement method using an averaging approach has more advantages although bias errors exist between the measured transmission coefficients and predicted which was attributed to the theoretical model.

1.2.2 Large frameworks of beams

Beam frames that comprise several isolated beam junctions have been studied by many researchers, particularly periodic beam structures which exhibit the periodic properties of pass and stop bands [e.g. 47,48,49,50,51].

Heckl [31] derived the bending and torsional transmission coefficients on the isolated T and X-junctions which formed a one dimensional beam with periodic discontinuity and a two-dimensional periodic beam grillage. The attenuation of bending waves on the grillage structure was solved using wave theory. Xiao [51] analysed the periodic truss beam using periodic structure theory and FEM. It is shown that the periodic truss has an attenuation zone when only in-plane displacement was considered.

Phani *et al* [52] examined the band gaps and spatial filtering phenomenon on four specific planer beam frames: hexagonal honeycomb, the kagomé lattice, triangular honeycomb and a square honeycomb.

Uhrig [53] gave a detailed derivation of the transfer matrix, and Yun and Mak [54] studied a periodic dual-beam structure with transverse connections using Transfer Matrix Method (TMM). A coupling transfer matrix was used to describe the relationship between the velocities and the forces of the coupled bending and longitudinal waves at the two sides of the connecting beams. Using the dynamic continuity conditions at joints and Bloch wave theory, propagation constants of flexural and longitudinal waves were calculated. Experimental validation showed close agreement with TMM by measuring the mobility at the junction [55].

Langley [56] applied the direct-dynamic stiffness method to a six-collinear beam frame and a beam grillage. It was pointed out that this method treats each beam in the frame as a single element regardless of the frequency and spatial distribution of excitations because the mean power flow is calculated.

Shanker and Keane [57] presented a general method to evaluate the power flow in beam frames of rigid joint. This method was based on the receptance theory, and the global response was predicted by summation of individual uncoupled beams from Green functions.

Sablik *et al* [58] studied a three-dimensional framework of beams with bending, longitudinal and torsional waves using transmission coefficients incorporated in SEA. Structural resonance was introduced in the SEA analysis which provided large fluctuations in the response. Comparison with measurements indicated that these fluctuations did not always occur.

1.2.3 Statistical Energy Analysis

Statistical Energy Analysis (SEA) is intended for the prediction of vibration transmission between weakly coupled subsystems where the response is multi-modal in the frequency band of interest [59]. Fahy and Mohammed [60] showed that coupling loss factors determined from bending wave theory provided suitable estimates when the larger of the modal overlap factors for two coupled beams was at least unit, although the effect of low mode counts was not investigated for beams. Compared to plates, the local modes of beams are relatively widely spaced which means that mode counts are often low when using constant percentage bandwidths; hence when considering bending modes in one-third octave bands there may only be one mode in each band over a wide frequency range [61]. If the modal overlap is sufficiently high, then Davies and Wahab [62] have shown that reasonable predictions can be achieved with SEA even when the bending mode count is only one or two on each beam. Craik and Galbrun [63] have shown that fluctuations in the coupling between bending waves on two beams can be estimated based upon the mobility of the receiving beam subsystem; however, this is only feasible for one wave type. Bending mode counts in constant percentage bandwidths increase with increasing frequency; however, they only start to become greater than unit at a frequency where modes begin to occur that correspond to

longitudinal and/or torsional wave motion. So just as the bending mode count becomes multi-modal, longitudinal and/or torsional modes occur with mode counts that are unit. SEA is well-suited to the analysis of structure-borne sound where there is wave conversion at junctions between subsystems; hence this thesis assesses the application of SEA to frameworks of beams which support more than one wave type.

1.2.4 Advanced Statistical Energy Analysis

Statistical Energy Analysis (SEA) has been shown to be successful in solving many vibro-acoustic problems in engineering [64]. However, there are instances where errors occur with some types of structural assembly [65,66,67]. You *et al* [68] compared random energy flow analysis with SEA to investigate structural vibration power flow in planar beam frameworks. The energy levels on subsystems that are distant from the excited subsystem showed that large differences exist between the two methods indicating that SEA was less reliable. For coupled structural subsystems, the assumption in SEA is that there is no coupling between physically disconnected subsystems. However, in some situations there can be significant indirect coupling, i.e. tunnelling mechanisms [67,69]. To incorporate indirect coupling within a statistical framework of analysis, Heron [2] developed Advanced Statistical Energy Analysis (ASEA) which combines SEA and ray tracing (ignoring phase effects) to track the power transmitted between coupled subsystems. This approach was validated with excitation of longitudinal waves at one end of an in-line array of six rods. ASEA agreed well with the exact result which was in contrast to SEA which overestimated the vibration response for subsystems that were physically disconnected from the source subsystem. However, this example primarily confirmed the ability of ASEA to account for propagation losses rather than indirect coupling between non-adjacent rods. Yin and Hopkins [3] used ASEA to predict bending wave transmission across two coupled plates where one plate was a periodic ribbed plate. ASEA was used at high frequencies where each bay supported local modes and could be modelled as a separate subsystem. This showed that indirect coupling between bays at high-frequencies was sufficiently dominant that SEA underestimated the response by ≈40dB on the furthest bay whereas ASEA gave close agreement with measurements and FEM models. The reason for this was that ASEA accounted for spatial filtering due to transmission across each rib that led to non-diffuse vibration fields on the most distant bays. Wilson and Hopkins [70] extended the

application of ASEA to large structures built from many coupled plates by introducing a beam tracing method to increase the computational efficiency. This allowed modelling of large periodic box-like structures for which spatial filtering of bending waves becomes apparent in the low- and mid-frequency ranges after only a few structural junctions. This showed that the inclusion of indirect coupling in ASEA was able to provide significantly better estimates than SEA when plates had at least one or two bending modes in each one-third octave band (modal overlap was relatively high due to significant coupling losses). Therefore, this thesis considers the application of ASEA to beams across a wide frequency range. In the high-frequency range the Timoshenko bending theory is applicable and propagation losses are expected to become increasingly important due to lower group speeds than that in the case of the Euler-Bernoulli theory. Heron [2] considered the possibility that ASEA could be extended to multiple wave types, but no results were reported. This extension to multiple wave types is considered in this thesis.

1.2.5 Discussion

Many researchers have focused on isolated junctions of beams but relatively little work has been carried out using these models to predict vibration transmission on larger frameworks of beams in engineering structures many of which have repeating patterns. In addition, the wave theory derivations are scattered across the literature, with different assumptions about which beams have identical material properties and cross-section. Many structures such as framed-walls or floors have a framework of beams that can be described by L-, T- and X- junctions (i.e. right-angled junctions) where the collinear beams usually have identical material properties and cross-section. Hence, this thesis provides a consistent set of derivations for these types of junctions for B, BL and BT models.

The literature review in this chapter indicates that a few researchers have carried out analysis up to sufficiently high frequencies and commented that Timoshenko beam theory [26,27] is required. However, the literature does not consider how Timoshenko theory can be incorporated in SEA and ASEA. In this thesis prediction and experimental work will be carried out over the audio frequency range (20 Hz-20 kHz) in order to assess the differences between Euler-Bernoulli and Timoshenko theory.

The literature on SEA indicates that relatively few studies have considered its use with large frameworks of beams. Hence there are few validations on systems of coupled beams, which consider the following combination of factors: low mode counts, low modal overlap, multiple wave types, different bending wave theories, propagation losses and indirect coupling as well as increasing uncertainty in measurements at high frequencies. ASEA has not previously been used to model realistic engineering frameworks of beams and has only considered one wave type hence this thesis investigates whether ASEA could be used to model frameworks of beams with multiple wave types.

In the literature, validations of analytical models for vibration transmission on coupled beams have been carried out using Finite Element Method (FEM) [71, 72] and experimental work. Both these approaches will be used in this thesis.

1.3 Thesis aims

This thesis investigates the prediction of vibration transmission using FEM, SEA and ASEA for frameworks of beams with multiple wave types up to high frequencies where Timoshenko beam theory is valid. The frameworks under consideration are comprised of beams that are connected at right-angles to each other.

The four main aims and original aspects of this thesis are:

1. To implement ASEA for frameworks of beams with multiple wave types.
2. To identify the local mode requirements in terms of mode counts and modal overlap factors such that SEA and/or ASEA give reasonable estimates of the dynamic response on frameworks of beams that support multiple wave types.
3. To investigate whether SEA and ASEA models can incorporate both Euler-Bernoulli and Timoshenko theory by changing over from Euler-Bernoulli to Timoshenko group velocity when calculating the coupling loss factors, and to identify a suitable crossover frequency.
4. To investigate whether ASEA can provide more accurate predictions than SEA by accounting for propagation losses and/or indirect coupling (i.e. tunnelling).

1.4 Thesis layout

Chapter 2 describes the different wave types and contains the wave theory derivations used to determine the transmission coefficients between L-, T- and X-junctions for three different models (B, BL and BT models).

Chapter 3 describes Statistical Energy Analysis (SEA) and Advanced Statistical Energy Analysis (ASEA) that are used to predict vibration transmission on coupled frameworks of beams.

Chapter 4 describes Finite Element Methods used to model the frameworks of coupled beams.

Chapter 5 describes the experimental work used to measure material properties of Perspex (Young's modulus and internal loss factors) and vibration level differences on coupled Perspex beams.

Chapter 6 compares measurements, FEM, SEA and ASEA for two models (BL and BT models) of an L-junction, a rectangular beam frame and a three-bay truss beam. This chapter considers both Euler-Bernoulli and Timoshenko theory for FEM, SEA and ASEA models in order to assess (a) the validity of FEM elements and (b) the proposal to implement thick beam theory in SEA and ASEA by accounting for the change in group velocity.

Chapter 7 describes the results from parametric studies using numerical experiments with FEM, SEA and ASEA to investigate:

1. The effect of different junction and boundary conditions with an L-junction.
2. The effect of uncertainty in the material properties on the validity of zero transmission coefficients predicted using wave theory for T- and X-junctions.
3. The effect of uncertainty in the material properties with periodic frameworks of beams using a five-bay truss beam as an example.

2. Wave theory for junctions of beams

2.1 Introduction

In this chapter, descriptions are given of wave equations on beams and solutions of the transmission coefficients for bending, longitudinal and torsional wave excitations on various right-angled, rigid beam junctions which form frame structures. This is in preparation for the calculation of transmission coefficients for combinations of semi-infinite beams. This is to give confidence into the calculation of the coupling loss factors required for the network of beam structures described in chapter 3.

The combination of semi-infinite beams with right angels can be divided into L-, T- and X-junctions. Transmission coefficients for the B model are calculated in one direction and the consistency relationship is used to determine values in the opposite direction. However, this is not possible with the BL and BT models; hence the transmission coefficients are calculated in both directions. Therefore the T-junction is considered as a T123- junction and a T124-junction in which beam 1 is always chosen as the source beam. In all four beam junctions, namely L-, T123-, T124- and X- junctions, two different wave types are individually considered as incident waves with BL or BT model.

2.2 Wave types

2.2.1 Longitudinal waves

For an infinite solid, pure longitudinal waves can occur, but for finite structures such as beams it is a ‘quasi-longitudinal wave’ although for brevity it is often referred to as a longitudinal wave. For quasi-longitudinal waves in beams, the wave motion equation can be found in [5, 6]

$$E\frac{\partial^2(F_{\mathrm{L}},v_{\mathrm{L}})}{\partial x^2}=\rho\frac{\partial^2(F_{\mathrm{L}},v_{\mathrm{L}})}{\partial t^2} \tag{2-1}$$

where E is the Young’s modulus, F_{L} is axial force and v_{L} is axial velocity. The corresponding propagating wave speed is

$$c_{\mathrm{L}} = \sqrt{\frac{E}{\rho}} \tag{2-2}$$

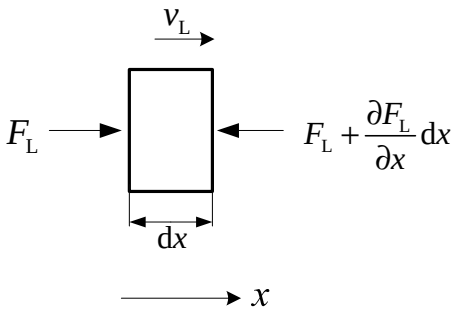

Figure 2.1 Force relation in a beam element for longitudinal wave motion.

From Figure 2.1 one can readily write the force equation according Newton' Law

$$F_{\mathrm{L}} - \left(F_{\mathrm{L}} + \frac{\partial F_{\mathrm{L}}}{\partial x}\mathrm{d}x \right) = \rho A(\mathrm{d}x)\frac{\partial v_{\mathrm{L}}}{\partial t} \tag{2-3}$$

Thus one can solve axial force F_{L} as follows

$$F_{\mathrm{L}} = -\rho A \int \frac{\partial v_{\mathrm{L}}}{\partial t}\mathrm{d}x \tag{2-4}$$

This equation can be used for derivation of axial force when velocity expression is assumed. One can also write another equation about axial force by introducing the force impedance $Z_{\mathrm{L}} = A\sqrt{G\rho} = \rho A c_{\mathrm{L}}$ on a semi-infinite beam [73]

$$F_{\mathrm{L}} = Z_{\mathrm{L}} v_{\mathrm{L}} \tag{2-5}$$

This gives the power transmitted by the axial force in the x direction as [11]

$$\begin{aligned} P_{\mathrm{L}} &= \frac{1}{2}\mathrm{Re}(F_{\mathrm{L}} \cdot v_{\mathrm{L}}^{*}) = \frac{1}{2}\mathrm{Re}(Z_{\mathrm{L}} v_{\mathrm{L}} \cdot v_{\mathrm{L}}^{*}) \\ &= \frac{1}{2}\mathrm{Re}(Z_{\mathrm{L}})\left|v_{\mathrm{L}}\right|^{2} = \frac{1}{2}\rho A c_{\mathrm{L}}\left|v_{\mathrm{L}}\right|^{2} \end{aligned} \tag{2-6}$$

where * indicates the complex conjugate .

2.2.2 Torsional waves

Beams can also support torsional wave motion where all points of the same cross-section experience circumferential displacements about the beam axis. The relationship between the torsional moment M_{T} on each cross-section and the rotation θ_{T} is [5,61]

$$M_{\mathrm{T}} = T\frac{\partial \theta_{\mathrm{T}}}{\partial x} \tag{2-7}$$

where T is the torsional stiffness.

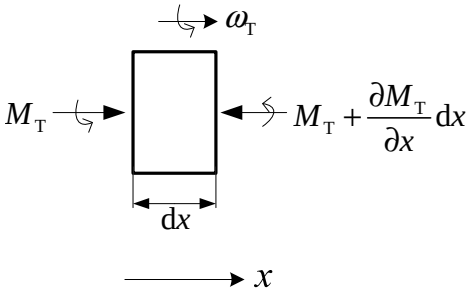

Figure 2.2 Moment relation in a beam element for torsional wave motion.

By calculating the torque equilibrium relation on a small piece of the beam element in Figure 2.2, one has

$$M_{\mathrm{T}} - \left(M_{\mathrm{T}} + \frac{\partial M_{\mathrm{T}}}{\partial x}\mathrm{d}x \right) = \Theta \mathrm{d}x \frac{\partial \omega_{\mathrm{T}}}{\partial t} \tag{2-8}$$

The angular velocity ω_{T} is given by

$$\omega_{\mathrm{T}} = \partial \theta_{\mathrm{T}} / \partial t \tag{2-9}$$

and the mass moment of inertia per unit length is defined as

$$\Theta = \rho J \tag{2-10}$$

Solving equation (2-8) gives

$$M_{\mathrm{T}} = -\Theta \int \frac{\partial \omega_{\mathrm{T}}}{\partial t}\mathrm{d}x \tag{2-11}$$

By combining the two equations (2-7) and (2-8) one can obtain the equation for torsional wave motion [6]

$$T\frac{\partial^2\left(M_{\mathrm{T}},\omega_{\mathrm{T}}\right)}{\partial x^2}=\Theta\frac{\partial^2\left(M_{\mathrm{T}},\omega_{\mathrm{T}}\right)}{\partial t^2} \tag{2-12}$$

The torsional wave speed is then given by

$$c_{\mathrm{T}}=\sqrt{\frac{T}{\Theta}}=\sqrt{\frac{T}{\rho J}} \tag{2-13}$$

For beam with circular cross-section, the torsional stiffness T is the product of shear modulus G and the polar moment of inertia J. So the torsional wave velocity for circular cross-section is

$$c_{\mathrm{T}}=\sqrt{\frac{T}{\rho J}}=\sqrt{\frac{G}{\rho}} \tag{2-14}$$

For a rectangular beam cross-section $b \times h$ (assuming $b \geq h$), the polar moment of inertia is

$$J=\frac{bh^3+b^3h}{12} \tag{2-15}$$

and the torsional stiffness can be calculated using [74,61]

$$T=\frac{Gbh^3}{3}\left[1-\frac{192h}{\pi^5 b}\tanh\left(\frac{\pi b}{2h}\right)\right] \tag{2-16}$$

On a semi-infinite beam the moment impedance is [73]

$$Z_{\mathrm{T}}=\frac{M_{\mathrm{T}}}{\theta_{\mathrm{T}}}=\Theta c_{\mathrm{T}} \tag{2-17}$$

Thus the power transmitted by torsional wave can be calculated as [11]

$$P_{\mathrm{T}} = \frac{1}{2}\mathrm{Re}(M_{\mathrm{T}} \cdot \omega_{\mathrm{T}}^{*}) = \frac{1}{2}\mathrm{Re}(Z_{\mathrm{T}}\omega_{\mathrm{T}} \cdot \omega_{\mathrm{T}}^{*})$$
$$= \frac{1}{2}\mathrm{Re}(Z_{\mathrm{T}})\left|\omega_{\mathrm{T}}\right|^{2} = \frac{1}{2}\Theta c_{\mathrm{T}}\left|\omega_{\mathrm{T}}\right|^{2} \tag{2-18}$$

2.2.3 Bending waves

2.2.3.1 Euler –Bernoulli theory

Analysis of bending wave considers flexural motion along the *y* direction and rotational motion about *z* axis. Generally only pure bending wave is considered in thin beams which have cross-sectional dimensions that are much smaller than the wavelength. Thin beam theory is often referred to as Euler-Bernoulli theory. As the wavelength decreases with frequency, there exists a limiting frequency for thin beam theory. The thin beam limit is defined as the frequency at which the bending wavelength equals six times the cross-sectional dimension undergoing lateral displacement [5].

Take a beam element into consideration shown in Figure 2.3. The rotational inertia of the cross-section for thin beam is ignored when writing the moment equilibrium relation equation. The shear force on the cross-section of thin beam will only make contribution to the lateral displacement ξ. Hence the deflection angle only includes the slope angle caused by the moment. Therefore the angle of rotation (or slope) θ_{B} can be approximately expressed as

$$\theta_{\mathrm{B}} = \frac{\partial \xi}{\partial x} \tag{2-19}$$

Differentiation with respect of time produces the relation between angular velocity ω_{B} and the lateral velocity v_{B} giving

$$\omega_{\mathrm{B}} = \frac{\partial \theta_{\mathrm{B}}}{\partial t} = \frac{\partial^{2} \xi}{\partial x \partial t} = \frac{\partial v_{\mathrm{B}}}{\partial x} \tag{2-20}$$

From the basic geometric analysis, the bending moment can be related to the radius of the neutral surface

$$-\frac{M_{\mathrm{B}}}{EI}=\frac{1}{R_0}=\frac{\dfrac{\partial^2\xi}{\partial x^2}}{\left(1+\left(\dfrac{\partial\xi}{\partial x}\right)^2\right)^{3/2}}\approx\frac{\partial^2\xi}{\partial x^2} \tag{2-21}$$

where I is the moment of inertia of cross-section about z axis. The product of EI is bending stiffness B and the bending moment is usually given as

$$M_{\mathrm{B}}=-EI\frac{\partial^2\xi}{\partial x^2} \tag{2-22}$$

The negative algebraic sign indicates that the direction of the moment is opposite to that which can produce positive curvature.

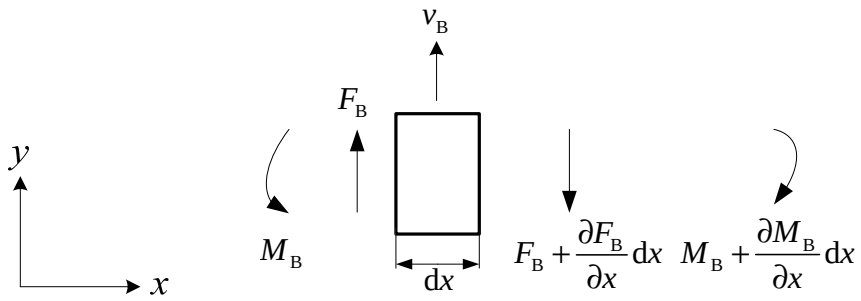

Figure 2.3 Force and moment relation in a beam element for bending wave motion.

By ignoring the moment of inertia, one can write the moment equilibrium of an element on the right side in Figure 2.3 as

$$M_{\mathrm{B}}-\left(M_{\mathrm{B}}+\frac{\partial M_{\mathrm{B}}}{\partial x}\mathrm{d}x\right)-F_{\mathrm{B}}\mathrm{d}x=0 \tag{2-23}$$

Then the shear force is given by

$$F_{\mathrm{B}}=-\frac{\partial M_{\mathrm{B}}}{\partial x}=EI\frac{\partial^3\xi}{\partial x^3} \tag{2-24}$$

Differentiating with respect to time for equations (2-22) and(2-24), one can solve the moment and shear force in terms of the velocity

$$M_{\mathrm{B}} = -EI\int \frac{\partial^2 v_{\mathrm{B}}}{\partial x^2}\mathrm{d}t \tag{2-25}$$

$$F_{\mathrm{B}} = EI\int \frac{\partial^3 v_{\mathrm{B}}}{\partial x^3}\mathrm{d}t \tag{2-26}$$

The velocity can be described in the form $v_{\mathrm{B}} = v_{\mathrm{B}}(x)e^{i\omega t}$, which allows the moment and force to be written as

$$M_{\mathrm{B}} = -\frac{EI}{i\omega}\frac{\partial^2 v_{\mathrm{B}}(x)}{\partial x^2} \tag{2-27}$$

$$F_{\mathrm{B}} = \frac{EI}{i\omega}\frac{\partial^3 v_{\mathrm{B}}(x)}{\partial x^3} \tag{2-28}$$

According to the Newton's law, the force relation of an element in the *y* direction is

$$F_{\mathrm{B}} - \left(F_{\mathrm{B}} + \frac{\partial F_{\mathrm{B}}}{\partial x}\mathrm{d}x\right) = \rho A\frac{\partial v_{\mathrm{B}}}{\partial t} \tag{2-29}$$

where *A* is the cross-section area.

Then the one-dimensional form of bending wave equation is [5, 6]

$$-EI\frac{\partial^4}{\partial x^4}(v_{\mathrm{B}}, \omega_{\mathrm{B}}, M_{\mathrm{B}}, F_{\mathrm{B}}) = \rho A\frac{\partial^2}{\partial t^2}(v_{\mathrm{B}}, \omega_{\mathrm{B}}, M_{\mathrm{B}}, F_{\mathrm{B}}) \tag{2-30}$$

This fourth-order differential equation has four roots corresponding to propagating waves and near-fields in the positive and the negative direction. The bending wavenumber is

$$k = \sqrt[4]{\frac{\rho A\omega^2}{EI}} \tag{2-31}$$

The phase velocity of bending wave is defined by the ratio of angular velocity to wavenumber

$$c_{\mathrm{B}} = \frac{\omega}{k} = \sqrt[4]{\frac{EI\omega^2}{\rho A}} \tag{2-32}$$

In contrast to longitudinal and torsional waves, the phase velocity for bending wave is frequency dependant; hence, bending waves are described as dispersive. For this reason it is necessary to calculate the group velocity at which the bending energy travels since the group velocity is not the same as phase velocity. From equation (2-31) one can solve

$$c_{\mathrm{g}} = \frac{\mathrm{d}\omega}{\mathrm{d}k} = 2\frac{\omega}{k} = 2c_{\mathrm{B}} \tag{2-33}$$

When evaluating the power carried by bending waves, one has to take the both flexural wave motion and rotational motion into account [81]. From Fahy [73] the force impedance on semi-infinite beam is

$$Z_{\mathrm{B}} = \frac{F_{\mathrm{B}}}{v_{\mathrm{B}}} = \frac{EIk_{\mathrm{B}}^3}{\omega(1-i)} = \frac{1+i}{2}\rho A c_{\mathrm{B}} \tag{2-34}$$

and the moment impedance on semi-infinite beam is

$$Z_{\mathrm{M}} = \frac{M_{\mathrm{B}}}{\omega_{\mathrm{B}}} = \frac{EIk_{\mathrm{B}}}{\omega(1+i)} = \frac{1-i}{2}\frac{\rho A c_{\mathrm{B}}}{k_{\mathrm{B}}^2} \tag{2-35}$$

Thus the bending wave power on a beam can be expressed as

$$\begin{aligned} P_{\mathrm{B}} &= \frac{1}{2}\mathrm{Re}\left(F_{\mathrm{B}} \cdot v_{\mathrm{B}}^*\right) + \frac{1}{2}\mathrm{Re}\left(M_{\mathrm{B}} \cdot \omega_{\mathrm{B}}^*\right) = \frac{1}{2}\mathrm{Re}\left(Z_{\mathrm{B}} v_{\mathrm{B}} \cdot v_{\mathrm{B}}^*\right) + \frac{1}{2}\mathrm{Re}\left(Z_{\mathrm{M}}\omega_{\mathrm{B}} \cdot \omega_{\mathrm{B}}^*\right) \\ &= \frac{1}{2}\mathrm{Re}(Z_{\mathrm{B}})\left|v_{\mathrm{B}}\right|^2 + \frac{1}{2}\mathrm{Re}(Z_{\mathrm{M}})\left|\omega_{\mathrm{B}}\right|^2 \end{aligned} \tag{2-36}$$

Considering the relationships (2-20), (2-34) and (2-35) the bending wave power is calculated as

$$P_{\mathrm{B}} = \frac{1}{2}\mathrm{Re}(Z_{\mathrm{B}})\left|v_{\mathrm{B}}\right|^2 + \frac{1}{2}\mathrm{Re}(Z_{\mathrm{M}})k_B^2\left|v_{\mathrm{B}}\right|^2 = \rho A c_{\mathrm{B}}\left|v_{\mathrm{B}}\right|^2 \tag{2-37}$$

2.2.3.2 Timoshenko theory

In contrast to Euler-Bernoulli theory, both rotatory inertia and shear deformation are considered in Timoshenko theory [75]. The angle of rotation consists of two parts: the angle for pure transverse bending θ and the angle γ for shear force deformation. The total angle of rotation (or slope) is

$$\frac{\mathrm{d}\xi}{\mathrm{d}x} = \theta + \gamma \tag{2-38}$$

The shear force is given by

$$F = -K\gamma \tag{2-39}$$

where K is the shear stiffness. For homogeneous beam cross-section, the shear stiffness obeys

$$K = \frac{GA}{\kappa} \tag{2-40}$$

The parameter κ is called the 'shear stress distribution parameter' which is related to the shape of the beam cross-section [5]. For a rectangular cross-section, it is 1.2, and for circular section it is 1.18. In some literature [e.g. 76,77] the shear coefficient κ' is used in Timoshenko beam theory, which is related to the shear stress distribution parameter by

$$\kappa' = \frac{1}{\kappa} \tag{2-41}$$

The table below is taken from [77] and gives the calculation of shear coefficient in terms of Poisson's ratio μ for different cross-sections.

Table 2.1 Shear coefficients

Cross-section	Shear coefficient κ'
Circular	$\frac{6(1+\mu)}{7+6\mu}$
Hollow circular $m = r_{\text{inner}} / r_{\text{outer}}$	$\frac{6(1+\mu)(1+m^2)^2}{(7+6\mu)(1+m^2)^2+(20+12\mu)m^2}$
Rectangular	$\frac{10(1+\mu)}{12+11\mu}$
Thin-walled round tube	$\frac{2(1+\mu)}{4+3\mu}$
Thin-walled square tube	$\frac{20(1+\mu)}{48+39\mu}$

Substituting (2-38) and (2-40) into (2-39) gives

$$F = -\frac{GA}{\kappa}\gamma = -\frac{GA}{\kappa}\left(\frac{\mathrm{d}\xi}{\mathrm{d}x} - \theta\right) \tag{2-42}$$

As with the Euler-Bernoulli theory, the bending moment is given by

$$M = EI\frac{\mathrm{d}\theta}{\mathrm{d}x} \tag{2-43}$$

Equilibrium of rotational motion gives the following equation of motion

$$F\mathrm{d}x + M - \left(M + \frac{\partial M}{\partial x}\mathrm{d}x\right) = -\rho I \mathrm{d}x \frac{\partial^2 \theta}{\partial t^2} \tag{2-44}$$

and the differential equation for force in the *y* direction is

$$F - \left(F + \frac{\partial F}{\partial x}\mathrm{d}x\right) = \rho A \mathrm{d}x \frac{\partial^2 \xi}{\partial t^2} \tag{2-45}$$

Inserting (2-42) and (2-43) into (2-44) and (2-45) generates the following equations

$$\frac{GA}{\kappa}\left(\frac{\partial \xi}{\partial x}-\theta\right)+EI\frac{\partial^2\theta}{\partial x^2}-\rho I\frac{\partial^2\theta}{\partial t^2}=0 \tag{2-46}$$

$$\frac{GA}{\kappa}\left(\frac{\partial^2 \xi}{\partial x^2}-\frac{\partial\theta}{\partial x}\right)-\rho A\frac{\partial^2\xi}{\partial t^2}=0 \tag{2-47}$$

By eliminating the parameter θ one can obtain the following fourth-order differential equation for bending wave motion on a Timoshenko beam

$$EI\frac{\partial^4\xi}{\partial x^4}+\rho A\frac{\partial^2\xi}{\partial t^2}-\rho I\left(1+\frac{E\kappa}{G}\right)\frac{\partial^4\xi}{\partial x^2\partial t^2}+\frac{\rho^2 I\kappa}{G}\frac{\partial^4\xi}{\partial t^4}=0 \tag{2-48}$$

The detailed derivation is given in Appendix 1. In comparison with Euler-Bernoulli theory, one can find that three additional terms are introduced. Timoshenko [75] shows that only the term with the coefficient ρI appears when only the moment of inertia of the cross-section is taken into account. Note that the fourth item with coefficient $\rho I\frac{E\kappa}{G}$ is always larger than the third term because E is greater than G, and κ is always larger than unit for homogeneous structures [5]. Hence it can be concluded that shear deformation is more significant than the moment of inertia of cross-section for a thick beam. From Cremer *et al* [5], the last term in equation (2-48) is negligible since it represents the higher-order correction which results from the combined effects of moment of inertia and shear deformation.

To solve this equation, we assume the following general solution by separating variables

$$\xi(x,t)=e^{i\omega t}\phi(x) \tag{2-49}$$

Inserting this equation into (2-48) yields

$$\frac{\mathrm{d}^4\phi(x)}{\mathrm{d}x^4}+a\frac{\mathrm{d}^2\phi(x)}{\mathrm{d}x^2}+\frac{b}{4}\phi(x)=0 \tag{2-50}$$

where

$$a=\frac{\rho\omega^2}{M_r} \tag{2-51}$$

$$b = \frac{4\rho^2\omega^2\kappa}{EG}\left(\omega^2 - \omega_{co}{}^2\right) \tag{2-52}$$

which are defined by the reduced modulus, M_r, [78] and the second spectrum cut-off frequency, f_{co} [79] as follows

$$\frac{1}{M_r} = \frac{1}{E} + \frac{\kappa}{G} \tag{2-53}$$

$$\omega_{co} = 2\pi f_{co} = \sqrt{\frac{GA}{\rho I \kappa}} \tag{2-54}$$

For beams with idealised boundary conditions, Stephen *et al* [80,79] propose that Timoshenko theory should only be used below the second spectrum cut-off frequency.

The characteristic equation corresponding to the fourth-order differential equation (2-50) is

$$k^4 + ak^2 + \frac{b}{4} = 0 \tag{2-55}$$

This equation has four solutions of the wavenumber k

$$\begin{aligned} k_1 &= -\sqrt{\frac{-a - \sqrt{a^2 - b}}{2}} \qquad & k_2 &= \sqrt{\frac{-a - \sqrt{a^2 - b}}{2}} \\ k_3 &= -\sqrt{\frac{-a + \sqrt{a^2 - b}}{2}} \qquad & k_4 &= \sqrt{\frac{-a + \sqrt{a^2 - b}}{2}} \end{aligned} \tag{2-56}$$

and the general solution for the Timoshenko wave equation (2-48) can be written as

$$\xi = e^{i\omega t}\left(a_1 e^{k_1 x} + a_2 e^{k_2 x} + a_3 e^{k_3 x} + a_4 e^{k_4 x}\right) \tag{2-57}$$

where a_1, a_2, a_3 and a_4 are to be determined by the initial conditions. As a is positive, a^2-b can also be shown to be positive as follows

$$
\begin{aligned}
a^2 - b &= \left(\frac{\rho\omega^2}{M_\mathrm{r}}\right)^2 - \frac{4\rho^2\omega^2\kappa}{EG}\left(\omega^2 - {\omega_\mathrm{co}}^2\right) \\
&= \left[\rho^2\left(\frac{E\kappa+G}{EG}\right)^2 - \frac{4\rho^2\kappa}{EG}\right]\omega^4 + \frac{4\rho^2\kappa}{EG}{\omega_\mathrm{co}}^2\omega^2 \\
&= \rho^2\left(\frac{E\kappa-G}{EG}\right)^2\omega^4 + \frac{4\rho^2\kappa}{EG}{\omega_\mathrm{co}}^2\omega^2 \quad \geq 0
\end{aligned}
\tag{2-58}
$$

The two variables k_1 and k_2 are purely imaginary and correspond to positive and negative traveling waves. When $\omega \leq \omega_\mathrm{co}$, then b is negative. This results in a positive value for $-a + \sqrt{a^2 - b}$. Thus k_3 and k_4 are real values which represent nearfield waves. However, the two variables k_3 and k_4 will be purely imaginary when $\omega \geq \omega_\mathrm{co}$. In this case the evanescent near field waves become propagating waves. The parameter ω_co is also called second spectrum cut-off frequency in Timoshenko beam theory.

The bending phase velocity of the propagating wave can be calculated using

$$
c_\mathrm{B} = \frac{\omega}{ik_1} \tag{2-59}
$$

To determine the group velocity for Timoshenko theory, differentiating equation (2-55) with respect to k gives

$$
4k^3 + \frac{\mathrm{d}a}{\mathrm{d}\omega}\frac{\mathrm{d}\omega}{\mathrm{d}k}k^2 + 2ak + \frac{1}{4}\frac{\mathrm{d}b}{\mathrm{d}\omega}\frac{\mathrm{d}\omega}{\mathrm{d}k} = 0 \tag{2-60}
$$

hence for the propagating bending wave (k_1) in the positive x-direction, the group velocity is

$$
c_\mathrm{g} = \frac{\mathrm{d}\omega}{\mathrm{d}k_1} = -\frac{4k_1^3 + 2ak_1}{\frac{\mathrm{d}a}{\mathrm{d}\omega}k_1^2 + \frac{1}{4}\frac{\mathrm{d}b}{\mathrm{d}\omega}} \tag{2-61}
$$

and inserting a and b gives

$$
c_\mathrm{g} = -\frac{2EGk_1^3 + \rho(E\kappa+G)k_1\omega^2}{2\rho^2\kappa\omega^3 + \rho(E\kappa+G)k_1^2\omega - \rho^2\kappa\omega_\mathrm{co}^2\omega} \tag{2-62}
$$

As the wavenumber, k_1, is complex, the imaginary part of the group velocity is used in the calculation of the coupling loss factors.

2.2.3.3 Thin beam limit

As noted earlier, Euler-Bernoulli theory applies when the wavelength is much larger than the cross-sectional dimensions. A crossover frequency from the Euler-Bernoulli to Timoshenko theory can be defined by the percentage difference between the phase velocity for Euler-Bernoulli theory and that of the Timoshenko theory. Assuming the solution of the equation (2-48) has a sinusoidal form with unit amplitude

$$\xi(x,t) = e^{-ik_B x} e^{i\omega t} \tag{2-63}$$

Inserting this solution into equation (2-48) and ignoring the last term as justified by Cremer *et al* [5] produce

$$\frac{EI}{\rho A}\left(\frac{\omega}{c_B}\right)^4 - \omega^2 - \frac{I}{A}\left(1+\frac{E\kappa}{G}\right)\omega^2\left(\frac{2\pi}{\lambda_B}\right)^2 = 0 \tag{2-64}$$

which can be rewritten as

$$\frac{c_B}{c_{B(thin)}} = \left(1+4\pi^2\left(1+\frac{E\kappa}{G}\right)\frac{I}{A\lambda_B{}^2}\right)^{-\frac{1}{4}} \tag{2-65}$$

where $c_{B(thin)}$ is the phase velocity of Euler-Bernoulli theory defined in equation (2-32). For circular cross-section with diameter d,

$$\frac{I}{A\lambda_B{}^2} = \frac{1}{16}\left(\frac{d}{\lambda_B}\right)^2 \tag{2-66}$$

and for rectangular cross-section,

$$\frac{I}{A\lambda_B{}^2} = \frac{1}{12}\left(\frac{h}{\lambda_B}\right)^2 \tag{2-67}$$

In both cases this term approaches zero where the wavelength is much larger than the dimensions of beam cross-section. Thus, using the second-order Taylor expansion on the right side, equation (2-65) can be rewritten as

$$\frac{c_{\mathrm{B}}}{c_{\mathrm{B(thin)}}} \approx 1-\pi^2\left(1+\frac{E\kappa}{G}\right)\frac{I}{A\lambda_{\mathrm{B}}{}^2} \tag{2-68}$$

Consider a beam with rectangular cross-section (κ=1.2), and the Poisson ratio μ=0.3, equation (2-68) becomes

$$\frac{c_{\mathrm{B}}}{c_{\mathrm{B(thin)}}} = 1-3.39\left(\frac{h}{\lambda_{\mathrm{B}}}\right)^2 \tag{2-69}$$

Thus, the difference would be less than 10% only when the wavelength satisfies

$$\lambda_{\mathrm{B}} \geq 5.8h \tag{2-70}$$

Following the approach by Hopkins [61], the percentage difference between phase velocities is defined as

$$\frac{c_{\mathrm{B(thin)}}-c_{\mathrm{B}}}{c_{\mathrm{B(thin)}}} = \frac{X\%}{100} \tag{2-71}$$

Combining equations (2-71) and (2-68) gives

$$\frac{X\%}{100} = \pi^2\left(1+\frac{E\kappa}{G}\right)\frac{I}{A\lambda_{\mathrm{B}}{}^2} \tag{2-72}$$

From the relationship between wavelength and wavenumber, one can calculate that

$$\lambda_{\mathrm{B}}{}^2 = \left(\frac{2\pi}{k_{\mathrm{B}}}\right)^2 = \frac{2\pi}{f}\sqrt{\frac{EI}{\rho A}} \tag{2-73}$$

By inserting equation (2-73) into equation (2-72) one can get the thin beam bending limit, $f_{\mathrm{B(thin)}}$, for an X% difference between thin beam and thick beam phase velocity

$$f_{\mathrm{B(thin)}} = \frac{X\%}{100}\frac{2}{\pi}\sqrt{\frac{EA}{\rho I}}\left(1+\frac{E\kappa}{G}\right)^{-1} \tag{2-74}$$

or in terms of the longitudinal phase velocity in beams

$$f_{\mathrm{B(thin)}} = \frac{X\%}{100}\frac{2c_{\mathrm{L}}}{\pi}\sqrt{\frac{A}{I}}\left(1+\frac{E\kappa}{G}\right)^{-1} \tag{2-75}$$

Note the thin beam bending limit can also be applied for plates and Cremer *et al* [5] based the thin plate limit on X=10%.

2.2.4 Modal density and modal overlap

When studying coupled beams the exact boundary conditions are not always known exactly, but idealised boundary conditions can be used to give analytical calculations of the natural frequencies for the isolated beams (i.e. for local modes which are relevant to modelling with SEA and ASEA). Thus the local modes for isolated beams with different boundary conditions are given in Table 2.2 [73].

Table 2.2 Natural frequencies for beams.

Wave type	Boundary condition	Natural frequency (Hz)
Longitudinal	Clamped-clamped, Free-free	$\frac{n}{2L}c_{\mathrm{L}}$, n=1, 2, 3, …
	Clamped-free	$\frac{2n-1}{4L}c_{\mathrm{L}}$, n=1, 2, 3, …
Torsional	Clamped-clamped, Free-free	$\frac{n}{2L}c_{\mathrm{T}}$, n=1, 2, 3, …
	Clamped-free	$\frac{2n-1}{4L}c_{\mathrm{T}}$, n=1, 2, 3, …
Bending	Clamped-clamped, Free-free	$\frac{\pi}{8}\sqrt{\frac{EI}{\rho A}}\left(\frac{2n+1}{L}\right)^2$, n=1, 2, 3, …
	Clamped-free	$\frac{\pi}{8}\sqrt{\frac{EI}{\rho A}}\left(\frac{2n-1}{L}\right)^2$, n=1, 2, 3, …
	Clamped-pinned, Free-pinned	$\frac{\pi}{32}\sqrt{\frac{EI}{\rho A}}\left(\frac{4n+1}{L}\right)^2$, n=1, 2, 3, …
	Pinned-pinned	$\frac{\pi}{2}\sqrt{\frac{EI}{\rho A}}\left(\frac{n}{L}\right)^2$, n=1, 2, 3, …

With group velocities for different wave types in the former sections, one can calculate the statistical modal density, $n(f)$, using

$$n(f) = \frac{2L}{c_g} \tag{2-76}$$

The modal overlap factor, M, is defined to indicate the degree of overlap in the modal response.

$$M = \frac{\Delta f_{3dB}}{\Delta f} = f \eta n(f) \tag{2-77}$$

where Δf_{3dB} is the half power bandwidth, Δf is the average frequency-spacing between adjacent mode frequencies, and η is the loss factor.

2.3 Properties of beams used for parametric studies and calculation examples for wave theory transmission coefficients

Along with the derivations on basic beam junctions, the material properties and dimensions for these models are given in Table 2.3.

Table 2.3 Material properties and dimensions of beams used for parametric studies and calculation examples for wave theory transmission coefficients.

Material	Density (kg/m^3)	Young's modulus (Pa)	Cross-section (m)	Poisson's ratio	Length of beam 1 and 2 (m)	Internal loss factor
Perspex	1250	6.9×10^9	0.02x0.01	0.3	1.3, 1.0	0.06

Low mode counts tend to occur in beam systems, particularly for longitudinal wave motion in the low-frequency range. Figure 2.4, Figure 2.5, Figure 2.6, Figure 2.7, Figure 2.8 and Figure 2.9 show the local mode counts for Type A bending, longitudinal, Type B bending and torsional modes for the two isolated beams (lengths, 1.3m and 1.0 m) for one-third octave bands over the frequency range from 10 Hz to 20 kHz.

These mode counts are calculated assuming three boundary conditions. These are pinned-pinned, pinned-free, and free-free. The results apply directly to the isolated beams with these idealised boundary conditions and are indicative of the mode counts for the coupled beams in the junctions and frameworks.

The first longitudinal mode occurs in the 1000 Hz one-third octave band for the pinned-pinned and free-free 1.3 m beam, and in the 500 Hz one-third octave band for the pinned-free 1.3 m beam. The first torsional mode occurs in the 400 Hz one-third octave band for the pinned-pinned and free-free 1.3 m beam, while it is in the 200 Hz one-third octave band for the free-pinned 1.3 m beam.

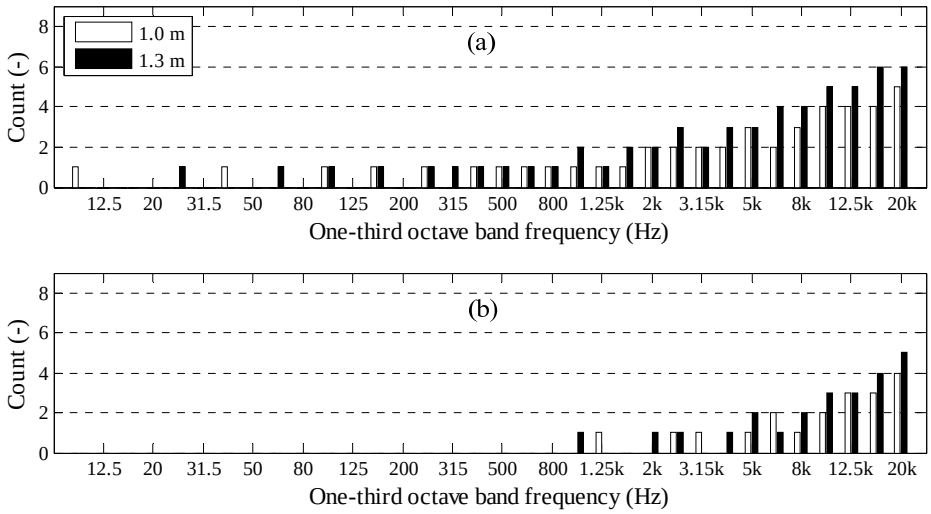

Figure 2.4 Mode counts in one-third octave bands for pinned-pinned beam: (a) Type A bending wave, (b) longitudinal wave.

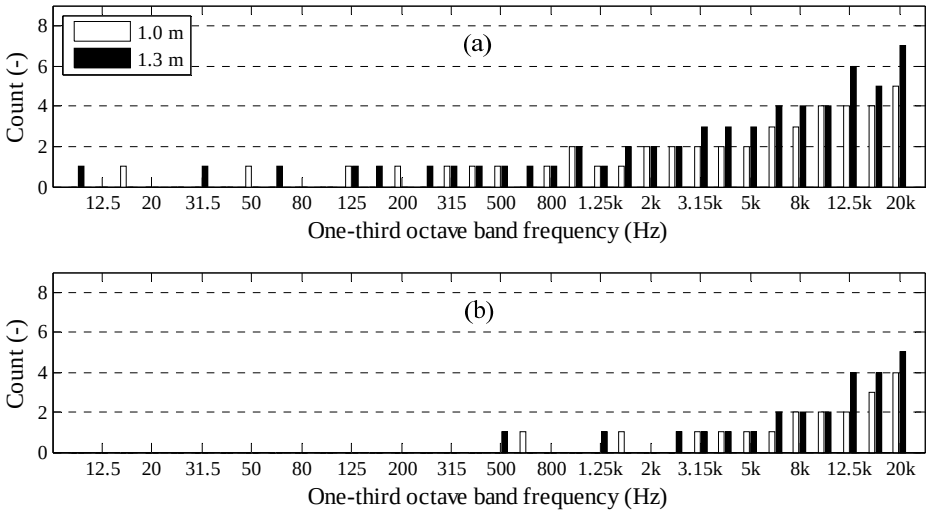

Figure 2.5 Mode counts in one-third octave bands for free-pinned beam: (a) Type A bending wave, (b) longitudinal wave.

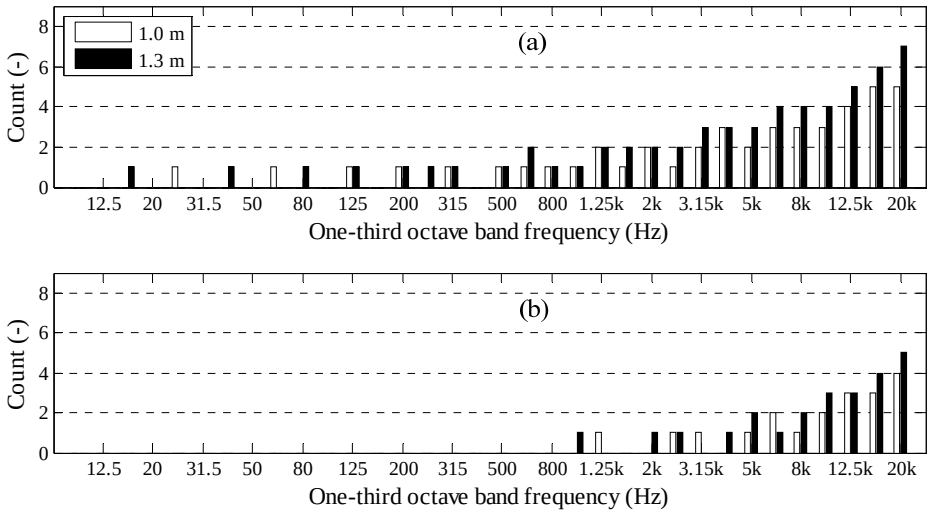

Figure 2.6 Mode counts in one-third octave bands for free-free beam: (a) Type A bending wave, (b) longitudinal wave.

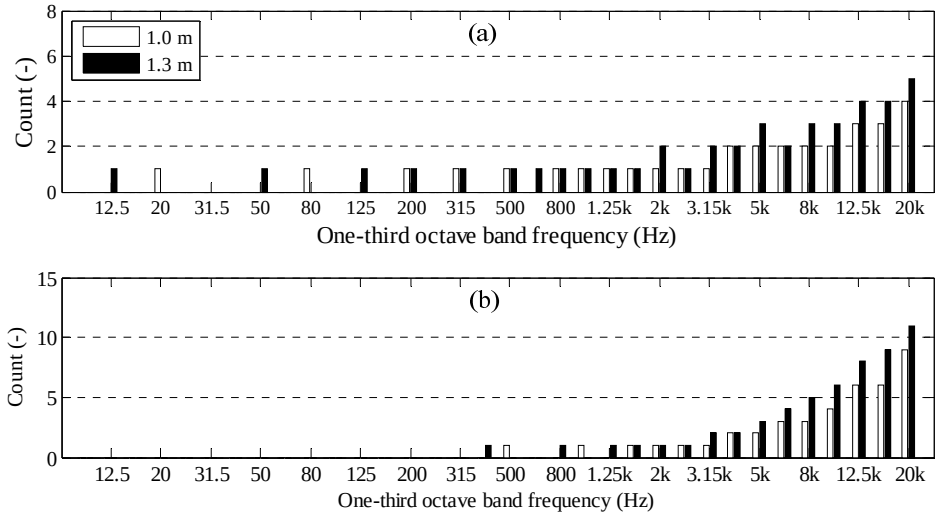

Figure 2.7 Mode counts in one-third octave bands for pinned-pinned beam: (a) Type B bending wave, (b) torsional wave.

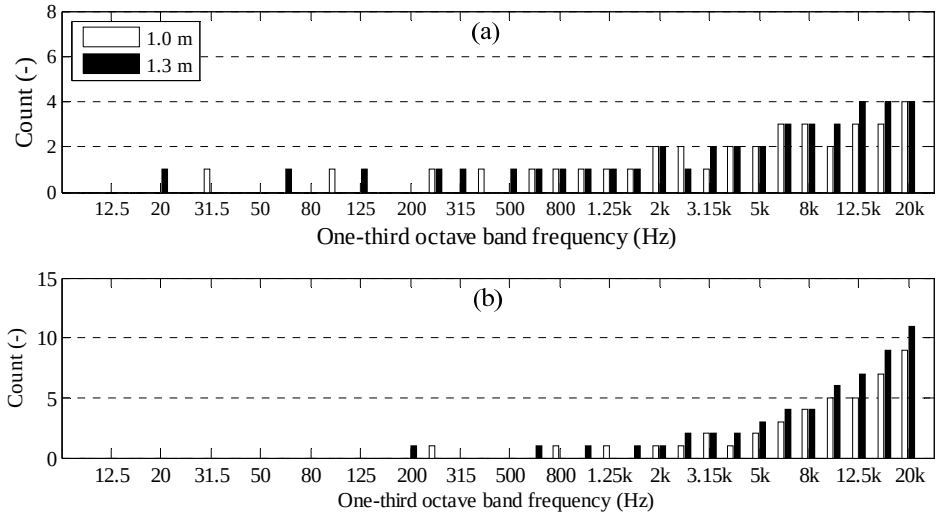

Figure 2.8 Mode counts in one-third octave bands for free-pinned beam: (a) Type B bending wave, (b) torsional wave.

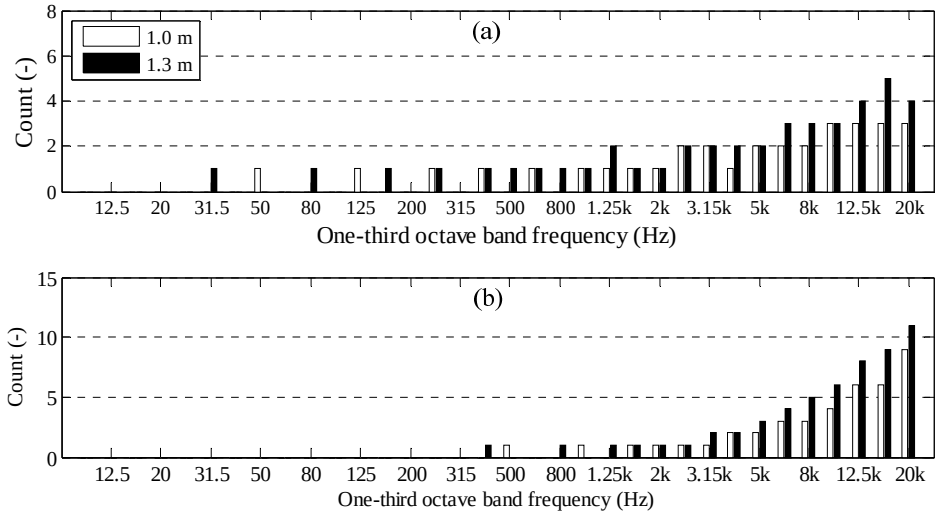

Figure 2.9 Mode counts in one-third octave bands for free-free beam: (a) Type B bending wave, (b) torsional wave.

2.4 Bending only model (B model)

For a bending only model, Craik [81] solved the reflection and transmission coefficients in detail for plates that form X-junction, T-junction, and L-junction from the wave fields of displacements. These results can be readily converted into a bending only model for beam junctions as long as the incident wave angle is zero. This section derives the

transmission coefficients based on the wave fields of velocity for consistency with the BL and BT models derived later in this chapter.

For B model, a rigid massless junction beam is used to transmit bending moments with zero displacement (pinned) at the beam junction itself. The derivation is initially shown for an X-junction, as this can subsequently be used to derive transmission coefficients for the T- and L-junctions.

2.4.1 X-junction

The coordinate system for an X-junction is shown in Figure 2.10 showing the bending moments and the velocities for each beam. It is assumed that beams 1 and 3 are identical, as are beams 2 and 4.

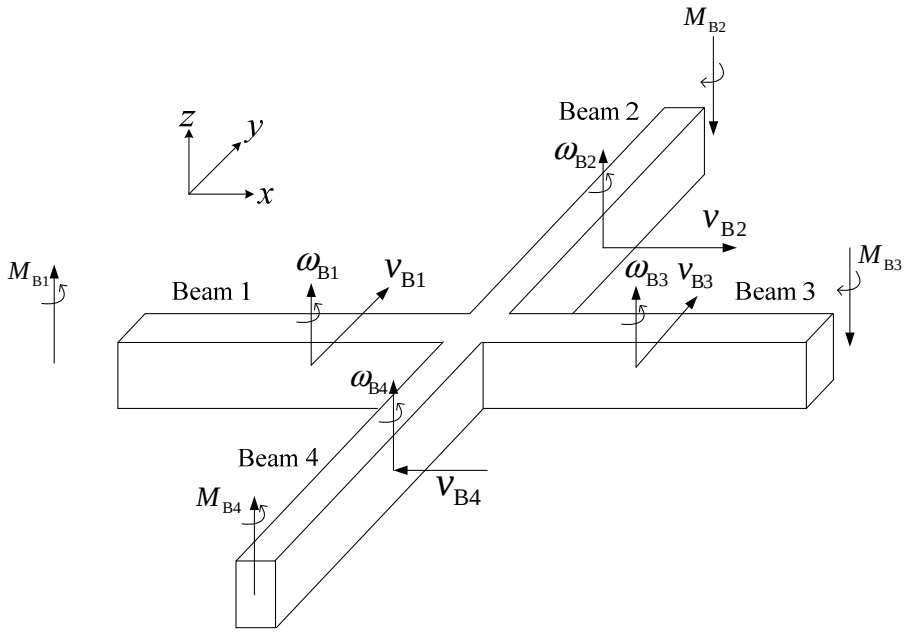

Figure 2.10 X-junction: B model, Type A bending wave excitation on beam 1.

Consider an incident bending wave (Type A) with unit amplitude travelling in the positive *x*-direction towards the junction on beam 1, the velocity of the incident wave is

$$v_{B1+} = e^{-ik_{B1}x} e^{i\omega t} \tag{2-78}$$

The bending wave field of beam 1 can be described as the sum of incident wave, reflected wave and nearfield. That is

$$v_{\mathrm{B1}} = \left(e^{-ik_{\mathrm{B1}}x} + r_{\mathrm{B1B1}}e^{ik_{\mathrm{B1}}x} + r_{\mathrm{N1}}e^{k_{\mathrm{B1}}x}\right)e^{i\omega t} \tag{2-79}$$

In beam 2, 3 and 4, the bending velocities can be written as the sum of the transmitted bending wave and nearfield:

$$v_{\mathrm{B2}} = \left(t_{\mathrm{B1B2}}e^{-ik_{\mathrm{B2}}y} + t_{\mathrm{N2}}e^{-k_{\mathrm{B2}}y}\right)e^{i\omega t} \tag{2-80}$$

$$v_{\mathrm{B3}} = \left(t_{\mathrm{B1B3}}e^{-ik_{\mathrm{B3}}x} + t_{\mathrm{N3}}e^{-k_{\mathrm{B3}}x}\right)e^{i\omega t} \tag{2-81}$$

$$v_{\mathrm{B4}} = -\left(t_{\mathrm{B1B4}}e^{ik_{\mathrm{B4}}y} + t_{\mathrm{N4}}e^{k_{\mathrm{B4}}y}\right)e^{i\omega t} \tag{2-82}$$

where subscripts B and N represent bending waves and nearfields respectively, *r* indicates the complex amplitude of the reflected wave, *t* indicates the complex amplitude of the transmitted wave.

For the bending only model, the beam junction is assumed to be free to rotate and can only transmit moments (i.e. a pinned boundary condition) where

$$v_{\mathrm{B1}} = 1 + r_{\mathrm{B1B1}} + r_{\mathrm{N1}} = 0 \tag{2-83}$$

$$v_{\mathrm{B2}} = t_{\mathrm{B1B2}} + t_{\mathrm{N2}} = 0 \tag{2-84}$$

$$v_{\mathrm{B3}} = t_{\mathrm{B1B3}} + t_{\mathrm{N3}} = 0 \tag{2-85}$$

$$v_{\mathrm{B4}} = -t_{\mathrm{B1B4}} - t_{\mathrm{N4}} = 0 \tag{2-86}$$

Continuity of angular velocity at the junction requires that

$$\frac{\partial v_{\mathrm{B1}}}{\partial x} = \frac{\partial v_{\mathrm{B2}}}{\partial y} \tag{2-87}$$

$$\frac{\partial v_{\mathrm{B1}}}{\partial x} = \frac{\partial v_{\mathrm{B3}}}{\partial x} \tag{2-88}$$

$$\frac{\partial v_{\mathrm{B1}}}{\partial x} = \frac{\partial v_{\mathrm{B4}}}{\partial y} \tag{2-89}$$

Inserting the velocities into the last three equations gives

$$-ik_{B1}+ik_{B1}r_{B1B1}+k_{B1}r_{N1}=-ik_{B2}t_{B1B2}-k_{B2}t_{N2} \tag{2-90}$$

$$-ik_{B1}+ik_{B1}r_{B1B1}+k_{B1}r_{N1}=-ik_{B3}t_{B1B3}-k_{B3}t_{N3} \tag{2-91}$$

$$-ik_{B1}+ik_{B1}r_{B1B1}+k_{B1}r_{N1}=-ik_{B4}t_{B1B4}-k_{B4}t_{N4} \tag{2-92}$$

The moment equilibrium condition requires that the sum of all the moments acting on the junction equals zero, hence

$$M_{B1}-M_{B2}-M_{B3}+M_{B4}=0 \tag{2-93}$$

By using equation(2-25), the moments due to bending motions are calculated as

$$\begin{aligned} M_{B1}&=-B_1\int\frac{\partial^2 v_{B1}}{\partial x^2}\mathrm{d}t=\frac{-B_1}{i\omega}\left[\left(-ik_{B1}\right)^2+\left(ik_{B1}\right)^2 r_{B1B1}+k_{B1}^2 r_{N1}\right]e^{i\omega t}\\ &=\frac{-B_1k_{B1}^2}{i\omega}\left(-1-r_{B1B1}+r_{N1}\right)e^{i\omega t}\end{aligned} \tag{2-94}$$

$$\begin{aligned} M_{B2}&=-B_2\int\frac{\partial^2 v_{B2}}{\partial y^2}\mathrm{d}t=\frac{-B_2}{i\omega}\left[\left(-ik_{B2}\right)^2 t_{B1B2}+\left(-k_{B2}\right)^2 t_{N2}\right]e^{i\omega t}\\ &=\frac{-B_2k_{B2}^2}{i\omega}\left(-t_{B1B2}+t_{N2}\right)e^{i\omega t}\end{aligned} \tag{2-95}$$

$$\begin{aligned} M_{B3}&=-B_3\int\frac{\partial^2 v_{B3}}{\partial x^2}\mathrm{d}t=\frac{-B_3}{i\omega}\left[\left(-ik_{B3}\right)^2 t_{B1B3}+\left(-k_{B3}\right)^2 t_{N3}\right]e^{i\omega t}\\ &=\frac{-B_3k_{B3}^2}{i\omega}\left(-t_{B1B3}+t_{N3}\right)e^{i\omega t}\end{aligned} \tag{2-96}$$

$$\begin{aligned} M_{B4}&=-B_4\int\frac{\partial^2 v_{B4}}{\partial y^2}\mathrm{d}t=\frac{-B_4}{i\omega}\left[\left(-ik_{B4}\right)^2 t_{B1B4}+\left(-k_{B4}\right)^2 t_{N4}\right]e^{i\omega t}\\ &=\frac{-B_4k_{B4}^2}{i\omega}\left(-t_{B1B4}+t_{N4}\right)e^{i\omega t}\end{aligned} \tag{2-97}$$

Then the equation (2-93) becomes

$$\begin{aligned} &k_{B1}^2B_1+k_{B1}^2B_1r_{B1B1}-k_{B1}^2B_1r_{N1}-k_{B2}^2B_2t_{B1B2}+k_{B2}^2B_2t_{N2}\\ &-k_{B3}^2B_3t_{B1B3}+k_{B3}^2B_3t_{N3}-k_{B4}^2B_4t_{B1B4}+k_{B4}^2B_4t_{N4}=0\end{aligned} \tag{2-98}$$

From equations (2-83), (2-84), (2-85) and (2-86) one can get the four parameters r_{N1}, t_{N2}, t_{N2} and t_{N4} in terms of r_{B1B1}, t_{B1B2}, t_{B1B3} and t_{B1B4}. Combining equations (2-90), (2-91), (2-92) and (2-98), and eliminating r_{N1}, t_{N2}, t_{N3} and t_{N4} gives the following equations of r_{B1B1}, t_{B1B2}, t_{B1B3} and t_{B1B4}, which can be solved to give the amplitude of the transmitted waves.

$$\begin{bmatrix} -k_{B1}+ik_{B1} & -k_{B2}+ik_{B2} & 0 & 0 \\ -k_{B1}+ik_{B1} & 0 & -k_{B3}+ik_{B3} & 0 \\ -k_{B1}+ik_{B1} & 0 & 0 & -k_{B4}+ik_{B4} \\ k_{B1}^2B_1 & -k_{B2}^2B_2 & -k_{B3}^2B_3 & -k_{B4}^2B_4 \end{bmatrix} \begin{bmatrix} r_{B1B1} \\ t_{B1B2} \\ t_{B1B3} \\ t_{B1B4} \end{bmatrix} = \begin{bmatrix} k_{B1}+ik_{B1} \\ k_{B1}+ik_{B1} \\ k_{B1}+ik_{B1} \\ -k_{B1}^2B_1 \end{bmatrix} \quad (2\text{-}99)$$

It is assumed that beams 1 and 3 are identical, as are beams 2 and 4, such that $k_{B1}=k_{B3}$, $k_{B2}=k_{B4}$. Two parameters χ and ψ can now be defined as

$$\chi=\frac{k_{B2}}{k_{B1}},\quad \psi=\frac{B_2k_{B2}^2}{B_1k_{B1}^2} \quad (2\text{-}100)$$

Solving the matrix equation (2-99) gives

$$r_{B1B1}=\frac{(1-i)\psi-i\chi}{(1+i)(\chi+\psi)} \quad (2\text{-}101)$$

$$t_{B1B2}=t_{B1B4}=\frac{1-i}{2(\chi+\psi)} \quad (2\text{-}102)$$

$$t_{B1B3}=\frac{\chi}{(1+i)(\chi+\psi)} \quad (2\text{-}103)$$

Using the bending wave power defined in equation(2-36), the transmission efficiencies for each beam are

$$\tau_{B1B1}=\frac{m_1'c_{B1}\left|v_{B1-}\right|^2}{m_1'c_{B1}\left|v_{B1+}\right|^2}=\left|r_{B1B1}\right|^2=\frac{(\chi+2\psi)^2+\chi^2}{4(\chi+\psi)^2} \quad (2\text{-}104)$$

$$\tau_{B1B2} = \tau_{B1B4} = \frac{m_2' c_{B2} \left| v_{B2+} \right|^2}{m_1' c_{B1} \left| v_{B1+} \right|^2} = \chi\psi \left| t_{B1B2} \right|^2 = \frac{\chi\psi}{2(\chi+\psi)^2} = \frac{0.5}{\left(\sqrt{\frac{\chi}{\psi}} + \sqrt{\frac{\psi}{\chi}} \right)^2} \quad (2\text{-}105)$$

$$\tau_{B1B3} = \frac{m_1' c_{B1} \left| v_{B3+} \right|^2}{m_1' c_{B1} \left| v_{B1+} \right|^2} = \left| t_{B1B3} \right|^2 = \frac{\chi^2}{2(\chi+\psi)^2} = \frac{0.5}{\left(1+\frac{\psi}{\chi} \right)^2} \quad (2\text{-}106)$$

The subscript positive sign refers to incident waves and transmitted propagating waves, while the negative sign corresponds to reflected bending waves. For conservation of energy it can be checked that the total transmission coefficient equals unit,

$$\tau_{B1B1} + \tau_{B1B2} + \tau_{B1B3} + \tau_{B1B4} = 1 \quad (2\text{-}107)$$

If the material properties and dimensions of beam 1 are the same as beam 2, then χ=ψ=1, and τ_{B1B2} reaches its maximum value where τ_{B1B1}=0.625, and τ_{B1B2}= τ_{B1B3}= τ_{B1B4}=0.125.

2.4.2 T-junction

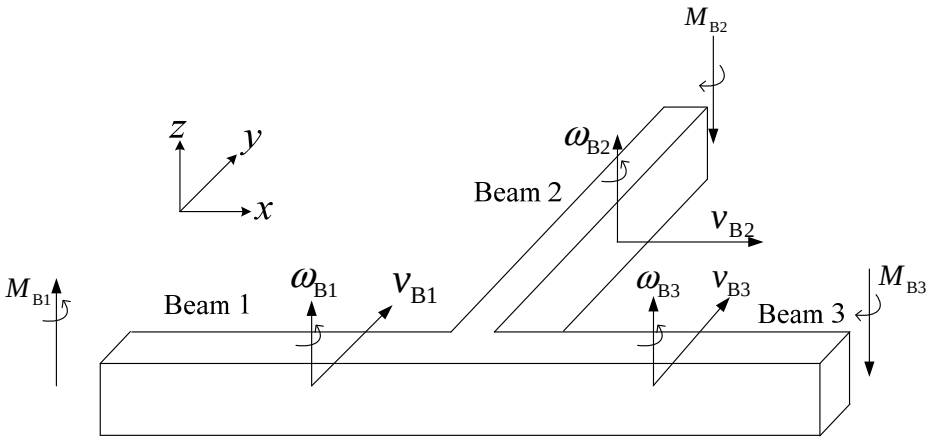

Figure 2.11 T123-junction: B model, Type A bending wave excitation on beam 1.

The T-junction can be seen as a variant of an X-junction without beam 3 (T124-junction) or without beam 4 (T123-junction). The wave fields on each beam of T-junction are the same as that of X-junction. For the T123-junction showed in Figure 2.11, the boundary conditions are the same as X-junction except equations (2-86) and (2-89). The matrix equation (2-99) is reduced to

$$\begin{bmatrix} -k_{B1}+ik_{B1} & -k_{B2}+ik_{B2} & 0 \\ -k_{B1}+ik_{B1} & 0 & -k_{B3}+ik_{B3} \\ k_{B1}^2B_1 & -k_{B2}^2B_2 & -k_{B3}^2B_3 \end{bmatrix} \begin{bmatrix} r_{B1B1} \\ t_{B1B2} \\ t_{B1B3} \end{bmatrix} = \begin{bmatrix} k_{B1}+ik_{B1} \\ k_{B1}+ik_{B1} \\ -k_{B1}^2B_1 \end{bmatrix} \tag{2-108}$$

The solution is given by

$$r_{B1B1} = \frac{\psi + (1-i)\chi}{i(2\chi+\psi)} \tag{2-109}$$

$$t_{B1B2} = \frac{1-i}{(2\chi+\psi)} \tag{2-110}$$

$$t_{B1B3} = \frac{2\chi}{(1+j)(2\chi+\psi)} \tag{2-111}$$

from which the transmission efficiencies are calculated as

$$\tau_{B1B1} = \frac{m_1' c_{B1} |v_{B1-}|^2}{m_1' c_{B1} |v_{B1+}|^2} = |r_{B1B1}|^2 = \frac{(\chi+\psi)^2 + \chi^2}{(2\chi+\psi)^2} \tag{2-112}$$

$$\tau_{B1B2} = \frac{m_2' c_{B2} |v_{B2+}|^2}{m_1' c_{B1} |v_{B1+}|^2} = \chi\psi |t_{B1B2}|^2 = \frac{2\chi\psi}{(2\chi+\psi)^2} = \frac{1}{\left(\sqrt{\frac{2\chi}{\psi}} + \sqrt{\frac{\psi}{2\chi}}\right)^2} \tag{2-113}$$

$$\tau_{B1B3} = \frac{m_1' c_{B1} |v_{B3+}|^2}{m_1' c_{B1} |v_{B1+}|^2} = |t_{B1B3}|^2 = \frac{2\chi^2}{(2\chi+\psi)^2} = \frac{0.5}{\left(1+\frac{\psi}{2\chi}\right)^2} \tag{2-114}$$

For conservation of energy it is checked that the sum of all transmission coefficients on the T123-junction equals unit.

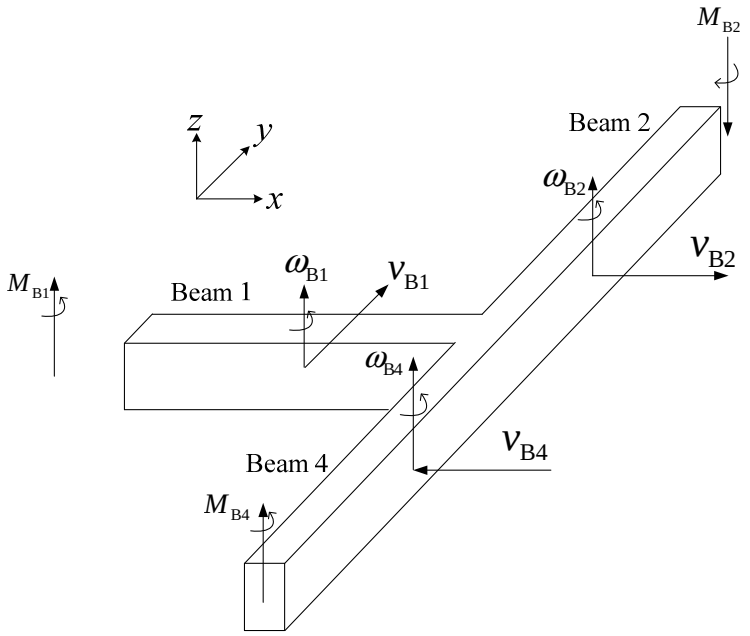

Figure 2.12 T124-junction: Bending only model, Type A bending wave excitation on beam 1.

Figure 2.12 considers bending wave excitation (Type A) of beam 1 on the T124-junction. Similarly, one can get the following reduced matrix equation to calculate r_{B1B1}, t_{B1B2} and t_{B1B4}:

$$\begin{bmatrix} -k_{B1}+ik_{B1} & -k_{B2}+ik_{B2} & 0 \\ -k_{B1}+ik_{B1} & 0 & -k_{B4}+ik_{B4} \\ k_{B1}^2 B_1 & -k_{B2}^2 B_2 & -k_{B4}^2 B_4 \end{bmatrix} \begin{bmatrix} r_{B1B1} \\ t_{B1B2} \\ t_{B1B4} \end{bmatrix} = \begin{bmatrix} k_{B1}+ik_{B1} \\ k_{B1}+ik_{B1} \\ -k_{B1}^2 B_1 \end{bmatrix} \tag{2-115}$$

Solving this matrix equation gives

$$r_{B1B1} = -\frac{\chi + 2j\psi}{\chi + 2\psi} \tag{2-116}$$

$$t_{B1B2} = t_{B1B4} = \frac{1-j}{\chi + 2\psi} \tag{2-117}$$

and the transmission efficiencies of the T124 junction are

$$\tau_{B1B1} = \frac{m_1' c_{B1} \left| v_{B1-} \right|^2}{m_1' c_{B1} \left| v_{B1+} \right|^2} = \left| r_{B1B1} \right|^2 = \frac{\chi^2 + (2\psi)^2}{(\chi + 2\psi)^2} \tag{2-118}$$

$$\tau_{\mathrm{B1B2}} = \tau_{\mathrm{B1B4}} = \frac{m_2' c_{\mathrm{B2}} \left| v_{\mathrm{B2+}} \right|^2}{m_1' c_{\mathrm{B1}} \left| v_{\mathrm{B1+}} \right|^2} = \chi\psi \left| t_{\mathrm{B1B2}} \right|^2 = \frac{2\chi\psi}{\left(\chi + 2\psi\right)^2} = \frac{1}{\left(\sqrt{\frac{\chi}{2\psi}} + \sqrt{\frac{2\psi}{\chi}} \right)^2} \quad (2\text{-}119)$$

As before, conservation of energy can be checked to ensure that $\tau_{\mathrm{B1B1}} + \tau_{\mathrm{B1B2}} + \tau_{\mathrm{B1B4}} = 1$.

2.4.3 L-junction

The L-junction under consideration is shown in Figure 2.13.

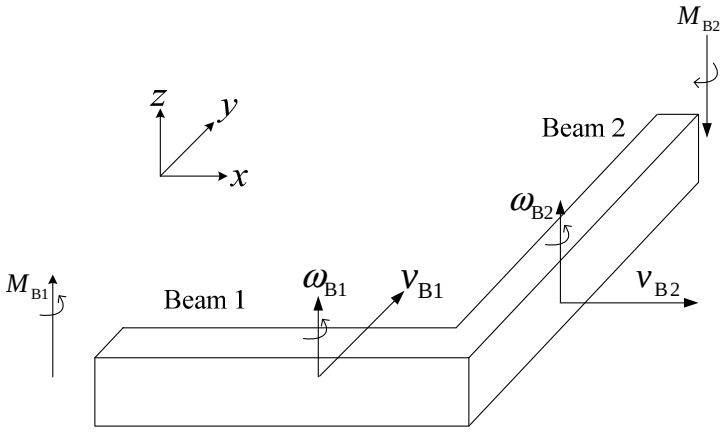

Figure 2.13 L-junction: Bending only model, Type A bending wave excitation on beam 1.

The continuity of rotational velocity is the same as equation (2-87) and the moment equilibrium condition is M_{B1}-M_{B2}=0, therefore the matrix equation for L-junction is

$$\begin{bmatrix} -k_{\mathrm{B1}} + ik_{\mathrm{B1}} & -k_{\mathrm{B2}} + ik_{\mathrm{B2}} \\ k_{\mathrm{B1}}^2 B_1 & -k_{\mathrm{B2}}^2 B_2 \end{bmatrix} \begin{bmatrix} r_{\mathrm{B1B1}} \\ t_{\mathrm{B1B2}} \end{bmatrix} = \begin{bmatrix} k_{\mathrm{B1}} + ik_{\mathrm{B1}} \\ -k_{\mathrm{B1}}^2 B_1 \end{bmatrix} \quad (2\text{-}120)$$

Solving this equation gives

$$r_{\mathrm{B1B1}} = -\frac{\chi + i\psi}{\chi + \psi} \quad (2\text{-}121)$$

$$t_{\mathrm{B1B2}} = \frac{1 - i}{\chi + \psi} \quad (2\text{-}122)$$

The transmission efficiencies are

$$\tau_{\mathrm{B1B1}} = \frac{m_1' c_{\mathrm{B1}} \left| v_{\mathrm{B1-}} \right|^2}{m_1' c_{\mathrm{B1}} \left| v_{\mathrm{B1+}} \right|^2} = \left| r_{\mathrm{B1B1}} \right|^2 = \frac{\chi^2 + \psi^2}{\left(\chi + \psi \right)^2} \tag{2-123}$$

$$\tau_{\mathrm{B1B2}} = \frac{m_2' c_{\mathrm{B2}} \left| v_{\mathrm{B2+}} \right|^2}{m_1' c_{\mathrm{B1}} \left| v_{\mathrm{B1+}} \right|^2} = \chi\psi \left| t_{\mathrm{B1B2}} \right|^2 = \frac{2\chi\psi}{\left(\chi + \psi \right)^2} = \frac{2}{\left(\sqrt{\frac{\chi}{\psi}} + \sqrt{\frac{\psi}{\chi}} \right)^2} \tag{2-124}$$

Conversation of energy requires that $\tau_{B1B1} + \tau_{B1B2} = 1$. Table 2.4 shows the transmission coefficients for X-, T- and L- junctions with bending only models when all beams are identical.

Table 2.4 Transmission coefficients of bending only model for χ=ψ=1.

	τ_{B1B1}	τ_{B1B2}	τ_{B1B3}	τ_{B1B4}
X-junction	5/8	1/8	1/8	1/8
T123-junction	5/9	2/9	2/9	
T124-junction	5/9	2/9		2/9
L-junction	1/2	1/2		

2.5 Bending and longitudinal wave model (BL model)

For the bending and longitudinal wave model (BL model) it is not possible to treat the T-junction and L-junction as a special case of X-junction. Due to the structural symmetry in the X-junction and T-junction, not all beams transmit two wave types. The consistency relationship is no longer useful with multiple wave types; hence in this section (and in section 2.6), different beam junctions are considered separately with respect to the incident wave type and structural symmetry.

In this section, bending and longitudinal wave models are derived for the X-junction, T-junction and L-junction. An incident bending or longitudinal wave is applied on the source beam 1 and the beam junction is unpinned to allow generation of longitudinal waves at the junction.

2.5.1 X-junction

2.5.1.1 Bending wave excitation

Figure 2.14 shows the X-junction under consideration. Beams 1 and 3 and beams 2 and 4 are identical in X-junction.

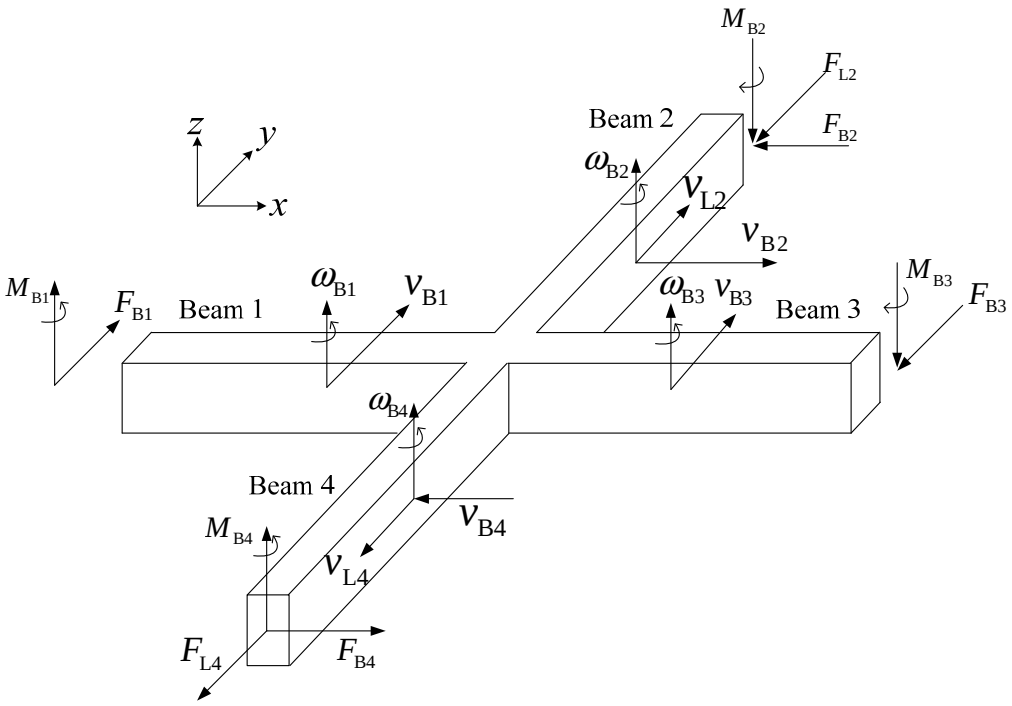

Figure 2.14 X-junction: BL model, Type A bending wave excitation on beam 1.

Assume that an incident bending wave (Type A) with unit amplitude travels on beam 1 of an X-junction in the positive x-direction. The bending wave field on beam 1 is composed of three parts, namely the incident wave, reflected wave, and nearfield. Both bending and longitudinal waves are transmitted onto beams 2 and 4. Due to structural symmetry, the bending waves on beams 2 and 4 have the same magnitude but propagate in opposite directions. Hence there will be zero displacement in the *x*-direction at the junction. Also, the magnitude of longitudinal wave motions on beams 2 and 4 are the same, but the phases differ. The wave fields on each beam are described by

$$v_{B1} = \left(e^{-ik_{B1}x} + r_{B1B1}e^{ik_{B1}x} + r_{N1}e^{k_{B1}x}\right)e^{i\omega t} \tag{2-125}$$

$$v_{B2} = \left(t_{B1B2}e^{-ik_{B2}y} + t_{N2}e^{-k_{B2}y}\right)e^{i\omega t} \tag{2-126}$$

$$v_{\mathrm{B3}} = \left(t_{\mathrm{B1B3}} e^{-ik_{\mathrm{B1}}x} + t_{\mathrm{N3}} e^{-k_{\mathrm{B1}}x}\right) e^{i\omega t} \tag{2-127}$$

$$v_{\mathrm{B4}} = -\left(t_{\mathrm{B1B2}} e^{ik_{\mathrm{B2}}y} + t_{\mathrm{N2}} e^{k_{\mathrm{B2}}y}\right) e^{i\omega t} \tag{2-128}$$

$$v_{\mathrm{L1}} = v_{\mathrm{L3}} = 0 \tag{2-129}$$

$$v_{\mathrm{L2}} = t_{\mathrm{B1L2}} e^{-ik_{\mathrm{L2}}y} e^{i\omega t} \tag{2-130}$$

$$v_{\mathrm{L4}} = -t_{\mathrm{B1L2}} e^{ik_{\mathrm{L2}}y} e^{i\omega t} \tag{2-131}$$

where *r* indicates the complex amplitude of the reflected wave and *t* indicates the complex amplitude of the transmitted wave with subscripts B, L, and N indicating bending waves, longitudinal waves and nearfield waves, respectively.

In addition to the two parameters χ and ψ defined in (2-100), two more frequency-dependant parameters are defined here

$$\beta_1 = \frac{m_2' c_{\mathrm{B2}}}{m_1' c_{\mathrm{L1}}}, \quad \beta_2 = \frac{m_1' c_{\mathrm{B1}}}{m_2' c_{\mathrm{L2}}} \tag{2-132}$$

where m_1' and m_2' are the mass per unit lengths.

Continuity of the angular velocity at the junction requires that

$$\frac{\partial v_{\mathrm{B1}}}{\partial x} = \frac{\partial v_{\mathrm{B2}}}{\partial y}, \quad \frac{\partial v_{\mathrm{B1}}}{\partial x} = \frac{\partial v_{\mathrm{B3}}}{\partial x} \tag{2-133}$$

which yields

$$ir_{\mathrm{B1B1}} + r_{\mathrm{N1}} + i\chi t_{\mathrm{B1B2}} + \chi t_{\mathrm{N2}} = i \tag{2-134}$$

$$ir_{\mathrm{B1B1}} + r_{\mathrm{N1}} + it_{\mathrm{B1B3}} + t_{\mathrm{N3}} = i \tag{2-135}$$

Continuity of the velocity in the *y*-direction at the junction requires that

$$v_{\mathrm{B1}} = v_{\mathrm{L2}}, \quad v_{\mathrm{B1}} = v_{\mathrm{B3}} \tag{2-136}$$

Thus one gets the following two equations

$$r_{\mathrm{B1B1}} + r_{\mathrm{N1}} - t_{\mathrm{B1L2}} = -1 \tag{2-137}$$

$$r_{\mathrm{B1B1}} + r_{\mathrm{N1}} - t_{\mathrm{B1B3}} - t_{\mathrm{N3}} = -1 \tag{2-138}$$

In the *x*-direction the displacement is zero, such that

$$v_{\mathrm{B2}} = 0 (= v_{\mathrm{L1}}) \tag{2-139}$$

hence,

$$t_{\mathrm{B1B2}} + t_{\mathrm{N2}} = 0 \tag{2-140}$$

At the junction (*x*,*y*)=(0,0), zero displacement in the *x*-direction does not mean that the force in the *x*-direction is also zero. Due to symmetry, the bending motion on beams 2 and 4 are symmetric about the *x*-axis, whilst the shear force due to bending in beams 2 and 4 are balanced in the *x*-direction, F_{B2}-F_{B4}=0. Also, in the *y*-direction, F_{L2}=F_{L4}, and force equilibrium requires that

$$F_{\mathrm{B1}} - 2F_{\mathrm{L2}} - F_{\mathrm{B3}} = 0 \tag{2-141}$$

According to equation(2-4), the axial force due to the longitudinal wave in beam 2 can be written as

$$F_{\mathrm{L2}} = -m_2' \int \frac{\partial v_{\mathrm{L2}}}{\partial t} \mathrm{d}y = -i\omega m_2' \frac{1}{-ik_{\mathrm{L2}}} t_{\mathrm{B1L2}} e^{i\omega t} = m_2' c_{\mathrm{L2}} t_{\mathrm{B1L2}} e^{i\omega t} \tag{2-142}$$

The shear force due to the bending wave is calculated according to equation (2-26)

$$\begin{aligned} F_{\mathrm{B1}} &= B_1 \int \frac{\partial^3 v_{\mathrm{B1}}}{\partial x^3} \mathrm{d}t = \frac{B_1}{i\omega} \left[\left(-ik_{\mathrm{B1}}\right)^3 + \left(ik_{\mathrm{B1}}\right)^3 r_{\mathrm{B1B1}} + \left(k_{\mathrm{B1}}\right)^3 r_{\mathrm{N1}} \right] e^{i\omega t} \\ &= \frac{B_1 k_{\mathrm{B1}}^3}{\omega} \left(1 - r_{\mathrm{B1B1}} - i r_{\mathrm{N1}}\right) e^{i\omega t} = m_1' c_{\mathrm{B1}} \left(1 - r_{\mathrm{B1B1}} - i r_{\mathrm{N1}}\right) e^{i\omega t} \end{aligned} \tag{2-143}$$

$$\begin{aligned} F_{\mathrm{B3}} &= B_1 \int \frac{\partial^3 v_{\mathrm{B3}}}{\partial x^3} \mathrm{d}t = \frac{B_1}{i\omega} \left[\left(-ik_{\mathrm{B1}}\right)^3 t_{\mathrm{B1B3}} + \left(-k_{\mathrm{B1}}\right)^3 t_{\mathrm{N3}} \right] e^{i\omega t} \\ &= \frac{B_1 k_{\mathrm{B1}}^3}{\omega} \left(t_{\mathrm{B1B3}} + i t_{\mathrm{N3}}\right) e^{i\omega t} = m_1' c_{\mathrm{B1}} \left(t_{\mathrm{B1B3}} + i t_{\mathrm{N3}}\right) e^{i\omega t} \end{aligned} \tag{2-144}$$

Inserting (2-142), (2-143) and (2-144) into (2-141), one gets

$$\beta_2 r_{\mathrm{B1B1}} + i\beta_2 r_{\mathrm{N1}} + \beta_2 t_{\mathrm{B1B3}} + i\beta_2 t_{\mathrm{N3}} + 2t_{\mathrm{B1L2}} = \beta_2 \tag{2-145}$$

At the junction, M_{B2}=-M_{B4}, and moment equilibrium gives

$$M_{\mathrm{B1}} - 2M_{\mathrm{B2}} - M_{\mathrm{B3}} = 0 \tag{2-146}$$

Based on (2-25), the moments due to bending motions are

$$\begin{aligned} M_{\mathrm{B1}} &= -B_1 \int \frac{\partial^2 v_{\mathrm{B1}}}{\partial x^2}\,\mathrm{d}t = \frac{-B_1}{i\omega}\left[\left(-ik_{\mathrm{B1}}\right)^2 + \left(ik_{\mathrm{B1}}\right)^2 r_{\mathrm{B1B1}} + k_{\mathrm{B1}}^2 r_{\mathrm{N1}}\right] e^{i\omega t} \\ &= \frac{-B_1 k_{\mathrm{B1}}^2}{i\omega}\left(-1 - r_{\mathrm{B1B1}} + r_{\mathrm{N1}}\right) e^{i\omega t} \end{aligned} \tag{2-147}$$

$$\begin{aligned} M_{\mathrm{B2}} &= -B_2 \int \frac{\partial^2 v_{\mathrm{B2}}}{\partial y^2}\,\mathrm{d}t = \frac{-B_2}{i\omega}\left[\left(-ik_{\mathrm{B2}}\right)^2 t_{\mathrm{B1B2}} + \left(-k_{\mathrm{B2}}\right)^2 t_{\mathrm{N2}}\right] e^{i\omega t} \\ &= \frac{-B_2 k_{\mathrm{B2}}^2}{i\omega}\left(-t_{\mathrm{B1B2}} + t_{\mathrm{N2}}\right) e^{i\omega t} \end{aligned} \tag{2-148}$$

$$\begin{aligned} M_{\mathrm{B3}} &= -B_1 \int \frac{\partial^2 v_{\mathrm{B1}}}{\partial x^2}\,\mathrm{d}t = \frac{-B_1}{i\omega}\left[\left(-ik_{\mathrm{B1}}\right)^2 t_{\mathrm{B1B3}} + \left(-k_{\mathrm{B1}}\right)^2 t_{\mathrm{N3}}\right] e^{i\omega t} \\ &= \frac{-B_1 k_{\mathrm{B1}}^2}{i\omega}\left(-t_{\mathrm{B1B3}} + t_{\mathrm{N3}}\right) e^{i\omega t} \end{aligned} \tag{2-149}$$

Inserting these results into (2-146) gives

$$-r_{\mathrm{B1B1}} + r_{\mathrm{N1}} + 2\psi t_{\mathrm{B1B2}} - 2\psi t_{\mathrm{N2}} + t_{\mathrm{B1B3}} - t_{\mathrm{N3}} = 1 \tag{2-150}$$

Combining (2-134), (2-135), (2-137), (2-138), (2-140), (2-145) and (2-150) gives a matrix with seven unknowns

$$\begin{bmatrix} i & 1 & i\chi & \chi & 0 & 0 & 0 \\ i & 1 & 0 & 0 & i & 1 & 0 \\ 1 & 1 & 0 & 0 & 0 & 0 & -1 \\ 1 & 1 & 0 & 0 & -1 & -1 & 0 \\ 0 & 0 & 1 & 1 & 0 & 0 & 0 \\ \beta_2 & i\beta_2 & 0 & 0 & \beta_2 & i\beta_2 & 2 \\ -1 & -1 & 2\psi & -2\psi & 1 & -1 & 0 \end{bmatrix} \begin{bmatrix} r_{\mathrm{B1B1}} \\ r_{\mathrm{N1}} \\ t_{\mathrm{B1B2}} \\ t_{\mathrm{N2}} \\ t_{\mathrm{B1B3}} \\ t_{\mathrm{N3}} \\ t_{\mathrm{B1L2}} \end{bmatrix} = \begin{bmatrix} i \\ i \\ -1 \\ -1 \\ 0 \\ \beta_2 \\ 1 \end{bmatrix} \tag{2-151}$$

The transmission coefficients can now be derived from (2-6) and (2-36)

$$\tau_{\mathrm{B1B1}} = \frac{m_1' c_{\mathrm{B1}} \left| v_{\mathrm{B1-}} \right|^2}{m_1' c_{\mathrm{B1}} \left| v_{\mathrm{B1+}} \right|^2} = \left| r_{\mathrm{B1B1}} \right|^2 \tag{2-152}$$

$$\tau_{\mathrm{B1B2}} = \tau_{\mathrm{B1B4}} = \frac{m_2' c_{\mathrm{B2}} \left| v_{\mathrm{B2+}} \right|^2}{m_1' c_{\mathrm{B1}} \left| v_{\mathrm{B1+}} \right|^2} = \chi \psi \left| t_{\mathrm{B1B2}} \right|^2 \tag{2-153}$$

$$\tau_{\mathrm{B1B3}} = \frac{m_1' c_{\mathrm{B1}} \left| v_{\mathrm{B3+}} \right|^2}{m_1' c_{\mathrm{B1}} \left| v_{\mathrm{B1+}} \right|^2} = \left| t_{\mathrm{B1B3}} \right|^2 \tag{2-154}$$

$$\tau_{\mathrm{B1L1}} = \tau_{\mathrm{B1L3}} = 0 \tag{2-155}$$

$$\tau_{\mathrm{B1L2}} = \tau_{\mathrm{B1L4}} = \frac{\frac{1}{2} m_2' c_{\mathrm{L2}} \left| v_{\mathrm{L2+}} \right|^2}{m_1' c_{\mathrm{B1}} \left| v_{\mathrm{B1+}} \right|^2} = \frac{1}{2\beta_2} \left| t_{\mathrm{B1L2}} \right|^2 \tag{2-156}$$

Example transmission coefficients are plotted in Figure 2.15 using the material properties and dimensions in Table 2.3. This confirms that the sum of the transmission coefficients is unit hence there is conservation of energy. Note that τ_{B1B2} and τ_{B1B4} are constant whereas other transmission coefficients are frequency-dependant (unless they are zero at all frequencies).

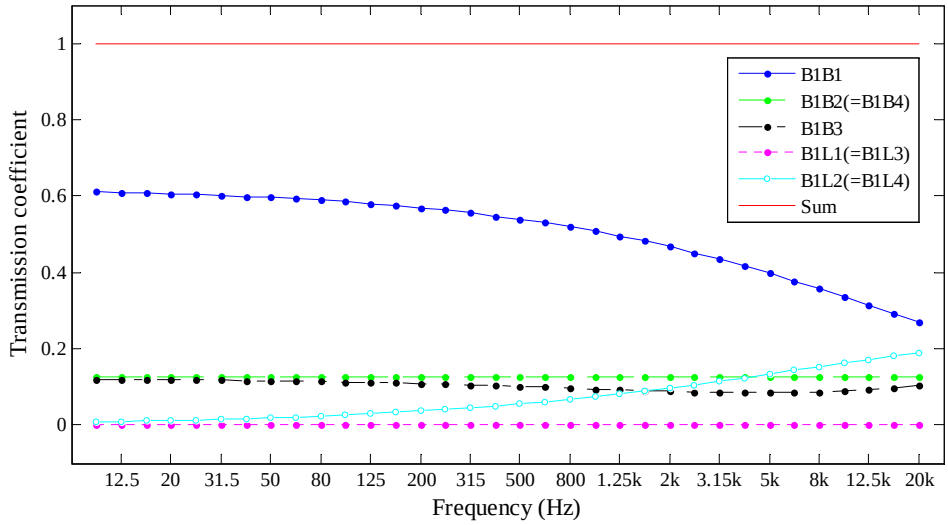

Figure 2.15 Transmission coefficients for X-junction: BL model, incident bending wave on beam 1.

2.5.1.2 Longitudinal wave excitation

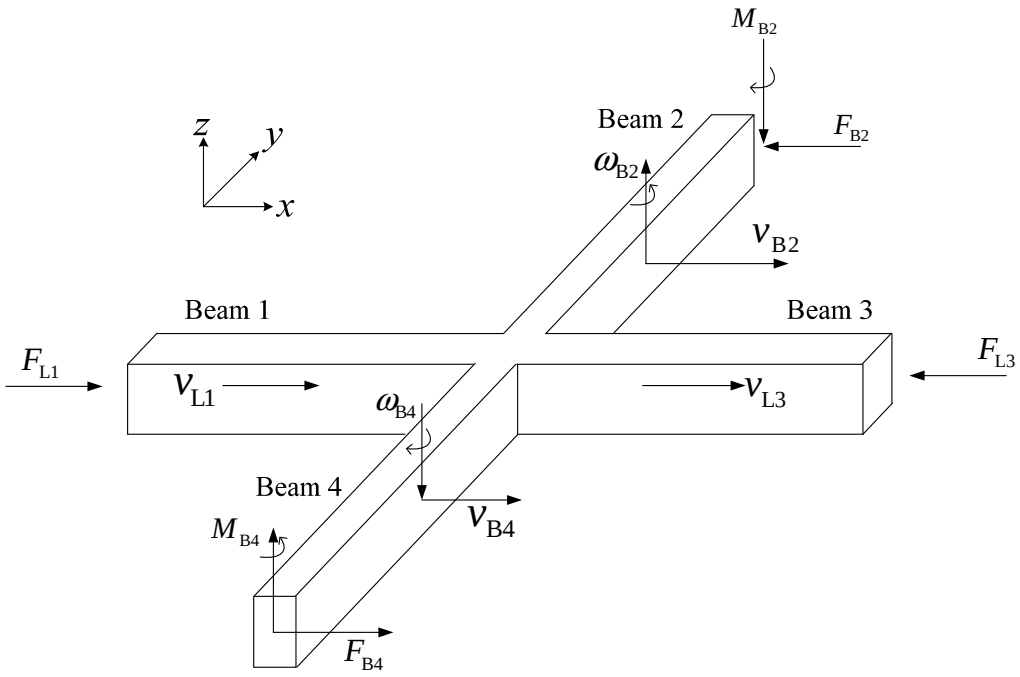

Figure 2.16 X-junction: BL model, longitudinal wave excitation on beam 1.

Consider an incident longitudinal wave travelling in the positive *x*-direction towards the X-junction on beam 1. This will generate bending waves (Type A) on beams 2 and 4, and a longitudinal wave on beam 3. Due to structural symmetry, the bending motions on beam 2 and 4 have the same amplitude but travel to opposite directions, which will lead to balanced moments in the *z*-direction and zero rotational displacement at the junction. Hence no bending wave is reflected to beam 1 or transmitted to beam 3. The wave fields for each beam are

$$v_{L1} = \left(e^{-ik_{L1}x} + r_{L1L1}e^{ik_{L1}x}\right)e^{i\omega t} \tag{2-157}$$

$$v_{L2} = v_{L4} = 0 \tag{2-158}$$

$$v_{L3} = t_{L1L3}e^{-ik_{L1}x}e^{i\omega t} \tag{2-159}$$

$$v_{B1} = v_{B3} = 0 \tag{2-160}$$

$$v_{B2} = \left(t_{L1B2}e^{-ik_{B2}y} + t_{N2}e^{-k_{B2}y}\right)e^{i\omega t} \tag{2-161}$$

$$v_{\mathrm{B4}} = \left(t_{\mathrm{L1B2}} e^{ik_{\mathrm{B2}}y} + t_{\mathrm{N2}} e^{k_{\mathrm{B2}}y} \right) e^{i\omega t} \tag{2-162}$$

As discussed, the rotational displacement at the junction is zero. This can be translated as

$$\frac{\partial v_{\mathrm{B2}}}{\partial y} = 0 \tag{2-163}$$

Then one can solve the following expression

$$it_{\mathrm{L1B2}} + t_{\mathrm{N2}} = 0 \tag{2-164}$$

Continuity of velocity in the *x*-direction at the junction requires that

$$v_{\mathrm{L1}} = v_{\mathrm{B2}}, \quad v_{\mathrm{L1}} = v_{\mathrm{L3}} \tag{2-165}$$

which gives the following two equations to be solved

$$-r_{\mathrm{L1L1}} + t_{\mathrm{L1B2}} + t_{\mathrm{N2}} = 1 \tag{2-166}$$

$$-r_{\mathrm{L1L1}} + t_{\mathrm{L1L3}} = 1 \tag{2-167}$$

In the *x*-direction, F_{B2}=-F_{B4}, and force equilibrium requires that

$$F_{\mathrm{L1}} - 2F_{\mathrm{B2}} - F_{\mathrm{L3}} = 0 \tag{2-168}$$

The forces can be calculated using (2-4) and (2-28),

$$\begin{aligned} F_{\mathrm{L1}} &= -m_1' \int \frac{\partial v_{\mathrm{L1}}}{\partial t} \mathrm{d}x = -i\omega m_1' \left(\frac{1}{-ik_{\mathrm{L1}}} + \frac{1}{ik_{\mathrm{L1}}} r_{\mathrm{L1L1}} \right) e^{i\omega t} \\ &= m_1' c_{\mathrm{L1}} \left(1 - r_{\mathrm{L1L1}} \right) e^{i\omega t} \end{aligned} \tag{2-169}$$

$$\begin{aligned} F_{\mathrm{B2}} &= B_2 \int \frac{\partial^3 v_{\mathrm{B2}}}{\partial y^3} \mathrm{d}t = \frac{B_2}{i\omega} \left[\left(-ik_{\mathrm{B2}} \right)^3 t_{\mathrm{L1B2}} + \left(-k_{\mathrm{B2}} \right)^3 t_{\mathrm{N2}} \right] e^{i\omega t} \\ &= \frac{B_2 k_{\mathrm{B2}}^3}{\omega} \left(t_{\mathrm{L1B2}} + it_{\mathrm{N2}} \right) e^{i\omega t} = m_2' c_{\mathrm{B2}} \left(t_{\mathrm{L1B2}} + it_{\mathrm{N2}} \right) e^{i\omega t} \end{aligned} \tag{2-170}$$

$$F_{\mathrm{L3}} = -m_1' \int \frac{\partial v_{\mathrm{L3}}}{\partial t} \mathrm{d}x = -i\omega m_1' \frac{1}{-ik_{\mathrm{L1}}} t_{\mathrm{L1L3}} e^{i\omega t} = m_1' c_{\mathrm{L1}} t_{\mathrm{L1L3}} e^{i\omega t} \tag{2-171}$$

Substituting these forces into equation (2-168) produces

$$r_{\mathrm{L1L1}} + t_{\mathrm{L1L3}} + 2\beta_1 t_{\mathrm{L1B2}} + 2i\beta_1 t_{\mathrm{N2}} = 1 \tag{2-172}$$

Combining (2-164), (2-166), (2-167) and (2-172), one can solve the four unknown parameters r_{L1L1}, t_{L1L3}, t_{L1B2} and t_{N2} from the matrix equation set

$$\begin{bmatrix} 0 & 0 & i & 1 \\ -1 & 0 & 1 & 1 \\ -1 & 1 & 0 & 0 \\ 1 & 1 & 2\beta_1 & 2i\beta_1 \end{bmatrix} \begin{bmatrix} r_{\mathrm{L1L1}} \\ t_{\mathrm{L1L3}} \\ t_{\mathrm{L1B2}} \\ t_{\mathrm{N2}} \end{bmatrix} = \begin{bmatrix} 0 \\ 1 \\ 1 \\ 1 \end{bmatrix} \tag{2-173}$$

Solution of equation (2-173) allows the reflection and transmission coefficients to be calculated using

$$\tau_{\mathrm{L1L1}} = \frac{\frac{1}{2} m_1' c_{\mathrm{L1}} \left| v_{\mathrm{L1-}} \right|^2}{\frac{1}{2} m_1' c_{\mathrm{L1}} \left| v_{\mathrm{L1+}} \right|^2} = \left| r_{\mathrm{L1L1}} \right|^2 \tag{2-174}$$

$$\tau_{\mathrm{L1L2}} = \tau_{\mathrm{L1L4}} = 0 \tag{2-175}$$

$$\tau_{\mathrm{L1L3}} = \frac{\frac{1}{2} m_1' c_{\mathrm{L1}} \left| v_{\mathrm{L3+}} \right|^2}{\frac{1}{2} m_1' c_{\mathrm{L1}} \left| v_{\mathrm{L1+}} \right|^2} = \left| t_{\mathrm{L1L3}} \right|^2 \tag{2-176}$$

$$\tau_{\mathrm{L1B1}} = \tau_{\mathrm{L1B3}} = 0 \tag{2-177}$$

$$\tau_{\mathrm{L1B2}} = \tau_{\mathrm{L1B4}} = \frac{m_2' c_{\mathrm{B2}} \left| v_{\mathrm{B2+}} \right|^2}{\frac{1}{2} m_1' c_{\mathrm{L1}} \left| v_{\mathrm{L1+}} \right|^2} = 2\beta_1 \left| t_{\mathrm{L1B2}} \right|^2 \tag{2-178}$$

Example transmission coefficients are shown in Figure 2.17 using the material properties and dimensions in Table 2.3.

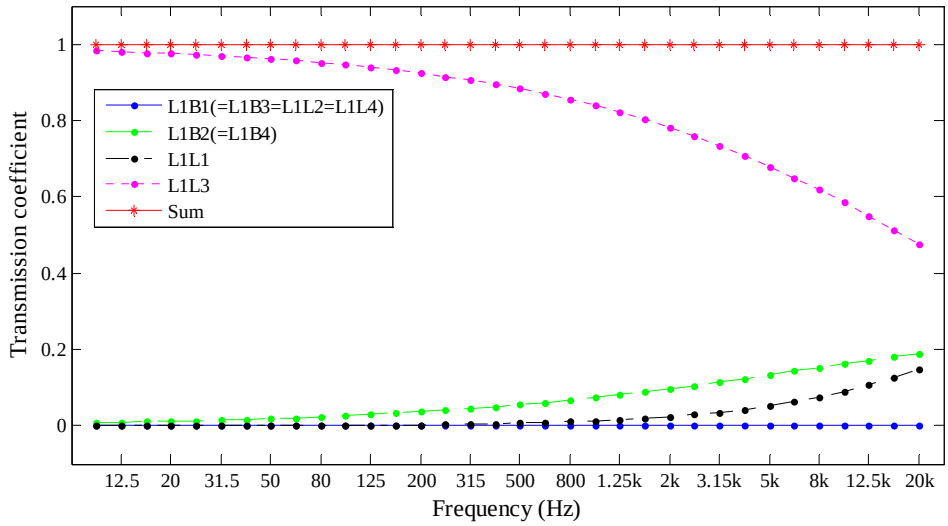

Figure 2.17 Transmission coefficients for X-junction: BL model, incident longitudinal wave on beam 1.

2.5.2 T123-junction

For the T-junction, Figure 2.18 shows the two cases that are considered for excitation on the cantilever beam of the T124-junction and one of the other beams for the T123-junction. It is assumed that the material properties and the cross-sectional dimensions are identical for beams 1 and 3 and beams 2 and 4.

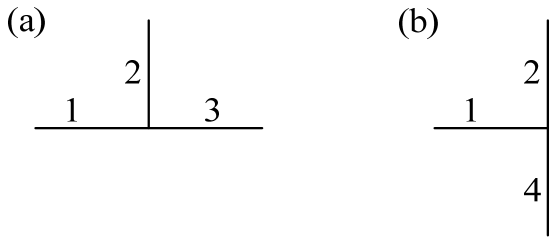

Figure 2.18 T-junction: (a) T123-junction; (b) T124-jucntion.

2.5.2.1 Bending wave excitation

Figure 2.19 shows the T123-junction under consideration for which the coordinates of the junction line are (x,y)=(0,0).

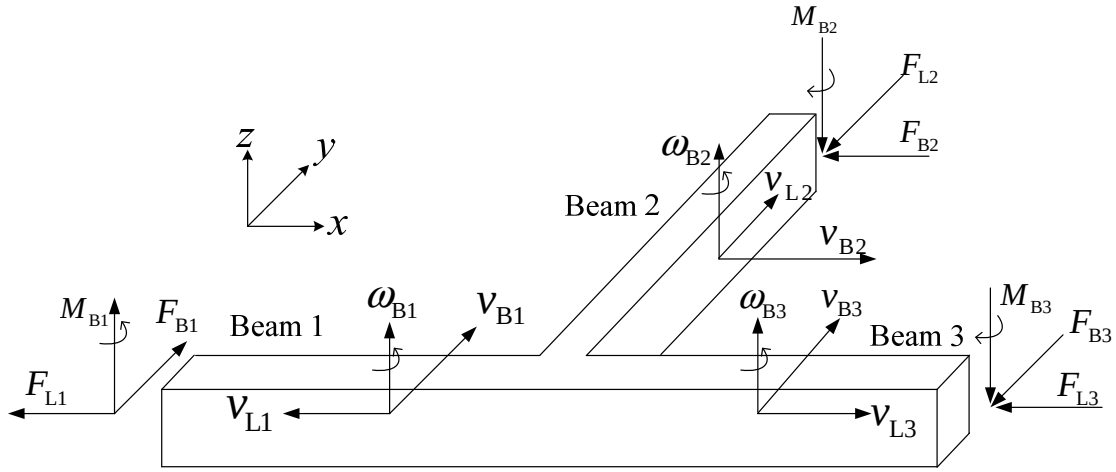

Figure 2.19 T123-junction: BL model, Type A bending wave excitation on beam 1.

Consider an incident bending wave (Type A) travelling in the positive x-direction towards the junction on beam 1. Both bending and longitudinal waves will be transmitted to beam 2. Due to symmetry, longitudinal waves in beams 1 and 3 have the same magnitude but travel in opposite directions. The incident wave is assumed to have unit amplitude and the wave fields are given by

$$v_{B1} = \left(e^{-ik_{B1}x} + r_{B1B1}e^{ik_{B1}x} + r_{N1}e^{k_{B1}x}\right)e^{i\omega t} \tag{2-179}$$

$$v_{B2} = \left(t_{B1B2}e^{-ik_{B2}y} + t_{N2}e^{-k_{B2}y}\right)e^{i\omega t} \tag{2-180}$$

$$v_{B3} = \left(t_{B1B3}e^{-ik_{B1}x} + t_{N3}e^{-k_{B1}x}\right)e^{i\omega t} \tag{2-181}$$

$$v_{L1} = r_{B1L1}e^{ik_{L1}x}e^{i\omega t} \tag{2-182}$$

$$v_{L2} = t_{B1L2}e^{-ik_{L2}y}e^{i\omega t} \tag{2-183}$$

$$v_{L3} = -r_{B1L1}e^{-ik_{L1}x}e^{i\omega t} \tag{2-184}$$

There are eight unknowns to be solved; hence eight equations need to be established.

Continuity of velocity in both *x* and *y* directions at the junction requires that

$$v_{B1} = v_{L2} = v_{B3}, \quad v_{L1} = -v_{B2} \tag{2-185}$$

which gives three equations

$$r_{\mathrm{B1B1}} + r_{\mathrm{N1}} - t_{\mathrm{B1L2}} = -1 \tag{2-186}$$

$$r_{\mathrm{B1B1}} + r_{\mathrm{N1}} - t_{\mathrm{B1B3}} - t_{\mathrm{N3}} = -1 \tag{2-187}$$

$$r_{\mathrm{B1L1}} + t_{\mathrm{B1B2}} + t_{\mathrm{N2}} = 0 \tag{2-188}$$

Continuity of angular velocity at the joint requires that

$$\frac{\partial v_{\mathrm{B1}}}{\partial x} = \frac{\partial v_{\mathrm{B2}}}{\partial y}, \quad \frac{\partial v_{\mathrm{B1}}}{\partial x} = \frac{\partial v_{\mathrm{B3}}}{\partial x} \tag{2-189}$$

from which

$$ir_{\mathrm{B1B1}} + r_{\mathrm{N1}} + i\chi t_{\mathrm{B1B2}} + \chi t_{\mathrm{N2}} = i \tag{2-190}$$

$$ir_{\mathrm{B1B1}} + r_{\mathrm{N1}} + it_{\mathrm{B1B3}} + t_{\mathrm{N3}} = i \tag{2-191}$$

Force equilibrium relationships in the *x*- and *y*-directions are given by

$$F_{\mathrm{L1}} + F_{\mathrm{B2}} + F_{\mathrm{L3}} = 0 \tag{2-192}$$

$$F_{\mathrm{B1}} - F_{\mathrm{L2}} - F_{\mathrm{B3}} = 0 \tag{2-193}$$

Based on equations (2-4) and (2-28) the last two equations yield the following two expressions

$$2ir_{\mathrm{B1L1}} - i\beta_1 t_{\mathrm{B1B2}} + \beta_1 t_{\mathrm{N2}} = 0 \tag{2-194}$$

$$-i\beta_2 r_{\mathrm{B1B1}} + \beta_2 r_{\mathrm{N1}} - i\beta_2 t_{\mathrm{B1B3}} + \beta_2 t_{\mathrm{N3}} - it_{\mathrm{B1L2}} = -i\beta_2 \tag{2-195}$$

Moment equilibrium for bending motion on the three beams is described by

$$M_{\mathrm{B1}} - M_{\mathrm{B2}} - M_{\mathrm{B3}} = 0 \tag{2-196}$$

from which one can solve the following equation according to (2-25)

$$r_{\mathrm{B1B1}} - r_{\mathrm{N1}} - \psi t_{\mathrm{B1B2}} + \psi t_{\mathrm{N2}} - t_{\mathrm{B1B3}} + t_{\mathrm{N3}} = -1 \tag{2-197}$$

Thus, the eight boundary conditions give the matrix equation as

$$\begin{bmatrix} 1 & 1 & 0 & 0 & 0 & 0 & 0 & -1 \\ 1 & 1 & 0 & 0 & -1 & -1 & 0 & 0 \\ 0 & 0 & 1 & 1 & 0 & 0 & 1 & 0 \\ i & 1 & i\chi & \chi & 0 & 0 & 0 & 0 \\ i & 1 & 0 & 0 & i & 1 & 0 & 0 \\ 0 & 0 & -i\beta_1 & \beta_1 & 0 & 0 & 2i & 0 \\ -i\beta_2 & \beta_2 & 0 & 0 & -i\beta_2 & \beta_2 & 0 & -i \\ 1 & -1 & -\psi & \psi & -1 & 1 & 0 & 0 \end{bmatrix} \begin{bmatrix} r_{\mathrm{B1B1}} \\ r_{\mathrm{N1}} \\ t_{\mathrm{B1B2}} \\ t_{\mathrm{N2}} \\ t_{\mathrm{B1B3}} \\ t_{\mathrm{N3}} \\ r_{\mathrm{B1L1}} \\ t_{\mathrm{B1L2}} \end{bmatrix} = \begin{bmatrix} -1 \\ -1 \\ 0 \\ i \\ i \\ 0 \\ -i\beta_2 \\ -1 \end{bmatrix} \tag{2-198}$$

Solution of equation (2-198) allows the reflection and transmission coefficients to be calculated using

$$\tau_{\mathrm{B1B1}} = \frac{m_1' c_{\mathrm{B1}} \left| v_{\mathrm{B1-}} \right|^2}{m_1' c_{\mathrm{B1}} \left| v_{\mathrm{B1+}} \right|^2} = \left| r_{\mathrm{B1B1}} \right|^2 \tag{2-199}$$

$$\tau_{\mathrm{B1B2}} = \frac{m_2' c_{\mathrm{B2}} \left| v_{\mathrm{B2+}} \right|^2}{m_1' c_{\mathrm{B1}} \left| v_{\mathrm{B1+}} \right|^2} = \chi\psi \left| t_{\mathrm{B1B2}} \right|^2 \tag{2-200}$$

$$\tau_{\mathrm{B1B3}} = \frac{m_1' c_{\mathrm{B1}} \left| v_{\mathrm{B3+}} \right|^2}{m_1' c_{\mathrm{B1}} \left| v_{\mathrm{B1+}} \right|^2} = \left| t_{\mathrm{B1B3}} \right|^2 \tag{2-201}$$

$$\tau_{\mathrm{B1L1}} = \tau_{\mathrm{B1L3}} = \frac{\frac{1}{2} m_1' c_{\mathrm{L1}} \left| v_{\mathrm{L1-}} \right|^2}{m_1' c_{\mathrm{B1}} \left| v_{\mathrm{B1+}} \right|^2} = \frac{\chi\psi}{2\beta_2} \left| r_{\mathrm{B1L1}} \right|^2 \tag{2-202}$$

$$\tau_{\mathrm{B1L2}} = \frac{\frac{1}{2} m_1' c_{\mathrm{L2}} \left| v_{\mathrm{L2+}} \right|^2}{m_1' c_{\mathrm{B1}} \left| v_{\mathrm{B1+}} \right|^2} = \frac{1}{2\beta_2} \left| t_{\mathrm{B1L2}} \right|^2 \tag{2-203}$$

Example transmission coefficients are shown in Figure 2.20 using the material properties and dimensions in Section Table 2.3. This indicates the importance of wave conversion as τ_{B1L2} increases with increasing frequency although τ_{B1L1} and τ_{B1L3} are nearly zero.

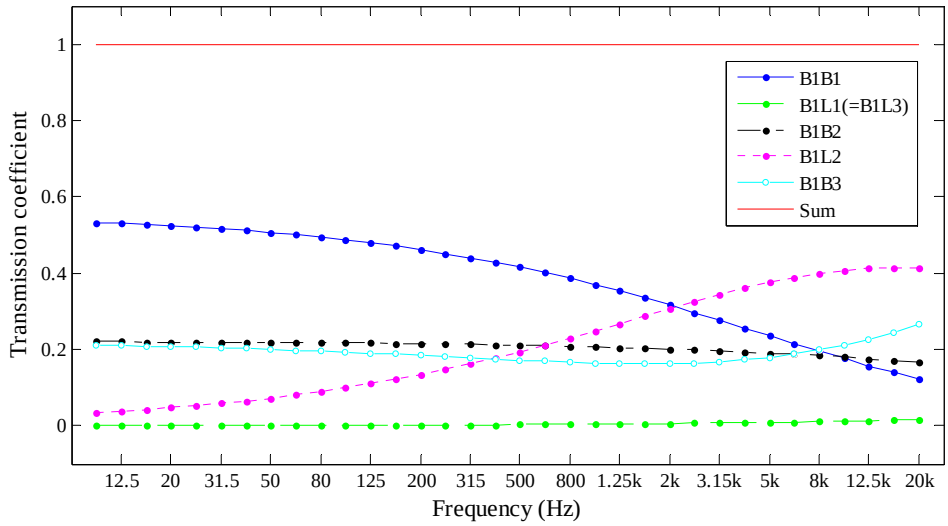

Figure 2.20 Transmission coefficients for T123-junction: BL model, incident bending wave (Type A) on beam 1.

2.5.2.2 Longitudinal wave excitation

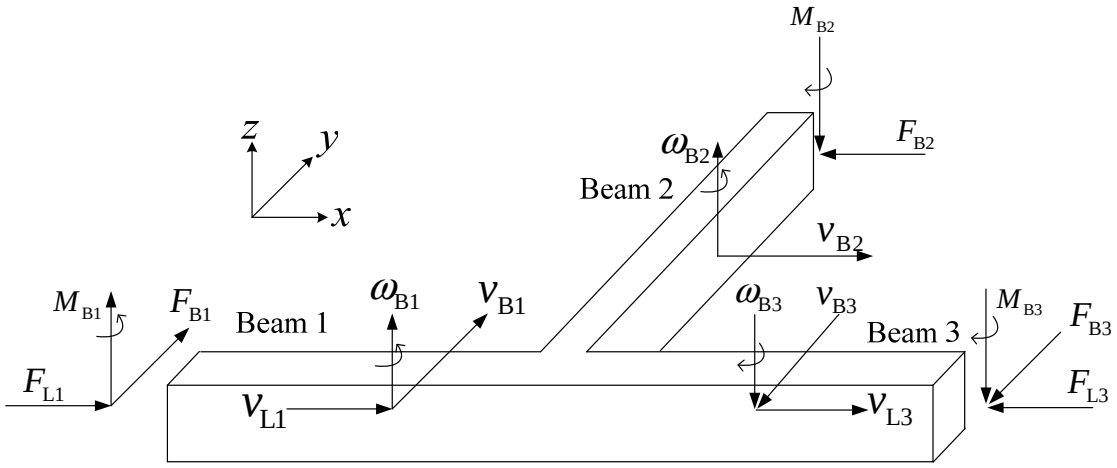

Figure 2.21 T123-junction: BL model, longitudinal wave excitation on beam 1.

Now consider an incident longitudinal wave travelling in the positive x-direction towards the junction on beam 1. This will lead to bending waves (Type A) on beams 1, 2 and 3, a longitudinal wave reflected onto beam 1, and a longitudinal wave transmitted to beam 3. Due to structural symmetry, Type A bending waves on beams 1 and 3 have the same magnitudes but travel in opposite directions with a phase difference of π between them. This causes zero displacement in the *y*-direction at the junction. Thus, in

beam 2 there is only bending wave motion. The incident wave is assumed to have unit amplitude; hence the wave fields can be described as follows

$$v_{\mathrm{L1}} = \left(e^{-ik_{\mathrm{L1}}x} + r_{\mathrm{L1L1}}e^{ik_{\mathrm{L1}}x}\right)e^{i\omega t} \tag{2-204}$$

$$v_{\mathrm{L2}} = 0 \tag{2-205}$$

$$v_{\mathrm{L3}} = t_{\mathrm{L1L3}}e^{-ik_{\mathrm{L1}}x}e^{i\omega t} \tag{2-206}$$

$$v_{\mathrm{B1}} = \left(t_{\mathrm{L1B1}}e^{ik_{\mathrm{B1}}x} + t_{\mathrm{N1}}e^{k_{\mathrm{B1}}x}\right)e^{i\omega t} \tag{2-207}$$

$$v_{\mathrm{B2}} = \left(t_{\mathrm{L1B2}}e^{-ik_{\mathrm{B2}}y} + t_{\mathrm{N2}}e^{-k_{\mathrm{B2}}y}\right)e^{i\omega t} \tag{2-208}$$

$$v_{\mathrm{B3}} = -\left(t_{\mathrm{L1B1}}e^{-ik_{\mathrm{B1}}x} + t_{\mathrm{N3}}e^{-k_{\mathrm{B1}}x}\right)e^{i\omega t} \tag{2-209}$$

Continuity of angular velocity at the junction requires that

$$\frac{\partial v_{\mathrm{B1}}}{\partial x} = \frac{\partial v_{\mathrm{B2}}}{\partial y}\left(= -\frac{\partial v_{\mathrm{B3}}}{\partial x}\right) \tag{2-210}$$

which produces

$$it_{\mathrm{L1B1}} + t_{\mathrm{N1}} + i\chi t_{\mathrm{L1B2}} + \chi t_{\mathrm{N2}} = 0 \tag{2-211}$$

Continuity of translational velocity at the junction in *x*- and *y*-directions requires that

$$v_{\mathrm{L1}} = v_{\mathrm{B2}} = v_{\mathrm{L3}} \quad , v_{\mathrm{B1}} = -v_{\mathrm{B3}} = 0 \tag{2-212}$$

which gives

$$t_{\mathrm{L1B2}} + t_{\mathrm{N2}} - r_{\mathrm{L1L1}} = 1 \tag{2-213}$$

$$-r_{\mathrm{L1L1}} + t_{\mathrm{L1L3}} = 1 \tag{2-214}$$

$$t_{\mathrm{L1B1}} + t_{\mathrm{N1}} = 0 \tag{2-215}$$

In the *y*-direction, F_{B1}-F_{B3}=0, and in the *x*-direction, equilibrium of forces requires that

$$F_{\mathrm{L1}} - F_{\mathrm{B2}} - F_{\mathrm{L3}} = 0 \tag{2-216}$$

Equations (2-4) and (2-28) gives

$$\beta_1 t_{\mathrm{L1B2}} + i\beta_1 t_{\mathrm{N2}} + r_{\mathrm{L1L1}} + t_{\mathrm{L1L3}} = 1 \tag{2-217}$$

At the junction, $\mathrm{M_{B1}}$=M_{B3}, and moment equilibrium gives

$$2M_{\mathrm{B1}} - M_{\mathrm{B2}} = 0 \tag{2-218}$$

According to (2-27), one can derive that

$$2t_{\mathrm{L1B1}} - 2t_{\mathrm{N1}} - \psi t_{\mathrm{L1B2}} + \psi t_{\mathrm{N2}} = 0 \tag{2-219}$$

The six boundary conditions generate the following matrix equation,

$$\begin{bmatrix} i & 1 & i\chi & \chi & 0 & 0 \\ 0 & 0 & 1 & 1 & -1 & 0 \\ 0 & 0 & 0 & 0 & -1 & 1 \\ 1 & 1 & 0 & 0 & 0 & 0 \\ 0 & 0 & \beta_1 & i\beta_1 & 1 & 1 \\ 2 & -2 & -\psi & \psi & 0 & 0 \end{bmatrix} \begin{bmatrix} t_{\mathrm{L1B1}} \\ t_{N1} \\ t_{\mathrm{L1B2}} \\ t_{\mathrm{N2}} \\ r_{\mathrm{L1L1}} \\ t_{\mathrm{L1L3}} \end{bmatrix} = \begin{bmatrix} 0 \\ 1 \\ 1 \\ 0 \\ 1 \\ 0 \end{bmatrix} \tag{2-220}$$

Solution of (2-220) allows the reflection and transmission coefficients to be calculated using

$$\tau_{\mathrm{L1B1}} = \tau_{\mathrm{L1B3}} = \frac{m_1' c_{\mathrm{B1}} \left| v_{\mathrm{B1-}} \right|^2}{\frac{1}{2} m_1' c_{\mathrm{L1}} \left| v_{\mathrm{L1+}} \right|^2} = \frac{2\beta_1}{\chi\psi} \left| t_{\mathrm{L1B1}} \right|^2 \tag{2-221}$$

$$\tau_{\mathrm{L1B2}} = \frac{m_2' c_{\mathrm{B2}} \left| v_{\mathrm{B2+}} \right|^2}{\frac{1}{2} m_1' c_{\mathrm{L1}} \left| v_{\mathrm{L1+}} \right|^2} = 2\beta_1 \left| t_{\mathrm{L1B2}} \right|^2 \tag{2-222}$$

$$\tau_{\mathrm{L1L1}} = \frac{\frac{1}{2} m_1' c_{\mathrm{L1}} \left| v_{\mathrm{L1-}} \right|^2}{\frac{1}{2} m_1' c_{\mathrm{L1}} \left| v_{\mathrm{L1+}} \right|^2} = \left| r_{\mathrm{L1L1}} \right|^2 \tag{2-223}$$

$$\tau_{\mathrm{L1L2}} = 0 \tag{2-224}$$

$$\tau_{\mathrm{L1L3}} = \frac{\frac{1}{2} m_1' c_{\mathrm{L1}} \left| v_{\mathrm{L3+}} \right|^2}{\frac{1}{2} m_1' c_{\mathrm{L1}} \left| v_{\mathrm{L1+}} \right|^2} = \left| t_{\mathrm{L1L3}} \right|^2 \tag{2-225}$$

Example transmission coefficients are shown in Figure 2.22 using the material properties and dimensions in Table 2.3. Apart from τ_{L1B2} and τ_{L1L3}, the transmission coefficients are zero or nearly zero.

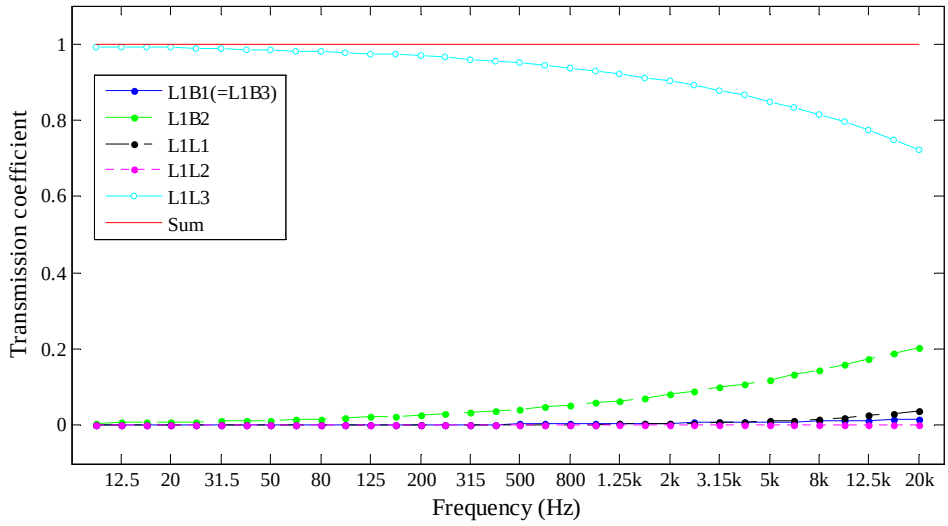

Figure 2.22 Transmission coefficients for T123-junction: BL model, incident longitudinal wave on beam 1.

2.5.3 T124-junction

2.5.3.1 Bending wave excitation

Figure 2.23 shows the T124-junction under consideration for which the coordinates of the junction line are (x,y)=(0,0).

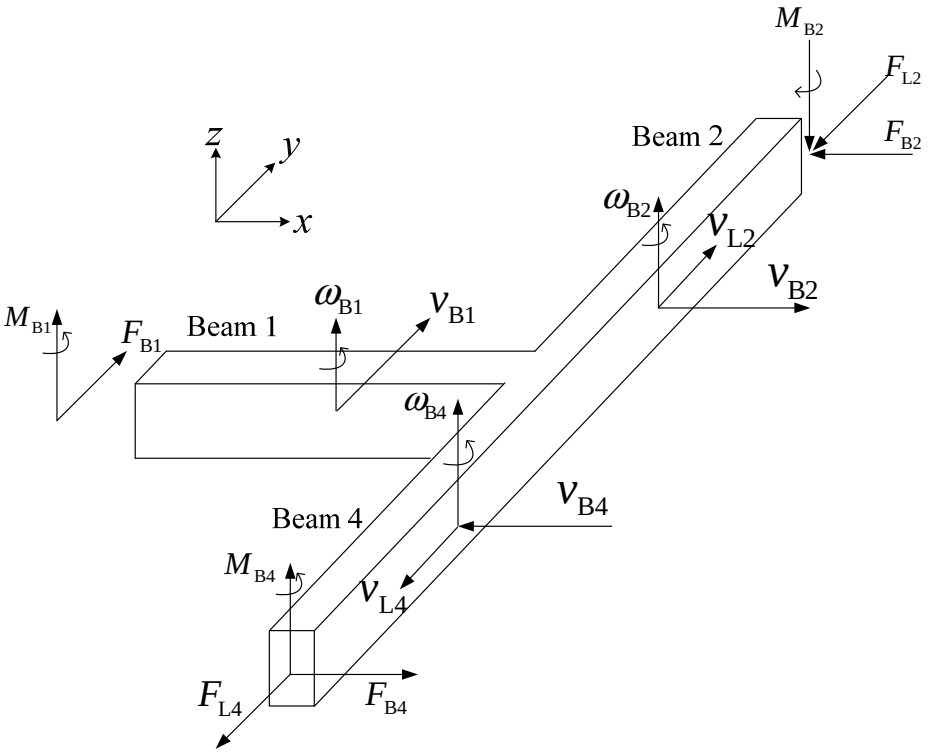

Figure 2.23 T124-junction: BL model, Type A bending wave excitation on beam 1.

Consider an incident bending wave (Type A) travelling in the positive x-direction towards the junction on beam 1. Both bending and longitudinal waves will be transmitted onto beams 2 and 4. Due to symmetry, Type A bending waves on beams 2 and 4 have the same magnitude but travel in opposite directions. Hence there will be zero displacement in the *x*-direction at the junction. Similarly, the phases are different but magnitudes are the same for longitudinal waves on beams 2 and 4. The wave fields of T124-junction for bending wave excitation are described by

$$v_{B1} = \left(e^{-ik_{B1}x} + r_{B1B1}e^{ik_{B1}x} + r_{N1}e^{k_{B1}x}\right)e^{i\omega t} \tag{2-226}$$

$$v_{B2} = \left(t_{B1B2}e^{-ik_{B2}y} + t_{N2}e^{-k_{B2}y}\right)e^{i\omega t} \tag{2-227}$$

$$v_{B4} = -\left(t_{B1B2}e^{ik_{B2}y} + t_{N2}e^{k_{B2}y}\right)e^{i\omega t} \tag{2-228}$$

$$v_{L1} = 0 \tag{2-229}$$

$$v_{L2} = t_{B1L2}e^{-ik_{L2}y}e^{i\omega t} \tag{2-230}$$

$$v_{\mathrm{L4}} = -t_{\mathrm{B1L2}} e^{ik_{\mathrm{L2}}y} e^{i\omega t} \tag{2-231}$$

Totally there are five unknown variables to be solved, which will need the following five boundary condition equations.

For continuity of angular velocity at the junction,

$$\frac{\partial v_{\mathrm{B1}}}{\partial x} = \frac{\partial v_{\mathrm{B2}}}{\partial y} \tag{2-232}$$

Continuity of velocity in *x*- and *y*-directions at the junction gives

$$v_{\mathrm{B1}} = v_{\mathrm{L2}} \quad , v_{\mathrm{B2}} = -v_{\mathrm{B4}} = 0 \tag{2-233}$$

In the *x*-direction, F_{B2}-F_{B4}=0, and in the *y*-direction, F_{L2}=F_{L4}, and force equilibrium requires that

$$F_{\mathrm{B1}} - 2F_{\mathrm{L2}} = 0 \tag{2-234}$$

At the junction, M_{B2}=-M_{B4}, and moment equilibrium gives

$$M_{\mathrm{B1}} - 2M_{\mathrm{B2}} = 0 \tag{2-235}$$

Solve these boundary condition equations as previous part; one can get the following matrix equation

$$\begin{bmatrix} i & 1 & i\chi & \chi & 0 \\ 1 & 1 & 0 & 0 & -1 \\ 0 & 0 & 1 & 1 & 0 \\ \beta_2 & i\beta_2 & 0 & 0 & 2 \\ 1 & -1 & -2\psi & 2\psi & 0 \end{bmatrix} \begin{bmatrix} r_{\mathrm{B1B1}} \\ r_{N1} \\ t_{\mathrm{B1B2}} \\ t_{\mathrm{N2}} \\ t_{\mathrm{B1L2}} \end{bmatrix} = \begin{bmatrix} i \\ -1 \\ 0 \\ \beta_2 \\ -1 \end{bmatrix} \tag{2-236}$$

Solution of (2-236) allows the reflection and transmission coefficients to be calculated using

$$\tau_{\mathrm{B1B1}} = \frac{m_1' c_{\mathrm{B1}} \left| v_{\mathrm{B1-}} \right|^2}{m_1' c_{\mathrm{B1}} \left| v_{\mathrm{B1+}} \right|^2} = \left| r_{\mathrm{B1B1}} \right|^2 \tag{2-237}$$

$$\tau_{\mathrm{B1B2}} = \tau_{\mathrm{B1B4}} = \frac{m_2' c_{\mathrm{B2}} \left| v_{\mathrm{B2+}} \right|^2}{m_1' c_{\mathrm{B1}} \left| v_{\mathrm{B1+}} \right|^2} = \chi \psi \left| t_{\mathrm{B1B2}} \right|^2 \tag{2-238}$$

$$\tau_{\mathrm{B1L1}} = 0 \tag{2-239}$$

$$\tau_{\mathrm{B1L2}} = \frac{\frac{1}{2} m_1' c_{\mathrm{L2}} \left| v_{\mathrm{L2+}} \right|^2}{m_1' c_{\mathrm{B1}} \left| v_{\mathrm{B1+}} \right|^2} = \frac{1}{2\beta_2} \left| t_{\mathrm{B1L2}} \right|^2 \tag{2-240}$$

Example results for the perspex beam junction described in Table 2.3 are shown in Figure 2.24. With increasing frequency τ_{B1L2} increases from zero to 0.2 although τ_{B1B2} remains similar.

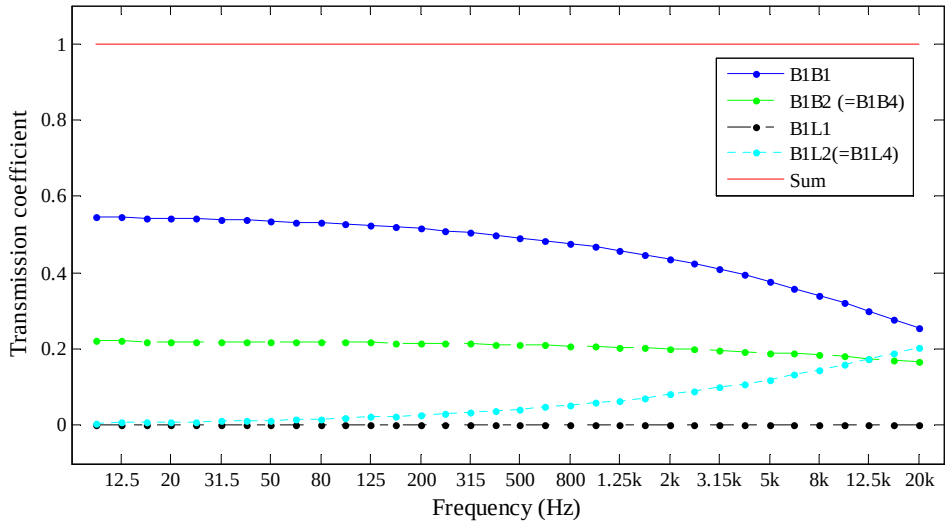

Figure 2.24 Transmission coefficients for T124-junction: BL model, incident bending wave (Type A) on beam 1.

2.5.3.2 Longitudinal wave excitation

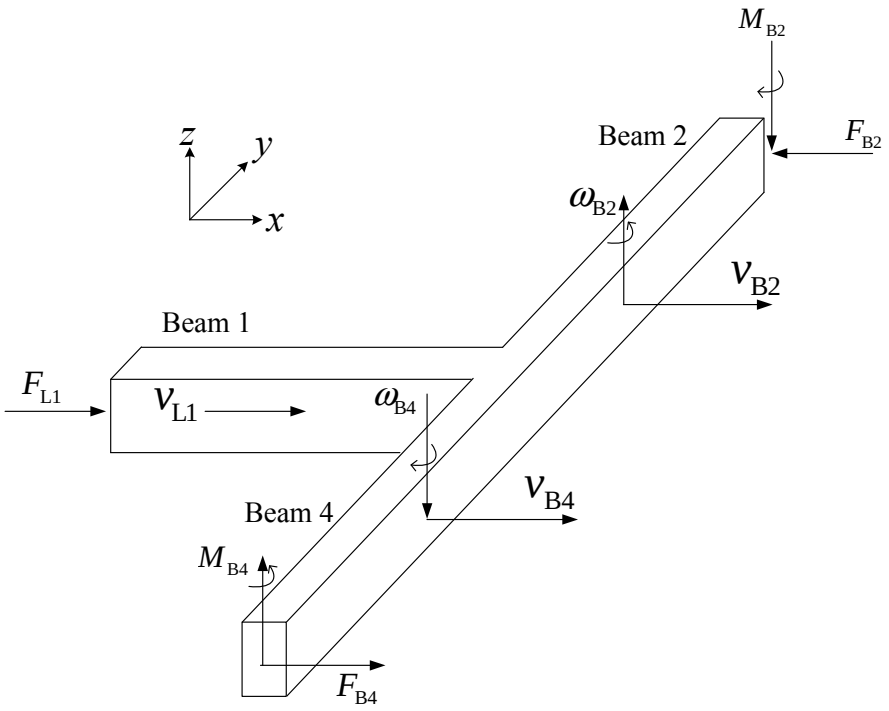

Figure 2.25 T124-junction: BL model, longitudinal wave excitation on beam 1.

Consider an incident longitudinal wave travelling in the positive x-direction towards the junction on beam 1. This will generate Type A bending waves on beams 2 and 4, and a longitudinal wave reflected on beam 1. At the junction, the rotational displacement is zero due to balanced bending moments from beams 2 and 4. The incident wave is assumed to have unit amplitude; hence the wave fields can be described as follows:

$$v_{L1} = \left(e^{-ik_{L1}x} + r_{L1L1}e^{ik_{L1}x}\right)e^{i\omega t} \tag{2-241}$$

$$v_{L2} = v_{L4} = 0 \tag{2-242}$$

$$v_{B1} = 0 \tag{2-243}$$

$$v_{B2} = \left(t_{L1B2}e^{-ik_{B2}y} + t_{N2}e^{-k_{B2}y}\right)e^{i\omega t} \tag{2-244}$$

$$v_{B4} = \left(t_{L1B2}e^{ik_{B2}y} + t_{N2}e^{k_{B2}y}\right)e^{i\omega t} \tag{2-245}$$

There are three unknowns; hence three boundary conditions are required. Continuity of velocity in the *x*-direction requires that

$$v_{\mathrm{L1}} = v_{\mathrm{B2}} \tag{2-246}$$

At the junction, the velocity is zero in the *y*-direction. In addition, the angular velocity is zero where

$$\frac{\partial v_{\mathrm{B2}}}{\partial y} = 0 \tag{2-247}$$

In the *x*-direction, F_{B2}=F_{B4}, and force equilibrium requires that

$$F_{\mathrm{L1}} - 2F_{\mathrm{B2}} = 0 \tag{2-248}$$

For the bending moment, M_{B2}-M_{B4}=0; hence these three equations give the following matrix equation

$$\begin{bmatrix} -1 & 1 & 1 \\ 0 & i & 1 \\ 1 & 2\beta_1 & 2i\beta_1 \end{bmatrix} \begin{bmatrix} r_{\mathrm{L1L1}} \\ t_{\mathrm{L1B2}} \\ t_{\mathrm{N2}} \end{bmatrix} = \begin{bmatrix} 1 \\ 0 \\ 1 \end{bmatrix} \tag{2-249}$$

Solution of (2-249) allows the reflection and transmission coefficients to be calculated using

$$\tau_{\mathrm{L1L1}} = \frac{\frac{1}{2} m_1' c_{\mathrm{L1}} \left| v_{\mathrm{L1-}} \right|^2}{\frac{1}{2} m_1' c_{\mathrm{L1}} \left| v_{\mathrm{L1+}} \right|^2} = \left| r_{\mathrm{L1L1}} \right|^2 \tag{2-250}$$

$$\tau_{\mathrm{L1L2}} = \tau_{\mathrm{L1L4}} = 0 \tag{2-251}$$

$$\tau_{\mathrm{L1B1}} = 0 \tag{2-252}$$

$$\tau_{\mathrm{L1B2}} = \tau_{\mathrm{L1B4}} = \frac{m_2' c_{\mathrm{B2}} \left| v_{\mathrm{B2+}} \right|^2}{\frac{1}{2} m_1' c_{\mathrm{L1}} \left| v_{\mathrm{L1+}} \right|^2} = 2\beta_1 \left| t_{\mathrm{L1B2}} \right|^2 \tag{2-253}$$

Example transmission coefficients are shown in Figure 2.26 using the material properties and dimensions in Table 2.3.

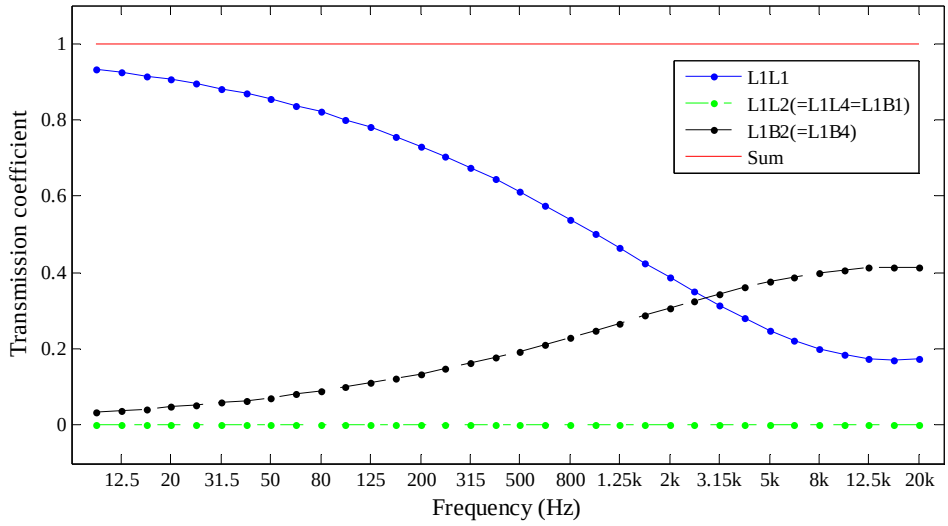

Figure 2.26 Transmission coefficients for T124-junction: BL model, incident longitudinal wave on beam 1.

2.5.4 L-junction

2.5.4.1 Bending wave excitation

Figure 2.27 shows the L-junction under consideration for which beams 1 and 2 have a different cross-section and material properties. The L-junction is an asymmetric structure; hence Type A bending waves and longitudinal waves are reflected or transmitted in all beams. The coordinates of the junction line are (x,y)=(0,0).

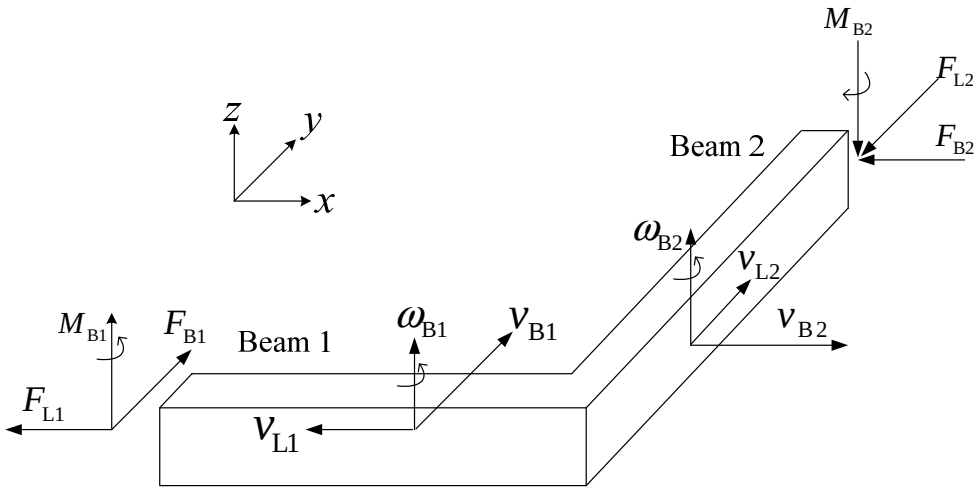

Figure 2.27 L-junction: BL model, Type A bending wave excitation on beam 1.

Consider an incident bending wave (Type A) with unit amplitude travelling in the positive *x*-direction towards the junction on beam 1. The wave fields on each beam can be described as follows:

$$v_{B1} = (e^{-ik_{B1}x} + r_{B1B1}e^{ik_{B1}x} + r_{N1}e^{k_{B1}x})e^{i\omega t} \tag{2-254}$$

$$v_{B2} = (t_{B1B2}e^{-ik_{B2}y} + t_{N2}e^{-k_{B2}y})e^{i\omega t} \tag{2-255}$$

$$v_{L1} = r_{B1L1}e^{ik_{L1}x}e^{i\omega t} \tag{2-256}$$

$$v_{L2} = t_{B1L2}e^{-ik_{L2}y}e^{i\omega t} \tag{2-257}$$

Continuity of angular velocity at the junction requires that

$$\frac{\partial v_{B1}}{\partial x} = \frac{\partial v_{B2}}{\partial y} \tag{2-258}$$

Continuity of velocity at the junction in *x* and *y* directions gives

$$v_{B1} = v_{L2}, \quad v_{L1} = -v_{B2} \tag{2-259}$$

As indicated in Figure 2.27, the relationships between shear and longitudinal forces are

$$F_{B1} = F_{L2}, \quad F_{L1} = -F_{B2} \tag{2-260}$$

The moment equilibrium relationship is

$$M_1 - M_2 = 0 \tag{2-261}$$

The six equations result in the following matrix to be solved for the reflection and transmission coefficients

$$\begin{bmatrix} i & 1 & i\chi & \chi & 0 & 0 \\ 1 & 1 & 0 & 0 & 0 & -1 \\ 0 & 0 & 1 & 1 & 1 & 0 \\ \beta_2 & i\beta_2 & 0 & 0 & 0 & 1 \\ 0 & 0 & \beta_1 & i\beta_1 & -1 & 0 \\ -1 & 1 & \psi & -\psi & 0 & 0 \end{bmatrix} \begin{bmatrix} r_{\mathrm{B1B1}} \\ r_{\mathrm{N1}} \\ t_{\mathrm{B1B2}} \\ t_{\mathrm{N2}} \\ r_{\mathrm{B1L1}} \\ t_{\mathrm{B1L2}} \end{bmatrix} = \begin{bmatrix} i \\ -1 \\ 0 \\ \beta_2 \\ 0 \\ 1 \end{bmatrix} \tag{2-262}$$

Solution of this matrix gives the same result as quoted in Cremer *et al* [5]. The transmission coefficients can be then calculated as follows

$$\tau_{\mathrm{B1B1}} = \frac{m_1' c_{\mathrm{B1}} \left| v_{\mathrm{B1-}} \right|^2}{m_1' c_{\mathrm{B1}} \left| v_{\mathrm{B1+}} \right|^2} = \left| r_{\mathrm{B1B1}} \right|^2 \tag{2-263}$$

$$\tau_{\mathrm{B1B2}} = \frac{m_2' c_{\mathrm{B2}} \left| v_{\mathrm{B2+}} \right|^2}{m_1' c_{\mathrm{B1}} \left| v_{\mathrm{B1+}} \right|^2} = \chi\psi \left| t_{\mathrm{B1B2}} \right|^2 \tag{2-264}$$

$$\tau_{\mathrm{B1L1}} = \frac{\frac{1}{2} m_1' c_{\mathrm{L1}} \left| v_{\mathrm{L1-}} \right|^2}{m_1' c_{\mathrm{B1}} \left| v_{\mathrm{B1+}} \right|^2} = \frac{\chi\psi}{2\beta_2} \left| r_{\mathrm{B1L1}} \right|^2 \tag{2-265}$$

$$\tau_{\mathrm{B1L2}} = \frac{\frac{1}{2} m_1' c_{\mathrm{L2}} \left| v_{\mathrm{L2+}} \right|^2}{m_1' c_{\mathrm{B1}} \left| v_{\mathrm{B1+}} \right|^2} = \frac{1}{2\beta_2} \left| t_{\mathrm{B1L2}} \right|^2 \tag{2-266}$$

Example transmission coefficients are shown in Figure 2.28 using the material properties and dimensions in Table 2.3.

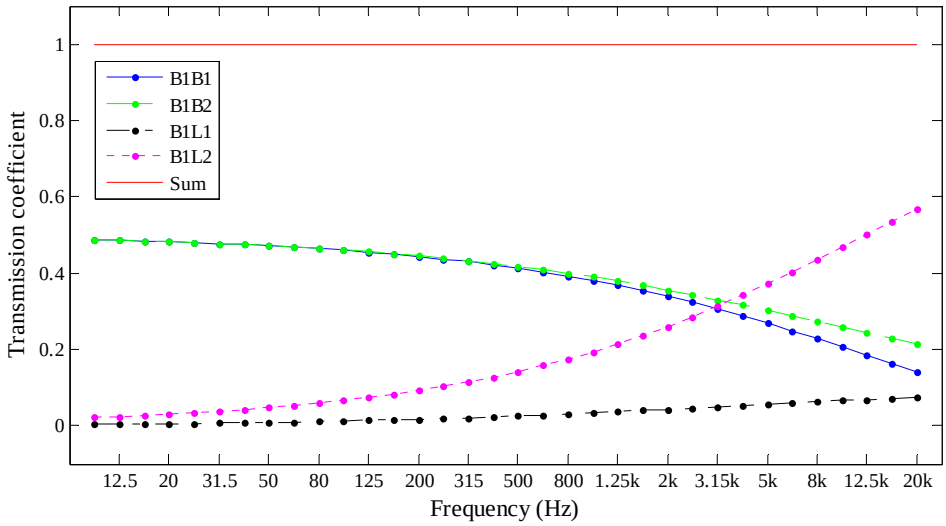

Figure 2.28 Transmission coefficients for L-junction: BL model, incident bending wave (Type A) on beam 1.

2.5.4.2 Longitudinal wave excitation

Consider an incident longitudinal wave with unit amplitude travelling in the positive x-direction towards the junction on beam 1 for which the wave fields on each beam are described as follows:

$$v_{\mathrm{L1}} = (e^{-ik_{\mathrm{L1}}x} + r_{\mathrm{L1L1}}e^{ik_{\mathrm{L1}}x})e^{i\omega t} \tag{2-267}$$

$$v_{\mathrm{L2}} = t_{\mathrm{L1L2}}e^{-ik_{\mathrm{L2}}y}e^{i\omega t} \tag{2-268}$$

$$v_{\mathrm{B1}} = (r_{\mathrm{L1B1}}e^{ik_{\mathrm{B1}}x} + r_{\mathrm{N1}}e^{k_{\mathrm{B1}}x})e^{i\omega t} \tag{2-269}$$

$$v_{\mathrm{B2}} = (t_{\mathrm{L1B2}}e^{-ik_{\mathrm{B2}}y} + t_{\mathrm{N2}j}e^{-k_{\mathrm{B2}}y})e^{i\omega t} \tag{2-270}$$

The boundary conditions are the same as that for bending wave excitation on the L-junction in part 2.5.4.1. This gives the following matrix equation from which the six variables r_{L1B1}, r_j, t_{L1B2}, t_{2j}, r_{L1L1} and t_{L1L2} can be determined.

$$\begin{bmatrix} i & 1 & i\chi & \chi & 0 & 0 \\ 1 & 1 & 0 & 0 & 0 & -1 \\ 0 & 0 & 1 & 1 & 1 & 0 \\ \beta_2 & i\beta_2 & 0 & 0 & 0 & 1 \\ 0 & 0 & \beta_1 & i\beta_1 & -1 & 0 \\ -1 & 1 & \psi & -\psi & 0 & 0 \end{bmatrix} \begin{bmatrix} r_{\mathrm{L1B1}} \\ r_{\mathrm{N1}} \\ t_{\mathrm{L1B2}} \\ t_{\mathrm{N2}} \\ r_{\mathrm{L1L1}} \\ t_{\mathrm{L1L2}} \end{bmatrix} = \begin{bmatrix} 0 \\ 0 \\ -1 \\ 0 \\ -1 \\ 0 \end{bmatrix} \tag{2-271}$$

Note that the coefficients in the left matrix are the same as (2-262); it is only the right side of the matrix equation that is different. The transmission coefficients are calculated using the following equations

$$\tau_{\mathrm{L1B1}} = \frac{m_1' c_{\mathrm{B1}} \left| v_{\mathrm{B1-}} \right|^2}{\frac{1}{2} m_1' c_{\mathrm{L1}} \left| v_{\mathrm{L1+}} \right|^2} = \frac{2\beta_1}{\chi\psi} \left| t_{\mathrm{L1B1}} \right|^2 \tag{2-272}$$

$$\tau_{\mathrm{L1B2}} = \frac{m_2' c_{\mathrm{B2}} \left| v_{\mathrm{B2+}} \right|^2}{\frac{1}{2} m_1' c_{\mathrm{L1}} \left| v_{\mathrm{L1+}} \right|^2} = 2\beta_1 \left| t_{\mathrm{L1B2}} \right|^2 \tag{2-273}$$

$$\tau_{\mathrm{L1L1}} = \frac{\frac{1}{2} m_1' c_{\mathrm{L1}} \left| v_{\mathrm{L1-}} \right|^2}{\frac{1}{2} m_1' c_{\mathrm{L1}} \left| v_{\mathrm{L1+}} \right|^2} = \left| r_{\mathrm{L1L1}} \right|^2 \tag{2-274}$$

$$\tau_{\mathrm{L1L2}} = \frac{\frac{1}{2} m_2' c_{\mathrm{L2}} \left| v_{\mathrm{L2+}} \right|^2}{\frac{1}{2} m_1' c_{\mathrm{L1}} \left| v_{\mathrm{L1+}} \right|^2} = \frac{\beta_1}{\chi\psi\beta_2} \left| t_{\mathrm{L1L2}} \right|^2 \tag{2-275}$$

Note that these are general solutions for which the material properties and dimensions of beams 1 and 2 are different whereas in Cremer *et al* [5] the results are given for the identical beams of L-junction.

Example transmission coefficients are shown in Figure 2.29 using the material properties and dimensions in Table 2.3.

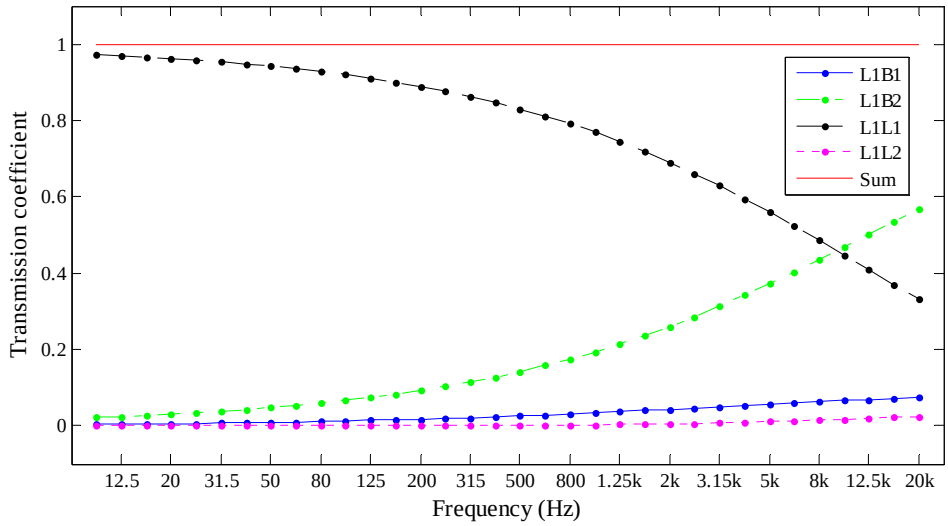

Figure 2.29 Transmission coefficients for L-junction: BL model, incident longitudinal wave on beam 1.

2.6 Bending and torsional wave model (BT model)

In the bending only model and the bending and longitudinal model, incident bending waves (Type A) have motion in the same plane as the junction such that only bending and longitudinal waves are generated at the junction. In this section, Type B bending wave motion is normal to the plane of the junction which results in the generation of torsional waves instead of longitudinal waves. Bending and torsional wave models (BT models) are derived for X-, T- and L-junctions which all have rigid unpinned junction and semi-infinite beams.

2.6.1 X-junction

2.6.1.1 Bending wave excitation

Figure 2.30 shows the X-junction under consideration for which the coordinates of the junction line are (x,y)=(0,0). Beams 1 and 3 and beams 2 and 4 are identical in X-junction.

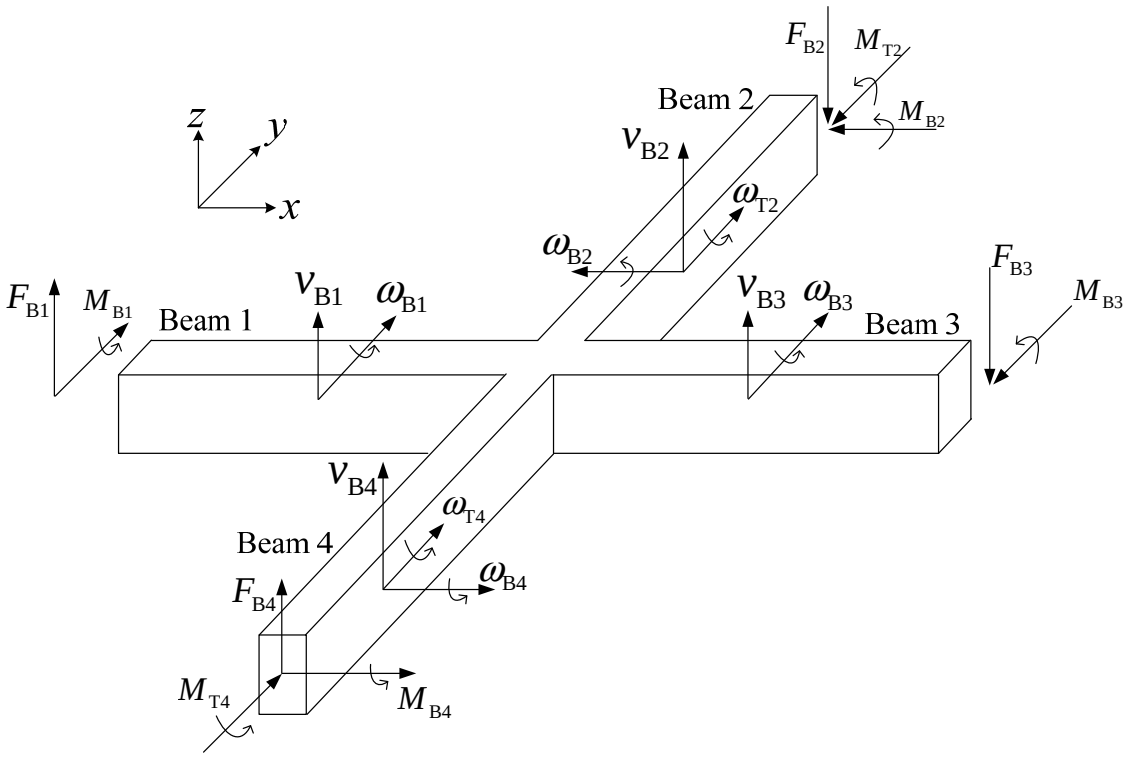

Figure 2.30 X-junction: BT model, Type B bending wave excitation on beam 1.

Consider an incident bending wave (Type B) with unit amplitude travelling on beam 1 in the positive *x*-direction towards the junction. The transmitted bending wave on beams 2 and 4 have opposite moments at the junction in the *x*-direction, hence there is no torsional wave motion on beams 1 and 3.

$$v_{B1} = \left(e^{-ik_{B1}x} + r_{B1B1}e^{ik_{B1}x} + r_{N1}e^{k_{B1}x}\right)e^{i\omega t} \tag{2-276}$$

$$v_{B2} = \left(t_{B1B2}e^{-ik_{B2}y} + t_{N2}e^{-k_{B2}y}\right)e^{i\omega t} \tag{2-277}$$

$$v_{B3} = \left(t_{B1B3}e^{-ik_{B1}x} + t_{N3}e^{-k_{B1}x}\right)e^{i\omega t} \tag{2-278}$$

$$v_{B4} = \left(t_{B1B2}e^{ik_{B2}y} + t_{N2}e^{k_{B2}y}\right)e^{i\omega t} \tag{2-279}$$

$$\omega_{T1} = \omega_{T3} = 0 \tag{2-280}$$

$$\omega_{T2} = \omega_0 t_{B1T2}e^{-ik_{T2}y}e^{i\omega t} = -ik_{B1}t_{B1T2}e^{-ik_{T2}y}e^{i\omega t} \tag{2-281}$$

$$\omega_{T4} = \omega_0 t_{B1T2}e^{ik_{T2}y}e^{i\omega t} = -ik_{B1}t_{B1T2}e^{ik_{T2}y}e^{i\omega t} \tag{2-282}$$

where subscripts B, T and N indicate bending waves, torsional waves and nearfields respectively, and ω_0=-ik_{B1} is the complex amplitude of the angular velocity due to the incident bending wave. The bending wave numbers correspond to bending wave motion that is out-of-plane of the junction.

The following parameters are defined for the BT model,

$$\mu_1 = \frac{\omega Z_{T2}}{B_1 k_{B1}}, \quad \mu_2 = \frac{\omega Z_{T1}}{B_2 k_{B2}} \tag{2-283}$$

$$\chi = \frac{k_{B2}}{k_{B1}}, \quad \beta = \frac{B_2 k_{B2}^3}{B_1 k_{B1}^3} \tag{2-284}$$

where Z_{T1} is the impedance for torsional wave motion. Note that the calculation of χ is different from that in the BL model since the bending wave motion is along a different dimension of the beam cross-section.

Continuity of bending velocity at the junction in the *z*-direction requires that

$$v_{B1} = v_{B2}, \quad v_{B1} = v_{B3} \tag{2-285}$$

Therefore

$$r_{B1B1} + r_{N1} - t_{B1B2} - t_{N2} = -1 \tag{2-286}$$

$$r_{B1B1} + r_{N1} - t_{B1B3} - t_{N3} = -1 \tag{2-287}$$

Continuity of rotational velocity in the *y*-direction requires that

$$\frac{\partial v_{B1}}{\partial x} = \omega_{T2}, \quad \frac{\partial v_{B3}}{\partial x} = \omega_{T2} \tag{2-288}$$

In the *x*-direction, rotational velocity at the junction is zero. Hence

$$\frac{\partial v_{B2}}{\partial y} = 0 \tag{2-289}$$

Thus one obtains the following three equations,

$$r_{\mathrm{B1B1}} - i r_{\mathrm{N1}} + t_{\mathrm{B1T2}} = 1 \tag{2-290}$$

$$t_{\mathrm{B1B3}} - i t_{\mathrm{N3}} = t_{\mathrm{B1T2}} \tag{2-291}$$

$$i t_{\mathrm{B1B2}} + t_{\mathrm{N2}} = 0 \tag{2-292}$$

The bending moments from beams 1 and 3 must be balanced by the moments from torsional wave motion on beams 2 and 4, hence M_{T2}=-M_{T4}. The moment equilibrium relation is expressed as

$$M_{\mathrm{B1}} - 2M_{\mathrm{T2}} - M_{\mathrm{B3}} = 0 \tag{2-293}$$

From (2-25) and (2-11) one has

$$\begin{aligned} M_{\mathrm{B1}} &= -B_1 \int \frac{\partial^2 v_{\mathrm{B1}}}{\partial x^2} \mathrm{d}t = \frac{-B_1}{i\omega} \left[\left(-ik_{\mathrm{B1}}\right)^2 + \left(ik_{\mathrm{B1}}\right)^2 r_{\mathrm{B1B1}} + k_{\mathrm{B1}}^2 r_{\mathrm{N1}} \right] e^{i\omega t} \\ &= \frac{-B_1 k_{\mathrm{B1}}^2}{i\omega} \left(-1 - r_{\mathrm{B1B1}} + r_{\mathrm{N1}}\right) e^{i\omega t} \end{aligned} \tag{2-294}$$

$$\begin{aligned} M_{\mathrm{B3}} &= -B_1 \int \frac{\partial^2 v_{\mathrm{B1}}}{\partial x^2} \mathrm{d}t = \frac{-B_1}{i\omega} \left[\left(-ik_{\mathrm{B1}}\right)^2 t_{\mathrm{B1B3}} + \left(-k_{\mathrm{B1}}\right)^2 t_{\mathrm{N3}} \right] e^{i\omega t} \\ &= \frac{-B_1 k_{\mathrm{B1}}^2}{i\omega} \left(-t_{\mathrm{B1B3}} + t_{\mathrm{N3}}\right) e^{i\omega t} \end{aligned} \tag{2-295}$$

$$\begin{aligned} M_{\mathrm{T2}} &= -\Theta_2 \int \frac{\partial \omega_{\mathrm{T2}}}{\partial t} \mathrm{d}y = -i\omega\Theta_2 \frac{-ik_{\mathrm{B1}} t_{\mathrm{B1T2}} e^{i\omega t}}{-ik_{\mathrm{T2}}} \\ &= -iZ_{\mathrm{T2}} k_{\mathrm{B1}} t_{\mathrm{B1T2}} e^{i\omega t} \end{aligned} \tag{2-296}$$

Thus equation (2-293) becomes

$$-r_{\mathrm{B1B1}} + r_{\mathrm{N1}} + t_{\mathrm{B1B3}} - t_{\mathrm{N3}} + 2\mu_1 t_{\mathrm{B1T2}} = 1 \tag{2-297}$$

For the shear forces due to bending motion in the *z*-direction,

$$F_{\mathrm{B1}} - 2F_{\mathrm{B2}} - F_{\mathrm{B3}} = 0 \tag{2-298}$$

From equation (2-28) the shear forces are

$$F_{B1} = B_1 \int \frac{\partial^3 v_{B1}}{\partial x^3} \mathrm{d}t = \frac{B_1}{i\omega}\left[\left(-ik_{B1}\right)^3 + \left(ik_{B1}\right)^3 r_{B1B1} + \left(k_{B1}\right)^3 r_{N1}\right] e^{i\omega t}$$
$$= \frac{B_1 k_{B1}^3}{\omega}(1 - r_{B1B1} - ir_{N1}) e^{i\omega t} \tag{2-299}$$

$$F_{B2} = B_2 \int \frac{\partial^3 v_{B2}}{\partial y^3} \mathrm{d}t = \frac{B_2}{i\omega}\left[\left(-ik_{B2}\right)^3 t_{B1B2} + \left(-k_{B2}\right)^3 t_{N2}\right] e^{i\omega t}$$
$$= \frac{B_2 k_{B2}^3}{\omega}\left(t_{B1B2} + it_{N2}\right) e^{i\omega t} \tag{2-300}$$

$$F_{B3} = B_1 \int \frac{\partial^3 v_{B3}}{\partial x^3} \mathrm{d}t = \frac{B_1}{i\omega}\left[\left(-ik_{B1}\right)^3 t_{B1B3} + \left(-k_{B1}\right)^3 t_{N3}\right] e^{i\omega t}$$
$$= \frac{B_1 k_{B1}^3}{\omega}\left(t_{B1B3} + it_{N3}\right) e^{i\omega t} \tag{2-301}$$

Then (2-298) can be reduced to

$$r_{B1B1} + ir_{N1} + 2\beta t_{B1B2} + 2i\beta t_{N2} + t_{B1B3} + it_{N3} = 1 \tag{2-302}$$

These boundary condition equations result in the following matrix,

$$\begin{bmatrix} 1 & 1 & -1 & -1 & 0 & 0 & 0 \\ 1 & 1 & 0 & 0 & -1 & -1 & 0 \\ 1 & -i & 0 & 0 & 0 & 0 & 1 \\ 0 & 0 & 0 & 0 & 1 & -i & -1 \\ 0 & 0 & i & 1 & 0 & 0 & 0 \\ -1 & 1 & 0 & 0 & 1 & -1 & 2\mu_1 \\ 1 & i & 2\beta & 2i\beta & 1 & i & 0 \end{bmatrix} \begin{bmatrix} r_{B1B1} \\ r_{N1} \\ t_{B1B2} \\ t_{N2} \\ t_{B1B3} \\ t_{N3} \\ t_{B1T2} \end{bmatrix} = \begin{bmatrix} -1 \\ -1 \\ 1 \\ 0 \\ 0 \\ 1 \\ 1 \end{bmatrix} \tag{2-303}$$

Solution of (2-303) allows the reflection and transmission coefficients to be calculated using

$$\tau_{B1B1} = \frac{m_1' c_{B1} \left|v_{B1-}\right|^2}{m_1' c_{B1} \left|v_{B1+}\right|^2} = \left|r_{B1B1}\right|^2 \tag{2-304}$$

$$\tau_{B1B2} = \tau_{B1B4} = \frac{m_2' c_{B2} \left|v_{B2+}\right|^2}{m_1' c_{B1} \left|v_{B1+}\right|^2} = \beta \left|t_{B1B2}\right|^2 \tag{2-305}$$

$$\tau_{\mathrm{B1B3}} = \frac{m_1' c_{\mathrm{B1}} \left| v_{\mathrm{B3+}} \right|^2}{m_1' c_{\mathrm{B1}} \left| v_{\mathrm{B1+}} \right|^2} = \left| t_{\mathrm{B1B3}} \right|^2 \tag{2-306}$$

$$\tau_{\mathrm{B1T1}} = \tau_{\mathrm{B1T3}} = 0 \tag{2-307}$$

$$\tau_{\mathrm{B1T2}} = \tau_{\mathrm{B1T4}} = \frac{\frac{1}{2}\Theta_2 c_{\mathrm{T2}} \left| \omega_{\mathrm{T2+}} \right|^2}{m_1' c_{\mathrm{B1}} \left| v_{\mathrm{B1+}} \right|^2} = \frac{\frac{1}{2}\Theta_2 c_{\mathrm{T2}} k_{\mathrm{B1}}^2}{m_1' c_{\mathrm{B1}}} \left| t_{\mathrm{B1T2}} \right|^2 = \frac{\mu_1}{2} \left| t_{\mathrm{B1T2}} \right|^2 \tag{2-308}$$

Example transmission coefficients are plotted in Figure 2.31 using the material properties and dimensions in Table 2.3.

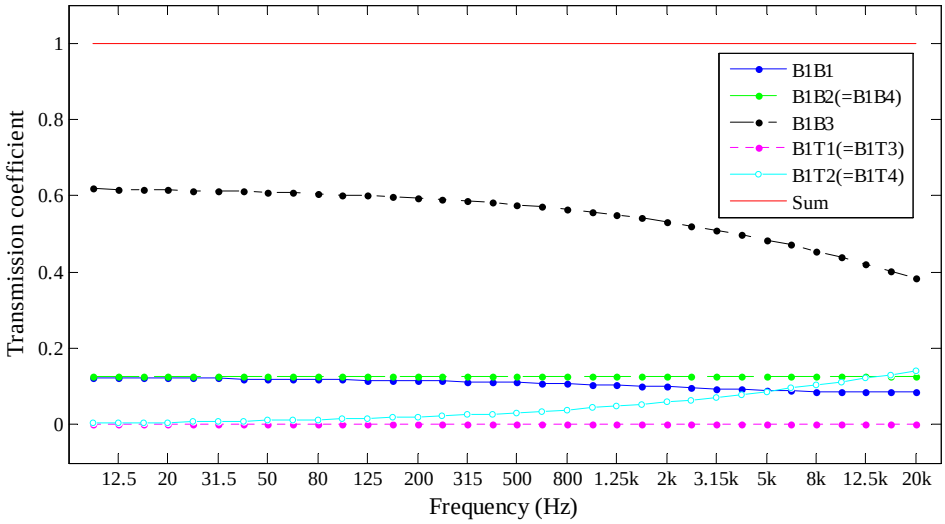

Figure 2.31 Transmission coefficients for X-junction: BT model, incident bending wave (Type B) on beam 1.

2.6.1.2 Torsional wave excitation

Figure 2.32 shows an incident torsional wave with unit amplitude travelling in the positive *x*-direction towards the junction on beam 1.

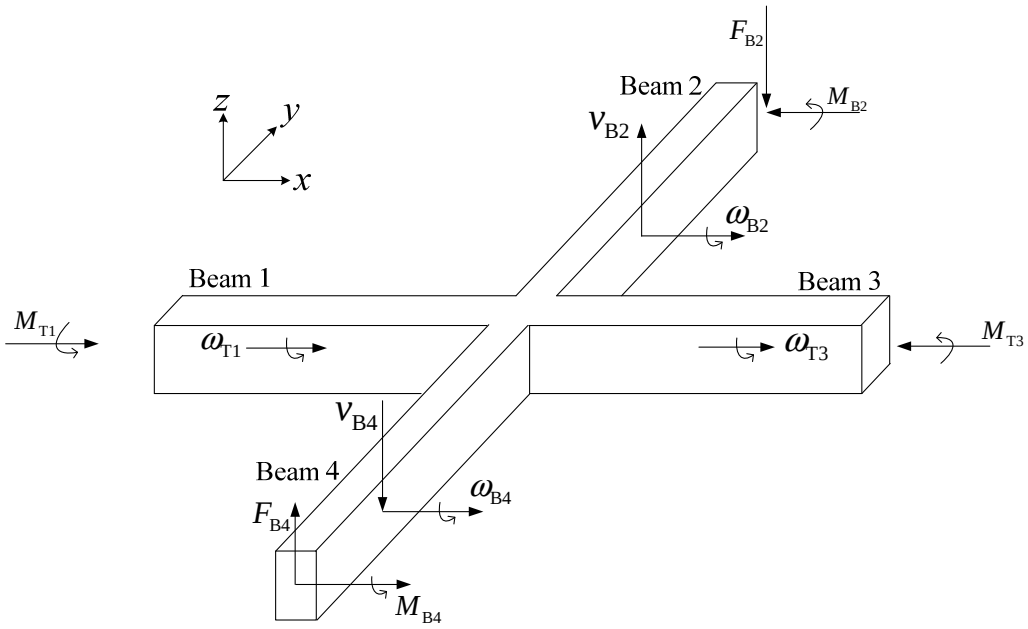

Figure 2.32 X-junction: BT model, torsional wave excitation on beam 1.

Due to structural symmetry, the transmitted bending waves (Type B) on beams 2 and 4 have the same magnitude but travel in opposite directions. Hence the shear forces from bending motion on beams 2 and 4 are balanced and bending displacement is zero in the *z*-direction at the junction. The wave fields are described by

$$\omega_{T1} = (e^{-ik_{T1}x} + r_{T1T1}e^{ik_{T1}x})e^{i\omega t} \tag{2-309}$$

$$\omega_{T2} = \omega_{T4} = 0 \tag{2-310}$$

$$\omega_{T3} = t_{T1T3}e^{-ik_{T1}x}e^{i\omega t} \tag{2-311}$$

$$v_{B1} = v_{B3} = 0 \tag{2-312}$$

$$v_{B2} = \frac{-i}{k_{B2}}\left(t_{T1B2}e^{-ik_{B2}y} + t_{N2}e^{-k_{B2}y}\right)e^{i\omega t} \tag{2-313}$$

$$v_{B4} = \frac{i}{k_{B2}}\left(t_{T1B2}e^{ik_{B2}y} + t_{N2}e^{k_{B2}y}\right)e^{i\omega t} \tag{2-314}$$

The following boundary conditions at the junction consist of continuity of angular velocity in *x*-direction, bending velocity equal to zero in the *z*-direction and equilibrium relation of moments in *x*-direction:

$$\omega_{\mathrm{T1}} = \omega_{\mathrm{T3}}, \quad \omega_{\mathrm{T1}} = \frac{\partial v_{\mathrm{B2}}}{\partial y} \tag{2-315}$$

$$v_{\mathrm{B2}} = 0 \tag{2-316}$$

$$M_{\mathrm{T1}} - 2M_{\mathrm{B2}} - M_{\mathrm{T3}} = 0 \tag{2-317}$$

In (2-317), the moments due to torsional wave motion and bending wave motion are calculated as follows based on (2-11) and (2-27)

$$M_{\mathrm{T1}} = -\Theta_1 \int \frac{\partial \omega_{\mathrm{T1}}}{\partial t} \mathrm{d}x = -i\omega\Theta_1 \left(\frac{1}{-ik_{\mathrm{T1}}} + \frac{r_{\mathrm{T1T1}}}{ik_{\mathrm{T1}}} \right) e^{i\omega t} = Z_{\mathrm{T1}} \left(1 - r_{\mathrm{T1T1}}\right) e^{i\omega t} \tag{2-318}$$

$$M_{\mathrm{T3}} = -\Theta_1 \int \frac{\partial \omega_{\mathrm{T3}}}{\partial t} \mathrm{d}x = -i\omega\Theta_1 \frac{t_{\mathrm{T1T3}} e^{i\omega t}}{-ik_{\mathrm{T1}}} = Z_{\mathrm{T1}} t_{\mathrm{T1T3}} e^{i\omega t} \tag{2-319}$$

$$\begin{aligned} M_{\mathrm{B2}} &= -B_2 \int \frac{\partial^2 v_{\mathrm{B2}}}{\partial y^2} \mathrm{d}t = \frac{-B_2}{i\omega} \frac{-i}{k_{\mathrm{B2}}} \left[\left(-ik_{\mathrm{B2}}\right)^2 t_{\mathrm{T1B2}} + \left(-k_{\mathrm{B2}}\right)^2 t_{\mathrm{N2}} \right] e^{i\omega t} \\ &= \frac{B_2 k_{\mathrm{B2}}}{\omega} \left(-t_{\mathrm{T1B2}} + t_{\mathrm{N2}}\right) e^{i\omega t} \end{aligned} \tag{2-320}$$

The above boundary conditions result in the following matrix equation

$$\begin{bmatrix} 0 & 0 & -1 & -1 \\ 1 & -i & 0 & 1 \\ 1 & 1 & 0 & 0 \\ 2 & -2 & -\mu_2 & -\mu_2 \end{bmatrix} \begin{bmatrix} t_{\mathrm{T1B2}} \\ t_{\mathrm{N2}} \\ r_{\mathrm{T1T1}} \\ t_{\mathrm{T1T3}} \end{bmatrix} = \begin{bmatrix} 1 \\ 0 \\ 0 \\ -\mu_2 \end{bmatrix} \tag{2-321}$$

Solving (2-321) gives the following reflection and transmission coefficients:

$$\tau_{\mathrm{T1T1}} = \frac{\frac{1}{2}\Theta_1 c_{\mathrm{T1}} \left|\omega_{\mathrm{T1-}}\right|^2}{\frac{1}{2}\Theta_1 c_{\mathrm{T1}} \left|\omega_{\mathrm{T1+}}\right|^2} = \left|r_{\mathrm{T1T1}}\right|^2 \tag{2-322}$$

$$\tau_{\mathrm{T1T2}} = \tau_{\mathrm{T1T4}} = 0 \tag{2-323}$$

$$\tau_{\mathrm{T1T3}} = \frac{\frac{1}{2}\Theta_1 c_{\mathrm{T1}} \left|\omega_{\mathrm{T3+}}\right|^2}{\frac{1}{2}\Theta_1 c_{\mathrm{T1}} \left|\omega_{\mathrm{T1+}}\right|^2} = \left|t_{\mathrm{T1T3}}\right|^2 \tag{2-324}$$

$$\tau_{\mathrm{T1B1}} = \tau_{\mathrm{T1B3}} = 0 \tag{2-325}$$

$$\tau_{\mathrm{T1B2}} = \tau_{\mathrm{T1B4}} = \frac{m_2' c_{\mathrm{B2}} \left|v_{\mathrm{B2+}}\right|^2}{\frac{1}{2}\Theta_1 c_{\mathrm{T1}} \left|\omega_{\mathrm{T1+}}\right|^2} = \frac{\frac{m_2' c_{\mathrm{B2}}}{k_{\mathrm{B2}}^2}}{\frac{1}{2}\Theta_1 c_{\mathrm{T1}}} \left|t_{\mathrm{T1B2}}\right|^2 = \frac{2}{\mu_2} \left|t_{\mathrm{T1B2}}\right|^2 \tag{2-326}$$

The energy conservation principle can be expressed as

$$\tau_{\mathrm{T1T1}} + 2\tau_{\mathrm{T1B2}} + \tau_{\mathrm{T1T3}} = 1 \tag{2-327}$$

Example transmission coefficients are plotted in Figure 2.33 using the material properties and dimensions in Table 2.3. A large proportion of the torsional wave power that is incident on the junction is reflected and the transmission coefficients are relatively small.

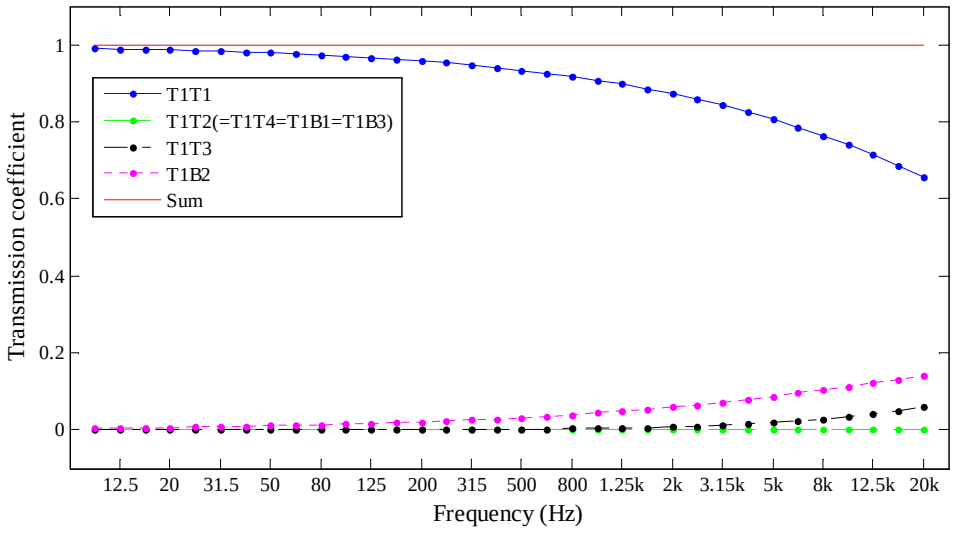

Figure 2.33 Transmission coefficients for X-junction: BT model, incident torsional wave on beam 1.

2.6.2 T123-junction

2.6.2.1 Bending wave excitation

Figure 2.34 shows the T123-junction under consideration for which the coordinates of the junction line are (x,y)=(0,0). It is assumed that the material properties and the cross-sectional dimensions are identical for beams 1 and 3.

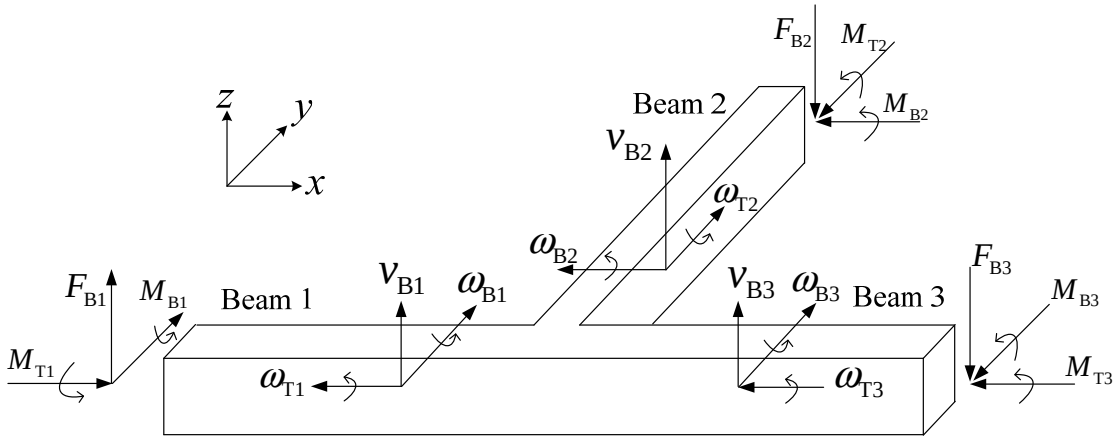

Figure 2.34 T123-junction: BT model, Type B bending wave excitation on beam 1.

An incident bending wave (Type B) with unit amplitude travels in the positive x-direction towards the junction on beam 1 and the wave fields can be described as:

$$v_{B1} = \left(e^{-ik_{B1}x} + r_{B1B1}e^{ik_{B1}x} + r_{N1}e^{k_{B1}x}\right)e^{i\omega t} \tag{2-328}$$

$$v_{B2} = \left(t_{B1B2}e^{-ik_{B2}y} + t_{N2}e^{-k_{B2}y}\right)e^{i\omega t} \tag{2-329}$$

$$v_{B3} = \left(t_{B1B3}e^{-ik_{B1}x} + t_{N3}e^{-k_{B1}x}\right)e^{i\omega t} \tag{2-330}$$

The torsional waves in beams 1 and 3 have the same magnitude but travel in opposite directions; hence the torsional wave fields for all beams can be written as

$$\omega_{T1} = \omega_0 t_{B1T1}e^{ik_{T1}x}e^{i\omega t} = -ik_{B1}t_{B1T1}e^{ik_{T1}x}e^{i\omega t} \tag{2-331}$$

$$\omega_{T2} = \omega_0 t_{B1T2}e^{-ik_{T2}y}e^{i\omega t} = -ik_{B1}t_{B1T2}e^{-ik_{T2}y}e^{i\omega t} \tag{2-332}$$

$$\omega_{T3} = \omega_0 t_{B1T1}e^{-ik_{T1}x}e^{i\omega t} = -ik_{B1}t_{B1T1}e^{-ik_{T1}x}e^{i\omega t} \tag{2-333}$$

Continuity of bending velocities in the *z*-direction at the junction requires

$$v_{B1} = v_{B2}, \quad v_{B1} = v_{B3} \tag{2-334}$$

This produces

$$r_{B1B1} + r_{N1} - t_{B1B2} - t_{N2} = -1 \tag{2-335}$$

$$r_{B1B1} + r_{N1} - t_{B1B3} - t_{N3} = -1 \tag{2-336}$$

The rotational velocity of bending motion in beams 1 and 3 must equal the angular velocity of torsional wave motion on beam 2. Also, the angular velocity of torsional wave motions in beams 1 and 3 must equal the rotational velocity of bending wave motion on beam 2. Therefore continuity of angular velocity at the junction requires that

$$\frac{\partial v_{B1}}{\partial x} = \omega_{T2}, \quad \frac{\partial v_{B3}}{\partial x} = \omega_{T2} \tag{2-337}$$

$$\omega_{T1} = \frac{\partial v_{B2}}{\partial y} \tag{2-338}$$

This results in three equations

$$r_{B1B1} - i r_{N1} + t_{B1T2} = 1 \tag{2-339}$$

$$t_{B1B3} - i t_{N3} - t_{B1B2} = 0 \tag{2-340}$$

$$i\chi t_{B1B2} + \chi t_{N2} - i t_{B1T1} = 0 \tag{2-341}$$

The shear force equilibrium relationship in the *z*-direction is given by

$$F_{B1} - F_{B2} - F_{B3} = 0 \tag{2-342}$$

The calculations of these forces are exactly the same as (2-299), (2-300) and(2-301). Then (2-342) becomes

$$r_{B1B1} + i r_{N1} + \beta t_{B1B2} + i\beta t_{N2} + t_{B1B3} + i t_{N3} = 1 \tag{2-343}$$

At the junction, M_{T1}=-M_{T3} and the moment equilibrium relationships in the *x*- and *y*-directions are

$$M_{\mathrm{T1}} - M_{\mathrm{B2}} - M_{\mathrm{T3}} = 2M_{\mathrm{T1}} - M_{\mathrm{B2}} = 0 \tag{2-344}$$

$$M_{\mathrm{B1}} - M_{\mathrm{B3}} - M_{\mathrm{T2}} = 0 \tag{2-345}$$

According to (2-11) and (2-25), $M_{\mathrm{T1}}$and M_{B2} are calculated as

$$M_{\mathrm{T1}} = -\Theta_1 \int \frac{\partial \omega_{\mathrm{T1}}}{\partial t} \mathrm{d}x = -i\omega\Theta_1 \frac{-ik_{\mathrm{B1}} t_{\mathrm{B1T1}} e^{i\omega t}}{ik_{\mathrm{T1}}} = iZ_{\mathrm{T1}} k_{\mathrm{B1}} t_{\mathrm{B1T1}} e^{i\omega t} \tag{2-346}$$

$$\begin{aligned} M_{\mathrm{B2}} &= -B_2 \int \frac{\partial^2 v_{\mathrm{B2}}}{\partial y^2} \mathrm{d}t = \frac{-B_2}{i\omega} \left[\left(-ik_{\mathrm{B2}}\right)^2 t_{\mathrm{B1B2}} + \left(-k_{\mathrm{B2}}\right)^2 t_{\mathrm{N2}} \right] e^{i\omega t} \\ &= \frac{-B_2 k_{\mathrm{B2}}^2}{i\omega} \left(-t_{\mathrm{B1B2}} + t_{\mathrm{N2}}\right) e^{i\omega t} \end{aligned} \tag{2-347}$$

Thus (2-344) becomes

$$\chi t_{\mathrm{B1B2}} - \chi t_{\mathrm{N2}} + 2\mu_2 t_{\mathrm{B1T1}} = 0 \tag{2-348}$$

The calculations for M_{B1}, M_{B3} and M_{T2} are the same as (2-294), (2-295) and (2-296). So, equation (2-345) becomes

$$-r_{\mathrm{B1B1}} + r_{N1} + t_{\mathrm{B1B3}} - t_{\mathrm{N3}} + \mu_1 t_{\mathrm{B1T2}} = 1 \tag{2-349}$$

Combining the eight boundary condition equations gives the following matrix equation

$$\begin{bmatrix} 1 & 1 & -1 & -1 & 0 & 0 & 0 & 0 \\ 1 & 1 & 0 & 0 & -1 & -1 & 0 & 0 \\ 1 & -i & 0 & 0 & 0 & 0 & 0 & 1 \\ 0 & 0 & 0 & 0 & 1 & -i & 0 & -1 \\ 0 & 0 & i\chi & \chi & 0 & 0 & -i & 0 \\ 1 & i & \beta & i\beta & 1 & i & 0 & 0 \\ 0 & 0 & \chi & -\chi & 0 & 0 & 2\mu_2 & 0 \\ -1 & 1 & 0 & 0 & 1 & -1 & 0 & \mu_1 \end{bmatrix} \begin{bmatrix} r_{\mathrm{B1B1}} \\ r_{\mathrm{N1}} \\ t_{\mathrm{B1B2}} \\ t_{\mathrm{N2}} \\ t_{\mathrm{B1B3}} \\ t_{\mathrm{N3}} \\ t_{\mathrm{B1T1}} \\ t_{\mathrm{B1T2}} \end{bmatrix} = \begin{bmatrix} -1 \\ -1 \\ 1 \\ 0 \\ 0 \\ 1 \\ 0 \\ 1 \end{bmatrix} \tag{2-350}$$

Solving (2-350) allows the following reflection and transmission coefficients to be calculated:

$$\tau_{\mathrm{B1B1}} = \frac{m_1' c_{\mathrm{B1}} \left| v_{\mathrm{B1-}} \right|^2}{m_1' c_{\mathrm{B1}} \left| v_{\mathrm{B1+}} \right|^2} = \left| r_{\mathrm{B1B1}} \right|^2 \tag{2-351}$$

$$\tau_{\mathrm{B1B2}} = \frac{m_2' c_{\mathrm{B2}} \left| v_{\mathrm{B2+}} \right|^2}{m_1' c_{\mathrm{B1}} \left| v_{\mathrm{B1+}} \right|^2} = \beta \left| t_{\mathrm{B1B2}} \right|^2 \tag{2-352}$$

$$\tau_{\mathrm{B1B3}} = \frac{m_1' c_{\mathrm{B1}} \left| v_{\mathrm{B3+}} \right|^2}{m_1' c_{\mathrm{B1}} \left| v_{\mathrm{B1+}} \right|^2} = \left| t_{\mathrm{B1B3}} \right|^2 \tag{2-353}$$

$$\tau_{\mathrm{B1T1}} = \tau_{\mathrm{B1T3}} = \frac{\frac{1}{2} \Theta_1 c_{\mathrm{T1}} \left| \omega_{\mathrm{T1-}} \right|^2}{m_1' c_{\mathrm{B1}} \left| v_{\mathrm{B1+}} \right|^2} = \frac{\frac{1}{2} \Theta_1 c_{\mathrm{T1}} k_{\mathrm{B1}}^2}{m_1' c_{\mathrm{B1}}} \left| t_{\mathrm{B1T1}} \right|^2 = \frac{\mu_2 \beta}{2 \chi^2} \left| t_{\mathrm{B1T1}} \right|^2 \tag{2-354}$$

$$\tau_{\mathrm{B1T2}} = \frac{\frac{1}{2} \Theta_2 c_{\mathrm{T2}} \left| \omega_{\mathrm{T2+}} \right|^2}{m_1' c_{\mathrm{B1}} \left| v_{\mathrm{B1+}} \right|^2} = \frac{\frac{1}{2} \Theta_2 c_{\mathrm{T2}} k_{\mathrm{B1}}^2}{m_1' c_{\mathrm{B1}}} \left| t_{\mathrm{B1T2}} \right|^2 = \frac{\mu_1}{2} \left| t_{\mathrm{B1T2}} \right|^2 \tag{2-355}$$

Example transmission coefficients are plotted in Figure 2.35 using the material properties and dimensions in Table 2.3.

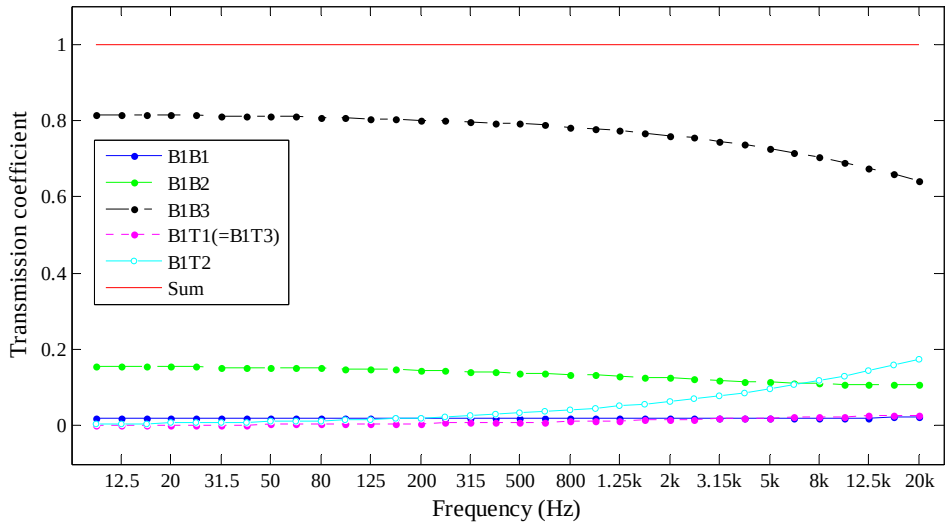

Figure 2.35 Transmission coefficients for T123-junction: BT model, incident bending wave (Type B) on beam 1.

2.6.2.2 Torsional wave excitation

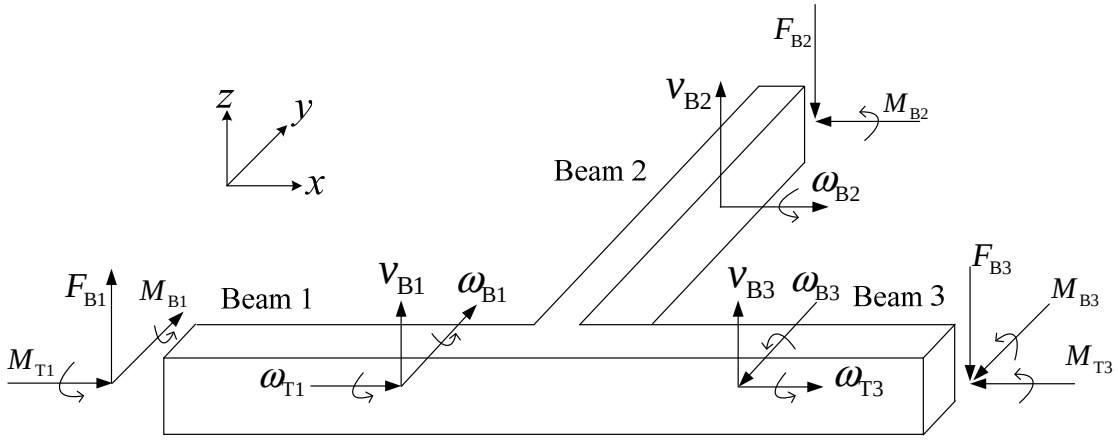

Figure 2.36 T123-junction: BT model, torsional wave excitation on beam 1.

Consider an incident torsional wave travelling in the positive *x*-direction towards the junction on beam 1 which generates bending waves (Type B) on beams 1, 2 and 3. Bending waves transmitted to beams 1 and 3 have the same magnitudes but travel in opposite directions. This causes balanced bending moments and zero rotation due to bending waves on beams 1 and 3 at the junction. This means that there is no torsional wave transmitted to beam 2. This incident wave is assumed to have unit amplitude; hence the wave fields can be described as follows:

$$\omega_{T1} = \left(e^{-ik_{T1}x} + r_{T1T1}e^{ik_{T1}x}\right)e^{i\omega t} \tag{2-356}$$

$$\omega_{T2} = 0 \tag{2-357}$$

$$\omega_{T3} = t_{T1T3}e^{-ik_{T1}x}e^{i\omega t} \tag{2-358}$$

$$v_{B1} = \frac{-i}{k_{B1}}\left(t_{T1B1}e^{ik_{B1}x} + t_{N1}e^{k_{B1}x}\right)e^{i\omega t} \tag{2-359}$$

$$v_{B2} = \frac{-i}{k_{B2}}\left(t_{T1B2}e^{-ik_{B2}y} + t_{N2}e^{-k_{B2}y}\right)e^{i\omega t} \tag{2-360}$$

$$v_{B3} = \frac{-i}{k_{B1}}\left(t_{T1B1}e^{-ik_{B1}x} + t_{N1}e^{-k_{B1}x}\right)e^{i\omega t} \tag{2-361}$$

Continuity of bending velocity and rotational velocity at the junction requires that

$$v_{B1} = v_{B2} \quad (\text{or} \quad v_{B3} = v_{B2}) \tag{2-362}$$

$$\frac{\partial v_{B1}}{\partial x} = \omega_{T2} = 0 \tag{2-363}$$

$$\frac{\partial v_{B2}}{\partial y} = \omega_{T1}, \quad \frac{\partial v_{B2}}{\partial y} = \omega_{T3} \tag{2-364}$$

This gives

$$\chi t_{T1B1} + \chi t_{N1} - t_{T1B2} - t_{N2} = 0 \tag{2-365}$$

$$it_{T1B1} + t_{N1} = 0 \tag{2-366}$$

$$-t_{T1B2} + it_{N2} - r_{T1T1} = 1 \tag{2-367}$$

$$-t_{T1B2} + it_{N2} - t_{T1T3} = 0 \tag{2-368}$$

Equilibrium of shear forces in the z-direction requires that

$$F_{B1} - F_{B2} - F_{B3} = 2F_{B1} - F_{B2} = 0 \tag{2-369}$$

According to (2-28), one can calculate that

$$\begin{aligned} F_{\mathrm{B1}} &= B_1 \int \frac{\partial^3 v_{\mathrm{B1}}}{\partial x^3} \mathrm{d}t = \frac{B_1}{i\omega} \frac{-i}{k_{\mathrm{B1}}} \left[\left(ik_{\mathrm{B1}} \right)^3 t_{\mathrm{T1B1}} + {k_{\mathrm{B1}}}^3 t_{\mathrm{N1}} \right] e^{i\omega t} \\ &= \frac{B_1 k_{\mathrm{B1}}^3}{k_{\mathrm{B1}} \omega} \left(i t_{\mathrm{T1B1}} - t_{\mathrm{N1}} \right) e^{i\omega t} \end{aligned} \tag{2-370}$$

$$\begin{aligned} F_{\mathrm{B2}} &= B_2 \int \frac{\partial^3 v_{\mathrm{B2}}}{\partial y^3} \mathrm{d}t = \frac{B_2}{i\omega} \frac{-i}{k_{\mathrm{B2}}} \left[\left(-ik_{\mathrm{B2}} \right)^3 t_{\mathrm{T1B2}} + \left(-k_{\mathrm{B2}} \right)^3 t_{\mathrm{N2}} \right] e^{i\omega t} \\ &= \frac{B_2 k_{\mathrm{B2}}^3}{k_{\mathrm{B2}} \omega} \left(-i t_{\mathrm{T1B2}} + t_{\mathrm{N2}} \right) e^{i\omega t} \end{aligned} \tag{2-371}$$

Then (2-369) is reduced to

$$2i\chi t_{\mathrm{T1B1}} - 2\chi t_{\mathrm{N1}} + i\beta t_{\mathrm{T1B2}} - \beta t_{\mathrm{N2}} = 0 \tag{2-372}$$

Bending moments in the *y*-direction are balanced by bending motion on beams 1 and 3. The equilibrium relationship for moments in the *x*-direction can be expressed as

$$M_{\mathrm{T1}} - M_{\mathrm{B2}} - M_{\mathrm{T3}} = 0 \tag{2-373}$$

Since the wave fields of ω_{T1}, ω_{T3} and v_{B2} are the same as that in section 2.6.1.2, the calculations of M_{T1}, M_{B2} and M_{T3} are also the same as shown in (2-318), (2-319) and (2-320). From (2-373) one can get

$$-t_{\mathrm{T1B2}} + t_{\mathrm{N2}} + \mu_2 r_{\mathrm{T1T1}} + \mu_2 t_{\mathrm{T1T3}} = \mu_2 \tag{2-374}$$

Combining the six boundary condition equations gives the matrix equation as

$$\begin{bmatrix} \chi & \chi & -1 & -1 & 0 & 0 \\ i & 1 & 0 & 0 & 0 & 0 \\ 0 & 0 & -1 & i & -1 & 0 \\ 0 & 0 & -1 & i & 0 & -1 \\ 2i\chi & -2\chi & i\beta & -\beta & 0 & 0 \\ 0 & 0 & -1 & 1 & \mu_2 & \mu_2 \end{bmatrix} \begin{bmatrix} t_{\mathrm{T1B1}} \\ t_{\mathrm{N1}} \\ t_{\mathrm{T1B2}} \\ t_{\mathrm{N2}} \\ r_{\mathrm{T1T1}} \\ t_{\mathrm{T1T3}} \end{bmatrix} = \begin{bmatrix} 0 \\ 0 \\ 1 \\ 0 \\ 0 \\ \mu_2 \end{bmatrix} \tag{2-375}$$

Transmission coefficients for torsional wave excitation on the T123-junction are calculated using

$$\tau_{\mathrm{T1T1}} = \frac{\frac{1}{2}\Theta_1 c_{\mathrm{T1}} \left|\omega_{\mathrm{T1-}}\right|^2}{\frac{1}{2}\Theta_1 c_{\mathrm{T1}} \left|\omega_{\mathrm{T1+}}\right|^2} = \left|r_{\mathrm{T1T1}}\right|^2 \tag{2-376}$$

$$\tau_{\mathrm{T1T2}} = 0 \tag{2-377}$$

$$\tau_{\mathrm{T1T3}} = \frac{\frac{1}{2}\Theta_1 c_{\mathrm{T1}} \left|\omega_{\mathrm{T3+}}\right|^2}{\frac{1}{2}\Theta_1 c_{\mathrm{T1}} \left|\omega_{\mathrm{T1+}}\right|^2} = \left|t_{\mathrm{T1T3}}\right|^2 \tag{2-378}$$

$$\tau_{\mathrm{T1B1}} = \tau_{\mathrm{T1B3}} = \frac{m_1' c_{\mathrm{B1}} \left|v_{\mathrm{B1+}}\right|^2}{\frac{1}{2}\Theta_1 c_{\mathrm{T1}} \left|\omega_{\mathrm{T1+}}\right|^2} = \frac{\frac{m_1' c_{\mathrm{B1}}}{k_{\mathrm{B1}}^2}}{\frac{1}{2}\Theta_1 c_{\mathrm{T1}}} \left|t_{\mathrm{T1B1}}\right|^2 = \frac{2\chi^2}{\mu_2 \beta} \left|t_{\mathrm{T1B1}}\right|^2 \tag{2-379}$$

$$\tau_{\mathrm{T1B2}} = \frac{m_2' c_{\mathrm{B2}} \left|v_{\mathrm{B2+}}\right|^2}{\frac{1}{2}\Theta_1 c_{\mathrm{T1}} \left|\omega_{\mathrm{T1+}}\right|^2} = \frac{\frac{m_2' c_{\mathrm{B2}}}{k_{\mathrm{B2}}^2}}{\frac{1}{2}\Theta_1 c_{\mathrm{T1}}} \left|t_{\mathrm{T1B2}}\right|^2 = \frac{2}{\mu_2} \left|t_{\mathrm{T1B2}}\right|^2 \tag{2-380}$$

Example transmission coefficients are plotted in Figure 2.37 using the material properties and dimensions in Table 2.3.

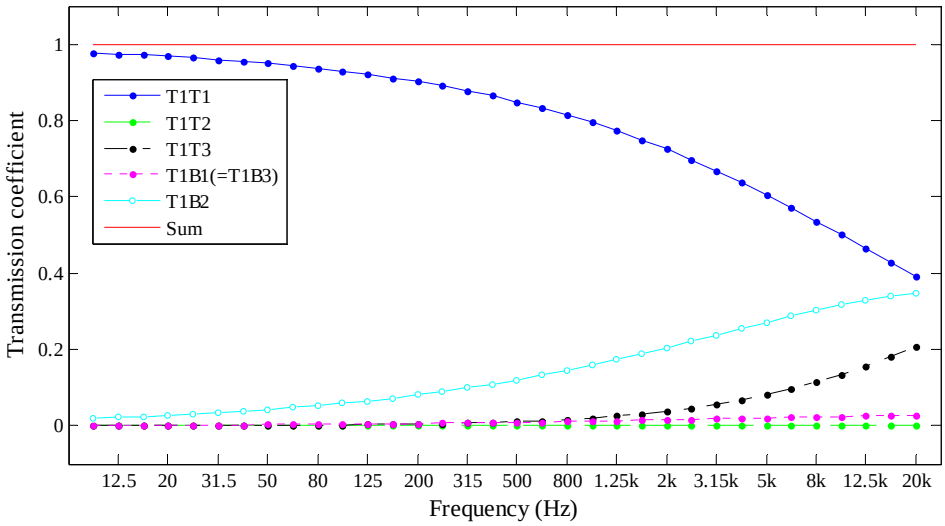

Figure 2.37 Transmission coefficients for T123-junction: BT model, incident torsional wave on beam 1.

2.6.3 T124-junction

2.6.3.1 Bending wave excitation

Figure 2.38 shows the T124-junction under consideration for which the coordinates of the junction line are (x,y)=(0,0). It is assumed that the material properties and the cross-sectional dimensions are identical for beams 2 and 4.

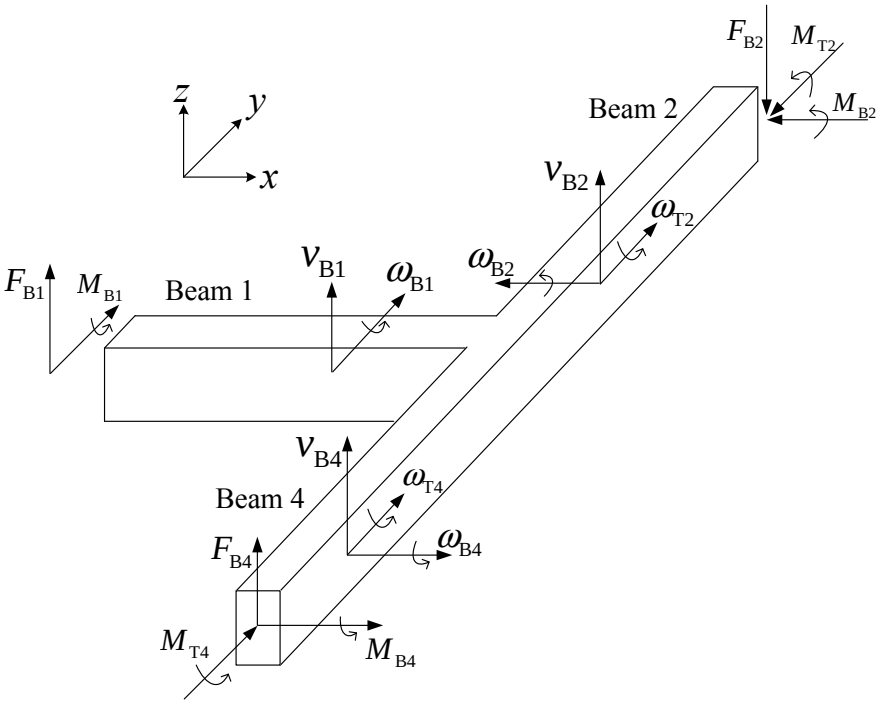

Figure 2.38 T124-junction: BT model, Type B bending wave excitation on beam 1.

Consider an incident bending wave (Type B) travelling in the positive *x*-direction towards the junction on beam 1. The transmitted bending waves (Type B) on beams 2 and 4 have opposite moments at the junction in the *x*-direction; hence there is no torsional wave motion on beam 1. The incident wave is assumed to have unit amplitude; hence the wave fields can be described as follows

$$v_{B1} = \left(e^{-ik_{B1}x} + r_{B1B1}e^{ik_{B1}x} + r_{N1}e^{k_{B1}x}\right)e^{i\omega t} \tag{2-381}$$

$$v_{B2} = \left(t_{B1B2}e^{-ik_{B2}y} + t_{N2}e^{-k_{B2}y}\right)e^{i\omega t} \tag{2-382}$$

$$v_{B4} = \left(t_{B1B2}e^{ik_{B2}y} + t_{N2}e^{k_{B2}y}\right)e^{i\omega t} \tag{2-383}$$

$$\omega_{T1} = 0 \tag{2-384}$$

$$\omega_{T2} = \omega_0 t_{B1T2}e^{-ik_{T2}y}e^{i\omega t} = -ik_{B1}t_{B1T2}e^{-ik_{T2}y}e^{i\omega t} \tag{2-385}$$

$$\omega_{T4} = \omega_0 t_{B1T2}e^{ik_{T2}y}e^{i\omega t} = -ik_{B1}t_{B1T2}e^{ik_{T2}y}e^{i\omega t} \tag{2-386}$$

At the junction continuity of bending velocity in the *z*-direction and rotational velocity in the *y*-direction requires that

$$v_{\mathrm{B1}} = v_{\mathrm{B2}} \tag{2-387}$$

$$\frac{\partial v_{\mathrm{B1}}}{\partial x} = \omega_{\mathrm{T2}} \tag{2-388}$$

Rotational velocity in the *x*-direction is zero,

$$\frac{\partial v_{\mathrm{B2}}}{\partial y} = 0 = \omega_{\mathrm{T1}} \tag{2-389}$$

Shear force and moment equilibrium requires that

$$F_{\mathrm{B1}} = 2F_{\mathrm{B2}} \tag{2-390}$$

$$M_{\mathrm{B1}} = 2M_{\mathrm{T2}} \tag{2-391}$$

The calculations of these forces and moments are exactly the same as in (2-293) and (2-298). The above five boundary condition equations define the matrix equation as

$$\begin{bmatrix} -1 & -1 & 1 & 1 & 0 \\ i & 1 & 0 & 0 & i \\ 0 & 0 & i & 1 & 0 \\ -1 & 1 & 0 & 0 & 2\mu_1 \\ i & -1 & 2i\beta & -2\beta & 0 \end{bmatrix} \begin{bmatrix} r_{\mathrm{B1B1}} \\ r_{\mathrm{N1}} \\ t_{\mathrm{B1B2}} \\ t_{\mathrm{N2}} \\ t_{\mathrm{B1T2}} \end{bmatrix} = \begin{bmatrix} 1 \\ i \\ 0 \\ 1 \\ i \end{bmatrix} \tag{2-392}$$

Solution of (2-392) allows the reflection and transmission coefficients to be calculated using

$$\tau_{\mathrm{B1B1}} = \frac{m_1' c_{\mathrm{B1}} \left| v_{\mathrm{B1-}} \right|^2}{m_1' c_{\mathrm{B1}} \left| v_{\mathrm{B1+}} \right|^2} = \left| r_{\mathrm{B1B1}} \right|^2 \tag{2-393}$$

$$\tau_{\mathrm{B1B2}} = \tau_{\mathrm{B1B4}} = \frac{m_2' c_{\mathrm{B2}} \left| v_{\mathrm{B2+}} \right|^2}{m_1' c_{\mathrm{B1}} \left| v_{\mathrm{B1+}} \right|^2} = \beta \left| t_{\mathrm{B1B2}} \right|^2 \tag{2-394}$$

$$\tau_{\mathrm{B1T1}} = 0 \tag{2-395}$$

$$\tau_{\mathrm{B1T2}} = \tau_{\mathrm{B1T4}} = \frac{\frac{1}{2}\Theta_2 c_{\mathrm{T2}} \left|\omega_{\mathrm{T2+}}\right|^2}{m_1' c_{\mathrm{B1}} \left|v_{\mathrm{B1+}}\right|^2} = \frac{\frac{1}{2}\Theta_2 c_{\mathrm{T2}} k_{\mathrm{B1}}^2}{m_1' c_{\mathrm{B1}}} \left|t_{\mathrm{B1T2}}\right|^2 = \frac{\mu_1}{2} \left|t_{\mathrm{B1T2}}\right|^2 \qquad (2\text{-}396)$$

Example transmission coefficients are plotted in Figure 2.39 using the material properties and dimensions in Table 2.3.

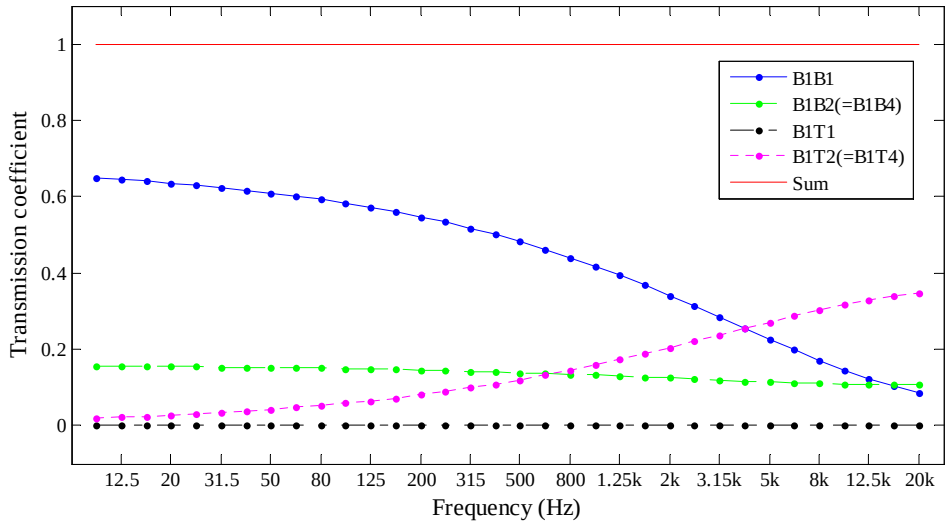

Figure 2.39 Transmission coefficients for T124-junction: BT model, incident bending wave (Type B) on beam 1.

2.6.3.2 Torsional wave excitation

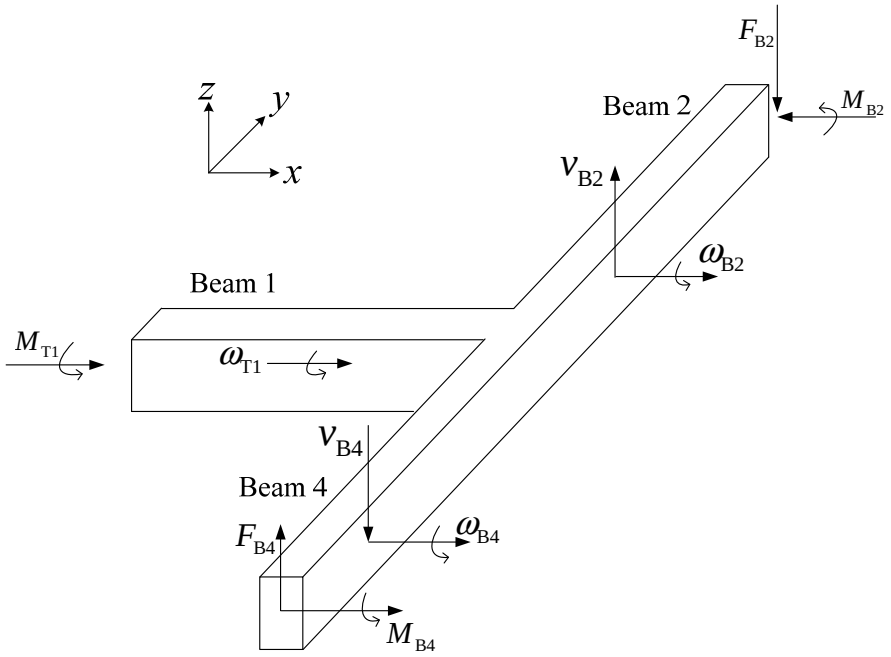

Figure 2.40 T124-junction: BT model, torsional wave excitation on beam 1.

Now consider an incident torsional wave travelling in the positive *x*-direction towards the junction on beam 1. Bending waves (Type B) are transmitted to beams 2 and 4. Due to structural symmetry, the shear forces from bending motion on beams 2 and 4 are balanced and bending displacement is zero in the *z*-direction at the junction. The incident wave is assumed to have unit amplitude; hence the wave fields can be described as follows:

$$\omega_{T1} = \left(e^{-ik_{T1}x} + r_{T1T1}e^{ik_{T1}x}\right)e^{i\omega t} \tag{2-397}$$

$$\omega_{T2} = \omega_{T4} = 0 \tag{2-398}$$

$$v_{B1} = 0 \tag{2-399}$$

$$v_{B2} = \frac{-i}{k_{B2}}\left(t_{T1B2}e^{-ik_{B2}y} + t_{N2}e^{-k_{B2}y}\right)e^{i\omega t} \tag{2-400}$$

$$v_{B4} = \frac{i}{k_{B2}}\left(t_{T1B2}e^{ik_{B2}y} + t_{N2}e^{k_{B2}y}\right)e^{i\omega t} \tag{2-401}$$

At the junction, continuity of angular velocity in the *x*-direction and bending velocity in *z* direction requires that

$$\omega_{\mathrm{T1}} = \frac{\partial v_{\mathrm{B2}}}{\partial y} \tag{2-402}$$

$$v_{\mathrm{B2}} = 0 = v_{\mathrm{B1}} \tag{2-403}$$

At the junction, M_{B2}=M_{B4}, and the moment equilibrium relationship in the *x*-direction gives

$$M_{\mathrm{T1}} - M_{\mathrm{B2}} + M_{\mathrm{B4}} = M_{\mathrm{T1}} - 2M_{\mathrm{B2}} = 0 \tag{2-404}$$

The calculations of the moments due to torsional motion and bending motion are the same as equations (2-318) and(2-320). The three boundary conditions give the following matrix equation

$$\begin{bmatrix} -1 & i & -1 \\ 1 & 1 & 0 \\ -2 & 2 & \mu_2 \end{bmatrix} \begin{bmatrix} t_{\mathrm{T1B2}} \\ t_{\mathrm{N2}} \\ r_{\mathrm{T1T1}} \end{bmatrix} = \begin{bmatrix} 1 \\ 0 \\ \mu_2 \end{bmatrix} \tag{2-405}$$

Solving (2-405) allows the following reflection and transmission coefficients to be calculated:

$$\tau_{\mathrm{T1T1}} = \frac{\frac{1}{2}\Theta_1 c_{\mathrm{T1}} \left|\omega_{\mathrm{T1-}}\right|^2}{\frac{1}{2}\Theta_1 c_{\mathrm{T1}} \left|\omega_{\mathrm{T1+}}\right|^2} = \left|r_{\mathrm{T1T1}}\right|^2 \tag{2-406}$$

$$\tau_{\mathrm{T1T2}} = \tau_{\mathrm{T1T4}} = 0 \tag{2-407}$$

$$\tau_{\mathrm{T1B1}} = 0 \tag{2-408}$$

$$\tau_{\mathrm{T1B2}} = \tau_{\mathrm{T1B4}} = \frac{m_2' c_{\mathrm{B2}} \left|v_{\mathrm{B2+}}\right|^2}{\frac{1}{2}\Theta_1 c_{\mathrm{T1}} \left|\omega_{\mathrm{T1+}}\right|^2} = \frac{\frac{m_2' c_{\mathrm{B2}}}{k_{\mathrm{B2}}^2}}{\frac{1}{2}\Theta_1 c_{\mathrm{T1}}} \left|t_{\mathrm{T1B2}}\right|^2 = \frac{2}{\mu_2} \left|t_{\mathrm{T1B2}}\right|^2 \tag{2-409}$$

The numerical calculation with the perspex T124-junction demonstrates that

$$\tau_{T1T1} + \tau_{T1B2} + \tau_{T1B4} = 1 \tag{2-410}$$

Example transmission coefficients are plotted in Figure 2.41 using the material properties and dimensions in Table 2.3.

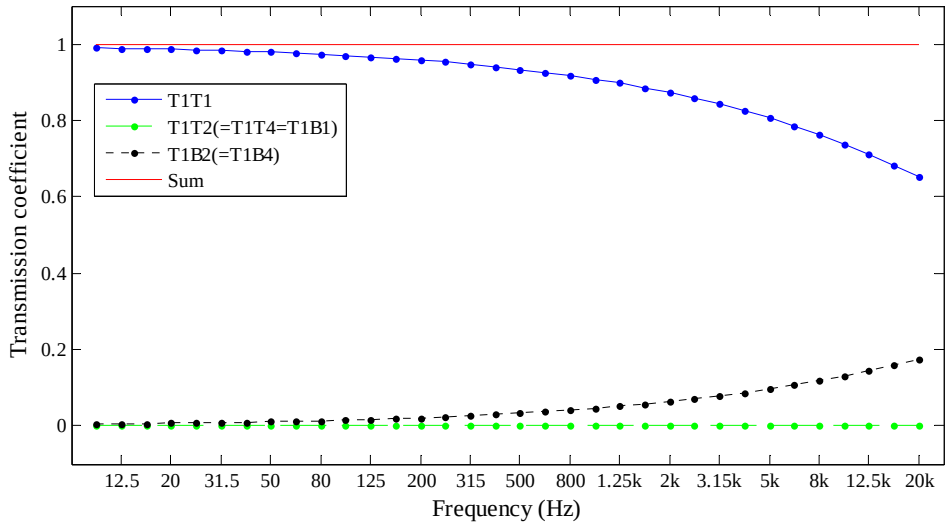

Figure 2.41 Transmission coefficients for T124-junction: BT model, incident torsional wave on beam 1.

2.6.4 L-junction

2.6.4.1 Bending wave excitation

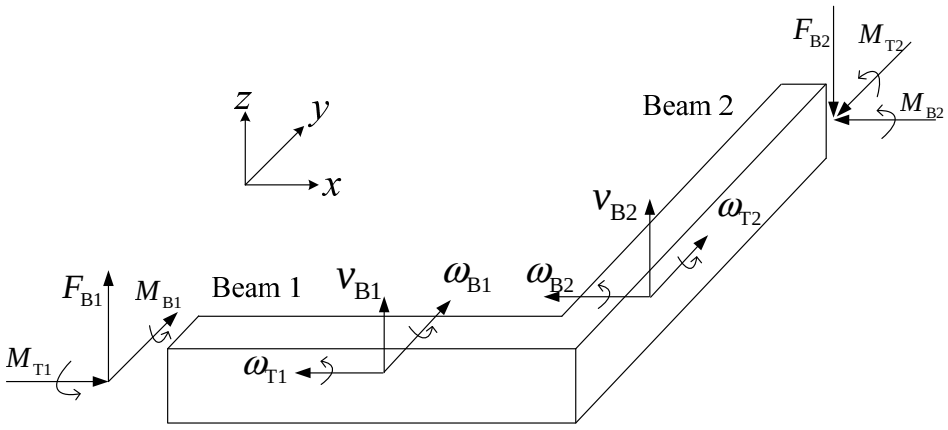

Figure 2.42 L-junction: BT model, Type B bending wave excitation on beam 1.

For the L-junction, both wave types exist under bending or torsional vibration load. In the first case, we assume a bending wave on beam 1. The directions of velocity are shown in Figure 2.42.

The wave fields for each beam are described as

$$v_{B1} = (e^{-ik_{B1}x} + r_{B1B1}e^{ik_{B1}x} + r_{N1}e^{k_{B1}x})e^{i\omega t} \tag{2-411}$$

$$v_{B2} = (t_{B1B2}e^{-ik_{B2}y} + t_{N2}e^{-k_{B2}y})e^{i\omega t} \tag{2-412}$$

$$\omega_{T1} = \omega_0 t_{B1T1}e^{ik_{T1}x}e^{i\omega t} = -ik_{B1}t_{B1T1}e^{ik_{T1}x}e^{i\omega t} \tag{2-413}$$

$$\omega_{T2} = \omega_0 t_{B1T2}e^{-ik_{T2}y}e^{i\omega t} = -ik_{B1}t_{B1T2}e^{-ik_{T2}y}e^{i\omega t} \tag{2-414}$$

As stated by Sablik [32], the parameter k_{B1} in equation (2-414) could also be replaced by k_{B2}. This would not affect the results because t_{B1T2} is always a frequency-dependant parameter. However, to continue using the calculations based on similar assumptions to previous parts, the parameter k_{B1} is used here.

The continuity of bending velocity and rotational velocity at the junction requires that

$$v_{B1} = v_{B2}, \quad \omega_{T1} = \frac{\partial v_{B2}}{\partial y}, \quad \omega_{T2} = \frac{\partial v_{B1}}{\partial x} \tag{2-415}$$

In the z-direction, the shear forces due to bending motions in beam 1 and 2 are balanced to each other.

$$F_{B1} = F_{B2} \tag{2-416}$$

At the joint, the bending moment in one beam should equal the moment of torsional wave motion in another beam. This boundary condition can be described as

$$M_{B1} = M_{T2}, \quad M_{T1} = M_{B2} \tag{2-417}$$

As the assumed wave fields are the same, the shear forces in equation (2-416) are the same as that in equation (2-298), whilst the moments in equation (2-417) are exactly the same as that in equation (2-293) and (2-344).

Thus, the six boundary conditions form the following matrix equation

$$\begin{bmatrix} 1 & 1 & -1 & -1 & 0 & 0 \\ 1 & -i & 0 & 0 & 0 & 1 \\ 0 & 0 & \chi & -i\chi & -1 & 0 \\ 1 & i & \beta & i\beta & 0 & 0 \\ -1 & 1 & 0 & 0 & 0 & \mu_1 \\ 0 & 0 & -\chi & \chi & -\mu_2 & 0 \end{bmatrix} \begin{bmatrix} r_{\mathrm{B1B1}} \\ r_{\mathrm{N1}} \\ t_{\mathrm{B1B2}} \\ t_{\mathrm{N2}} \\ t_{\mathrm{B1T1}} \\ t_{\mathrm{B1T2}} \end{bmatrix} = \begin{bmatrix} -1 \\ 1 \\ 0 \\ 1 \\ 1 \\ 0 \end{bmatrix} \tag{2-418}$$

By solving the matrix equation, one can calculate the transmission coefficients for bending wave excitation on L-junction using the following expressions

$$\tau_{\mathrm{B1B1}} = \frac{m_1' c_{\mathrm{B1}} \left| v_{\mathrm{B1-}} \right|^2}{m_1' c_{\mathrm{B1}} \left| v_{\mathrm{B1+}} \right|^2} = \left| r_{\mathrm{B1B1}} \right|^2 \tag{2-419}$$

$$\tau_{\mathrm{B1B2}} = \frac{m_2' c_{\mathrm{B2}} \left| v_{\mathrm{B2+}} \right|^2}{m_1' c_{\mathrm{B1}} \left| v_{\mathrm{B1+}} \right|^2} = \beta \left| t_{\mathrm{B1B2}} \right|^2 \tag{2-420}$$

$$\tau_{\mathrm{B1T1}} = \frac{\frac{1}{2}\Theta_1 c_{\mathrm{T1}} \left| \omega_{\mathrm{T1-}} \right|^2}{m_1' c_{\mathrm{B1}} \left| v_{\mathrm{B1+}} \right|^2} = \frac{\frac{1}{2}\Theta_1 c_{\mathrm{T1}} {k_{\mathrm{B1}}}^2}{m_1' c_{\mathrm{B1}}} \left| t_{\mathrm{B1T1}} \right|^2 = \frac{\mu_2 \beta}{2\chi^2} \left| t_{\mathrm{B1T1}} \right|^2 \tag{2-421}$$

$$\tau_{\mathrm{B1T2}} = \frac{\frac{1}{2}\Theta_2 c_{\mathrm{T2}} \left| \omega_{\mathrm{T2+}} \right|^2}{m_1' c_{\mathrm{B1}} \left| v_{\mathrm{B1+}} \right|^2} = \frac{\frac{1}{2}\Theta_2 c_{\mathrm{T2}} {k_{\mathrm{B1}}}^2}{m_1' c_{\mathrm{B1}}} \left| t_{\mathrm{B1T2}} \right|^2 = \frac{\mu_1}{2} \left| t_{\mathrm{B1T2}} \right|^2 \tag{2-422}$$

Example transmission coefficients are plotted in Figure 2.43 using the material properties and dimensions in Table 2.3.

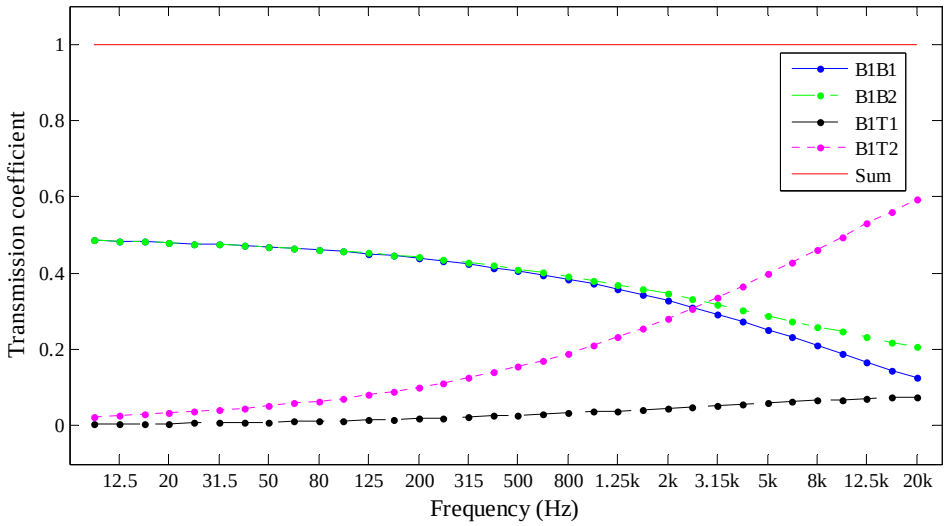

Figure 2.43 Transmission coefficients for L-junction: BT model, incident bending wave (Type B) on beam 1.

2.6.4.2 Torsional wave excitation

In this case, a torsional wave is excited on beam 2 whereas in the X- and T- junctions no torsional waves were generated under bending wave excitation. This incident wave is assumed to have unit amplitude; hence the wave fields can be described as follows:

$$\omega_{\mathrm{T1}} = \left(e^{-ik_{\mathrm{T1}}x} + r_{\mathrm{T1T1}}e^{ik_{\mathrm{T1}}x}\right)e^{i\omega t} \tag{2-423}$$

$$\omega_{\mathrm{T2}} = t_{\mathrm{T1T2}}e^{-ik_{\mathrm{T2}}y}e^{i\omega t} \tag{2-424}$$

$$v_{\mathrm{B1}} = \frac{i}{k_{\mathrm{B1}}}\left(t_{\mathrm{T1B1}}e^{ik_{\mathrm{B1}}x} + t_{\mathrm{N1}}e^{k_{\mathrm{B1}}x}\right)e^{i\omega t} \tag{2-425}$$

$$v_{B2} = \frac{i}{k_{\mathrm{B1}}}\left(t_{\mathrm{T1B2}}e^{-ik_{\mathrm{B2}}y} + t_{\mathrm{N2}}e^{-k_{\mathrm{B2}}y}\right)e^{i\omega t} \tag{2-426}$$

The boundary conditions are the same as that of bending wave excitation on L-junction in section 2.6.4.1. The only difference is due to the different inertial conditions. The shear forces from two bending motions are calculated as

$$F_{B1} = B_1 \int \frac{\partial^3 v_{B1}}{\partial x^3} \mathrm{d}t = \frac{B_1}{i\omega} \frac{i}{k_{B1}} \left[\left(ik_{B1} \right)^3 t_{T1B1} + \left(k_{B1} \right)^3 t_{N1} \right] e^{i\omega t}$$
$$= \frac{B_1 k_{B1}^3}{\omega k_{B1}} \left(-it_{T1B1} + t_{N1} \right) e^{i\omega t} \tag{2-427}$$

$$F_{B2} = B_2 \int \frac{\partial^3 v_{B2}}{\partial y^3} \mathrm{d}t = \frac{B_2}{i\omega} \frac{i}{k_{B1}} \left[\left(-ik_{B2} \right)^3 t_{T1B2} + \left(-k_{B2} \right)^3 t_{N2} \right] e^{i\omega t}$$
$$= \frac{B_2 k_{B2}^{\ 3}}{\omega k_{B1}} \left(it_{T1B2} - t_{N2} \right) e^{i\omega t} \tag{2-428}$$

The moments of bending motions and torsional motions in each beam are calculated as

$$M_{T1} = -\Theta_1 \int \frac{\partial \omega_{T1}}{\partial t} \mathrm{d}x = -i\omega\Theta_1 \left(\frac{1}{-ik_{T1}} + \frac{r_{T1T1}}{ik_{T1}} \right) e^{i\omega t} = Z_{T1} \left(1 - r_{T1T1} \right) e^{i\omega t} \tag{2-429}$$

$$M_{T2} = -\Theta_2 \int \frac{\partial \omega_{T2}}{\partial t} \mathrm{d}y = -i\omega\Theta_2 \frac{t_{T1T2}}{-ik_{T2}} e^{i\omega t} = Z_{T2} t_{T1T2} e^{i\omega t} \tag{2-430}$$

$$M_{B1} = -B_1 \int \frac{\partial^2 v_{B1}}{\partial x^2} \mathrm{d}t = \frac{-B_1}{i\omega} \frac{i}{k_{B1}} \left[\left(ik_{B1} \right)^2 t_{T1B1} + \left(k_{B1} \right)^2 t_{N1} \right] e^{i\omega t}$$
$$= \frac{-B_1 k_{B1}^2}{\omega k_{B1}} \left(-t_{T1B1} + t_{N1} \right) e^{i\omega t} \tag{2-431}$$

$$M_{B2} = -B_2 \int \frac{\partial^2 v_{B2}}{\partial y^2} \mathrm{d}t = \frac{-B_2}{i\omega} \frac{i}{k_{B1}} \left[\left(-ik_{B2} \right)^2 t_{T1B2} + \left(-k_{B2} \right)^2 t_{N2} \right] e^{i\omega t}$$
$$= \frac{-B_2 k_{B2}^2}{\omega k_{B1}} \left(-t_{T1B2} + t_{N2} \right) e^{i\omega t} \tag{2-432}$$

Applying these calculations in (2-416) and (2-417), and combining the boundary condition (2-415) one can obtain the matrix equation

$$\begin{bmatrix} 0 & 0 & 1 & 1 & -1 & -1 \\ 1 & 0 & 0 & 0 & -\chi & i\chi \\ 0 & 1 & 1 & -i & 0 & 0 \\ 0 & \mu_1 & -1 & 1 & 0 & 0 \\ \mu_2 & 0 & 0 & 0 & \chi & -\chi \\ 0 & 0 & i & -1 & i\beta & -\beta \end{bmatrix} \begin{bmatrix} r_{T1T1} \\ t_{T1T2} \\ t_{T1B1} \\ t_{N1} \\ t_{T1B2} \\ t_{N2} \end{bmatrix} = \begin{bmatrix} 0 \\ -1 \\ 0 \\ 0 \\ \mu_2 \\ 0 \end{bmatrix} \tag{2-433}$$

By solving the parameters r_{T1T1}, t_{T1T2}, t_{T1B1} and t_{T1B2}, one can calculate the power transmission for an incident torsional wave

$$\tau_{\mathrm{T1T1}} = \frac{\frac{1}{2}\Theta_1 c_{\mathrm{T1}} \left|\omega_{\mathrm{T1-}}\right|^2}{\frac{1}{2}\Theta_1 c_{\mathrm{T1}} \left|\omega_{\mathrm{T1+}}\right|^2} = \left|r_{\mathrm{T1T1}}\right|^2 \tag{2-434}$$

$$\tau_{\mathrm{T1T2}} = \frac{\frac{1}{2}\Theta_2 c_{\mathrm{T2}} \left|\omega_{\mathrm{T2+}}\right|^2}{\frac{1}{2}\Theta_1 c_{\mathrm{T1}} \left|\omega_{\mathrm{T1+}}\right|^2} = \frac{\mu_1 \chi^2}{\mu_2 \beta} \left|r_{\mathrm{T1T1}}\right|^2 \tag{2-435}$$

$$\tau_{\mathrm{T1B1}} = \frac{m_1' c_{\mathrm{B1}} \left|v_{\mathrm{B1+}}\right|^2}{\frac{1}{2}\Theta_1 c_{\mathrm{T1}} \left|\omega_{\mathrm{T1+}}\right|^2} = \frac{\frac{m_1' c_{\mathrm{B1}}}{k_{\mathrm{B1}}^2}}{\frac{1}{2}\Theta_1 c_{\mathrm{T1}}} \left|t_{\mathrm{T1B1}}\right|^2 = \frac{2\chi^2}{\mu_2 \beta} \left|t_{\mathrm{T1B1}}\right|^2 \tag{2-436}$$

$$\tau_{\mathrm{T1B2}} = \frac{m_2' c_{\mathrm{B2}} \left|v_{\mathrm{B2+}}\right|^2}{\frac{1}{2}\Theta_1 c_{\mathrm{T1}} \left|\omega_{\mathrm{T1+}}\right|^2} = \frac{\frac{m_2' c_{\mathrm{B2}}}{k_{\mathrm{B1}}^2}}{\frac{1}{2}\Theta_1 c_{\mathrm{T1}}} \left|t_{\mathrm{T1B2}}\right|^2 = \frac{2\chi^2}{\mu_2} \left|t_{\mathrm{T1B2}}\right|^2 \tag{2-437}$$

Example transmission coefficients are plotted in Figure 2.44 using the material properties and dimensions in Table 2.3.

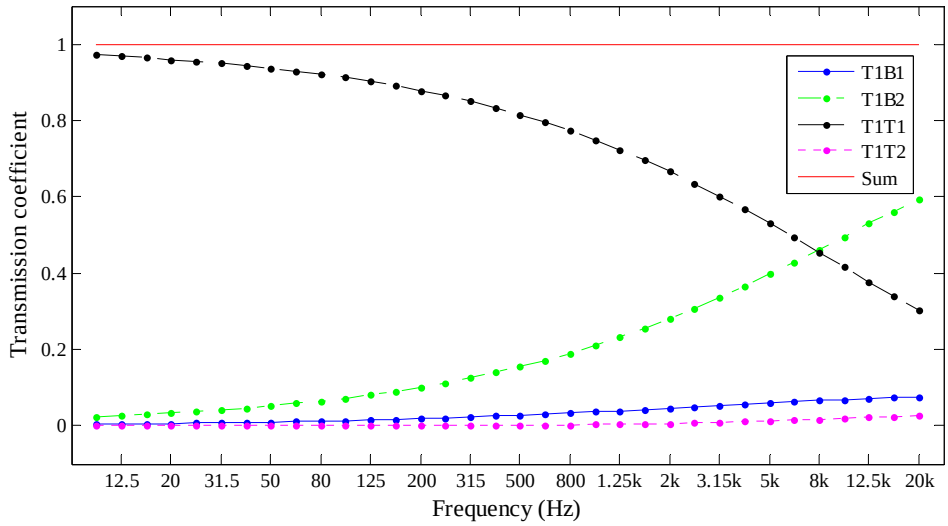

Figure 2.44 Transmission coefficients for L-junction: BT model, incident torsional wave on beam 1.

2.7 Comparison of transmission loss for bending waves on isolated beam junctions for the B and BL models

In this section, the transmission loss from an incident Type A bending wave to a transmitted Type A bending wave is compared for the B and BL models. This gives insight into the effect of longitudinal wave generation on bending wave transmission. Note that comparison with the BT model is not possible because this only considers Type B bending waves.

The transmission loss R on the isolated beam junctions is calculated using [5]

$$R = 10\log\left(\frac{1}{\tau}\right) \tag{2-438}$$

Figure 2.45 (a), Figure 2.45 (b), Figure 2.46 and Figure 2.47 allow comparison of transmission losses from the B and BL models for the L-junction, T124-junction, T123-junction and X-junction, respectively. The material properties and dimensions are given in Table 2.3.

For the B model the transmission loss is independent of frequency, whereas the transmission loss for the BL and BT models are frequency-dependent except with B1B2 for the BL model.

For the L-junction (Figure 2.45 (a)) the difference between B and BL models is less than 2 dB below 5 kHz, but this increases to 3.6 dB at 20 kHz.

For T123- and T124-junctions, transmission around the corner (B1B2) is exactly the same in the BL and BT models and the largest difference between B and BL (or B and BT) models is only 1.2 dB at 20 kHz.

For the X-junction, the frequency-independent transmission loss around the corner (B1B2) in B model is the same as that in BL model.

Figure 2.46 (b) and Figure 2.47 (b) show that transmission across the straight section (B1B3) in BL model initially increases with frequency but decreases in the high frequency range. However the largest difference between B and BL model for two cases is less than 2 dB.

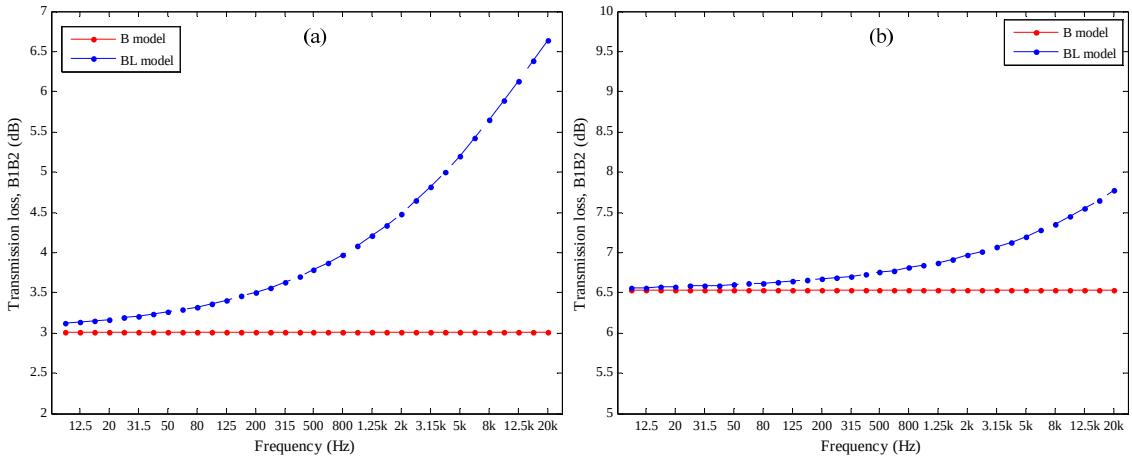

Figure 2.45 Comparison of transmission losses between B and BL model: (a) L-junction: (b) T124-junction.

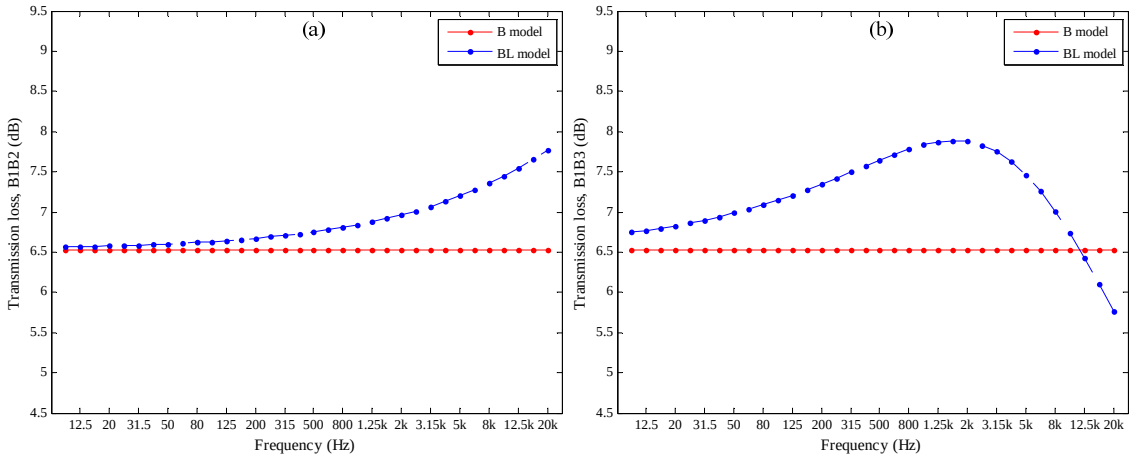

Figure 2.46 Comparison of transmission losses between B and BL model for the T123-junction.

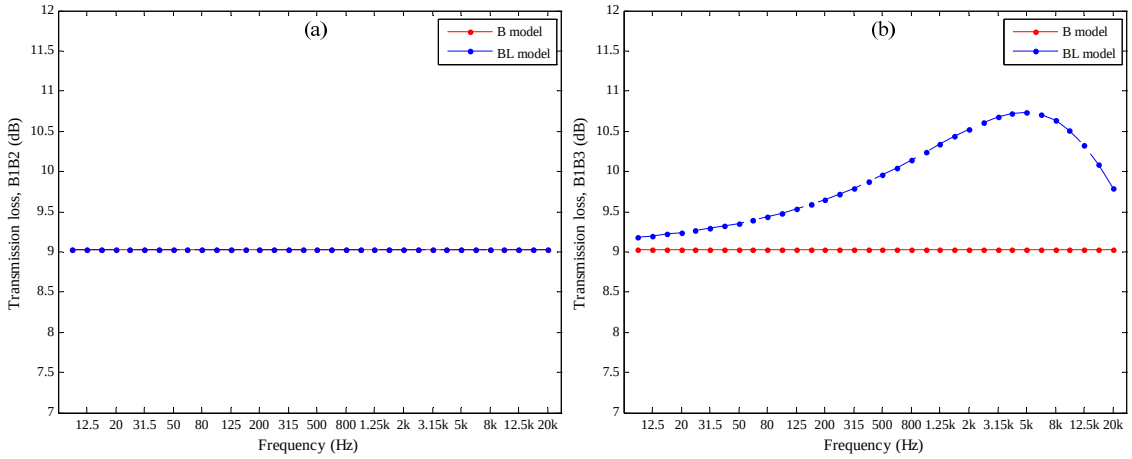

Figure 2.47 Comparison of transmission losses between B and BL model for the X-junction.

2.8 Summary

In this chapter, the theory describing bending, longitudinal and torsional waves on beams was introduced. For bending waves, the group velocity has been derived for Timoshenko theory considering both rotatory inertia and shear deformation. This makes it possible to introduce a new proposal in this thesis to incorporate Timoshenko theory in SEA and ASEA by changing over from Euler-Bernoulli to Timoshenko group velocity when calculating the coupling loss factors.

Full wave theory derivations are given for B, BL and BT models for L-, T- and X-junctions of semi-infinite beams assuming a rigid, massless junction and where only the co-linear beams on T- and X-junctions have identical material properties and cross-sectional dimensions.

Under this assumption, this work has originally derived these models which include:

(1) the bending only models on all beam junctions;
(2) the BL model of L-junction with longitudinal wave excitation;
(3) the BL model of T123- and T124- junctions;
(4) the updated BL model of X-junction;
(5) the BT model of T124-junction.

This provides a consistent set of derivations that are not available in the literatures.

3. Statistical energy analysis and advanced statistical energy analysis

3.1 Introduction

This section describes Statistical Energy Analysis (SEA) and Advanced Statistical Energy Analysis (ASEA) that are used to predict vibration transmission on coupled frameworks of beams.

3.2 Statistical energy analysis

3.2.1 Introduction

This section describes the framework of analysis, Statistical Energy Analysis (SEA) [1]. Application of this method requires prediction of the loss factors and then, from the power balance equations, prediction of the acoustic performance of the system to determine the energy in each subsystem.

3.2.2 Loss factors

In SEA, three loss factors are defined: internal loss factor (η_{ii}), coupling loss factor (η_{ij}) and total loss factor (η_i).

The internal loss factor (ILF) describes the inherent material damping. When the beam deforms while undergoing wave motion, the internal losses convert vibrational energy into heat. Compared with other parameters which describe material properties, such as density or Young's modulus, ILFs are not easy to predict. It depends on the type of wave motion, frequency, temperature, amplitude of vibration, and manufacturing process. However, uncertainty in the internal loss factor can often be tolerated when the sum of coupling loss factors is much greater than the internal loss factor.

The coupling loss factor (CLF) describes the energy losses from one subsystem (e.g. beam) via connections (e.g. mechanical connections, radiation coupling) to other subsystems. The power flow, W_{ij} from subsystem *i* to *j* is given by

$$W_{ij} = E_i \omega \eta_{ij} \tag{3-1}$$

In any system there will be power flow in both directions giving the net power flow, $\overline{W_{ij}}$ as

$$\overline{W_{ij}} = E_i \omega \eta_{ij} - E_j \omega \eta_{ji} \tag{3-2}$$

In general, the coupling from subsystem *i* to *j* will not be the same as coupling from *j* to *i* though they are related. The consistency relationship for subsystems *i* and *j* is

$$n_i \eta_{ij} = n_j \eta_{ji} \tag{3-3}$$

This equation relates the modal density, *n*, with the CLF in each direction. It is valid for coupling between all types of subsystem and can be used to calculate any CLF. For any type of wave on a subsystem, *i*, that is incident upon the junction connecting subsystems *i* and *j*, the transmission coefficient is

$$\tau_{ij} = \frac{W_{ij}}{W_{in,i}} = \frac{\omega \eta_{ij} E_i}{W_{in,i}} \tag{3-4}$$

where the incident power is $W_{in,i}$, and transmitted power is W_{ij}. The coupling loss factor is therefore given by

$$\eta_{ij} = \frac{\tau_{ij} W_{in,i}}{\omega E_i} \tag{3-5}$$

where the transmission coefficients for beam junctions have been calculated in Chapter 2. The power that is incident upon a boundary is determined by the mean free path which quantifies the number of times that vibration energy is reflected from the boundaries of a beam every second. For a beam *i* that is connected at both ends to other beams or plates, the mean free path is simply the length of the beam, and half the power will be incident on each end giving the relationship between CLF and τ_{ij} as

$$\eta_{ij} = \frac{c_{g,i} \tau_{ij}}{4\pi f L_i} \tag{3-6}$$

Based on (3-6), in this thesis it is proposed to introduce both the Euler-Bernoulli and the Timoshenko theory into the SEA and ASEA formulation by using the appropriate group velocity as derived in section 2.2.3.

The total loss factor (TLF) for subsystem *i* is the sum of the internal loss factor for subsystem *i* plus all the coupling loss factors from subsystem *i* to other subsystems,

$$\eta_i = \eta_{ii} + \sum_{j=1}^{J} \eta_{ij} \quad (i \neq j) \tag{3-7}$$

From (3-7) we can calculate the total loss factor. If accurate prediction is not possible, another simple method is to measure the reverberation time which is related to TLF by [81]

$$\eta_i = \frac{6 \ln 10}{2\pi f T} \tag{3-8}$$

3.2.3 Matrix SEA

The power balance equations for each subsystem form a matrix solution for N subsystems [61]

$$\begin{bmatrix} \eta_1 & -\eta_{21} & -\eta_{31} & \cdots & -\eta_{N1} \\ -\eta_{12} & \eta_2 & -\eta_{32} & \cdots & -\eta_{N2} \\ -\eta_{13} & -\eta_{23} & \eta_3 & \cdots & -\eta_{N3} \\ \cdots & \cdots & \cdots & \cdots & \cdots \\ -\eta_{1N} & -\eta_{2N} & -\eta_{3N} & \cdots & \eta_N \end{bmatrix} \begin{bmatrix} E_1 \\ E_2 \\ E_3 \\ \cdots \\ E_N \end{bmatrix} = \begin{bmatrix} W_{in,1}/\omega \\ W_{in,2}/\omega \\ W_{in,2}/\omega \\ \cdots \\ W_{in,N}/\omega \end{bmatrix} \tag{3-9}$$

The matrix elements [*i, j*] where $i \neq j$ are the coupling loss factors, and the diagonal elements are the total loss factor. This equation can be simplified into the form

$$[\eta][E] = \left[\frac{W_{in}}{\omega}\right] \tag{3-10}$$

where $[\eta]$ the square matrix of loss factors is, $[E]$ is the column matrix for energy of subsystems, and $\left[\frac{W_{in}}{\omega}\right]$ is the column matrix for power inputs divided by angular

frequency. Since the loss factors can be calculated from transmission coefficient, and the input power can be predicted or measured, the subsystem energies are determined by

$$[E] = [\eta]^{-1} \left[\frac{W_{in}}{\omega} \right] \tag{3-11}$$

For homogeneous beams, the energy associated with each bending and longitudinal wave is given by the product of mass of the beam and spatial average mean-square velocity associated with that wave motion,

$$E = m \left\langle v^2 \right\rangle_{t,s} \tag{3-12}$$

And for torsional wave it is

$$E = M \left\langle \omega^2 \right\rangle_{t,s} \tag{3-13}$$

Typically, we are interested in the vibration level difference, D_{ij}, between source subsystem i and receiver subsystem j,

$$D_{ij} = 10 \lg(\frac{E_i}{E_j}) = 10 \lg(\frac{v_i^2}{v_j^2}) + 10 \lg(\frac{m_i}{m_j}) \tag{3-14}$$

3.3 Advanced statistical energy analysis

3.3.1 Introduction

This section describes Advanced Statistical Energy Analysis (ASEA) as introduced by Heron [2].

For coupled structural subsystems, the assumption in SEA is that there is no coupling between physically disconnected subsystems. However, in some situations there can be significant indirect coupling, i.e. tunnelling mechanisms [67,69]. To incorporate indirect coupling within a statistical framework of analysis, Heron [2] developed Advanced Statistical Energy Analysis (ASEA) which combines SEA and ray tracing (ignoring phase effects) to track the power transmitted between coupled subsystems. This approach was validated with excitation of longitudinal waves at one end of an in-line array of six rods. ASEA agreed well with the exact result which was in contrast to SEA

which overestimated the vibration response for subsystems that were physically disconnected from the source subsystem. However, this example primarily confirmed the ability of ASEA to account for propagation losses rather than indirect coupling between non-adjacent rods. Heron [2] considered the possibility that ASEA could be extended to multiple wave types, but no results were reported. This extension to multiple wave types is considered in this thesis along with ASEA's ability to account for indirect coupling (tunnelling) as well as propagation losses.

3.3.2 Derivation

Returning to the SEA matrix, the general SEA power balance matrix equation for N subsystems can be rewritten as

$$\omega\begin{bmatrix} n_1\eta_{11}+\sum_{k\neq 1}^{N} n_1\eta_{1k} & -n_2\eta_{21} & \cdots & -n_N\eta_{N1} \\ -n_1\eta_{12} & n_2\eta_{22}+\sum_{k\neq 2}^{N} n_2\eta_{2k} & \cdots & -n_N\eta_{N2} \\ \vdots & & \ddots & \vdots \\ -n_1\eta_{1N} & \cdots\cdots & & n_N\eta_{NN}+\sum_{k\neq N}^{N} n_N\eta_{Nk} \end{bmatrix}\begin{bmatrix} E_1/n_1 \\ E_2/n_2 \\ \vdots \\ \vdots \\ E_N/n_N \end{bmatrix}=\begin{bmatrix} P_1 \\ P_2 \\ \vdots \\ \vdots \\ P_N \end{bmatrix} \quad (3\text{-}15)$$

where n_i is the modal density for subsystem i, η_{ii} is the internal loss factor for subsystem i, and η_{ij} is the coupling loss factor from subsystem i to subsystem j ($i \neq j$). With knowledge of the loss factors and power input, the subsystem energies can be calculated. Usually not all subsystems are physically connected to every other subsystem, so some coupling loss factors are zero in the loss factor matrix. In addition there is no indirect coupling between disconnected subsystems. In contrast, all subsystems in ASEA can transfer energy to each other whether they are directly connected or not. Indirect coupling between physically disconnected subsystems is also referred to as a 'tunnelling mechanism'.

Following the ASEA derivation by Heron [2], equation (3-15) can also be rewritten as follows

$$\boldsymbol{AE}+\boldsymbol{ME}=\boldsymbol{P} \quad (3\text{-}16)$$

where $\boldsymbol{E}$ is a column vector of modal energies as

$$\boldsymbol{E} = \begin{bmatrix} E_1 / n_1 & E_2 / n_2 & \cdots & E_N / n_N \end{bmatrix}^{\mathrm{T}} \tag{3-17}$$

$\boldsymbol{P}$ is a column vector of input power, $\boldsymbol{M}$ is a diagonal matrix of modal overlap factors, and $\boldsymbol{A}$ is a coupling matrix where

$$\boldsymbol{M} = \omega \begin{bmatrix} n_1\eta_{11} & 0 & \cdots & 0 \\ 0 & n_2\eta_{22} & \cdots & 0 \\ \vdots & \vdots & \ddots & \vdots \\ 0 & 0 & \cdots\cdots & n_N\eta_{NN} \end{bmatrix} \tag{3-18}$$

$$\boldsymbol{A} = \omega \begin{bmatrix} \sum_{k\neq 1}^{N} n_1\eta_{1\mathrm{k}} & -n_2\eta_{21} & \cdots & -n_N\eta_{N1} \\ -n_1\eta_{12} & \sum_{k\neq 2}^{N} n_2\eta_{2\mathrm{k}} & \cdots & -n_N\eta_{N2} \\ \vdots & & \ddots & \vdots \\ -n_1\eta_{1N} & \cdots\cdots & & \sum_{k\neq N}^{N} n_N\eta_{N\mathrm{k}} \end{bmatrix} \tag{3-19}$$

Note that each column of $\boldsymbol{A}$ sums to zero as required for power balance. $\boldsymbol{A}$ is a symmetric matrix due to the consistency relationship.

If we split the total modal energy $\boldsymbol{E}$ in equation (3-16) into two parts, available modal energy, $\boldsymbol{e}$, and unavailable modal energy, $\boldsymbol{d}$. Available energy is the stored modal energy considered in SEA whereas unavailable modal energy describes subsystem energy which is unavailable for further transmission which accounts for propagation losses as a wave travels across a subsystem. ASEA theory is then defined using the following two matrix equations [2]

$$\underset{\substack{\text{available power to} \\ \text{available power transfer}}}{\boldsymbol{Ae}} + \underset{\text{available power lost}}{\boldsymbol{Me}} = \underset{\text{available power input}}{\boldsymbol{P}} \tag{3-20}$$

$$\underset{\substack{\text{available power to} \\ \text{unavailable power transfer}}}{\boldsymbol{Be}} + \underset{\text{unavailable power lost}}{\boldsymbol{Md}} = \underset{\text{unavailable power input}}{\boldsymbol{Q}} \tag{3-21}$$

For N subsystems, $\boldsymbol{A}$ and $\boldsymbol{B}$ are $N \times N$ matrices in which the element $\boldsymbol{A(j,i)}$ represents the available power per unit modal energy transferred from subsystem i to available power per unit modal energy in subsystem j and element $\boldsymbol{B(j,i)}$ represents the available power per unit modal energy transferred from subsystem i to unavailable power per unit modal energy in subsystem j.

Once the $\boldsymbol{A}$, $\boldsymbol{B}$, $\boldsymbol{P}$ and $\boldsymbol{Q}$ are known, the subsystem response can be calculated from $\boldsymbol{e}+\boldsymbol{d}$. From equations (3-20) and (3-21) the total modal energy is given by

$$\boldsymbol{e}+\boldsymbol{d} = \boldsymbol{M}^{-1}(\boldsymbol{Q}+\boldsymbol{R}) \tag{3-22}$$

where $\boldsymbol{R} = (\boldsymbol{M}-\boldsymbol{B})(\boldsymbol{M}+\boldsymbol{A})^{-1}\boldsymbol{P}$. For rain-on-the-roof excitation (forces with unit magnitude and random phase over the entire source subsystem, see section 4.2), $\boldsymbol{Q}$ is zero because all the input power is available for transmission. Thus equation (3-22) can be simplified to

$$\boldsymbol{e}+\boldsymbol{d} = \boldsymbol{M}^{-1}(\boldsymbol{M}-\boldsymbol{B})(\boldsymbol{M}+\boldsymbol{A})^{-1}\boldsymbol{P} \tag{3-23}$$

Summing equations (3-20) and (3-21) gives

$$(\boldsymbol{A}+\boldsymbol{B})\boldsymbol{e}+\boldsymbol{M}(\boldsymbol{e}+\boldsymbol{d}) = \boldsymbol{P}+\boldsymbol{Q} \tag{3-24}$$

Compared to equation (3-16), we can find that in the process of splitting the total modal energy $\boldsymbol{E}$, the coefficient matrix $\boldsymbol{A}+\boldsymbol{B}$ must also meet the requirement of summing to zero for each column.

3.3.3 ASEA for a system of coupled beams

For a system of N coupled beam subsystems, consider a subsystem i with total available energy E_i. Modal energy e_i is given by $e_i = E_i / n_i$, where n_i is the modal density. For a beam, the modal density is $n_i = 2L_i / c_{g,i}$, where L_i and $c_{g,i}$ are the length and group velocity of subsystem i. Thus the modal energy can be rewritten as

$$\boldsymbol{e}_i = \frac{E_i c_{\mathrm{g},i}}{2L} \tag{3-25}$$

Assuming equipartition of energy travelling in both directions along the beam, the power P_i travelling in one direction along subsystem *i* can be calculated by

$$P_i = \frac{E_i/2}{t} \tag{3-26}$$

where t is the time for wave traveling from one end of the beam to the other,

$$t = \frac{d_{\text{mfp}}}{c_{\text{g},i}} = \frac{L_i}{c_{\text{g},i}} \tag{3-27}$$

Substituting (3-27) into (3-26) and combining with (3-25) gives the available power per unit modal energy $P_{a,i}$ which is the initial available power ready for transfer at each end of beam subsystem *i*. That is

$$P_{a,i} = \frac{P_i}{e_i} = 1 \tag{3-28}$$

With knowledge of the initial power per unit modal energy $P_{a,i}$ that is incident at the end of subsystem *i*, we can calculate matrices $\boldsymbol{A}$ and $\boldsymbol{B}$ by tracking the initial power across subsystems using the following steps:

Step 1: All elements of the $N \times N$ matrices $\boldsymbol{A}$ and $\boldsymbol{B}$ are set to zero at the beginning of the calculation. Further power transfer from available to unavailable or available power per unit modal energy is recorded and accumulated in matrices $\boldsymbol{A}$ and $\boldsymbol{B}$.

Step 2: The initial available power per unit modal energy $P_{a,i}$ is added to element (*i*, *i*) of matrix $\boldsymbol{A}$ as the initial available power per unit modal energy incident at a particular end of the subsystem *i*. Note that it is not critical which subsystem is chosen as subsystem *i* because every subsystem will eventually be considered and the power is always normalized to modal energy.

Step 3: Multiplying the initial power per unit modal energy $P_{a,i}$ by the appropriate transmission coefficient gives the incident power to the receiving subsystem *j* which is coupled to subsystem *i* at one end, where

$$P_{s,j} = \tau_{ij} P_{a,i} \tag{3-29}$$

and the power per unit modal energy that is reflected back to subsystem *i* is given by

$$P_{s,i} = r_{ii} P_{a,i} \tag{3-30}$$

where r_{ii} is the reflection coefficient. All subsystems which are coupled to subsystem *i* form different paths for power flow. These transmitted and reflected powers now become the 'starting available power' in subsystem *j* and *i*.

Step 4: Calculate the power loss. When the starting power per unit modal energy $P_{s,j}$ propagates along subsystem *j*, this available power per unit modal energy will have an exponential decay with distance L_j caused by the internal damping, as described by the internal loss factor η_{jj} . Thus the remaining power striking the far end of subsystem *j* is

$$P_{e,j} = P_{s,j} \exp(-\omega \eta_{jj} L_j / c_{g,j}) \tag{3-31}$$

The power per unit modal energy lost in subsystem *j* due to internal losses is

$$P_{l,j} = P_{s,j} - P_{e,j} \tag{3-32}$$

This lost power should be subtracted from element ***B(j,i)*** because it is transferred from available power per unit modal energy originated in subsystem *i* to unavailable power per unit modal energy in subsystem *j*, and is no longer available for further transmission.

Step 5: Calculated the new 'starting available power' for each subsystem. If subsystem *k* is coupled with subsystem *j*, the new 'starting available power' for subsystem *j* and *k* are

$$P_{s,k} = \tau_{jk} P_{e,j}, \quad P'_{s,j} = r_{jj} P_{e,j} \tag{3-33}$$

where τ_{jk} and r_{jj} are the transmission and reflection efficiencies. The reflected power per unit modal energy $P'_{s,j}$ may or may not be tracked any further. If it is not to be

tracked, it must be considered as residual power which must be subtracted from the element $\boldsymbol{B}(j,i)$.

Step 6: Track the new 'starting available power' and repeat steps 4 and 5. The matrices $\boldsymbol{A}$ and $\boldsymbol{B}$ are updated through the process with the elements in column i being recalculated. This whole process can stop at any stage leaving the remaining power in each subsystem. This remain power $P_{r,j}$ in subsystem j should be subtracted from the element (j, i) of matrix $\boldsymbol{A}$. Note that it is only the column i in the matrices $\boldsymbol{A}$ and $\boldsymbol{B}$ that require updating because all the power originates from subsystem i. Checks should be carried out to sum each column of $\boldsymbol{A}+\boldsymbol{B}$ as these must equal to zero at every stage.

The number of subsystems across which the initial power is tracked is called the ASEA level number. This also equals the number of times that the power is tracked in the source subsystem. When the level number is zero there is no transfer from available power to unavailable power and the result is equivalent to SEA. Use of ASEA therefore requires an indication that convergence has been achieved. For six in-line coupled rods, Heron [2] proposed a rule of convergence that the level number should be at least equal to the number of subsystems minus two. For ASEA on systems of coupled plates where each plate was coupled to at least four other plates, Wilson and Hopkins [70] used a level number equal to the number of subsystems plus four to give ≤0.1dB difference between ASEA level N and level N-1. For the coupled beam systems in this paper, a level number equal to the number of subsystems plus two has been used to give ≤0.02dB difference between ASEA level N and level N-1.

An example of ASEA levels is shown in Figure 3.1 for an in-line array of beams with three subsystems i, j and k.

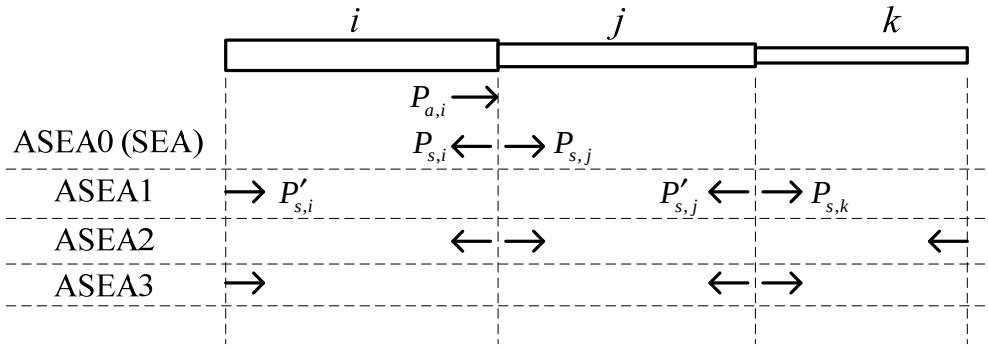

Figure 3.1 Example of ASEA level numbers up to ASEA3.

Step 7: Repeat steps 2 to 6 for all other beam junctions in subsystem *i*.

Step 8: Repeat steps 2 to 7 for all the other subsystems.

Step 9: The final results of matrices $\boldsymbol{A}$ and $\boldsymbol{B}$ are calculated from the summation of all matrices $\boldsymbol{A}_{i,k}$ and $\boldsymbol{B}_{i,k}$ produced in steps 6, 7 and 8.

$$\boldsymbol{A} = \sum_{k=1}^{J_1} \boldsymbol{A}_{1k} + \cdots + \sum_{k=1}^{J_i} \boldsymbol{A}_{ik} + \cdots + \sum_{k=1}^{J_N} \boldsymbol{A}_{Nk} \tag{3-34}$$

$$\boldsymbol{B} = \sum_{k=1}^{J_1} \boldsymbol{B}_{1k} + \cdots + \sum_{k=1}^{J_i} \boldsymbol{B}_{ik} + \cdots + \sum_{k=1}^{J_N} \boldsymbol{B}_{Nk} \tag{3-35}$$

where J_i is the number of junctions in subsystem *i* and the *N* is the number of total subsystems. Note that $\boldsymbol{A}_{i,k}$ and $\boldsymbol{B}_{i,k}$ correspond to the coupling between subsystem *i* with another subsystem through junction *k*.

Step 10: Solve equation (3-23) using matrices $\boldsymbol{A}$ and $\boldsymbol{B}$.

It is worth noting that without steps 4 and 5 the algorithm processes the power in exactly the same way as SEA, which is defined as ASEA0.

3.3.4 Example: Heron's six in-line rods

ASEA produces different results depending on the number of power transfer across subsystems. Thus ASEA can be thought as a series of approximations, ASEA0 (SEA), ASEA1, ASEA2, ASEA3 etc, which converge with increasing ASEA level number.

When the ASEA level number becomes larger, the elements of matrix A tend towards zero and the ASEA calculation essentially just becomes ray tracing.

As an example of ASEA, a simple structure is taken from Heron [2] that consists of six different rods arranged in a line. The six rods are of lengths 23, 28, 25, 24, 29 and 21 m and their mass per unit lengths are 1, 10, 3, 7, 8 and 2 kg/m, respectively. The longitudinal wave velocity is 5000 m/s, and the internal loss factor is 0.02. The driving point impedance for longitudinal excitation is determined using

$$Z_{\mathrm{L}} = \rho A c_{\mathrm{L}} \tag{3-36}$$

Longitudinal wave transmission coefficient from subsystem 1 to 2 on a discontinuity of beam is given by [5]

$$\tau_{\mathrm{L1L2}} = \frac{4}{\left(\sqrt{\frac{Z_{L1}}{Z_{L2}}} + \sqrt{\frac{Z_{L2}}{Z_{L1}}}\right)^2} \tag{3-37}$$

This structure is driven at the end of the first rod with a unit force. The velocity level differences for beams 2, 3, 4, 5 and 6 are calculated up to 10 kHz with a frequency bandwidth of 50 Hz.

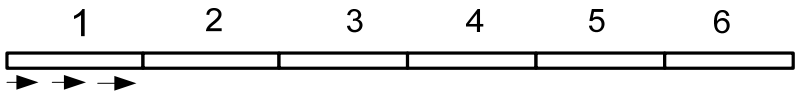

Figure 3.2 In-line array of six rods.

Figure 3.3 shows that with increasing frequency above 2 kHz, ASEA0 (or SEA) over-predicts the response on the receiving rod compared to ASEA; at 10 kHz, this over-prediction is ≈70 dB discrepancies for the most distance rod 6. Heron [2] noted that ASEA results converge such that the ASEA level number should be at least the number of subsystems minus two. Note that the convergence of ASEA is not monotonic with increasing ASEA level number because on rod 6, ASEA2 gives a better result than ASEA3.

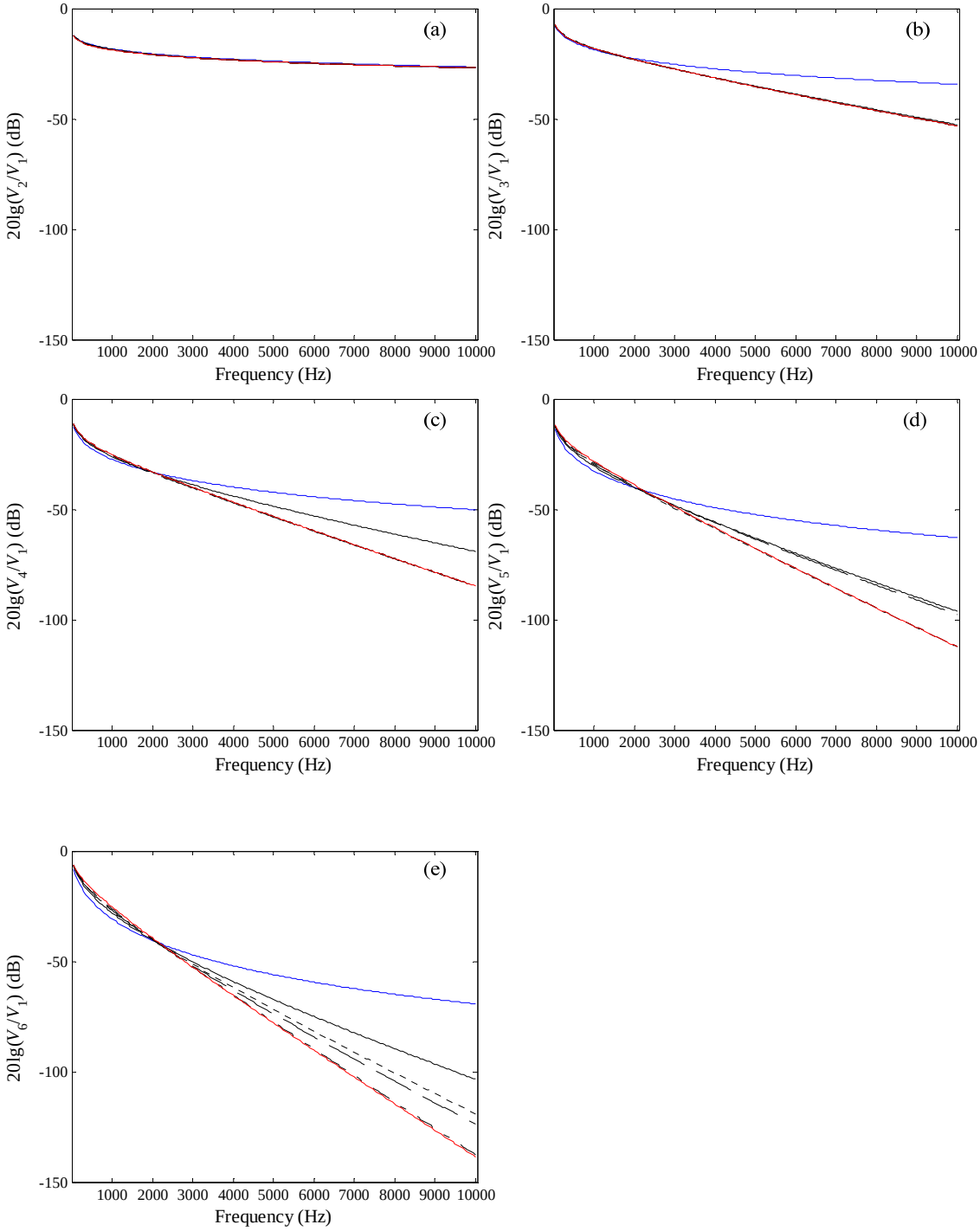

Figure 3.3 Velocity level difference: ——, ASEA0(SEA); ——, ASEA1; – – – –, ASEA2; ------, ASEA3; –·–·–, ASEA4; ——,ASEA6.

3.4 Summary

This chapter gives detailed descriptions of how SEA and ASEA have been implemented to predict vibration transmission across frameworks of beams.

Heron only validated the ability of ASEA to model a single wave type propagating along an in-line array of six very long beams (forming an unrealistic engineering structure). This structure had high propagation losses and did not show any significant tunnelling. In this thesis ASEA will be used to assess its ability to account for indirect coupling (tunnelling) as well as propagation losses with multiple wave types on more realistic engineering structures. To ensure convergence all ASEA calculations are carried out to an ASEA level number equal to the total number of subsystems plus two.

4. Finite element methods

This section describes the finite element method (FEM) used to model the beam junctions. In FEM, the structure under analysis is discretized into a mesh of elements that are connected at nodal points; the mass is lumped at the nodes in each element. With the *n* degrees of freedom of all nodes in the mesh as the unknown parameters, the general equation of motion for linear systems under steady-state excitation by sinusoidal point forces is [71]

$$\mathbf{M}\frac{\partial^2 \boldsymbol{\xi}}{\partial t^2} + \mathbf{C}\frac{\partial \boldsymbol{\xi}}{\partial t} + \mathbf{K}\boldsymbol{\xi} = \mathbf{F} \tag{4-1}$$

where $\boldsymbol{\xi}$ is the vector of displacement of the nodes, $\mathbf{F}$ is the vector of applied force, $\mathbf{M}$ is mass matrix, $\mathbf{C}$ is the damping matrix, and $\mathbf{K}$ is the stiffness matrix. Assuming the damping is proportional to the mass and stiffness matrix, that is

$$\mathbf{C} = a\mathbf{M} + b\mathbf{K} \tag{4-2}$$

where *a* and *b* are constant. Then the equation (4-1) can be decoupled as

$$\mathbf{M}_{\mathrm{p}}\frac{\partial^2 \boldsymbol{\xi}_{\mathrm{p}}}{\partial t^2} + \mathbf{C}_{\mathrm{p}}\frac{\partial \boldsymbol{\xi}_{\mathrm{p}}}{\partial t} + \mathbf{K}_{\mathrm{p}}\boldsymbol{\xi}_{\mathrm{p}} = \mathbf{F}_{\mathrm{p}} \tag{4-3}$$

by using the following transformation

$$\boldsymbol{\xi}_{\mathrm{p}} = \boldsymbol{\Phi}^{\mathrm{T}}\boldsymbol{\xi} \tag{4-4}$$

$$\mathbf{F}_{\mathrm{p}} = \boldsymbol{\Phi}^{\mathrm{T}}\mathbf{F} \tag{4-5}$$

$$\boldsymbol{\Phi}^{\mathrm{T}}\mathbf{M}\boldsymbol{\Phi} = diag\left(M_{p1}\cdots M_{pn}\right) = \mathbf{M}_{\mathrm{p}} \tag{4-6}$$

$$\boldsymbol{\Phi}^{\mathrm{T}}\mathbf{K}\boldsymbol{\Phi} = diag\left(K_{p1}\cdots K_{pn}\right) = \mathbf{K}_{\mathrm{p}} \tag{4-7}$$

$$\boldsymbol{\Phi}^{\mathrm{T}}\mathbf{C}\boldsymbol{\Phi} = diag\left(C_{p1}\cdots C_{pn}\right) = \mathbf{C}_{\mathrm{p}} \tag{4-8}$$

where **Φ** is the matrix of eigenvectors about **M** and **K**. $\mathbf{M}_p$, $\mathbf{C}_p$ and $\mathbf{K}_p$ are orthogonalized diagonal matrix.

The damping in FEM is applied using the critical damping or constant damping ratio, $\zeta_{cdr,i}$ for i^{th} order mode. It's defined as

$$\zeta_{\mathrm{cdr},i} = \frac{C_{pi}}{2\omega_i M_{pi}} \quad (i = 1,\ \ 2, \cdots n) \tag{4-9}$$

The relation between critical damping and internal loss factor is [61,82]

$$\zeta_{\mathrm{cdr},i} = \frac{\eta}{2} \tag{4-10}$$

4.1 Element type

For beam elements in ABAQUS, there are several different kinds of finite element types, including 'Euler-Bernoulli'-Type Beam and 'Timoshenko'-Type Beams with solid, thin-walled closed and thin-walled open cross-sections. Euler-Bernoulli beam elements in bending ignore the rotary inertia of the beam cross-section hence these elements don't allow transverse shear deformation. Plane sections that are initially normal to the beam axis will remain plane and normal the beam axis. In Abaqus/Standard, the Euler-Bernoulli beam elements include B23, B23H, B33, and B33H, which can be used only to model slender beam: the beam cross-section dimensions are much smaller than the typical distances along its axis. Timoshenko beam elements (B21, B22, B31, B310S, B32, B32OS, PIPE21, PIPE22, PIPE31, PIPE32, and their 'hybrid' equivalents) allow transverse shear deformation and can be used for both thick beams and slender beams. The element types are described in the Abaqus Analysis User's Manual [83].

4.2 Excitation

Rain-on-the-roof excitation is applied using forces with unit magnitude and random phase over all *N* nodes on the source subsystem. The reason to choose rain-on-the-roof excitation for SEA is that it provides statistically independent input forces. However, when rain-on-the-roof is applied in a numerical method like FEM, each set of random

numbers will give a different response. For this reason, each model is solved with 10 different sets of rain-on-the-roof in order to give a mean value with 95% confidence intervals [70].

Rain-on-the-roof tends to be used to excite bending waves [70], however, in this thesis it is also used to excite longitudinal and torsional waves.

4.3 Junction

For the FEM models that are compared with the B model, the displacement in the three coordinate directions is pinned but for the BL and BT models no constraints are applied to the junction nodes.

4.4 Element size and mesh error

The element size is chosen by considering the accuracy required and is usually described with bending wave length in the structure; a suitable size is usually smaller than $\lambda_B/6$ [61].

To check and assess the adequacy of the element size, the mesh error is assessed through the comparison of injected power and the power contained in the whole structure [84].

The injected power at a single frequency is calculated from all the random forces on N nodes and the relevant nodal velocities

$$W_{in} = \sum_{1}^{N} \frac{1}{2} \mathrm{Re}\left\{\mathbf{F} \bullet \mathbf{v}^{*}\right\} \tag{4-11}$$

The complex velocity can be written in terms of displacement as

$$\mathbf{v} = i\omega\boldsymbol{\xi} \tag{4-12}$$

The input power from ROTR forces is then given by

$$W_{in} = \frac{\omega}{2} \sum_{n=1}^{N} \left(\mathrm{Im}(\mathbf{F})\,\mathrm{Re}(\boldsymbol{\xi}) - \mathrm{Re}(\mathbf{F})\,\mathrm{Im}(\boldsymbol{\xi}) \right)_n \tag{4-13}$$

The total energy for bending waves within the structure is stored in the *P* nodes

$$E = m\left\langle \mathbf{v}^2 \right\rangle = \frac{1}{2}\omega^2 \sum_{n=1}^{P} m_n \left|\xi_n\right|^2 \tag{4-14}$$

Note that equations (4-13) and (4-14) can be applied both for bending and longitudinal wave motion. However in this thesis it is also necessary to assess the input power of torsional moment of force which is given by

$$\begin{aligned} W_{in} &= \sum_{n=1}^{P} \frac{1}{2} \mathrm{Re}\left\{\mathbf{M}\cdot\boldsymbol{\omega}^*\right\}_n = \sum_{n=1}^{P} \frac{1}{2} \mathrm{Re}\left\{\mathbf{M}\cdot(i\omega\boldsymbol{\theta})^*\right\}_n \\ &= \frac{\omega}{2}\sum_{n=1}^{P}\left\{\mathrm{Im}(\mathbf{M})\,\mathrm{Re}(\boldsymbol{\theta}) - \mathrm{Re}(\mathbf{M})\,\mathrm{Im}(\boldsymbol{\theta})\right\}_n \end{aligned} \tag{4-15}$$

where $\mathbf{M}$ and $\boldsymbol{\theta}$ are the input moment of force and responded torsional displacement on each node, respectively. The total rotational energy on a beam with *P* nodes can be calculated using

$$\begin{aligned} E &= \sum_{n=1}^{P}\left\{\int_A \frac{1}{2}(\rho L_n dA)\left|\boldsymbol{\omega}_n r\right|^2\right\} = \sum_{n=1}^{P}\left\{\int_A \frac{1}{2}(\rho L_n dA)\left|i\omega\boldsymbol{\theta}_n r\right|^2\right\} \\ &= \frac{1}{2}\omega^2 \sum_{n=1}^{P} \rho J L_n \left|\boldsymbol{\theta}_n\right|^2 \end{aligned} \tag{4-16}$$

where L_n is the element size, and J is the polar moment of inertia of the cross-section.

The power leaving the structure can be calculated from the total wave energy

$$W_{\mathrm{out}} = \omega\eta E \tag{4-17}$$

The element size can then be assessed by the percentage error, e_{mesh} between input power on source subsystem and output power on all subsystems

$$e_{\mathrm{mesh}} = \frac{\left|W_{\mathrm{in}} - W_{\mathrm{out}}\right|}{W_{\mathrm{in}}} \times 100\% \tag{4-18}$$

Since FEM is an asymptotic method, smaller element size means more accurate modelling. Mesh error, e_{mesh} can be used as an indicator to assess the mesh of FEM

model. Note that the output power is calculated as the sum of that from all subsystems of the structure, while the input power is from the source subsystems.

An example is considered for an L-junction with pinned ends with material properties given in Table 2.3. Rain-on-the-roof excitation of Type A bending waves are applied for B model, and for BL model Rain-on-the-roof excitation of Type A bending waves and longitudinal waves are applied. For BT model Rain-on-the-roof excitation of Type B bending waves and torsional waves are applied. The element type is B33, and the element size is 0.005 m. A comparison of input power and output power alongside the mesh error based on the B, BL and BT models are shown in Figure 4.1, Figure 4.2 and Figure 4.3.

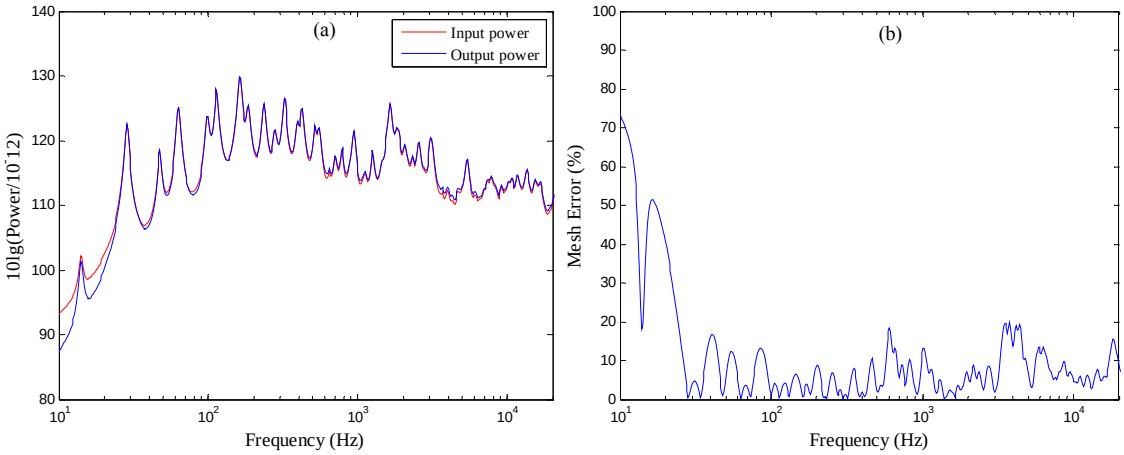

Figure 4.1 B model of L-junction: (a) comparison of incident power and output power under Type A bending wave excitation, (b) mesh error under Type A bending wave excitation.

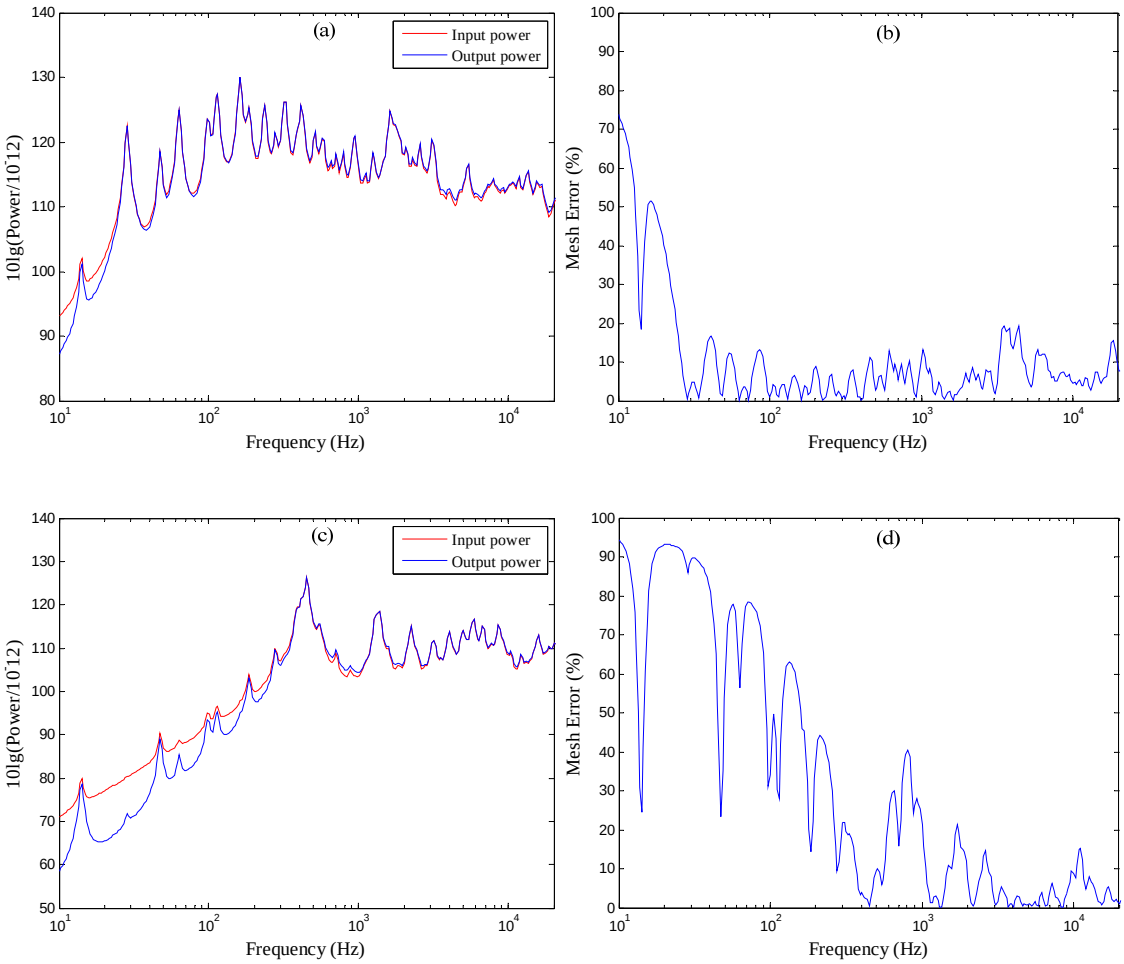

Figure 4.2 BL model of L-junction: (a) comparison of incident power and output power under Type A bending wave excitation, (b) mesh error under Type A bending wave

excitation, (c) comparison of incident power and output power under longitudinal wave excitation, (d) mesh error under longitudinal wave excitation.

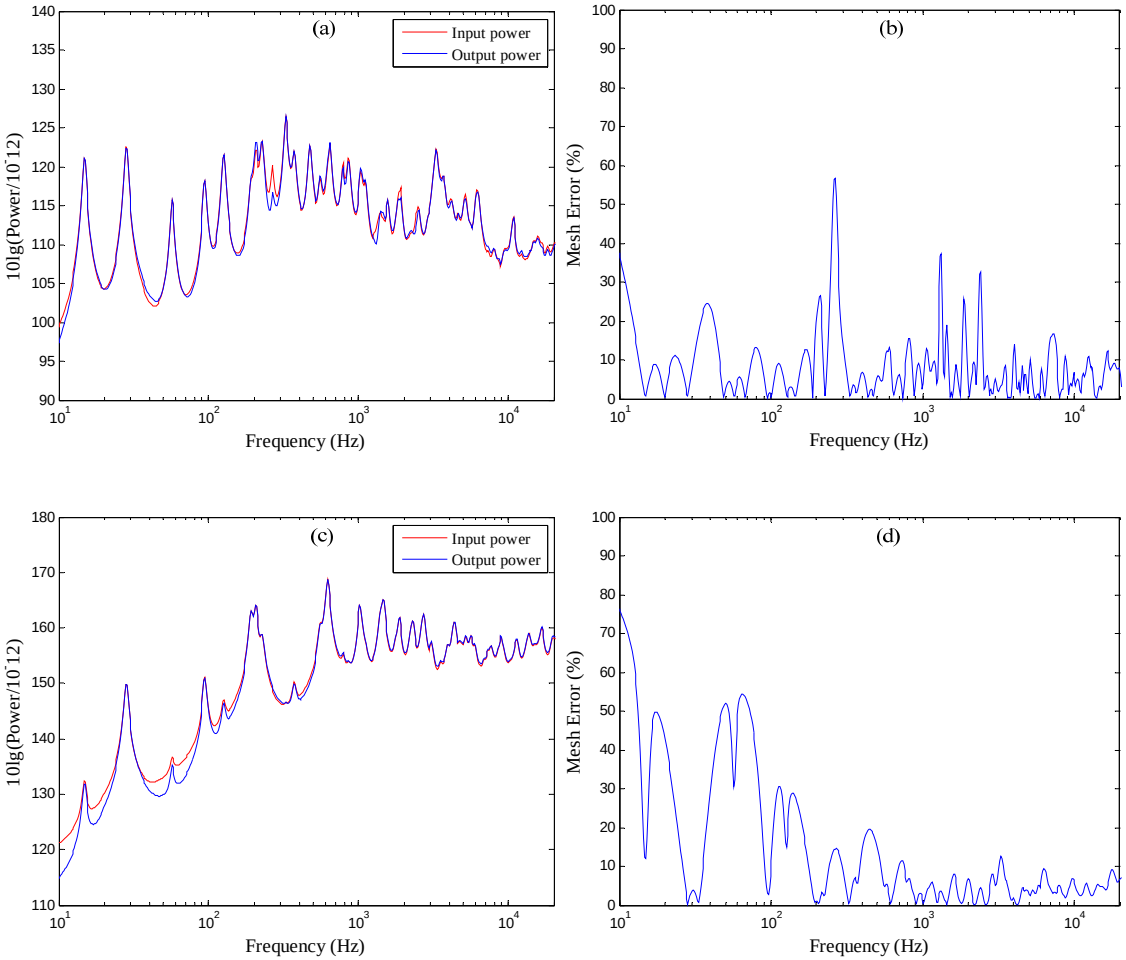

Figure 4.3 BT model of L-junction: (a) comparison of incident power and output power under Type B bending wave excitation, (b) mesh error under Type B bending wave excitation, (c) comparison of incident power and output power under torsional wave excitation, (d) mesh error under torsional wave excitation.

At 20 kHz the wave length λ_B of Type A bending and Type B bending are 0.046 m and 0.065 m, respectively. Thus, the element size of Type A and Type B bending should be $\leq \lambda_B / 10$ (about 0.005 m).

Referring back to 2.3 for pinned-pinned isolated beam, the fundamental mode of Type A bending, longitudinal, Type B bending and torsional waves are 10 Hz, 1 kHz, 12.5 Hz and 400 Hz, respectively. In general, above the fundamental mode the mesh error is always below 20% (e.g. the mesh error above 400 Hz for torsional excitation) except for

a few frequencies with the Type B bending excitation. This indicates the choice of element size is reasonable. In chapters 6 and 7, the element size is also chosen to be 0.005.

4.5 Comparison of driving-point mobility from FEM with an analytical model

A comparison is now made of the driving point mobility from Abaqus and the analytical result.

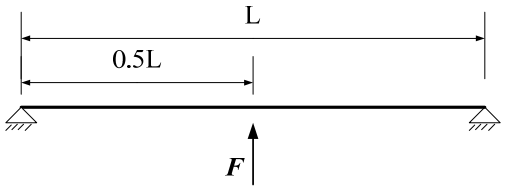

Figure 4.4 Simple supported beam.

The driving point mobility for a finite beam (Euler-Bernoulli theory) with idealised boundary conditions can be calculated using the natural frequencies and modes shapes. For force excitation at x_i and transverse velocity response at x_j, the mobility is given by Fahy [60]

$$Y_{ij} = \frac{v}{F} = i\omega \sum_{n=1}^{\infty} \frac{\psi_n(x_i)\psi_n(x_j)}{\rho SL\left[\omega_n^2(1+i\eta)-\omega^2\right]} \tag{4-19}$$

where $\psi_n(x)$ is the nth natural mode function, and ω_n is the natural radial frequency. For a pinned-pinned boundary condition, $\psi_n(x) = \sqrt{2}\sin k_{nb}x$, $k_{nb} = n\pi/L$ and n=1,2,3 etc.

The Perspex beam is 1 m x 0.02 m x 0.01 m with material properties described in section 2.3 FEM shows close agreement with the analytical result in Figure 4.5 which validates that the element type B33 and the element size are appropriate.

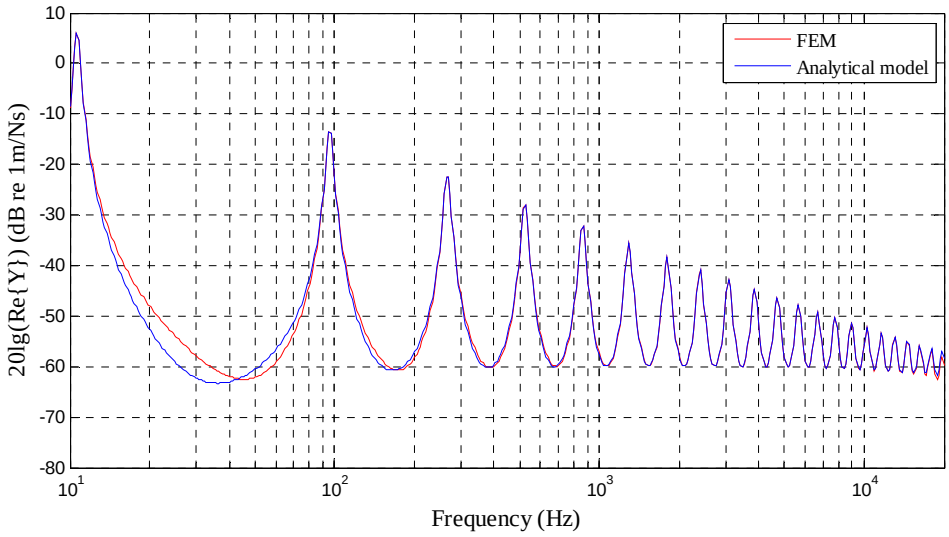

Figure 4.5 Driving-point mobility at the mid-point of a pinned-pinned beam.

4.6 In-plane vibration due to bending wave motion

Bending waves on a beam not only cause out-of-plane vibration but they also cause in-plane vibration. In this thesis it is necessary to calculate energy levels from FEM data that represent bending wave energy as well as longitudinal wave energy. Therefore this section investigates the in-plane vibration hat occurs due to bending wave motion.

4.6.1 Bending and in-plane motion on isolated beam

An isolated 1.0 m beam with pinned-pinned boundaries, free-pinned boundaries, and free-free boundaries is investigated to investigate in-plane motion under lateral single force excitation of bending wave motion. Figure 4.7 (a) shows that in-plane vibration is negligible compared to bending wave vibration for all boundary conditions.

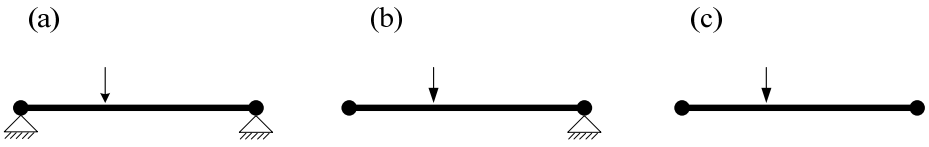

Figure 4.6 Point excitation on the one third of isolated beam with pinned-pinned, free-pinned, and free-free boundary conditions.

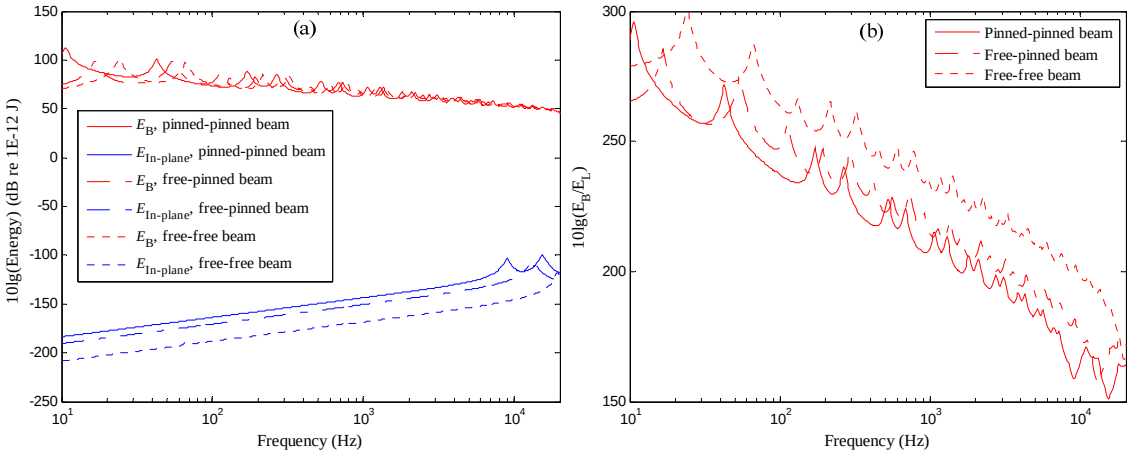

Figure 4.7 Bending and in-plane energy on isolated beam.

4.6.2 BL model: Coupling between bending and longitudinal waves on an L-junction with different boundary conditions

To assess the generation of longitudinal wave motion and its coupling with bending motion, the driving-point mobility at a point one-third of the way along beam 1 (1.3m) in the L-junction is determined when it has pinned ends (Figure 4.8 (a)) and free ends (Figure 4.8 (b)). The mobility is calculated using FEM and compared with the analytical result for a pinned-free beam and a free-free beam. The driving-point mobility is determined with a transverse force to excite bending wave motion, denoted Y_B, and with an axial force to excite longitudinal wave motion, denoted Y_L.

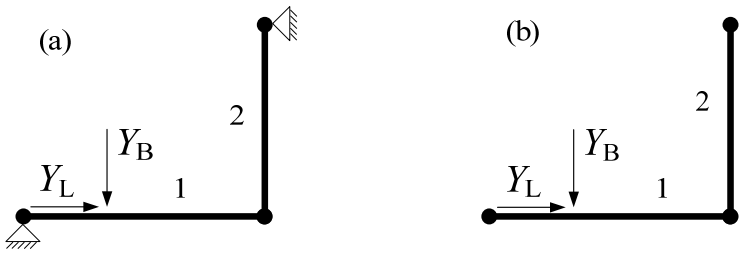

Figure 4.8 L-junction with (a) pinned ends and (b) free ends.

Figure 4.9 compares the driving-point mobilities on beam 1 that forms the L-junction with pinned ends with beam 1 as an isolated beam. The peaks in the driving-point mobility Y_B for beam 1 in the L-junction differ from those when beam 1 is isolated. The reason for this is that the former correspond to global bending modes of the L-junction and the latter correspond to local bending modes of the beam where the end that forms the junction has a free boundary. For this reason the mode frequencies are different.

On the isolated beam there are no local longitudinal modes below 400 Hz and Y_L calculated using FEM has lower values than that on the isolated pinned-free beam. On beam 1 in the L-junction there are low peaks that occur in Y_L that is predicted using FEM below 400 Hz. These correspond to the peaks in Y_B from FEM that occur at the global bending mode frequencies of the L-junction. This is due to the axial force exciting longitudinal waves on beam 1 that are converted back into bending waves on beam 1. Although bending wave motion has an in-plane velocity component that appears in Y_L, the latter is sufficiently low that it will not have a significant effect on estimates of the longitudinal wave energy. Above 400 Hz where there are longitudinal modes, values of Y_L calculated using FEM and the analytical model show close agreement at the modal peaks.

The driving-point mobilities for the L-junction where the beams have free ends are shown in Figure 4.10. Below 800 Hz there are no longitudinal modes but Y_L calculated using FEM for the L-junction has significantly higher values than the analytical values for the free-free beam with peaks corresponding to the global bending modes. Compared to Y_L calculated using FEM in Figure 4.9, the high peaks in Figure 4.10 indicate that free ends for the beams that form the L-junction produce significantly higher in-plane vibration due to bending wave motion than pinned ends. The peaks in Y_L calculated using FEM are typically 10-30 dB below the peaks in Y_B calculated using FEM. This has implications when calculating in-plane energy from FEM models because it is only appropriate to use FEM to calculate longitudinal wave energy at and above the fundamental longitudinal mode of each beam. For this reason the graphs of energy level differences calculated using FEM are only shown at frequencies above the fundamental longitudinal mode of each beam in Chapters 6 and 7.

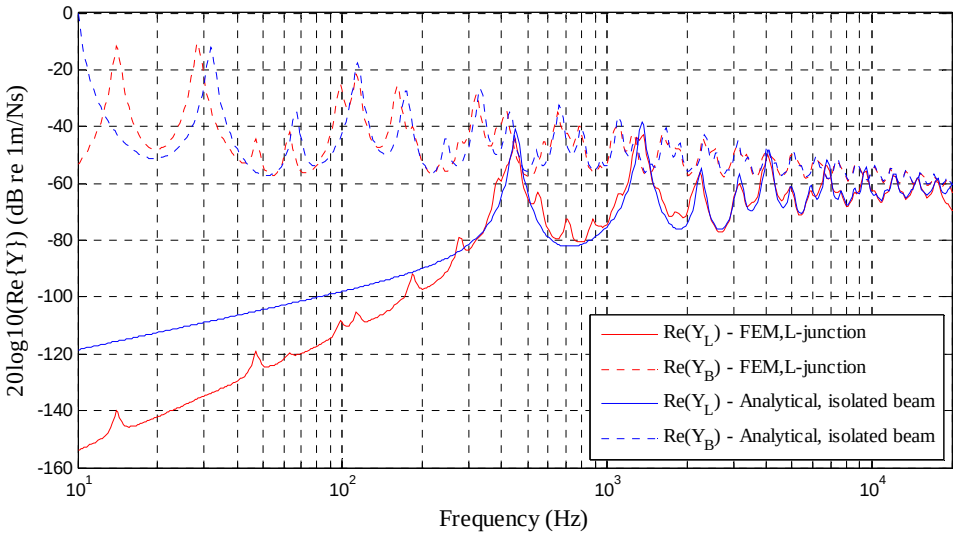

Figure 4.9 Driving-point mobility at a point that is one-third of the length along beam 1 in L-junction with pinned ends and when it is an isolated beam (pinned-free).

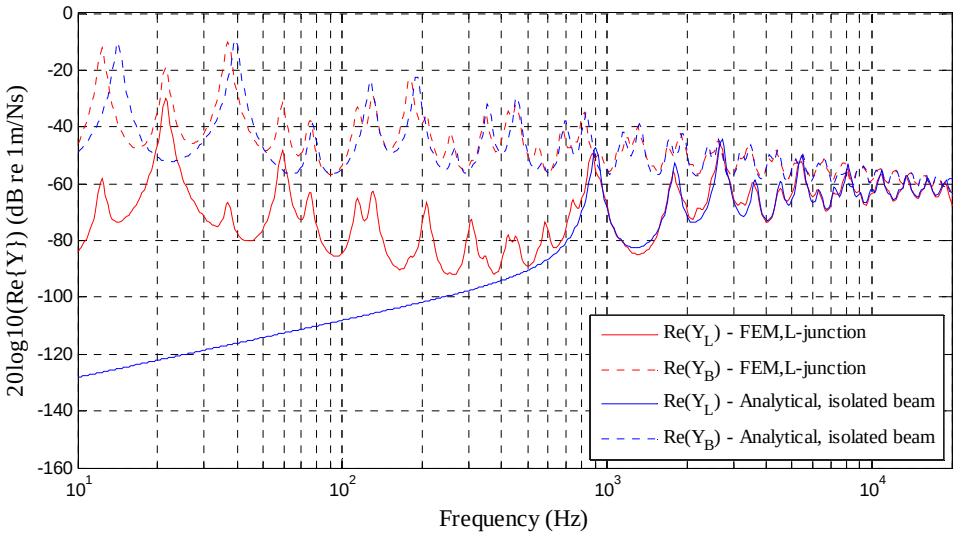

Figure 4.10 Driving-point mobility at a point that is one-third of the length along beam 1 in L-junction with free ends and when it is an isolated beam (free-free).

4.7 Summary

This chapter describes the approach used for the finite element models with a commercial code, Abaqus 6.12. Details are given on (a) the type of beam element used to model Euler-Bernoulli and Timoshenko theory, (b) rain-on-the-roof excitation, (c) the calculation and assessment of mesh errors when the beams support bending, longitudinal or torsional wave motion.

The calculation of mesh errors for beams supporting bending, longitudinal or torsional wave motion show that the element size is sufficient for Type A and Type B bending waves when the element size is $< \lambda_B/10$.

In this thesis FEM is used to calculate in-plane wave energy for longitudinal wave motion in the presence of bending wave motion. This is potentially problematic because bending waves also give rise to in-plane vibration. Investigations were therefore carried out check whether the in-plane motion this could be problematic when using FEM to validate BL models using SEA and ASEA in chapters 6 and 7. Two assessments were carried out: (a) investigating bending wave excitation on isolated beams with different boundary conditions and (b) investigating driving-point mobility on L-junctions of BL model with pinned ends and free ends. These confirmed that bending waves cause longitudinal motion below the fundamental longitudinal mode but that in-plane motion tends to be negligible compared to the bending wave motion. Hence it is important that FEM is only used to calculate longitudinal wave energy at and above the fundamental longitudinal mode of each beam. Therefore in the validation of FEM, SEA, ASEA against measurements in Chapter 6 any energy level differences involving longitudinal wave energy are only shown at frequencies above the fundamental longitudinal mode. In Chapter 7 (section 7.2), numerical experiments are used to investigate the effect of junction and boundary conditions with the L-junction and some examples of energy level differences involving longitudinal wave energy are shown below the fundamental longitudinal mode. One reason for this is that in purely experimental studies on complex beams it might be difficult to estimate the fundamental longitudinal mode; therefore it is of interest to see whether rain-on-the-roof excitation of longitudinal waves causes a wave field below the fundamental longitudinal mode which has similarities to a modal or diffuse longitudinal wave field.

5. Experimental work

This chapter describes the experimental work used to measure material properties of Perspex (Young's modulus and internal loss factors) and vibration level differences on coupled Perspex beams. Perspex was chosen for the beam because (a) it can be cut accurately, (b) it has smooth surfaces, (c) it can be joined to form a rigid junction using cyanoacrylate adhesive, and (d) it has higher internal losses than most metals. However, to test the prediction models in this thesis it is necessary to cover frequencies up to 20 kHz and it was not known whether properties such as the Young's modulus and internal loss factor varied over this frequency range. Hence it was critical that these properties were measured.

5.1 Measurement of Perspex properties

For the prediction models it is necessary to know dimensions, density, elastic modulus, Poisson's ratio and internal damping.

The measured density for the Perspex was 1184 kg/m^3.

Poisson's ratio was assumed to be 0.3 as indicated in [61].

The Young's modulus was determined from measurements according to ISO/PAS 16940 [85]. This requires measurement of the input impedance at the centre point of a short beam sample. This input impedance is the transfer function between the injected force and the velocity at the same point. The peaks in the impedance curve correspond to resonance frequencies, f_i of the beam sample. Then the Young's modulus can be calculated using the following equation [61].

$$E_i = \frac{m'}{I}\left(\frac{\pi L^2 f_i}{2\lambda_i^2}\right)^2 \tag{5-1}$$

where m' is the mass per unit length, I is the moment of inertia of the beam cross-section, L is the length of the beam, and the parameter λ_i is a constant corresponding to the i^{th} resonance frequency (λ_1=1.8750, λ_2=4.69410, λ_3=7.85476, λ_4=10.99554).

The internal loss factor can also be calculated using this impedance measurement. According to ISO/PAS 16940 [85], it can be calculated from the resonance frequency and the half-power bandwidth (3 dB down points) $\Delta f_{3dB,i}$ using

$$\eta_{\text{int},i} = \frac{\Delta f_{3dB,i}}{f_i} \tag{5-2}$$

Figure 5.1 shows the experimental setup of impedance test in this work in which the force transducer (B&K Type 8200) gives the force signal, while the laser vibrometer (Polytec PDV100) measures the velocity. The laser vibrometer is used instead of an accelerometer to avoid mass loading to the beam sample. The force transducer is screwed into the beam sample and connected to the shaker by bolt with two nuts, so that the beam sample could be excited at frequencies up to 20 kHz. Analysis was carried out using FFT analyser on B&K Pulse using excitation with white noise.

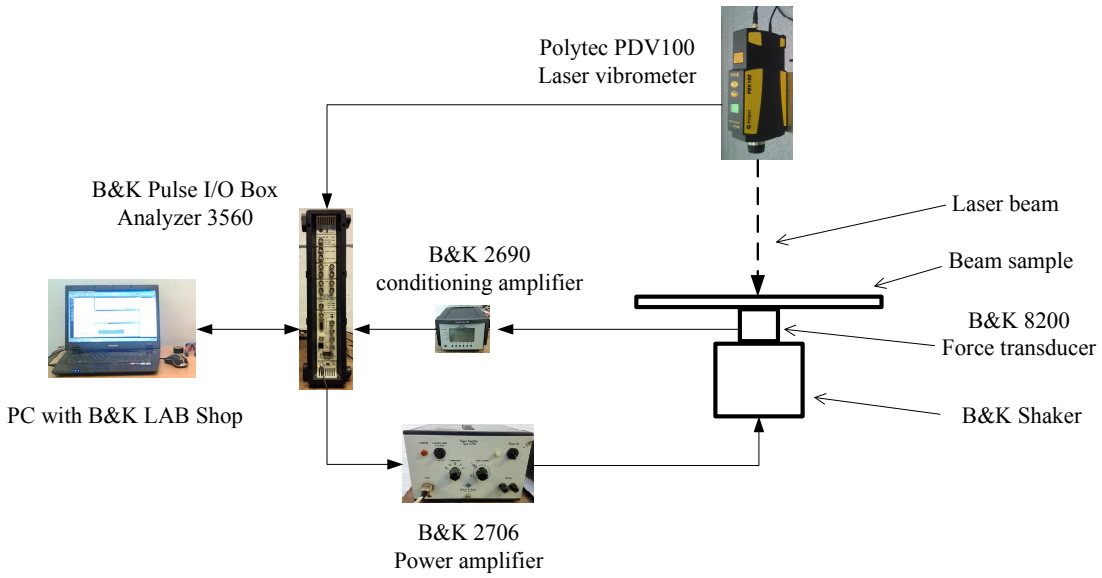

Figure 5.1 Experimental setup for measuring impedance of beam sample

Figure 5.2 shows an example of the measured impedance on a 0.5 m beam with first four resonance modes below 2000 Hz.

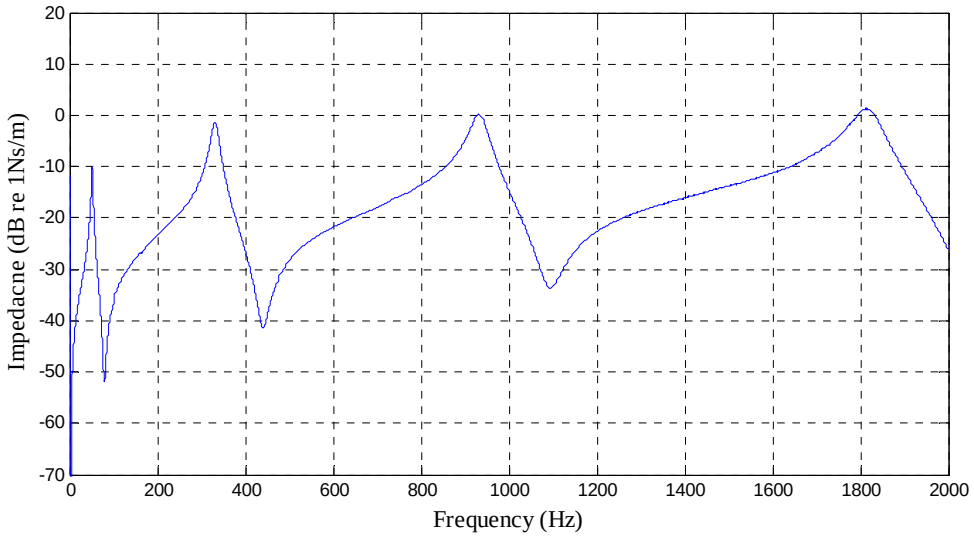

Figure 5.2 Driving-point impedance at the centre point of the 0.5 m beam sample.

To obtain modal responses up to 20 kHz, five Perspex beam samples are measured with lengths, 0.15 m, 0.17 m, 0.2 m and 0.5 m. All the samples have a cross-section, 0.02 m×0.01 m (as used for the junctions). The beam samples with a length of 0.15 m are used to give two different sets of modal frequencies by measuring across the different directions of the cross-section. The results for each beam sample are listed in Table 5.1.

Table 5.1 Perspex properties.

Beam length (m)	Mode	Frequency (Hz)	Young's modulus (GPa)	Internal loss factor (-)
0.15 (Bending Type A)	1	589.4	4.99	0.0467
	2	3567	4.65	0.0332
	3	9260	4.00	0.0328
	4	20380	5.04	0.0224
0.15 (Bending Type B)	1	1173.8	4.94	0.0398
	2	6280.3	3.60	0.0310
	3	18563	4.02	0.0350
0.17	1	465	5.12	0.0489
	2	2855.9	4.92	0.0354
	3	7486	4.31	0.0329
	4	13454	3.63	0.0346
0.2	1	336.5	5.14	0.0594
	2	2098.1	5.08	0.0364
	3	5627	4.66	0.0333
	4	10335	4.10	0.0308
0.5	1	51	4.61	0.0686
	2	331	4.94	0.0529
	3	929.8	4.97	0.0417
	4	1808.5	4.90	0.0379

Young's modulus shows no significant variation with increasing frequency, $\sigma/\mu \approx 0.11$; hence the mean value is used to describe Perspex at all frequencies up to 20 kHz. The mean value of the Young's modulus is 4.59×10^9 Pa with a standard deviation of 0.51×10^9 Pa.

The measured ILFs are plotted against frequency in Figure 5.3. This indicates that the internal loss factor varies with frequency. Below 3000 Hz the ILF increases with decreasing frequency. However the ILF is relatively constant between 3000 and 20000 Hz and has a mean value of 0.0330 with a standard deviation of 0.0015. Note that that this value is lower than the value of 0.06 that is sometimes quoted in the literature [e.g. 3]; hence it appears that the generic name 'Perspex' is insufficient to describe the properties of all the different varieties. For a viscoelastic material the damping and stiffness are dependent upon frequency and temperature. Three states, the rubbery region, the transition region and the glassy region can be used to describe the material behaviour [73,86,87] over a broad frequency range. The ILF is a maximum in the transition region, and then decreases into the glassy region. In this work, all the experiments are conducted at room temperature around 20°C and the ILF mainly depends on the frequency.

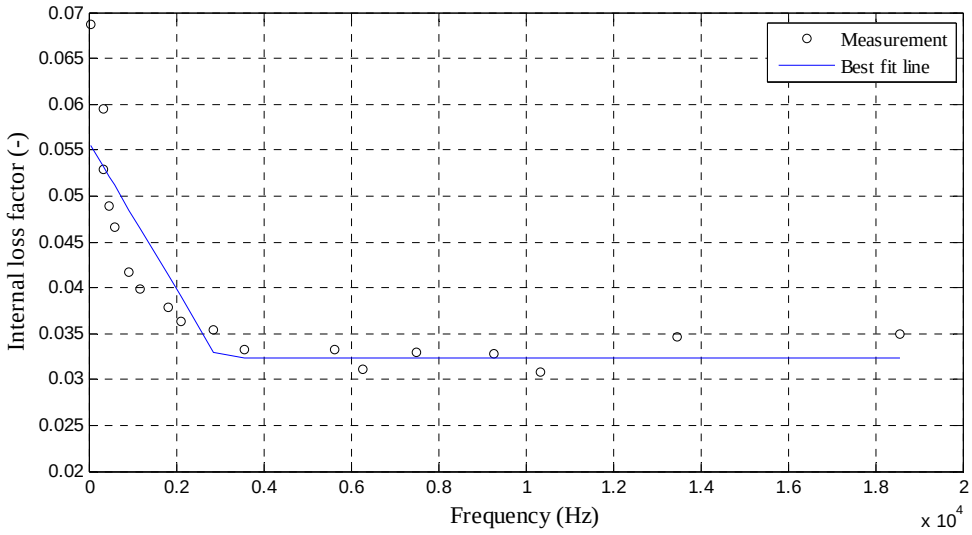

Figure 5.3 Measured internal loss factors.

For the prediction models it is convenient to have estimates of the ILFs for each one-third octave band, hence a linear polynomial fit to the measured ILFs is used to determine values at the one-third octave band centre frequencies. The polynomial fitted

ILFs shown in Figure 5.4 will be used in the comparison of analytical models and experiments. These internal loss factors (along with Poisson's ratio and Young's modulus) are summarized in Table 5.2.

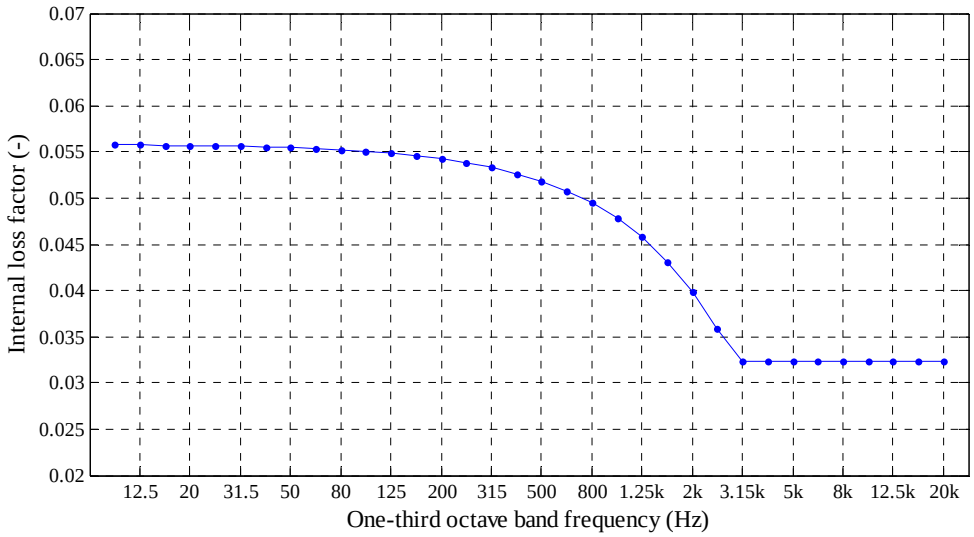

Figure 5.4 Internal loss factors for each third-octave band.

Table 5.2 Measured material properties of Perspex.

Material	Density (kg/m^3)	Young's modulus (Pa)	Poisson's ratio
Perspex	1183.74	4.59×10^9	0.3
Frequency (Hz)	Internal loss factor (-)	Frequency (Hz)	Internal loss factor (-)
10	0.0558	500	0.0519
12.5	0.0557	630	0.0508
16	0.0557	800	0.0495
20	0.0557	1000	0.0479
25	0.0556	1250	0.0459
31.5	0.0556	1600	0.0431
40	0.0555	2000	0.0399
50	0.0554	2500	0.0359
63	0.0553	3150	0.0324
80	0.0552	4000	0.0324
100	0.0550	5000	0.0324
125	0.0548	6300	0.0324
160	0.0546	8000	0.0324
200	0.0542	10000	0.0324
250	0.0538	12500	0.0324
315	0.0533	16000	0.0324
400	0.0527	20000	0.0324

5.2 Vibration measurement on coupled beams

5.2.1 Spatial average

The vibration transmission on frameworks of beams is evaluated by the energy level difference given by equation(3-14). In the FEM models it is possible to use rain-on-the-roof excitation but this is not feasible for laboratory measurements, hence the energy level difference is determined using point excitation for a number of different excitation positions by averaging the results. This approach can be used to approximate statistically independent excitation such as rain-on-the-roof [88].

For each excitation position on the source beam, the spatial average mean-square velocity is needed for the source and receiving beams for which the energy level difference specific to the excitation position is calculated using

$$D_{\mathrm{E},ij,s} = 10\lg \frac{m_i \frac{1}{M}\sum_{m=1}^{M} v_{i,m}{}^2}{m_j \frac{1}{N}\sum_{n=1}^{N} v_{j,n}{}^2} \tag{5-3}$$

where s is the s^{th} excitation position, M and N are the numbers of measuring points on source and receiving beams respectively, m_i and m_j are the mass of subsystems i and j.

The energy level difference, $D_{\mathrm{E,ij}}$, between the source and receiving subsystems is then calculated by taking the mean value of all energy level differences for all excitation positions using

$$D_{\mathrm{E},ij} = \frac{1}{T}\sum_{s=1}^{T} D_{\mathrm{E},ij,s} \tag{5-4}$$

The standard deviation s_{dB} of all T shaker positions can then be calculated by

$$s_{dB} = \sqrt{\frac{\sum_{s=1}^{T} D_{\mathrm{E},ij,s}^2 - \frac{1}{T}\left(\sum_{s=1}^{T} D_{\mathrm{E},ij,s}\right)^2}{T-1}} \tag{5-5}$$

According to [61] the spatial variation can be described with an estimate of 95% confidence interval calculated using the standard statistical formula

$$CI_{95\%} = \frac{s_{dB}}{\sqrt{T}} t_{0.975} \tag{5-6}$$

where $t_{0.975}$ is the value of student t-distribution for T-1 degrees of freedom and a probability of 0.975.

5.2.2 Experimental setup

The velocity levels on the beams are measured by the Polytec PDV100 laser vibrometer. A broadband excitation signal is applied over the frequency range from 10 Hz to 20000 Hz. A graphic equalizer (Ultragraph) is used to adjust the amplifications in each one-third octave band so that a relatively flat spectrum is obtained on the source beam. The experimental setup is shown in Figure 5.5.

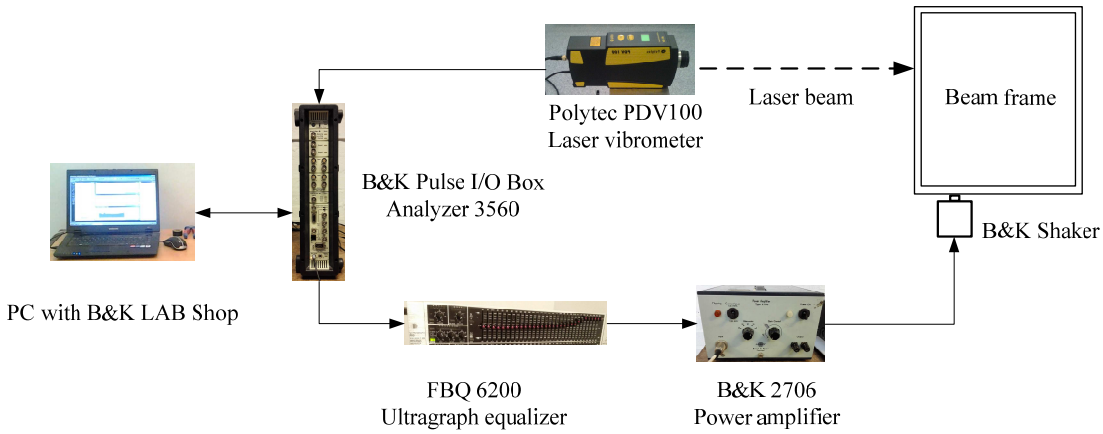

Figure 5.5 Experiment setup for vibration measurements on beam junctions.

Before the measurements, several beams with cross-section 0.02 m×0.01 m were cut from the same Perspex plate. These beams are connected using cyanoacrylate adhesive to form different beam junctions and a truss beam.

Each beam frame is suspended using elastic bands from several vertical supports. A spirit level is used to make sure that the beam frame lies in the horizontal plane. To ensure a well-focused laser spot on the transparent perspex beam, the positions to be measured on the beam are marked with dark blue pen. The laser vibrometer is placed on a platform for which the height can be adjusted.

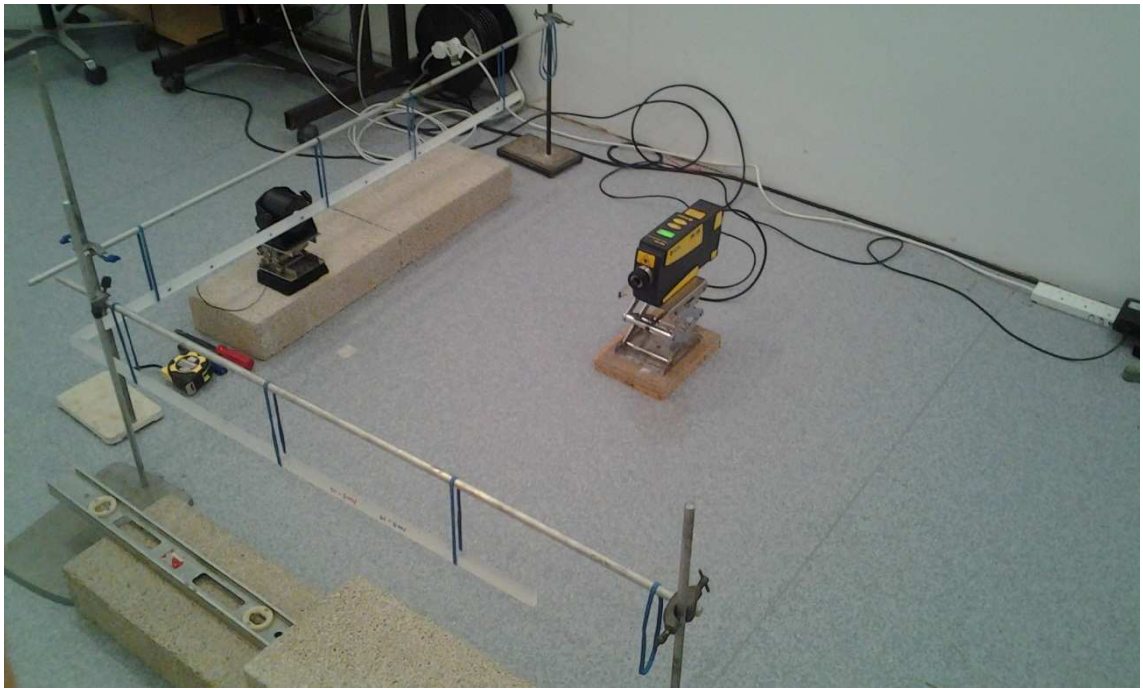

Figure 5.6 Experimental setup for measurement of Type A bending wave motion on L-junction (relevant to BL model).

As shown in Figure 5.6, Figure 5.9 and Figure 5.11 the source beam and the shaker are connected in the horizontal plane by a bolt which is screwed into the shaker. In this way the bending displacement occurs in the horizontal plane so that the BL model can be measured. If the source beam is excited in the vertical direction shown in Figure 5.7, out-of-plane bending wave motions and torsional wave motions can be generated in the beams. To measure the BT model, the laser vibrometer is placed on a tripod to measure the velocity on the upper surface of the beams shown in Figure 5.8, Figure 5.10 and Figure 5.12.

Background vibration was measured to ensure that the signal level is at least 10 dB above background at all points on all beams. The time average of each measuring points was carried out for 30 seconds.

Figure 5.7 Bolt connection between shaker and beam.

Figure 5.8 Experimental setup for measurement of Type B bending wave motion on L-junction (relevant to BT model).

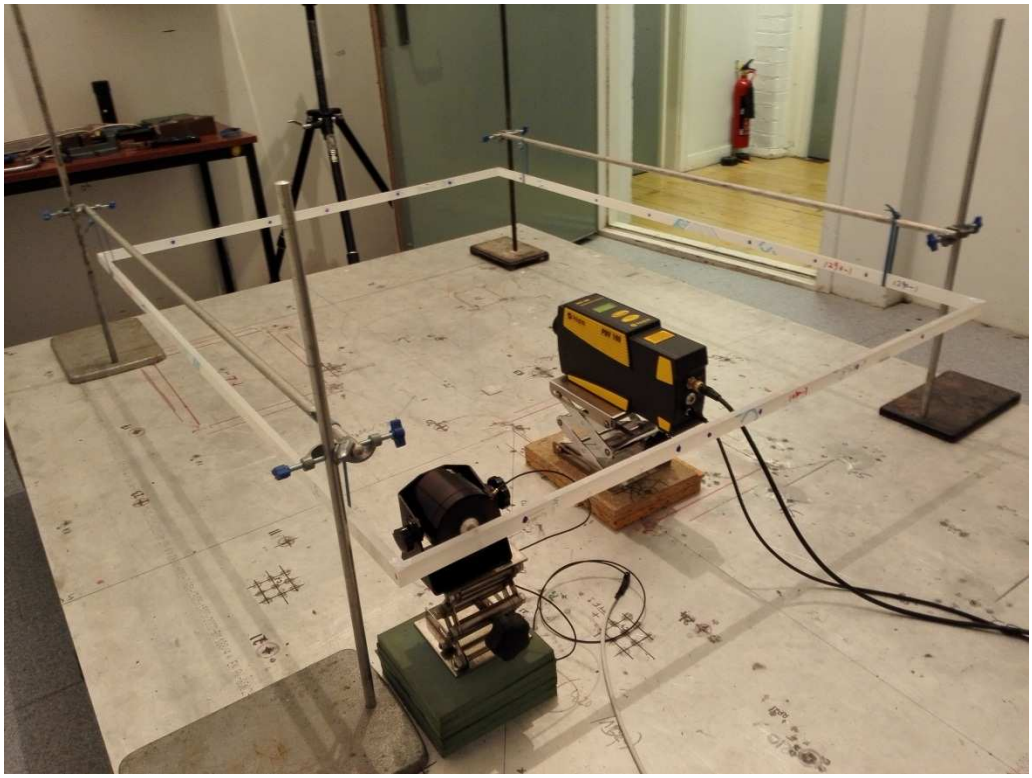

Figure 5.9 Experimental setup for measurement of Type A bending wave motion on rectangular beam frame (relevant to BL model).

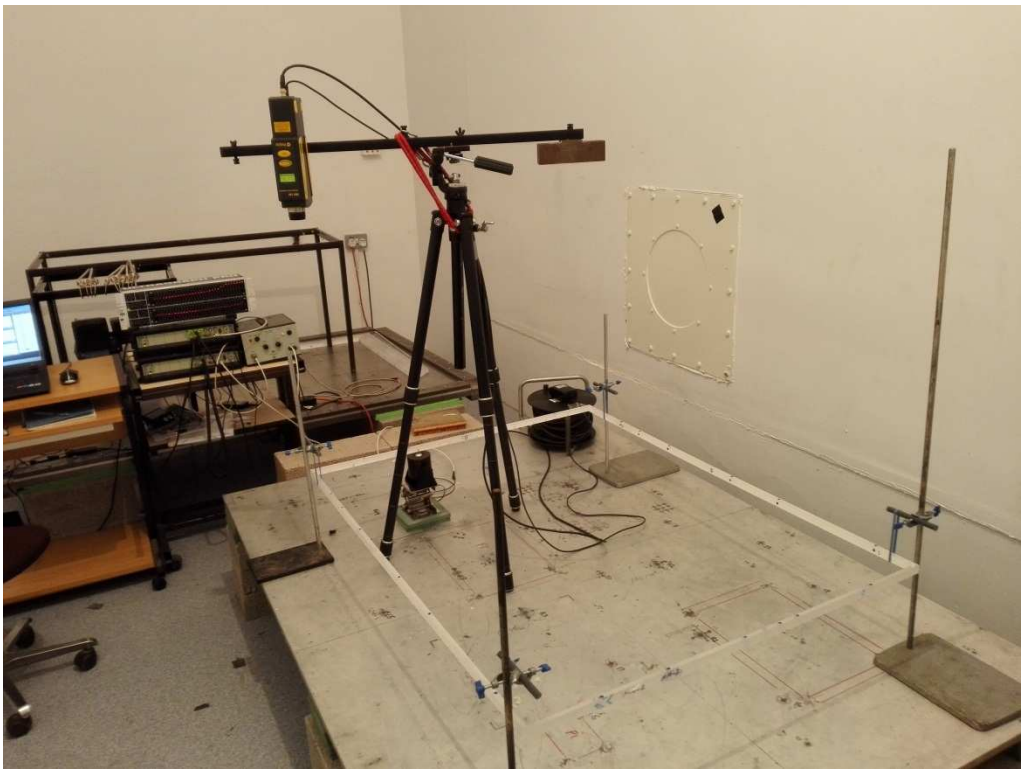

Figure 5.10 Experimental setup for measurement of Type B bending wave motion on rectangular beam frame (relevant to BT model).

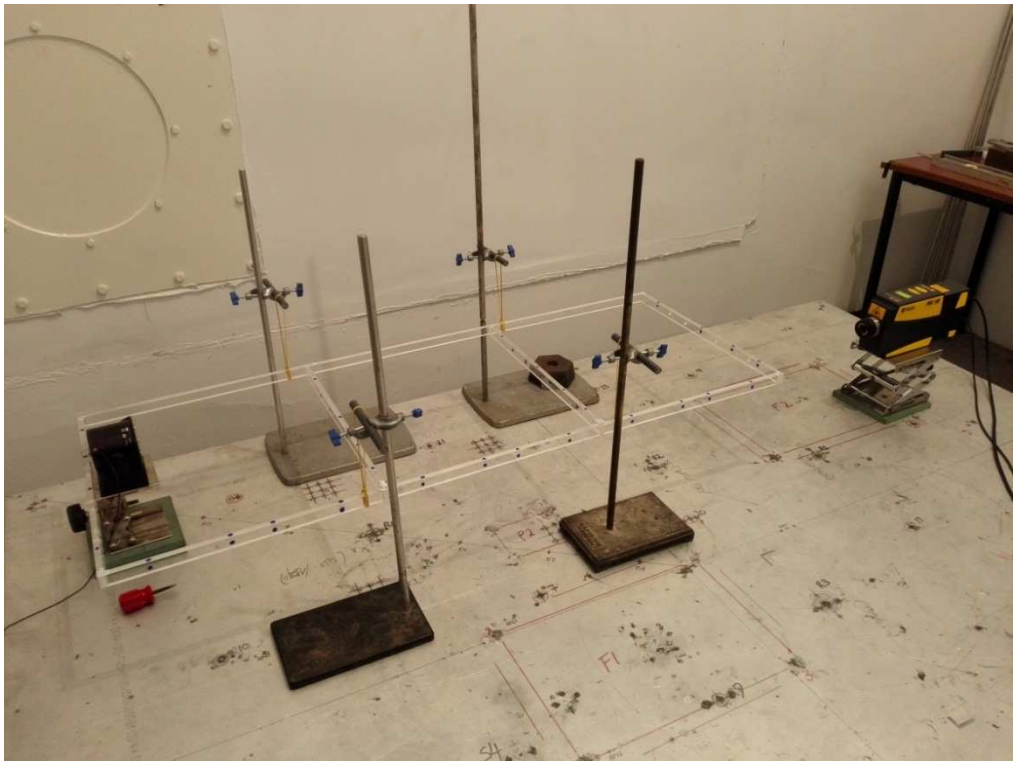

Figure 5.11 Experimental setup for measurement of Type A bending wave motion on three-bay truss beam (relevant to BL model).

Figure 5.12 Experimental setup for measurement of Type B bending wave motion on three-bay truss beam (relevant to BT model).

5.3 Beam constructions

Measurements were carried out on an L-junction, a square beam frame and a three-bay truss beam frame, each with excitation of Type A and B bending waves.

An L-junction was formed from a 1.3 m length (beam 1) and a 1.0 m length beam (beam 2) with a cross section of 0.02 m x 0.01 m. Beam lengths 1.3 m and 1.0 m were measured from the centre line of the joint. The rectangular beam frame was formed by joining together two L-junctions.

Ten excitation positions and six measurement positions were used for the L-junctions and the rectangular beam framework as indicated on Figure 5.13 (a) and (b). On the L-junction and the rectangular beam framework the measurement positions were chosen to be away from the nearest excitation position by at least 0.04 m and 0.05 m, respectively.

The three-bay truss beam was made from beams that were 0.40 m and 0.45 m in length with a cross-section of 0.02 m x 0.01 m. These beams are approximately half the length of the beams used in the rectangular beam framework in order to (a) reduce propagation losses, (b) increase the likelihood of indirect coupling and (c) allow measurable velocity levels on the furthest beam.

The three-bay truss beam is modelled as ten coupled beams in SEA and ASEA, but to minimise the number of glued joints it was built from six beams as indicated in Figure 5.13 (c). Four excitation positions and four measurement positions were used on each beam as shown in Figure 5.13 (c). Out-of-plane velocities were measured on all beams except beams 2, 5 and 8 which were not essential due to the structural symmetry.

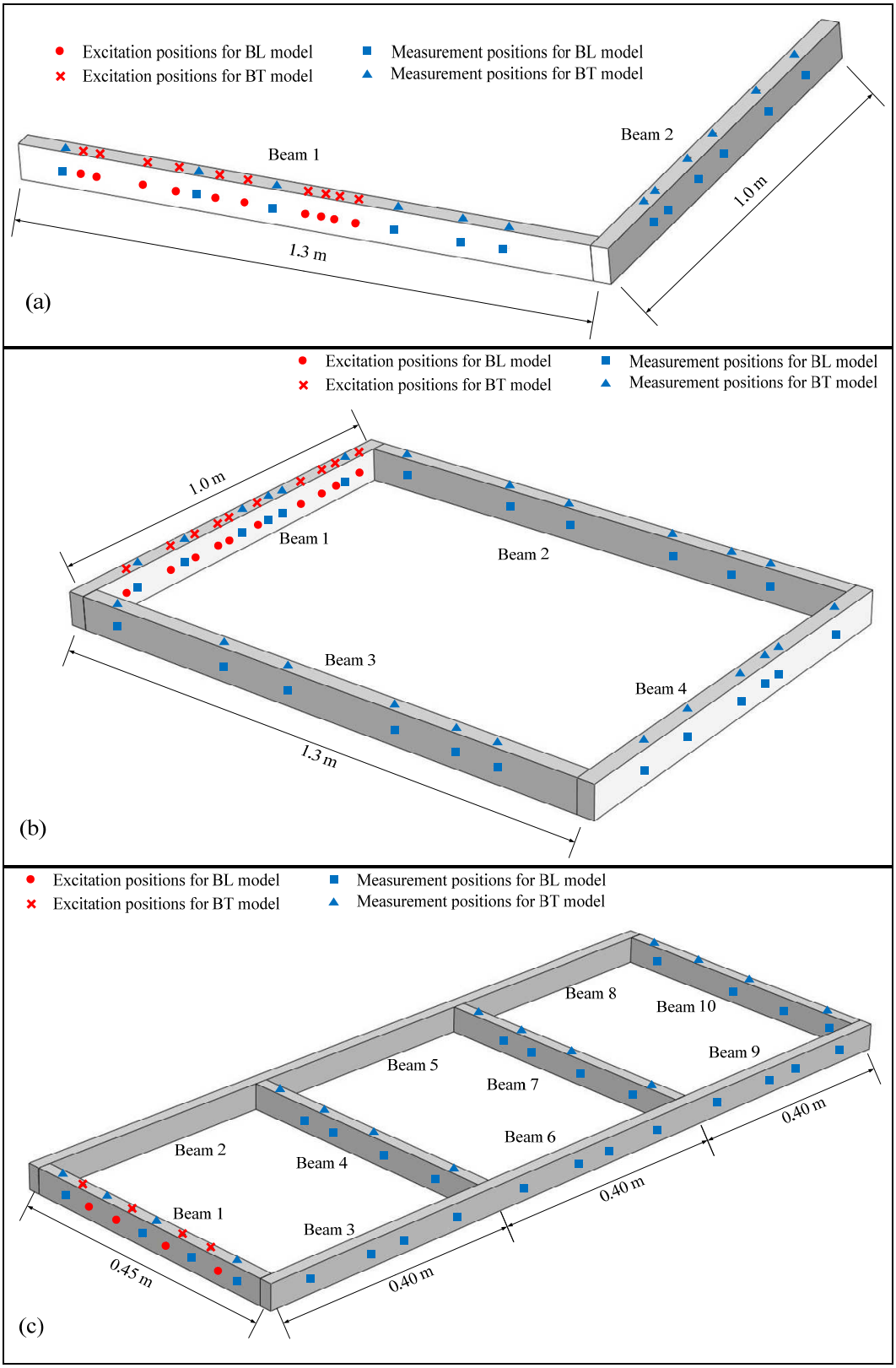

Figure 5.13 Sketch of the excitation and measurement positions on (a) L-junction, (b) rectangular beam frame, (c) three-bay truss beam frame.

5.4 Summary

In this chapter, measurements of the Perspex beam properties such as density, Young's modulus and internal loss factor are reported.

The Young's modulus and internal loss factor are determined using an impedance method. Based on five beam samples of which the resonance frequencies are distributed from 10 Hz to 20 kHz, the calculated internal loss factors show dependent on frequency. Thus the interpolated internal loss factors from the linear polynomial fitted values are given for each one-third octave band.

Measurements of vibration level differences were carried out on an L-junction, rectangular beam and three-bay truss. A laser vibrometer was used to measure out-of-plane velocity on the coupled beams in order to avoid errors due to mass loading at high frequencies. The experimental setup used for vibration measurements on coupled beams (BL and BT models) was described which will be used for the validation of the FEM, SEA and ASEA models in Chapter 6.

6. Comparison of measurements with FEM, SEA and ASEA

6.1 Introduction

This chapter compares the experimental results with predictions using FEM, SEA and ASEA. It begins with a summary of the dynamic properties of the beams in terms of the phase and group velocities, mode count and modal overlap factors in section 6.2. In later sections, comparisons of measurements, FEM, SEA and ASEA are carried out for BL and BT models of an L-junction, a rectangular beam frame and a three-bay truss beam.

In this chapter the modelling using FEM assumes that there is no uncertainty in the material properties of dimensions of beams that form the L-junction, rectangular beam frame and three-bay truss beam. This means that the three-bay truss beam represents a perfectly periodic structure.

This chapter considers both Euler-Bernoulli and Timoshenko theory for FEM, SEA and ASEA models in order to assess (a) the validity of FEM elements and (b) the proposal to implement thick beam theory in SEA and ASEA by accounting for the change in group velocity.

The material properties and geometric dimensions of the beams for measurements and analysis in this chapter are given in Table 5.2 and section 5.3.

6.2 Dynamic properties of the beams

6.2.1 Group and phase velocities

The analysis up to 20 kHz would be below the second spectrum cut-off frequency but which is sufficiently high to assess whether changing the group velocity in the coupling loss factor is sufficient for the SEA and ASEA models. For Type A bending waves (i.e. across the 10mm dimension), f_{co}=61441 Hz, and $f_{B(thin)}$=10537 Hz and for Type B bending waves (i.e. across the 20 mm thickness), f_{co}=30720 Hz and $f_{B(thin)}$=5268 Hz.

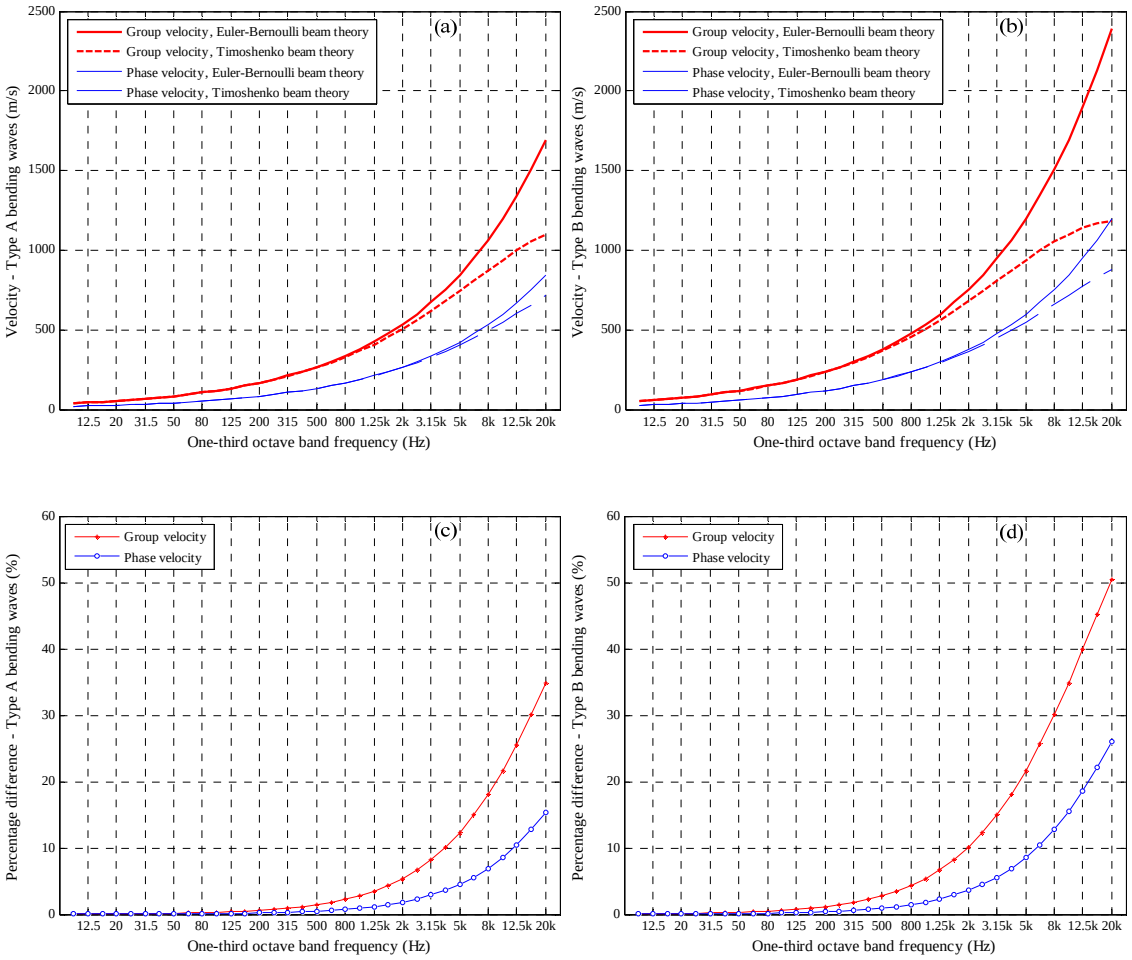

Figure 6.1 Group and phase velocities for (a) Type A bending waves and (b) Type B bending waves. Percentage difference in the group and phase velocities from Euler-Bernoulli and Timoshenko theories relative to Euler-Bernoulli theory for (c) Type A bending waves and (d) Type B bending waves.

Figure 6.1 (a) and (b) allows comparison of the group and phase velocities calculated with Euler-Bernoulli and Timoshenko beam theory. With increasing frequency, the effects of rotatory inertia and shear deformation become important. This leads to the phase and group velocities for Timoshenko theory being lower than with Euler-Bernoulli theory and tending towards a plateau rather than continually increasing with frequency. Figure 6.1 (c) and (d) shows that the percentage differences between Timoshenko and Euler-Bernoulli theory become larger for group velocity than phase velocity. Hence although the thin beam limit is based on a 10% difference in phase velocity, the corresponding percentage difference in group velocity is a factor of ≈2.5 times higher. It is the latter which is relevant to the calculation of the coupling loss

factor and will be assessed through comparison on measurements, FEM, SEA and ASEA.

6.2.2 Mode count and modal overlap

The local modes counts for 1.3 m and 1.0 m perspex beam in measurements are shown in Figure 6.2 assuming both ends of the beam are clamped for bending modes, longitudinal and torsional modes. This idealised boundary condition provides a reasonable estimate for the rectangular beam frame but conservative estimates for the L-junctions where each beam has one free boundary.

Below 315 Hz there is no more than one bending mode in each one-third octave band for Type A and Type B bending modes and no longitudinal or torsional modes. Of relevance to the BT model is that (a) between 315 Hz and 4 kHz there are no more than two torsional modes in each band and between one and three Type B bending modes and (b) between 5 kHz and 20 kHz there are between two and five Type B bending modes and between three and thirteen torsional modes in each band. Of relevance to the BL model is that (a) between 800 Hz and 4 kHz there is no more than one longitudinal mode in each band and between one and three Type A bending modes and (b) between 4 kHz and 20 kHz there are between two and seven Type A bending modes and between one and six longitudinal modes in each band. Hence it is only above 4 kHz that all wave types have at least two modes in each band and it is at this frequency that the transition from Euler-Bernoulli to Timoshenko theory is expected to be significant.

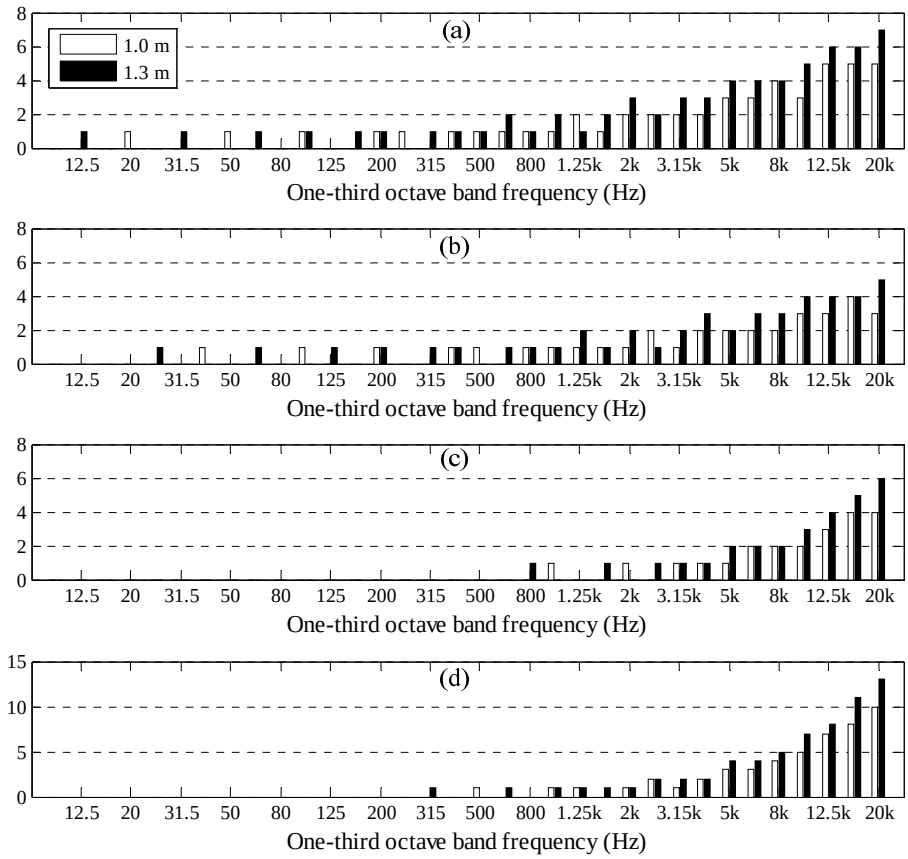

Figure 6.2 Mode counts for 1.3 m and 1.0 m beams. (a) Type A bending waves (b) Type B bending waves (c) Longitudinal waves (d) Torsional waves.

The modal overlap factors in Figure 6.3 are shown using lower and upper values that are determined from the two different beam lengths (1.0 m and 1.3 m) in the isolated L-junction and the rectangular beam frame. These are calculated using the statistical modal density, $n(f)$, instead of the mode count to give smoother curves. For bending and longitudinal waves the modal overlap factor does not begin to approach unit until 20 kHz although for torsional waves it reaches unit above 10 kHz.

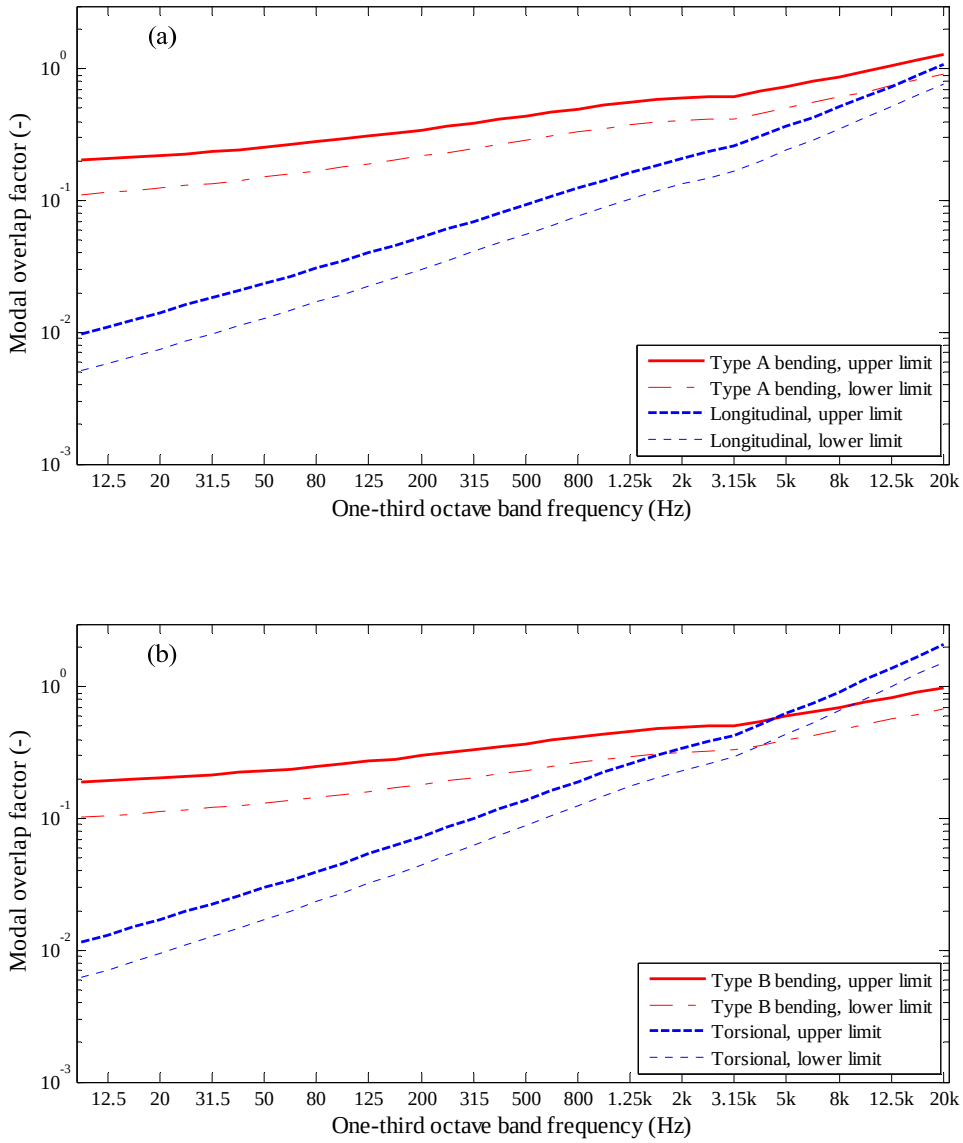

Figure 6.3 Modal overlap factors for 1.3 m and 1.0 m beams with (a) BL model and (b) BT model.

Local mode counts of the isolated beams (length 0.45 m and 0.4 m) are shown in Figure 6.4 and are calculated by assuming clamped boundaries at each end. The implication of using shorter beams than the former group of beams is that the lowest mode occurs in the 125 Hz octave band. In this chapter it is concluded that when consecutive frequency bands have at least one local mode on the source or receiving beams the modal fluctuations can be significantly reduced, and this facilitates comparison with SEA and ASEA. Hence using octave bands for the three-bay truss will satisfy this requirement.

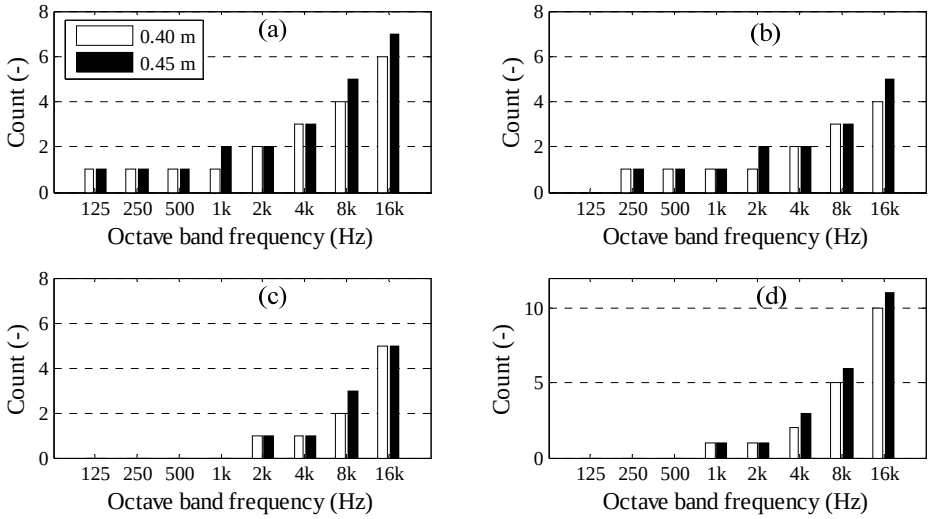

Figure 6.4 Mode counts for 0.45 m and 0.4 m beams. (a) Type A bending waves (b) Type B bending waves (c) Longitudinal waves (d) Torsional waves.

The modal overlap factors for the 0.45 m and 0.40 m beams are shown in Figure 6.5. These have been calculated using the statistical modal density in order to give smooth curves, and use the total loss factors that are determined from the two different lengths (0.45 m and 0.40 m) and two different cases in the three-bay truss. For Type A bending, Type B bending, longitudinal and torsional motions the modal overlap factors are all smaller than unit within the considered octave bands from 125 Hz to 16 kHz.

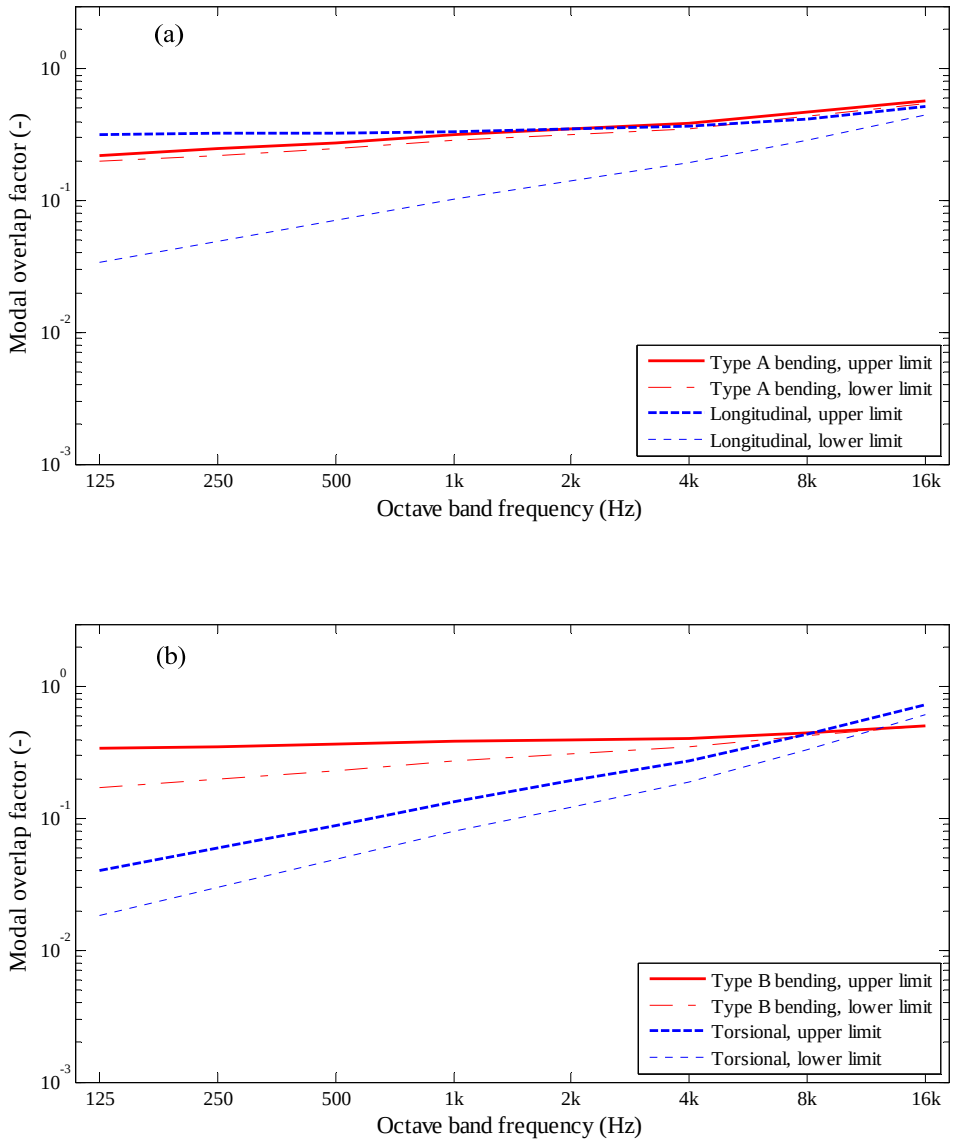

Figure 6.5 Modal overlap factors for 0.45m and 0.40 m beams with (a) BL model and (b) BT model.

6.3 BL model on L junction

Figure 6.6 shows results for the BL model of the L-junction with excitation of Type A bending waves on beam 1. For E_{B1}/E_{B2} the comparison of seven nominally identical L-junctions in Figure 6.6 (a) confirms that the bonding of the junctions and the test procedure is repeatable with 1.8 dB over the entire frequency range.

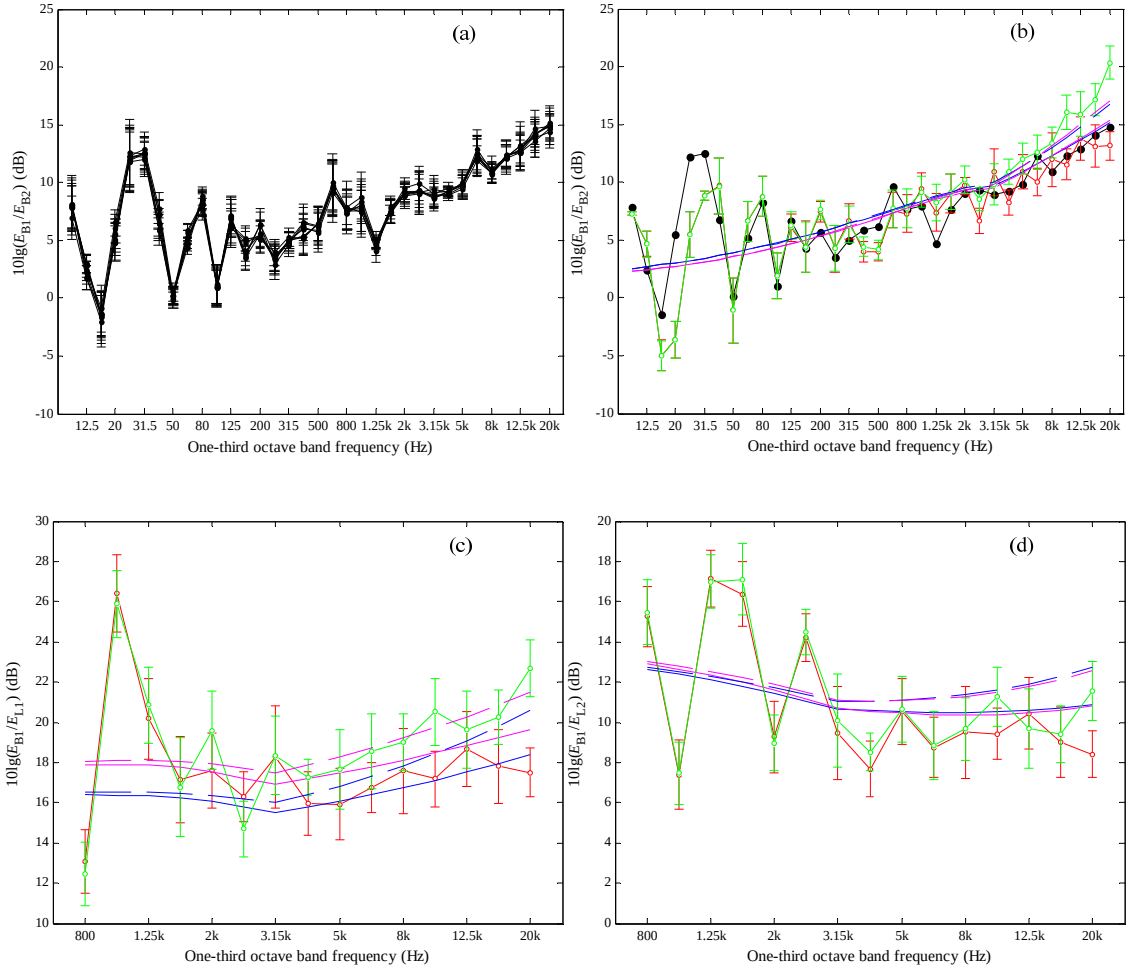

Figure 6.6 L-junction - BL model with bending wave excitation on subsystem B1: (a) comparison of measured data on seven nominally identical L-junctions; (b) comparison of measurements, FEM, SEA and ASEA; (c) and (d) comparison of FEM, SEA and ASEA. —●—, Measurement; —○—, FEM (Euler-Bernoulli elements); —○—, FEM (Timoshenko elements); ——, SEA (Euler-Bernoulli group velocity); – – – –, SEA (Timoshenko group velocity); ——, ASEA (Euler-Bernoulli group velocity); – – – –, ASEA (Timoshenko group velocity). Results from measurements and FEM are shown with 95% confidence intervals.

Figure 6.6 (b) compares measured and predicted E_{B1}/E_{B2}. Below 315Hz there are only bending modes and there are large modal fluctuations in the energy level difference. This is attributed to the fact that (a) each one-third octave band typically contains only one local bending mode which is attributed to either the source or the receiving beam and (b) modal overlap factors that are typically <0.2 (see Figure 6.3). Hence whilst there is reasonable agreement (≤ 6.5 dB) between measurements and FEM (nominally identical results for Euler-Bernoulli and Timoshenko elements), SEA and ASEA could

only give a reasonable estimate of the response if the frequency bands were much wider than one-third octave bands. Between 315 Hz and 2 kHz the mean values from the FEM models using Euler-Bernoulli and Timoshenko elements are within 1dB of each other. In this frequency range, measurements show reasonable agreement (≤ 2.7 dB) with FEM, SEA and ASEA models. Between 2 kHz and 12.5 kHz, the mean values from the FEM models using Euler-Bernoulli and Timoshenko elements become larger than 1dB but the 95% confidence intervals tend to overlap. At and above the 12.5 kHz band, the difference between Timoshenko and Euler-Bernoulli group velocities is ≥26%; meanwhile, the FEM models using Euler-Bernoulli and Timoshenko elements differ by 3.9 dB to 7.2 dB and the confidence intervals no longer overlap. Between 12.5 kHz and 20 kHz the two FEM models differ by 2.1dB to 7.2dB, the two SEA models by 1.1dB to 1.6dB and the two ASEA models by 1.2dB to 1.8dB; hence only FEM indicates significant differences. Between 12.5 kHz and 20 kHz, FEM using Euler-Bernoulli elements shows closest agreement with SEA and ASEA using Euler-Bernoulli group velocity, and FEM using Timoshenko elements shows closest agreement with SEA and ASEA using Timoshenko group velocity. However, the mean values for measurements show closer agreement with FEM, SEA and ASEA using Euler-Bernoulli elements, rather than Timoshenko elements which would have been expected. This can be attributed to the fact that the 95% confidence limits for the measurements are ≈2dB. With <2dB difference between the predicted values for Euler-Bernoulli and Timoshenko theories it is not possible to draw strong conclusions on the validity of Timoshenko theory from the measured data on this L-junction.

Figure 6.6 (c) and (d) allow an assessment of the conversion from bending waves on the source subsystem to longitudinal waves on a receiving subsystem. Between 10 Hz and 630 Hz there is in-plane motion but this is due to bending wave motion because there are no local longitudinal modes in this frequency range. Hence results are only shown from 800 Hz to 20 kHz. Above 2.5 kHz there is at least one longitudinal mode in consecutive frequency bands and the fluctuations are significantly reduced in comparison to those between 800 Hz and 2.5 kHz. Between 4 kHz and 20 kHz there are (a) at least two bending and two longitudinal modes in each band and (b) the modal overlap factors increase from 0.4 to 1 for bending modes, and from 0.1 to 0.9 for longitudinal modes. Compared to lower frequencies the FEM curves in this frequency range are smooth which facilitates comparison with SEA and ASEA. For E_{B1}/E_{L1} on

Figure 6.6 (c), the 95% confidence intervals for FEM using Euler-Bernoulli elements overlap the SEA and ASEA predictions using Euler-Bernoulli group velocity. However, the average values for FEM using Timoshenko elements show much closer agreement with ASEA using Timoshenko group velocity. For E_{B1}/E_{L2} on Figure 6.6 (d) the confidence intervals from FEM using Euler-Bernoulli and Timoshenko elements tend to overlap each other up to 16 kHz. These confidence intervals also overlap SEA and ASEA predictions using Euler-Bernoulli or Timoshenko group velocities; hence as with the bending energy level differences it is not possible to conclude which group velocity is more appropriate on this L-junction.

Figure 6.7 allows an assessment of conversion from longitudinal to bending waves with longitudinal waves excited on the source subsystem of the L-junction. In contrast to Figure 6.6 with bending wave excitation, the 95% confidence intervals for FEM data with Euler-Bernoulli and Timoshenko elements overlap; hence there is no significant difference between them. For E_{L1}/E_{L2} on Figure 6.7 (c), the fluctuations are significantly reduced above 2.5 kHz where both beams have at least one longitudinal mode in consecutive frequency bands.

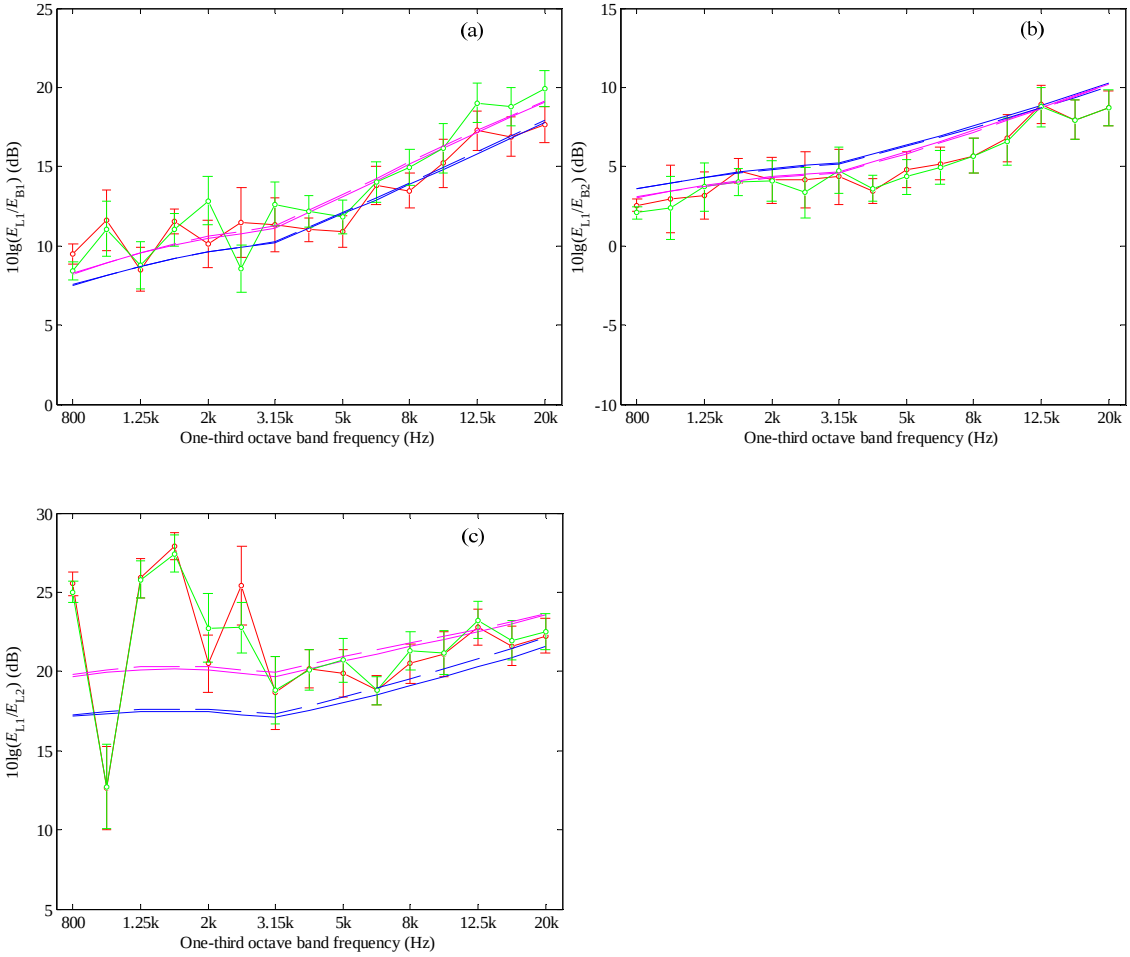

Figure 6.7 L-junction - BL model with longitudinal wave excitation on subsystem L1: comparison of FEM, SEA and ASEA. —○—, FEM (Euler-Bernoulli elements); —○—, FEM (Timoshenko elements); ——, SEA (Euler-Bernoulli group velocity); – – – –, SEA (Timoshenko group velocity); ——, ASEA (Euler-Bernoulli group velocity); – – – –, ASEA (Timoshenko group velocity). Results from FEM are shown with 95% confidence intervals.

6.4 BL model on rectangular beam frame

Figure 6.8 shows results for the BL model of the rectangular beam frame with excitation of Type A bending waves on beam 1.

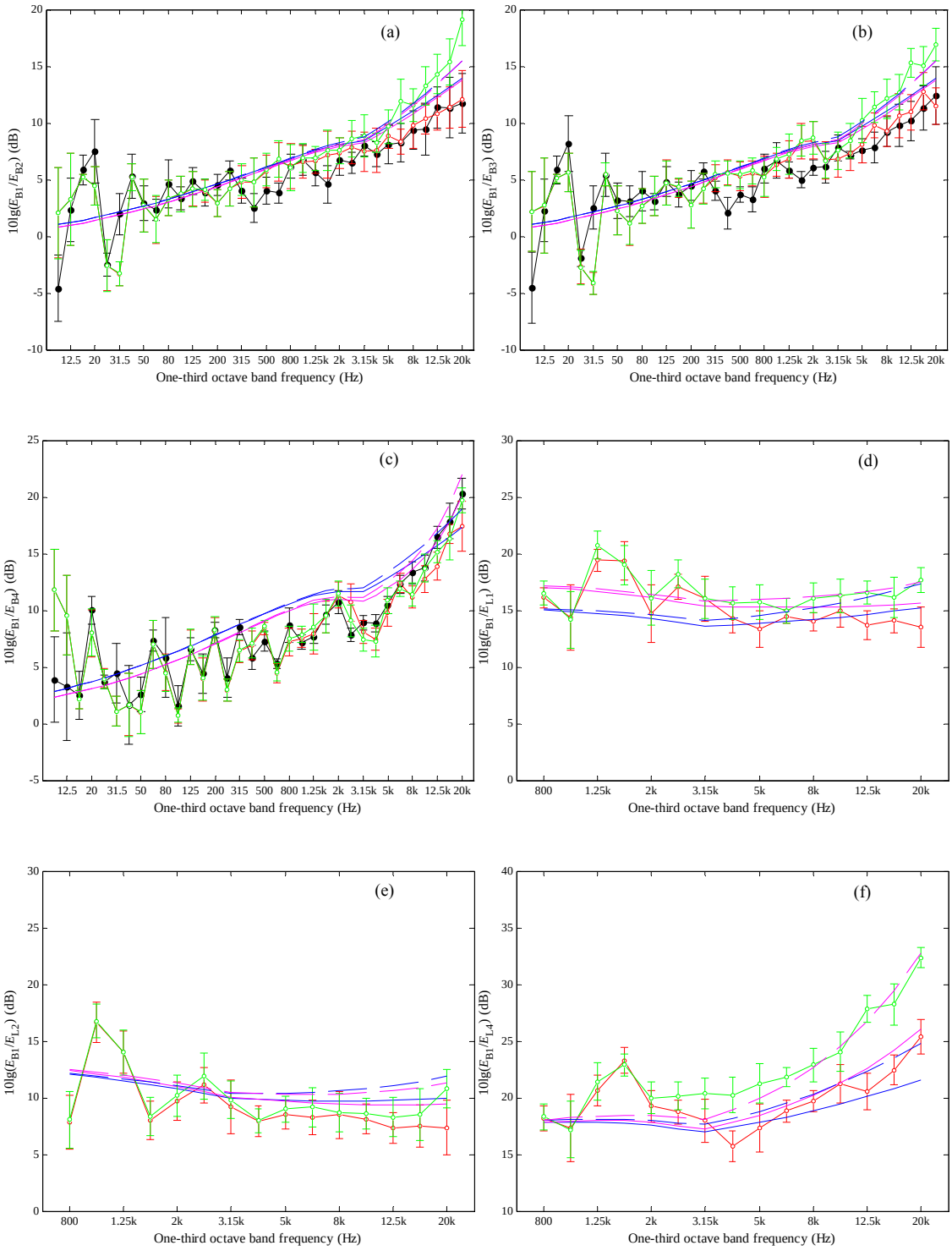

Figure 6.8 Rectangular beam frame - BL model with bending wave excitation on subsystem B1: (a), (b) and (c) comparison of measurements, FEM, SEA and ASEA; (d), (e) and (f) comparison of FEM, SEA and ASEA. —●—, Measurement; —○—, FEM (Euler-Bernoulli elements); —○—, FEM (Timoshenko elements); ——, SEA (Euler-Bernoulli group velocity); – – – –, SEA (Timoshenko group velocity); ——, ASEA

(Euler-Bernoulli group velocity); _ _ _ _, ASEA (Timoshenko group velocity). Results from measurements and FEM are shown with 95% confidence intervals.

As with the L-junction, the main difference between the Euler-Bernoulli and Timoshenko models occurs above 2 kHz for which the two FEM models differ by up to 7 dB whereas the two SEA models only differ by up to 1.6 dB and the two ASEA models by up to 1.7 dB. On Figure 6.8 (a) and (b), measurements above 2 kHz show closest agreement with FEM, SEA and ASEA using Euler-Bernoulli theory for transmission to beams 2 and 3 (both of which are directly connected to beam 1). However, for transmission to beam 4 (which is not physically connected to the source beam) the results in Figure 6.8 (c) indicate that FEM with either Euler-Bernoulli or Timoshenko elements agree closely with measurements. For transmission to beams 2 and 3, SEA and ASEA models are within 0.2 dB of each other. For transmission to beam 4, ASEA is ≈0.9 dB lower than SEA. Up to 10 kHz, ASEA is lower than SEA which indicates the presence of tunnelling mechanisms, but this indirect transmission appears to be underestimated because the level differences from measured and FEM data are lower than ASEA. Above 10 kHz, ASEA indicates that there is no tunnelling but there are significant propagation losses. These become more pronounced when using Timoshenko instead of Euler-Bernoulli theory due to the lower group speed which increases the power lost as the wave propagates across each beam.

Figure 6.8 (d), (e) and (f) assesses the conversion from bending waves on the source subsystem to longitudinal waves on a receiving subsystem. For E_{B1}/E_{L1} on Figure 6.8 (d), FEM using Euler-Bernoulli elements shows closest agreement with SEA using Euler-Bernoulli group velocity and FEM using Timoshenko elements shows closest agreement with ASEA using Timoshenko group velocity. For E_{B1}/E_{L2} on Figure 6.8 (e) the confidence intervals from FEM using Euler-Bernoulli and Timoshenko elements overlap up to 20 kHz and both show closest agreement with SEA or ASEA using Euler-Bernoulli group velocity. Above 2 kHz for E_{B1}/E_{L4} on Figure 6.8 (f) there is clear evidence that FEM with Euler-Bernoulli elements shows closest agreement with ASEA using Euler-Bernoulli group velocity, and FEM with Timoshenko elements shows closest agreement with ASEA using Timoshenko group velocity. At 20 kHz the difference between Euler-Bernoulli and Timoshenko models is ≈7dB for both FEM and ASEA. The fact that ASEA shows close agreement with FEM using Timoshenko

elements and that the energy level differences with ASEA are higher than SEA confirms the presence of significant propagation losses because this mechanism is included in ASEA, but not in SEA. It also confirms the assumption in ASEA that phase effects can be ignored.

6.5 BT model on L junction

Figure 6.9 shows results for the BT model of the L-junction with excitation of Type B bending waves on beam 1.

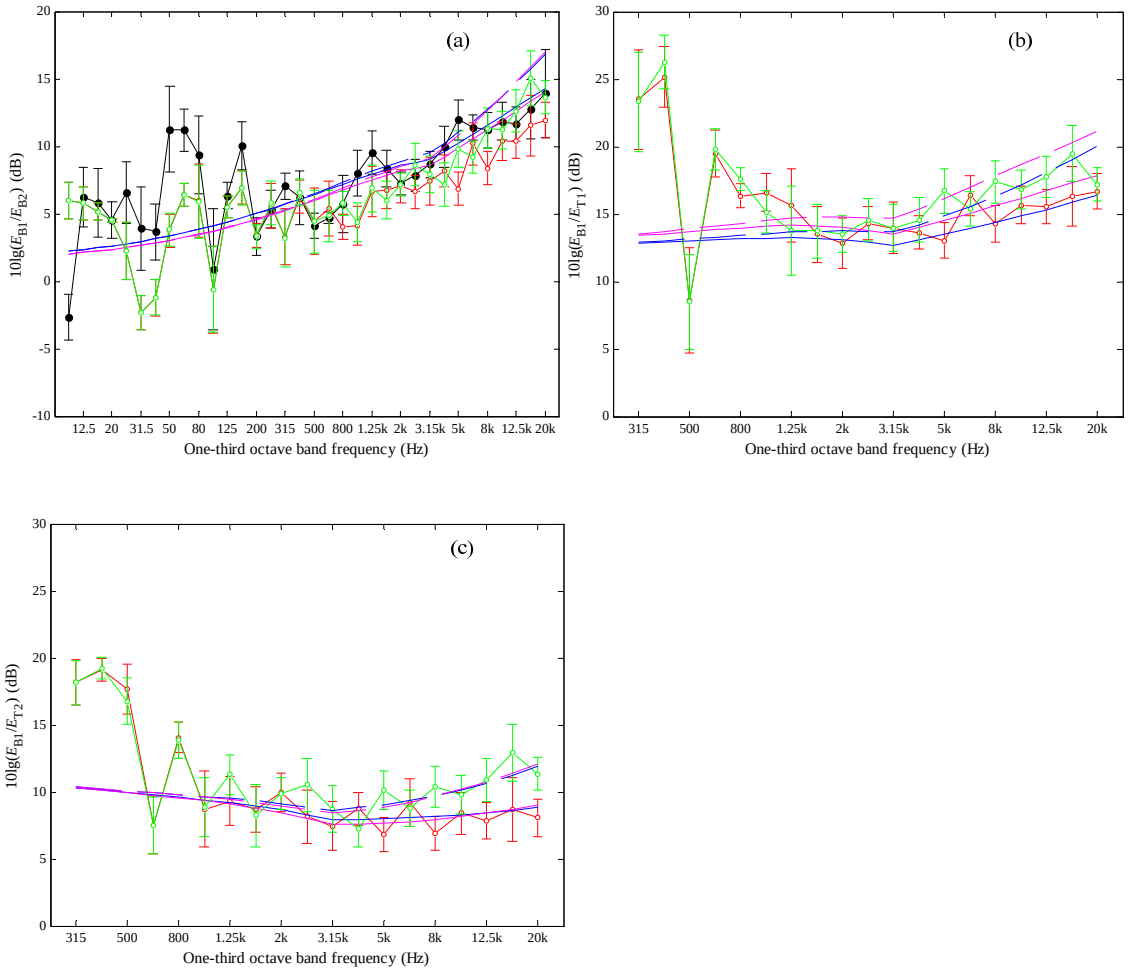

Figure 6.9 L-junction - BT model with bending wave excitation on subsystem B1: (a) comparison of measurements, FEM, SEA and ASEA; (b), (c) and (d) comparison of FEM, SEA and ASEA. ——●——, Measurement; ——○——, FEM (Euler-Bernoulli elements); ——○——, FEM (Timoshenko elements); ——, SEA (Euler-Bernoulli group velocity); - - - -, SEA (Timoshenko group velocity); ——, ASEA (Euler-Bernoulli group

velocity); _ _ _ _, ASEA (Timoshenko group velocity). Results from FEM are shown with 95% confidence intervals.

For E_{B1}/E_{B2}, Figure 6.9 (a) shows that below 315 Hz there are large fluctuations which are due to (a) only one local bending mode (no torsional modes) in either the source or the receiving beam in each frequency band and (b) modal overlap factors that are typically <0.2 (see Figure 6.3). These fluctuations reduce significantly as soon as consecutive frequency bands contain at least one local bending mode. As with the BL model there is reasonable agreement between measurements and FEM (Euler-Bernoulli and Timoshenko elements). Above 315 Hz there are both bending and torsional modes but there are large fluctuations in the first few bands which reduce significantly as soon as consecutive frequency bands contain at least one local torsional mode. Between 315 Hz and 5 kHz, the confidence limits of both measurements and FEM (Euler-Bernoulli and Timoshenko elements) tend to overlap both the SEA and ASEA predictions. At and above the 6.3 kHz band, the difference between Timoshenko and Euler-Bernoulli group velocities is ≥26%. For 6.3 kHz to 20 kHz it is found that the two FEM models differ by 1 dB to 3.5 dB, the two SEA models by 1dB to 2.6 dB and the two ASEA models by 1.2 dB to 2.9 dB. Up to 20 kHz there is overlap between the 95% confidence intervals from measurements and both FEM models such that both Euler-Bernoulli and Timoshenko elements can be considered as appropriate.

Figure 6.9 (b) and (c) allow an assessment of the conversion from bending waves on the source subsystem to torsional waves on a receiving subsystem. There are no local torsional modes between 10Hz and 250 Hz; however there is in-plane motion due to the bending wave motion. For this reason, results for E_{B1}/E_{T1} and E_{B1}/E_{T2} are only shown from 315 Hz to 20 kHz. Between 6.3kHz and 20 kHz there are (a) at least two bending and two torsional modes in each band and (b) the modal overlap factors increase from 0.4 to 0.7 for bending modes, and from 0.5 to 1.4 for torsional modes. In this frequency range the FEM results are relatively smooth. Above 6.3 kHz for E_{B1}/E_{T1} on Figure 6.9 (b) and E_{B1}/E_{T2} on Figure 6.9 (c), FEM using Euler-Bernoulli elements shows closest agreement with SEA or ASEA using Euler-Bernoulli group velocity, and FEM using Timoshenko elements shows closest agreement with SEA or ASEA using Timoshenko group velocity.

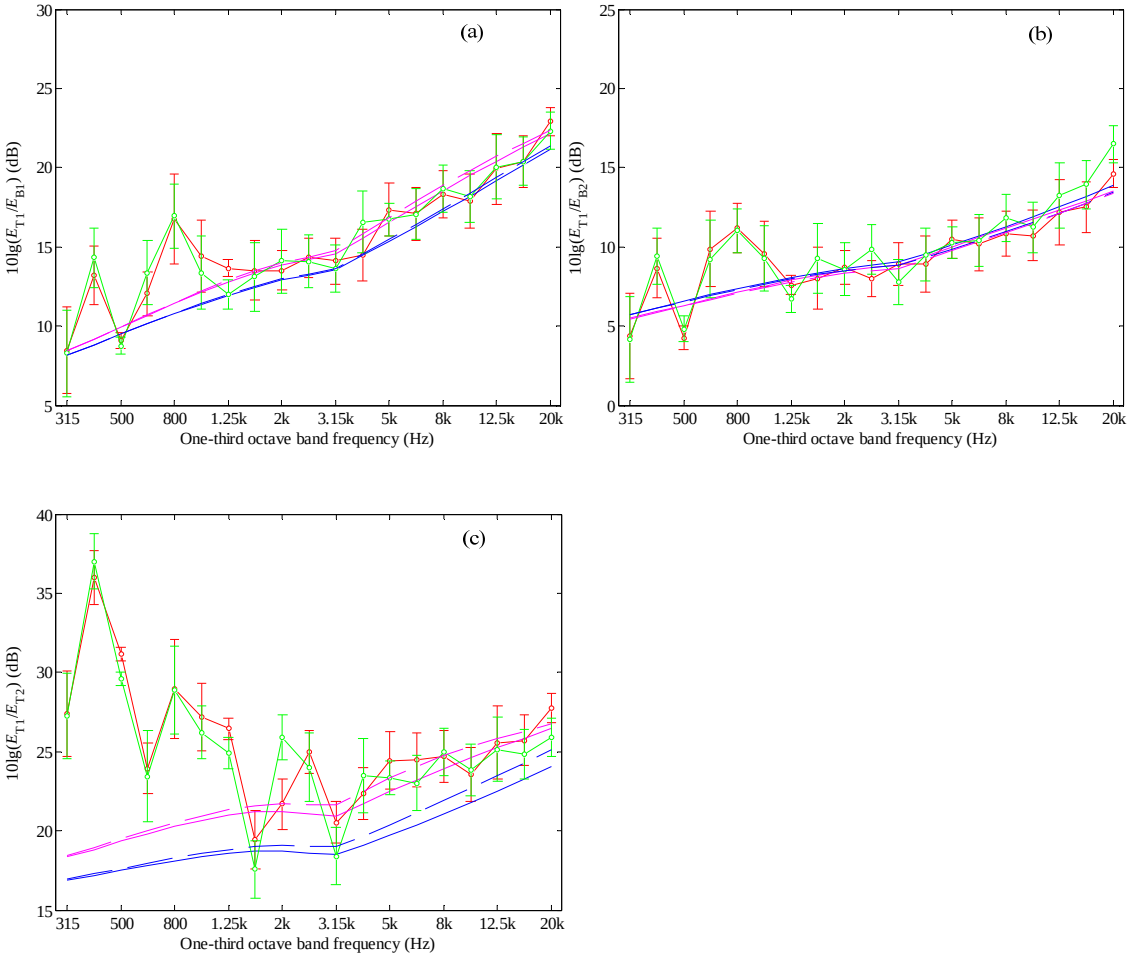

Figure 6.10 L-junction - BT model with torsional wave excitation on subsystem T1: comparison of FEM, SEA and ASEA. —○—, FEM (Euler-Bernoulli elements); —○—, FEM (Timoshenko elements); ——, SEA (Euler-Bernoulli group velocity); – – – –, SEA (Timoshenko group velocity); ——, ASEA (Euler-Bernoulli group velocity); – – – –, ASEA (Timoshenko group velocity). Results from measurements are shown with 95% confidence intervals.

Figure 6.10 allows an assessment of conversion from torsional to bending waves with torsional waves excited on the source subsystem of the L-junction. As with longitudinal wave excitation, FEM results with Euler-Bernoulli or Timoshenko elements are similar with overlapping 95% confidence intervals. For E_{T1}/E_{T2}, the mean FEM data follow ASEA rather than SEA above 3.15 kHz.

6.6 BT model on rectangular beam frame

Figure 6.11 shows the results for the BT model of the rectangular beam frame with excitation of Type B bending waves on beam 1.

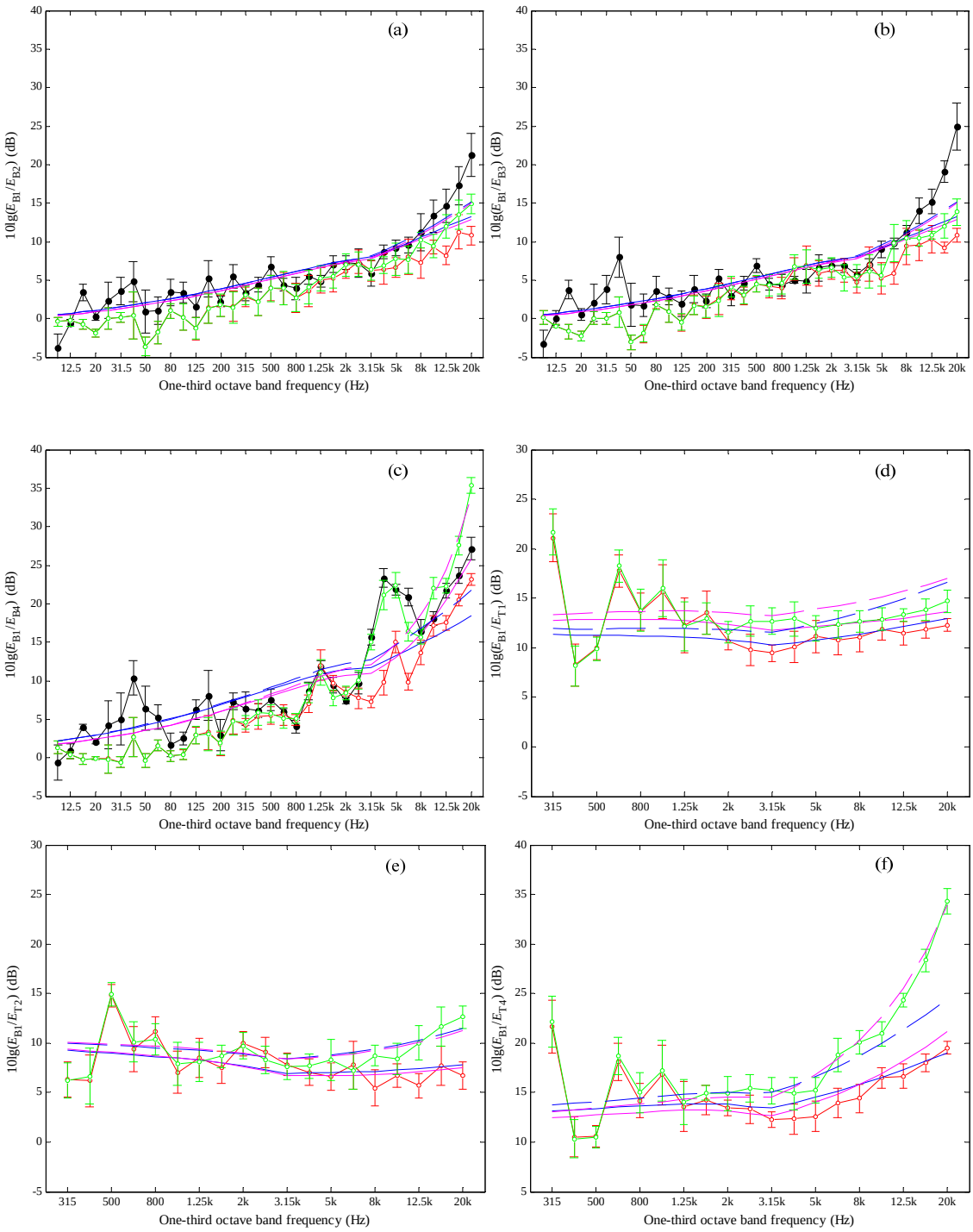

Figure 6.11 Rectangular beam frame - BT model with bending wave excitation on subsystem B1: (a), (b) and (c) comparison of measurements, FEM, SEA and ASEA; (d), (e) and (f) comparison of FEM, SEA and ASEA. —●—, Measurement; —○—, FEM

(Euler-Bernoulli elements); —○—, FEM (Timoshenko elements); ——, SEA (Euler-Bernoulli group velocity); – – – –, SEA (Timoshenko group velocity); ——, ASEA (Euler-Bernoulli group velocity); – – – –, ASEA (Timoshenko group velocity). Results from measurements and FEM are shown with 95% confidence intervals.

On Figure 6.11(a), (b) and (c) the confidence intervals for measurements and FEM (Euler-Bernoulli or Timoshenko elements) tend to overlap below 315 Hz. For E_{B1}/E_{B2} and E_{B1}/E_{B3} between 315 Hz and 5 kHz, FEM using Euler-Bernoulli and Timoshenko elements are nominally identical, and the difference compared with measurements is between 0.1 dB and 2.9 dB. For E_{B1}/E_{B4} between 315 Hz and 2 kHz, FEM using Euler-Bernoulli and Timoshenko elements are similar, and the difference compared with measurements is between 0.2 dB and 2.2 dB. However, for E_{B1}/E_{B4} above 2 kHz it is clear that there is closest agreement with FEM using Timoshenko elements; this is evident near the peak in the energy level difference at 4 kHz. In general, the measurements above 2 kHz follow the trends indicated by FEM using Timoshenko elements. Below 2 kHz, comparison of FEM with SEA and ASEA indicates that for E_{B1}/E_{B2}, E_{B1}/E_{B3} and E_{B1}/E_{B4}, SEA and ASEA tend to overestimate the energy level difference. Above 2 kHz, FEM using Euler-Bernoulli elements follows the general trends of SEA or ASEA using Euler-Bernoulli group velocity. In comparison, FEM using Timoshenko elements shows close agreement with SEA or ASEA using Timoshenko group velocity. For E_{B1}/E_{B4} above 6.3 kHz, FEM using Timoshenko elements closely follows ASEA using Timoshenko group velocity. This agreement, and the fact that ASEA has significantly higher energy level differences than SEA, indicates that ASEA correctly incorporates these high propagation losses.

Figure 6.11 (d), (e) and (f) allow an assessment of the conversion from bending waves on the source subsystem to torsional waves on a receiving subsystem. Above 2 kHz there are at least two bending and two torsional modes in each frequency band (modal overlap factor is at least 0.2 for both bending and two torsional waves) and the FEM curves become relatively smooth. For E_{B1}/E_{T2} and E_{B1}/E_{T4} between 2 kHz and 20 kHz, FEM using Euler-Bernoulli elements follows the general trends of SEA or ASEA using Euler-Bernoulli group velocity, and FEM using Timoshenko elements closely follows ASEA using Timoshenko group velocity. Again, this confirms the assumption in ASEA that phase effects can be ignored. Referring back section 0, the transmission coefficients

from bending waves on one beam to torsional waves on the other beam are highest above 6.3 kHz. Hence the combination of high propagation losses with Timoshenko group velocity and wave conversion at each junction results in high energy level differences (e.g. 34 dB for E_{B1}/E_{B4} at 20 kHz predicted using ASEA and FEM using Timoshenko elements).

6.7 BL model on the truss

6.7.1 Bending wave excitation

Figure 6.12 shows the results for the BL model of the three-bay truss with excitation of Type A bending waves on beam 1.

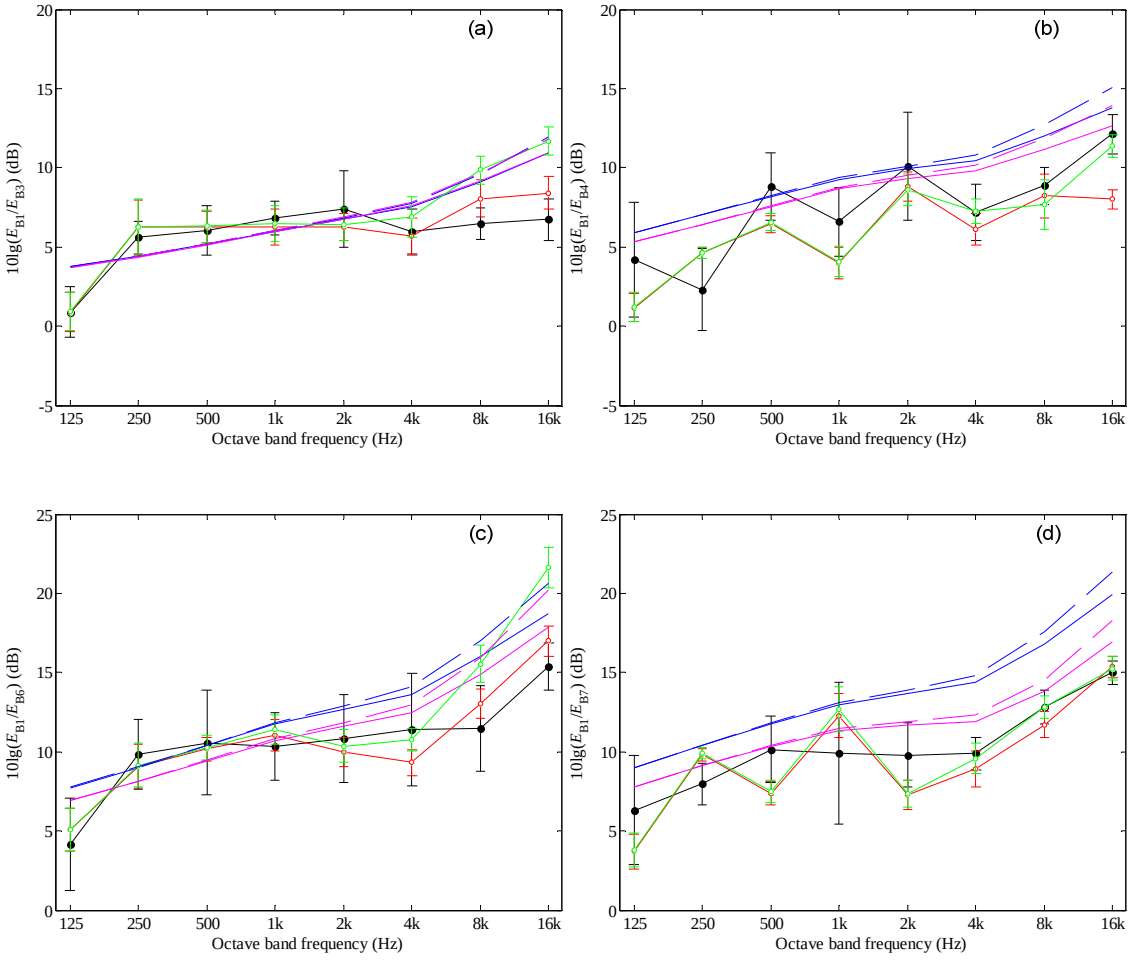

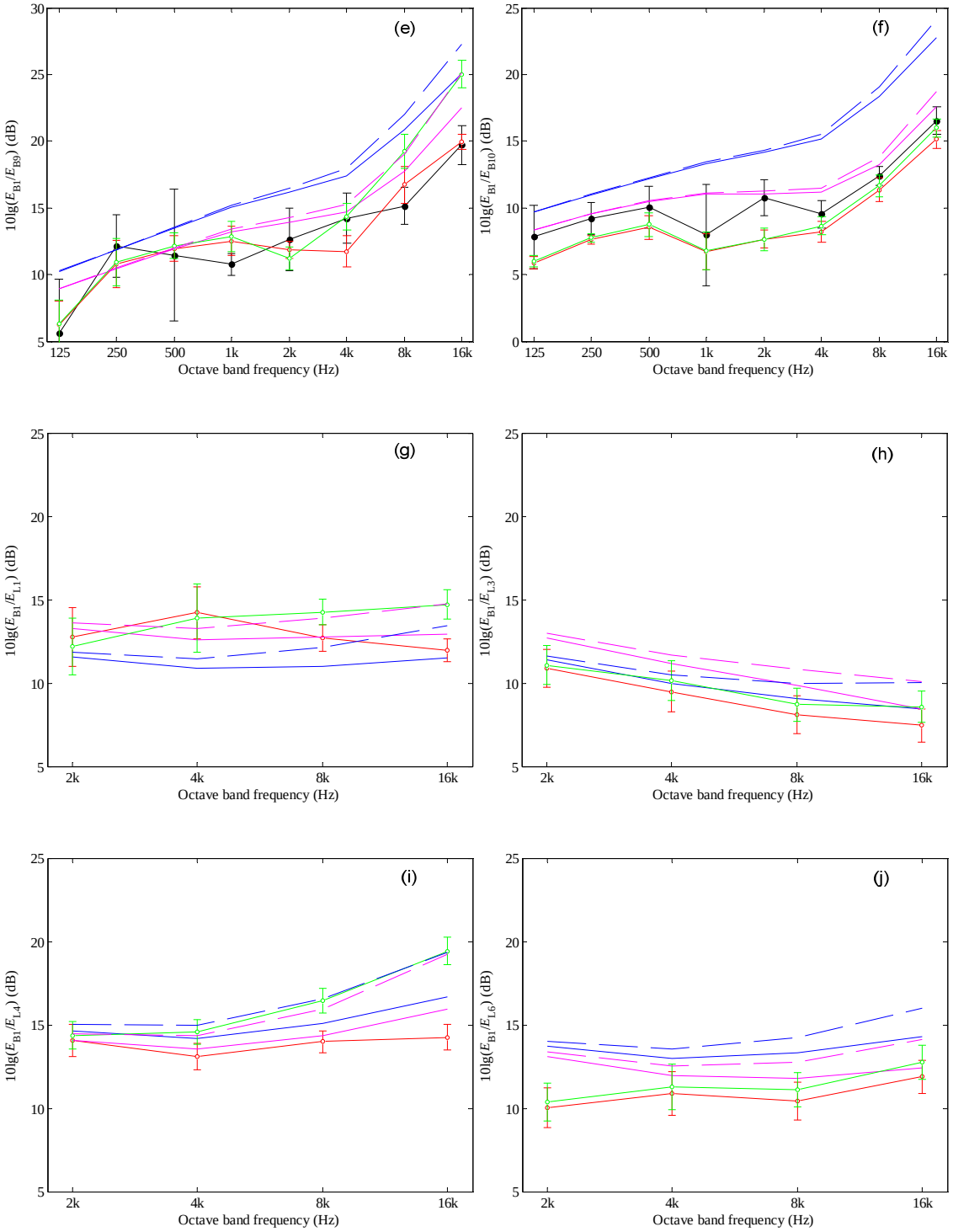
(e)
(f)
(g)
(h)
(i)
(j)
10lg(E_B1/E_B9) (dB)
10lg(E_B1/E_B10) (dB)
10lg(E_B1/E_L1) (dB)
10lg(E_B1/E_L3) (dB)
10lg(E_B1/E_L4) (dB)
10lg(E_B1/E_L6) (dB)
Octave band frequency (Hz)
125
250
500
1k
2k
4k
8k
16k

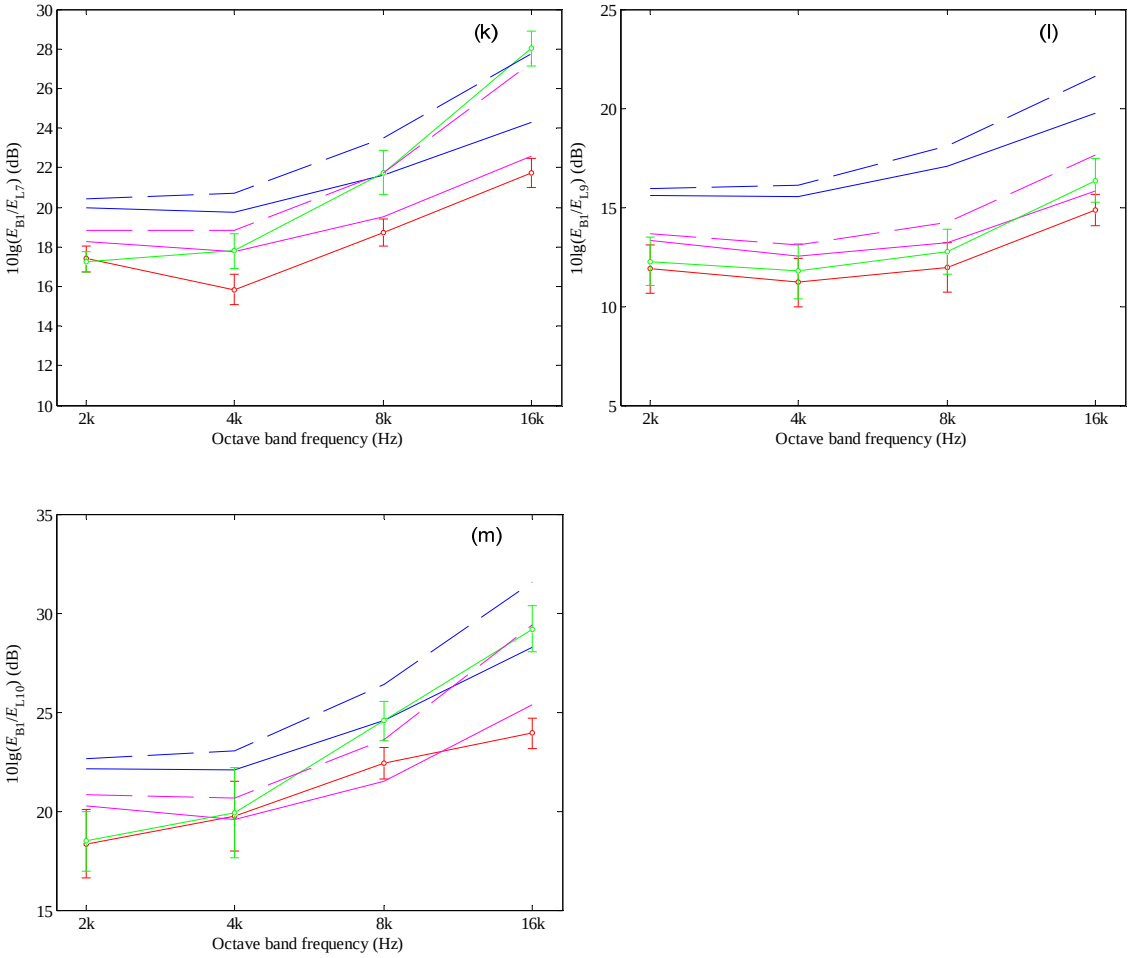

Figure 6.12 BL model of bending wave transmission on the truss beam frame (Source subsystem: B1): (a), (b), (c), (d), (e) and (f) comparison of FEM, SEA and ASEA predictions with measurements; (g), (h), (i), (j), (k), (l) and (m) comparison of FEM, SEA and ASEA predictions. —●—, Measurement; —○—, FEM (Euler-Bernoulli elements); —○—, FEM (Timoshenko elements); ——, SEA (Euler-Bernoulli group velocity); – – – –, SEA (Timoshenko group velocity); ——, ASEA (Euler-Bernoulli group velocity); – – – –, ASEA (Timoshenko group velocity). Results from measurements and FEM are shown with 95% confidence intervals.

Figure 6.12 (a) to (f) compares measured and predicted energy level differences for the BL model where bending waves are excited on the source subsystem and the receiving subsystem represents bending wave energy. For octave bands from 125 Hz to 1 kHz there are only bending modes and each band typically contains at least one local bending mode for the source and receiving beams. In general there is close agreement (<3 dB) between the average values from measurements, FEM (Euler-Bernoulli and Timoshenko elements) and ASEA (Euler-Bernoulli and Timoshenko group velocity).

For E_{B1}/E_{B3} (i.e. adjacent coupled beams) SEA and ASEA are nominally identical; however, as the source and receiving subsystems become more distant from each other, ASEA gives significantly lower energy level differences than SEA. This indicates the importance of indirect coupling when there is only bending wave motion.

Between 2 kHz and 16 kHz there are both bending and longitudinal modes. Measurements show closer agreement with FEM using Euler-Bernoulli elements than Timoshenko elements for E_{B1}/E_{B3}, E_{B1}/E_{B6}, and E_{B1}/E_{B9}. However, for E_{B1}/E_{B4}, E_{B1}/E_{B7}, and E_{B1}/E_{B10}, measurements and FEM using Euler-Bernoulli or Timoshenko elements are similar. In general, FEM using Euler-Bernoulli elements shows closest agreement with ASEA using Euler-Bernoulli group velocity, and FEM using Timoshenko elements shows closest agreement with ASEA using Timoshenko group velocity. This is clearer for E_{B1}/E_{B6} and E_{B1}/E_{B9} than for E_{B1}/E_{B4}, E_{B1}/E_{B7}, and E_{B1}/E_{B10}. With increasing frequency, the generation of longitudinal waves typically increases the indirect coupling and ASEA gives significantly lower energy level differences than SEA as the beams become more distant from the source. However, the largest differences between SEA and ASEA do not always occur in the highest frequency band; for example, the largest difference for E_{B1}/E_{B9} is ≈3 dB in the 8 kHz band which reduces to ≈2 dB at 16 kHz. In general, measurements and FEM show closer agreement with ASEA rather than SEA due to the existence of indirect coupling.

Figure 6.12 (g) to (m) allow comparison of predicted energy level differences for the BL model where bending waves are excited on the source subsystem and the receiving subsystem represents longitudinal wave energy. These results show similarly close agreement between FEM and ASEA that were identified above when both the source and receiving subsystems contain bending wave energy. The main finding is that ASEA provides a better estimate of vibration transmission than SEA.

6.7.2 Longitudinal wave excitation

Figure 6.13 shows the results for the BL model of the three-bay truss with excitation of longitudinal waves on beam 1.

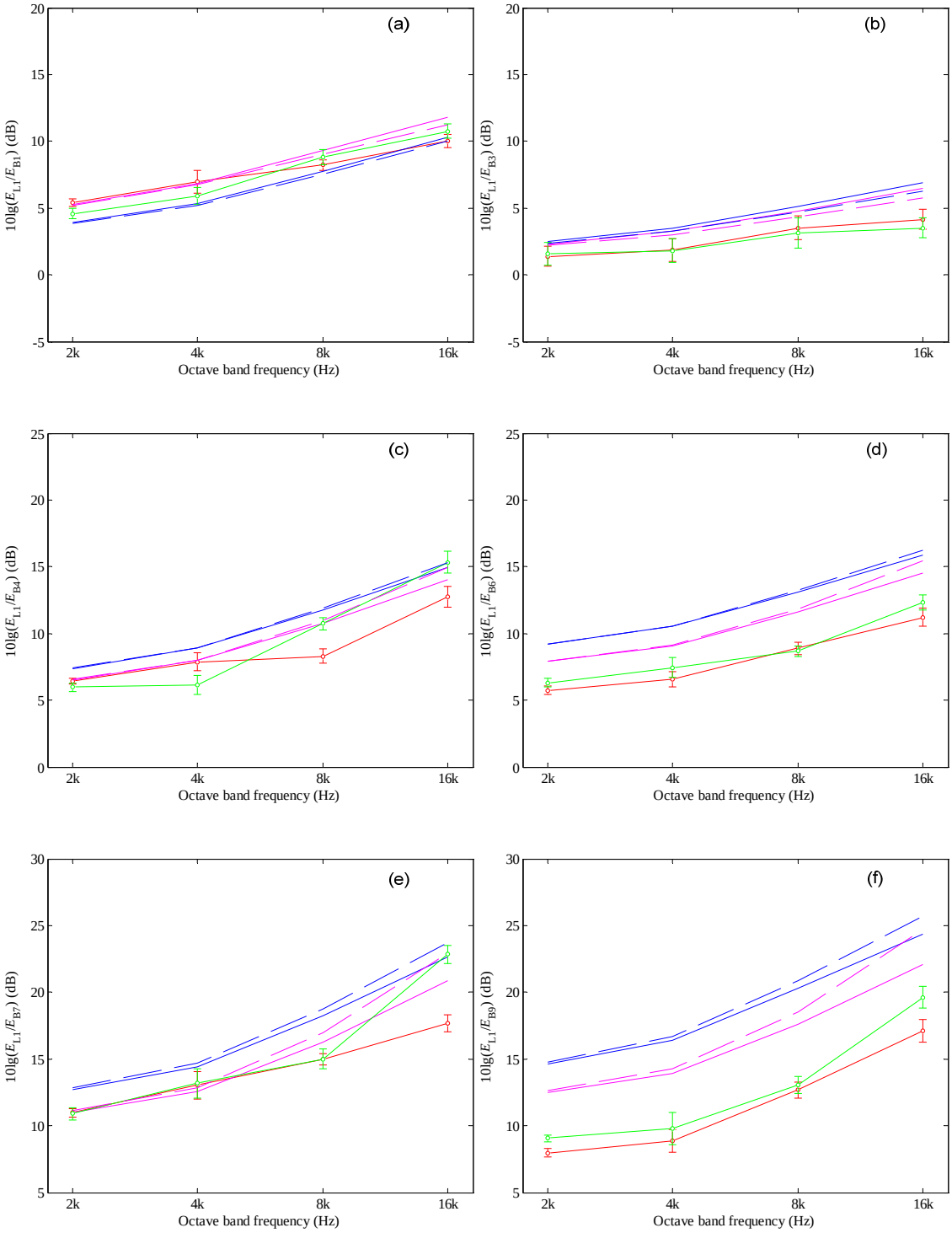
(a)
(b)
(c)
(d)
(e)
(f)
$10\lg(E_{L1}/E_{B1})$ (dB)
$10\lg(E_{L1}/E_{B3})$ (dB)
$10\lg(E_{L1}/E_{B4})$ (dB)
$10\lg(E_{L1}/E_{B6})$ (dB)
$10\lg(E_{L1}/E_{B7})$ (dB)
$10\lg(E_{L1}/E_{B9})$ (dB)
2k
4k
8k
16k
Octave band frequency (Hz)

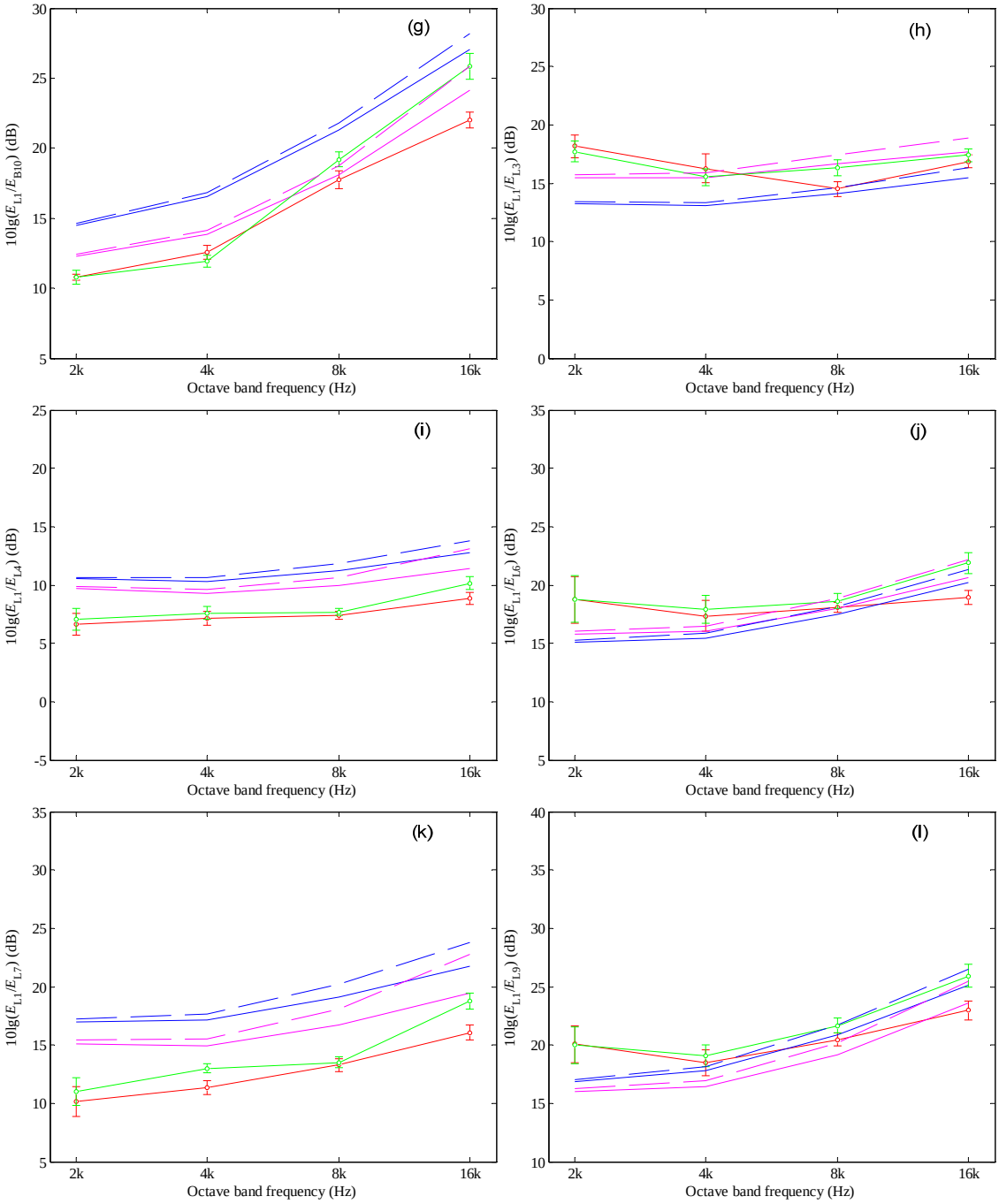
(g)
(h)
(i)
(j)
(k)
(l)
Octave band frequency (Hz)
2k
4k
8k
16k

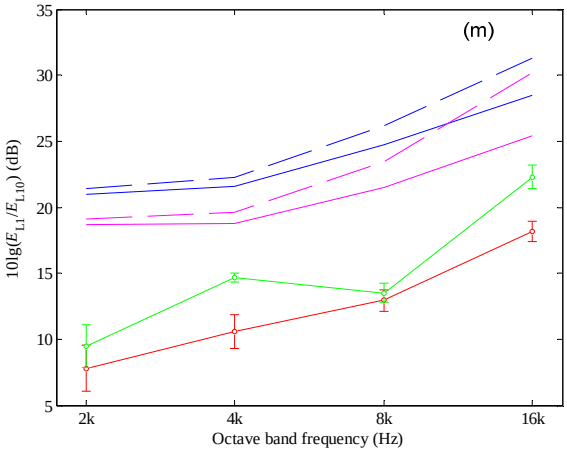

Figure 6.13 BL model of longitudinal wave transmission on the truss beam frame (Source subsystem: L1): comparison of FEM, SEA and ASEA predictions. —○—, FEM (Euler-Bernoulli elements); —○—, FEM (Timoshenko elements); ——, SEA (Euler-Bernoulli group velocity); – – – –, SEA (Timoshenko group velocity); ——, ASEA (Euler-Bernoulli group velocity); – – – –, ASEA (Timoshenko group velocity). Results from FEM are shown with 95% confidence intervals.

Figure 6.13 (a) to (g) allow comparison of predicted energy level differences for the BL model where longitudinal waves are excited on the source subsystem and the receiving subsystem represents bending wave energy. In general, E_{L1}/E_{B1}, E_{L1}/E_{B4}, E_{L1}/E_{B7} and E_{L1}/E_{B10} show closer agreement between FEM and ASEA than E_{L1}/E_{B3}, E_{L1}/E_{B6} and E_{L1}/E_{B9}. The largest difference between FEM and ASEA occurs with E_{L1}/E_{B9} and is ≈5 dB. This is unlikely to be attributed to low mode counts for longitudinal modes because this difference is almost constant between 2 kHz and 16 kHz over which the mode count increases from one to five modes on each beam.

Figure 6.13 (h) to (m) allow comparison of predicted energy level differences for the BL model where longitudinal waves are excited on the source subsystem and the receiving subsystem represents longitudinal wave energy. Referring back to Figure 2.22 for the T123-junction it is seen that the transmission coefficient $\tau_{L1L3} > 0.7$ above 2 kHz; hence there will be strong coupling of longitudinal wave energy between subsystems L3 and L6, and L6 and L9. However, there is reasonable agreement between FEM and ASEA for both Euler-Bernoulli and Timoshenko theory for E_{L1}/E_{L3}, E_{L1}/E_{L6} and E_{L1}/E_{L9}. In contrast, for E_{L1}/E_{L4}, E_{L1}/E_{L7} and E_{L1}/E_{L10} there are significant differences between FEM and ASEA and these differences become larger as the

receiving subsystem is more distant from the source subsystem, on average the differences are 3 dB, 5 dB and 10 dB respectively. This indicates that incorporating high coupling loss factors (due to high transmission coefficients) does not cause any obvious problems with strong coupling.

6.8 BT model on the truss

6.8.1 Bending wave excitation

Figure 6.14 shows the results for the BT model of the three-bay truss with excitation of Type B bending waves on beam 1.

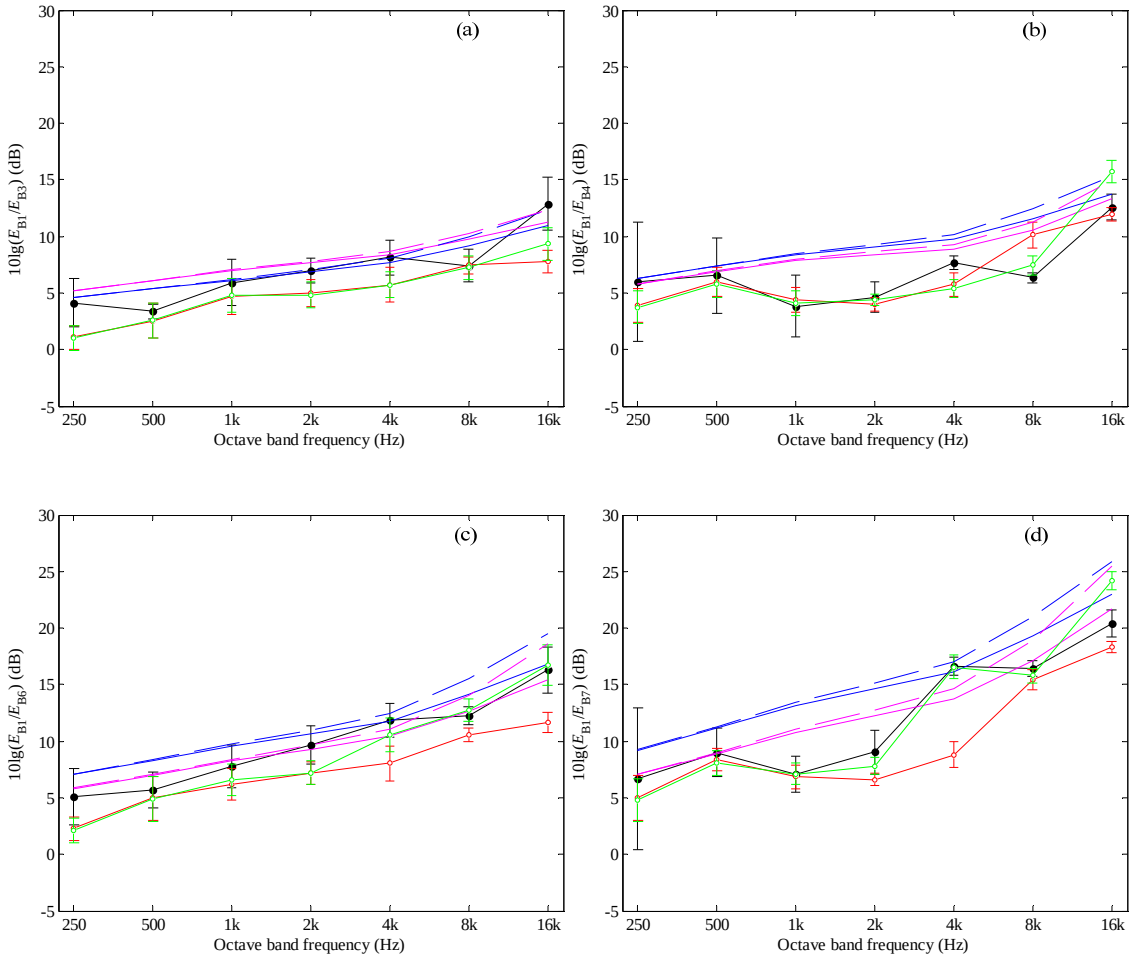

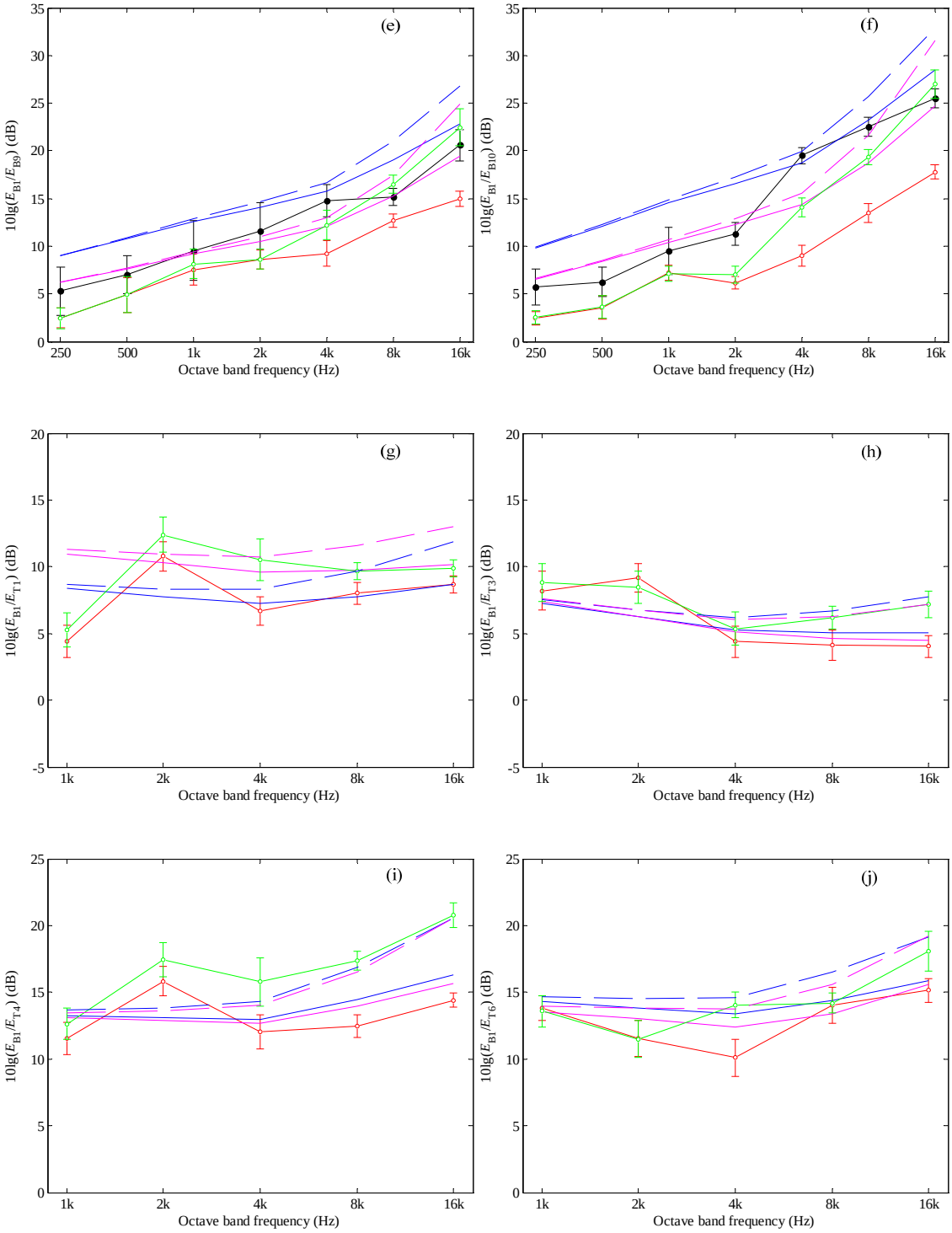
(e)
(f)
(g)
(h)
(i)
(j)
Octave band frequency (Hz)
250
500
1k
2k
4k
8k
16k

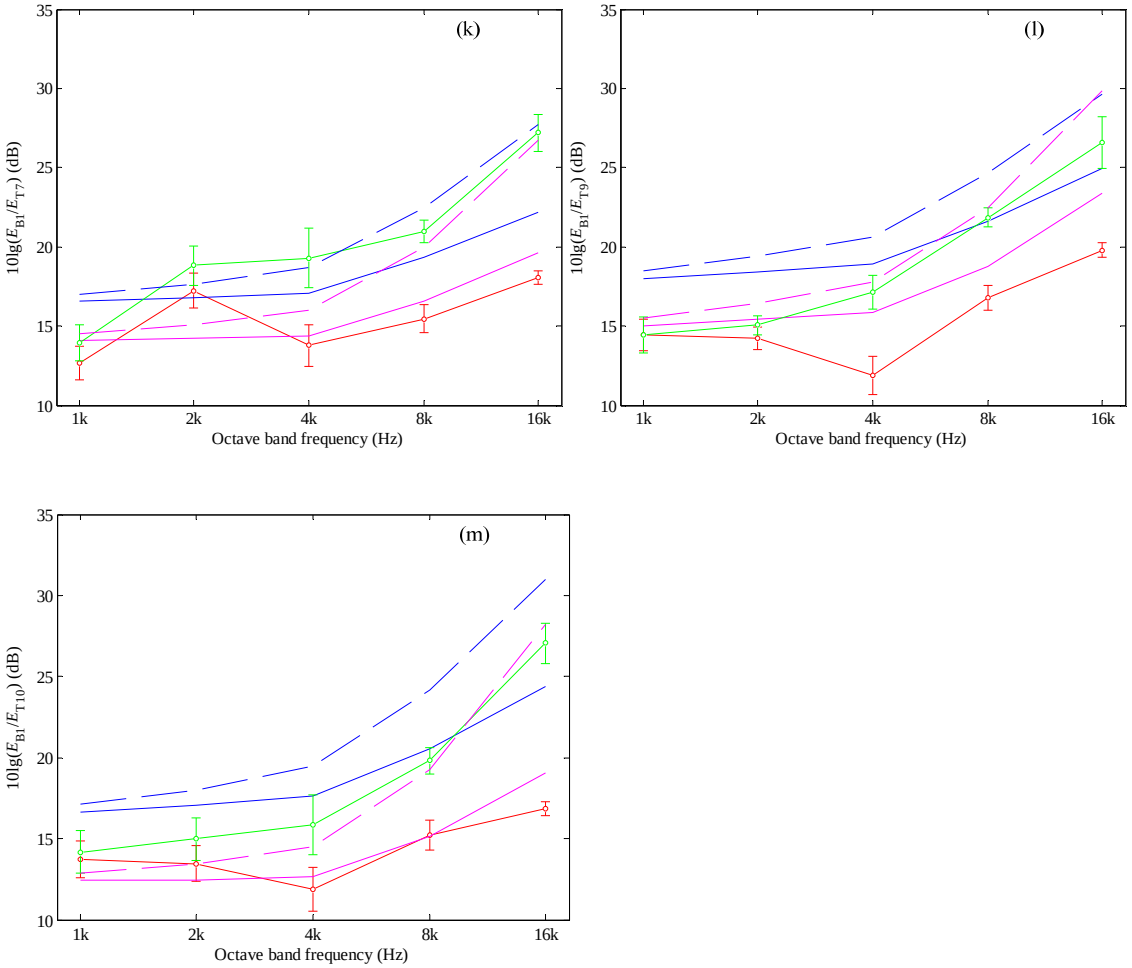

Figure 6.14 BT model of bending wave transmission on the truss beam frame (Source subsystem: B1): (a), (b), (c), (d), (e) and (f) comparison of FEM, SEA and ASEA predictions with measurements; (g), (h), (i), (j), (k), (l) and (m) comparison of FEM, SEA and ASEA predictions. —●—, Measurement; —○—, FEM (Euler-Bernoulli elements); —○—, FEM (Timoshenko elements); ——, SEA (Euler-Bernoulli group velocity); – – – –, SEA (Timoshenko group velocity); ——, ASEA (Euler-Bernoulli group velocity); – – – –, ASEA (Timoshenko group velocity). Results from measurements and FEM are shown with 95% confidence intervals.

Figure 6.14 (a) to (f) allow comparison of measured and predicted energy level differences for bending wave excitation where both source and receiving subsystems contain bending wave energy. The two octave bands from 250 Hz to 500 Hz have only bending modes and each band typically contains at least one local bending mode for the source and receiving beams. For E_{B1}/E_{B3}, E_{B1}/E_{B4}, E_{B1}/E_{B6}, and E_{B1}/E_{B7} there is close agreement (<3.5 dB) between measurements, FEM, SEA and ASEA (Euler-Bernoulli and Timoshenko theory are nominally identical). However, for the more distant

subsystems 9 and 10, SEA overestimates the energy level difference by ≈3.8 dB and there is closer agreement between measurements, FEM and ASEA (≤3.4dB with confidence interval overlapped each other).

For octave bands from 1 kHz to 16 kHz there are both bending and torsional modes. Measured data tends to show closest agreement (<3.6 dB) with FEM and ASEA using Timoshenko rather than Euler-Bernoulli theory. This is particularly evident at and above the 8 kHz band where the difference between Timoshenko and Euler-Bernoulli group velocities is ≥26%. Hence there is evidence to support using this crossover point to change from using Euler-Bernoulli to Timoshenko group velocity in ASEA.

However, one unexplained feature occurs with the furthest beam (Figure 6.14 (f)); FEM using Euler-Bernoulli elements and ASEA using Euler-Bernoulli group velocity does not show close agreement as it did with the furthest beam in the rectangular beam frame in section 6.6.

Figure 6.14 (g) to (m) allow comparison of predicted energy level differences for the BT model where bending waves are excited on the source subsystem and the receiving subsystem represents torsional wave energy. In general, FEM using Euler-Bernoulli elements shows closer agreement with ASEA using Euler-Bernoulli group velocity, and FEM using Timoshenko elements shows closer agreement with ASEA using Timoshenko group velocity.

6.8.2 Torsional wave excitation

Figure 6.15 shows the results for the BT model of the three-bay truss with excitation of torsional waves on beam 1.

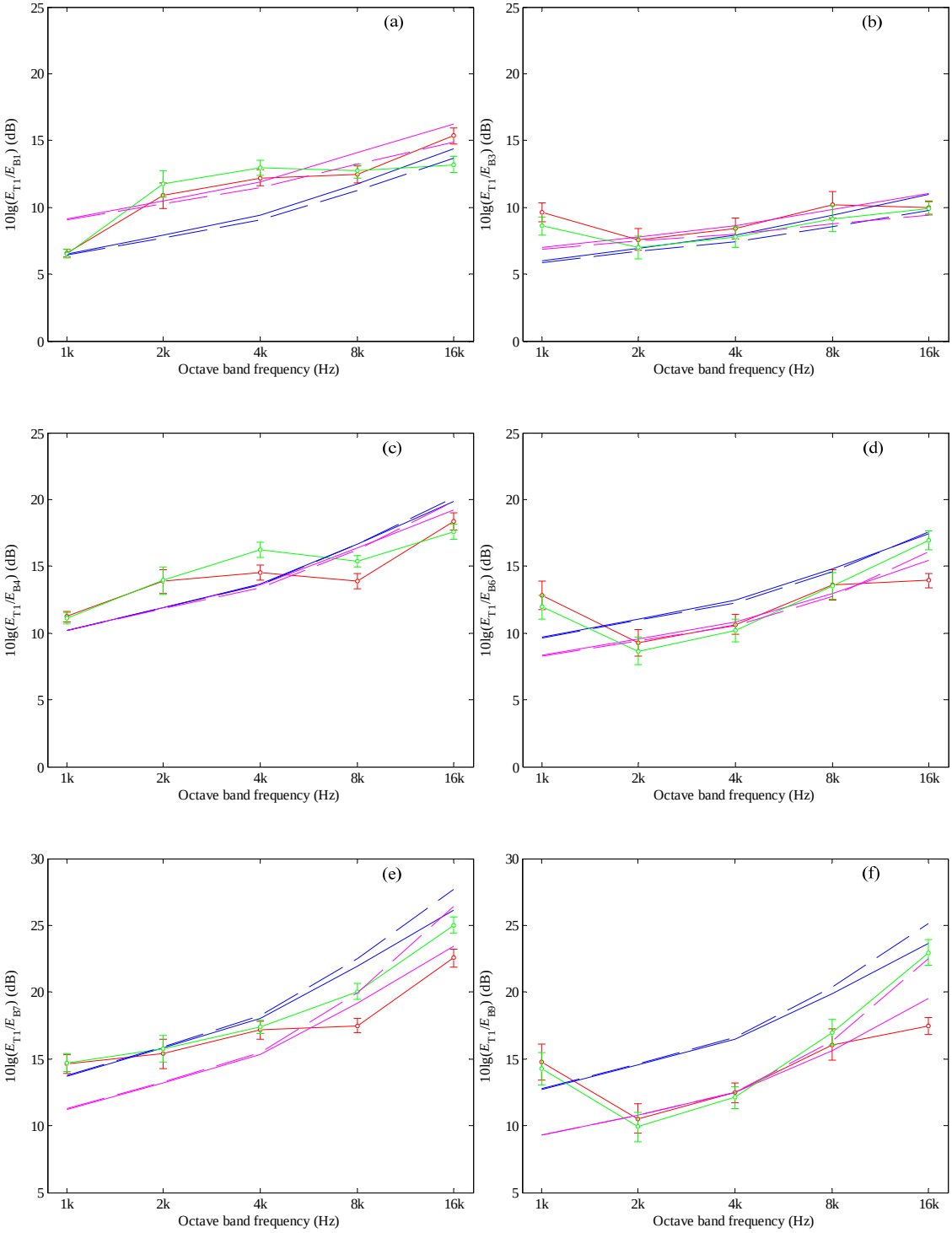
(a)
(b)
(c)
(d)
(e)
(f)
Octave band frequency (Hz)
1k
2k
4k
8k
16k

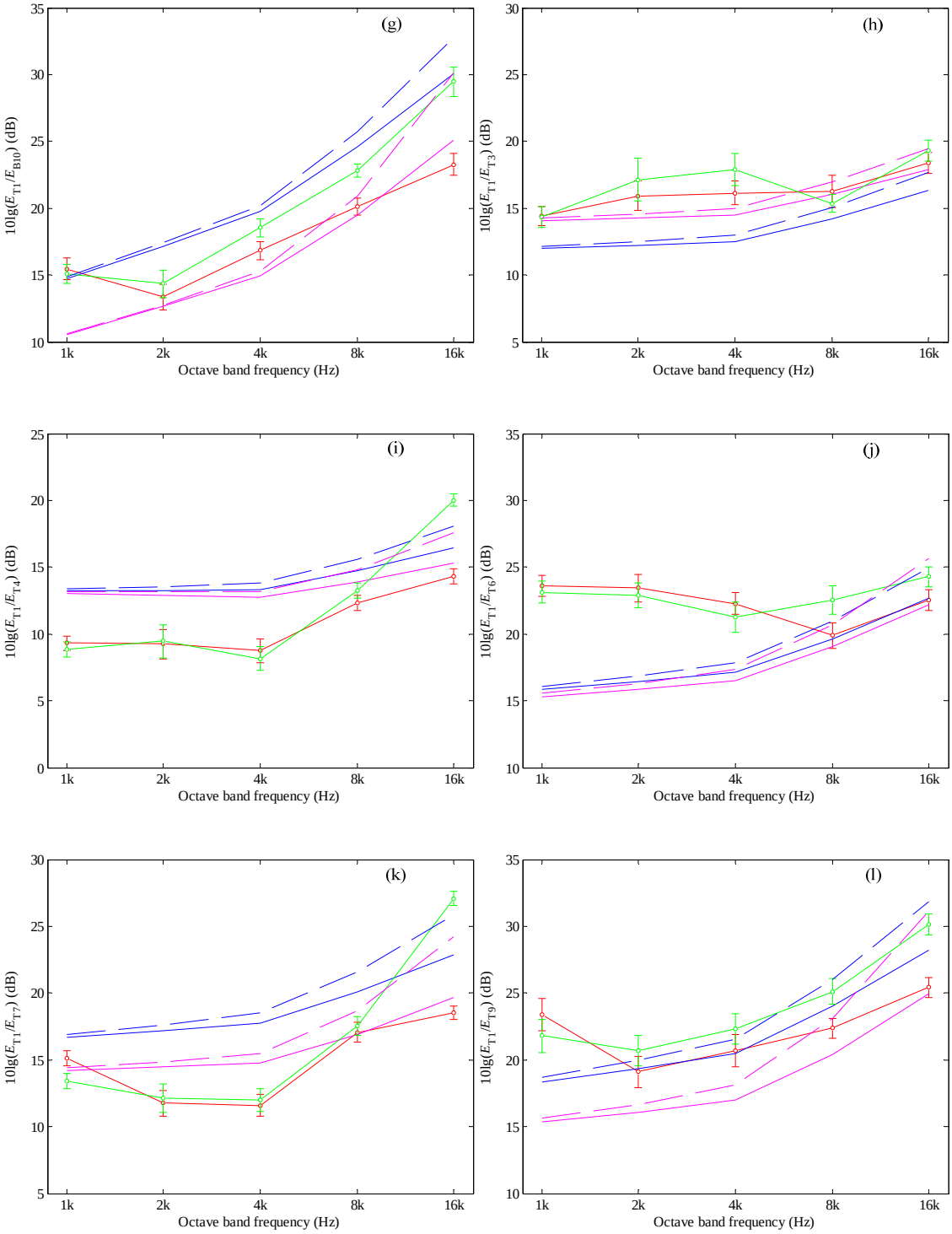
(g)
(h)
(i)
(j)
(k)
(l)
$10\lg(E_{T1}/E_{B10})$ (dB)
$10\lg(E_{T1}/E_{T3})$ (dB)
$10\lg(E_{T1}/E_{T4})$ (dB)
$10\lg(E_{T1}/E_{T6})$ (dB)
$10\lg(E_{T1}/E_{T7})$ (dB)
$10\lg(E_{T1}/E_{T9})$ (dB)
1k
2k
4k
8k
16k
Octave band frequency (Hz)

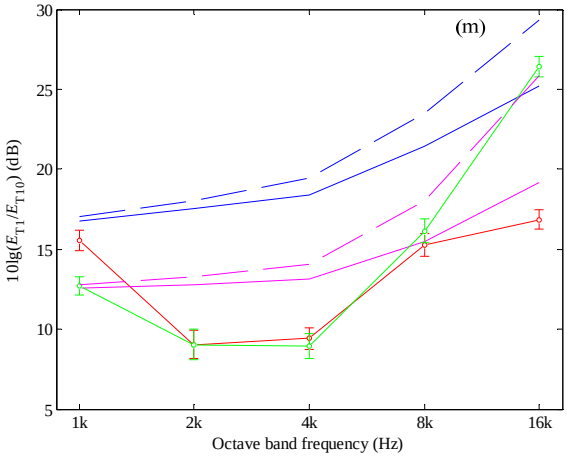

Figure 6.15 BT model of torsional wave transmission on the truss beam frame (Source subsystem: T1): comparison of FEM, SEA and ASEA predictions. —○—, FEM (Euler-Bernoulli elements); —○—, FEM (Timoshenko elements); ——, SEA (Euler-Bernoulli group velocity); – – – –, SEA (Timoshenko group velocity); ——, ASEA (Euler-Bernoulli group velocity); – – – –, ASEA (Timoshenko group velocity). Results from FEM are shown with 95% confidence intervals.

Figure 6.15 (a) to (g) allow comparison of predicted energy level differences for the BT model where torsional waves are excited on the source subsystem and the receiving subsystem represents bending wave energy. In general, and particularly at and above 8 kHz, the FEM (Euler-Bernoulli and Timoshenko elements) curves fall in-between the SEA and ASEA predictions.

Figure 6.15 (h) to (m) allow comparison of predicted energy level differences for the BL model where torsional waves are excited on the source subsystem and the receiving subsystem represents torsional wave energy. In contrast to Figure 6.15 (a) to (g), it is only at and above 8 kHz that FEM (Euler-Bernoulli and Timoshenko elements) curves fall in-between the SEA and ASEA predictions. Below 8 kHz, FEM is higher than SEA and ASEA for E_{T1}/E_{T3}, E_{T1}/E_{T6} and E_{T1}/E_{T9}, but FEM is lower than SEA and ASEA for E_{T1}/E_{T4}, E_{T1}/E_{T7} and E_{T1}/E_{T10}.

6.9 Summary

SEA and ASEA have been used to predict vibration transmission across beam frameworks that are formed by solid, rectangular cross-section beams which support multiple wave types. To assess the validity of these models at high frequencies where

Timoshenko beam theory is valid for bending wave motion, an assessment has been made into whether coupling loss factors can be calculated using wave transmission coefficients predicted using Euler-Bernoulli theory but using Timoshenko group velocity to calculate the coupling loss factors.

Comparison with measurements on Perspex beams and FEM using Euler-Bernoulli and Timoshenko elements have been carried out to gain insight into the validity of this approach when there are low mode counts, low modal overlap, multiple wave types, different bending wave theories, propagation losses and indirect coupling. An isolated L-junction of beams, a rectangular beam frame and a three-bay truss beam have been investigated for bending wave excitation leading to either bending and longitudinal wave motion, or bending and torsional wave motion on all beams. The rectangular beam framework has relatively long beams which give rise to high propagation losses. The three-bay truss beam is formed from relatively short beams and tunneling mechanisms were more important than propagation losses.

In general, there are large fluctuations in the energy level differences when (a) there is only one local mode in each frequency band in either the source or the receiving beam and (b) there are intermediate frequency bands with no local modes on the source and receiving beams. When consecutive frequency bands have at least one local mode on the source or receiving beams the fluctuations are significantly reduced. When each beam supports at least two local modes for each wave type in the frequency band of interest and the modal overlap factor is at least 0.1, FEM and measurement data tend to have average values which form smooth curves such as those predicted with SEA and ASEA.

When Timoshenko and Euler-Bernoulli group velocities differ by ≥26%, measurements using bending wave excitation showed closest agreement with FEM using Euler-Bernoulli elements when longitudinal waves were generated at the junction, but closest agreement with FEM using Timoshenko elements when torsional waves were generated at the junction. It would have been expected to be Timoshenko elements in both cases; for this reason clearer conclusions were sought through comparison of FEM, SEA and ASEA. The results showed that when the difference between Timoshenko and Euler-Bernoulli group velocities was ≥26% there were significant differences between FEM

models using Euler-Bernoulli and Timoshenko elements. For receiving subsystems that were not directly coupled to the source subsystem, FEM using Euler-Bernoulli and Timoshenko elements showed closest agreement with ASEA (rather than SEA) using Euler-Bernoulli and Timoshenko group velocities respectively. One reason for this is that wave conversion and propagation losses become more important for more distant subsystems; hence there were clear differences between SEA and ASEA. The agreement between FEM and ASEA indicates that it is a reasonable assumption that phase effects can be ignored in the ray tracing approach used with ASEA. ASEA results for the L-junctions and the rectangular beam frame demonstrated that unlike SEA it was able to incorporate high propagation losses.

The rectangular beam framework has high propagation losses at high frequencies whereas the response of the three-bay truss beam has indirect coupling. Comparison of measurements and FEM has not led to a conclusive decision on the validity of Euler-Bernoulli or Timoshenko theory at high frequencies. However when the difference between Timoshenko and Euler-Bernoulli group velocities was ≥26% there are significant differences between FEM models using Euler-Bernoulli and Timoshenko elements. For these FEM models there are closest agreement with ASEA (rather than SEA) using Euler-Bernoulli and Timoshenko group velocities respectively. This validates the approach proposed in this chapter to incorporate Timoshenko theory into SEA or ASEA purely by changing the group velocity used to calculate the coupling loss factors.

Analysis of the three-bay truss beam shows that ASEA can be used to predict vibration transmission across a finite periodic framework of beams where all beams supports local modes, even when the beams are identical in terms of material properties and dimensions. For periodic structures the existence of phase effects might be expected to invalidate the use of ASEA. However, close agreement between FEM and ASEA indicates that it is a reasonable assumption that phase effects can be ignored in the ray tracing approach used with ASEA. In Chapter 7 numerical experiments will be carried out to investigate a truss beam with high propagation losses and the effect of uncertainty in the material properties.

7. Parametric studies using FEM, SEA and ASEA

7.1 Introduction

This chapter uses parametric studies using numerical experiments with FEM, SEA and ASEA to investigate the following:

(1) The effect of different junction and boundary conditions with an L-junction.

For the experimental validation in Chapter 6 it was not considered feasible to have a pinned junction; hence only the BL and BT models were considered. However, with numerical simulations it is possible to investigate a pinned junction in order to assess the validity of the wave theory transmission coefficients for a bending only model. In addition, the experimental validation on an L-junction was only carried out with free boundary conditions but with numerical experiments it is now possible to compare free and pinned boundary conditions with the B and BL models.

(2) The effect of uncertainty in the material properties on the validity of zero transmission coefficients predicted using wave theory for T- and X-junctions.

This investigation is carried out because in Chapter 6 it was seen that there were some beams on the three-bay truss that were either perpendicular or parallel to the source beam that showed better agreement than those in the other orientation. One possible reason for this is that the zero transmission coefficients that were predicted using wave theory do not apply when there is uncertainty in the material properties. Hence this investigation looks at isolated T- and X-junctions for which zero transmission coefficients occur because with L-junctions all the transmission coefficients have a finite value. It is considered important to include this in the thesis because the existing literature [5,6] is either unclear on this issue, or makes no clear statements about it.

(3) The effect of uncertainty in the material properties with periodic frameworks of beams using a five-bay truss beam as an example.

This investigation is carried out because in Chapter 6 it was seen that on the three-bay truss some beams that were either perpendicular or parallel to the source beam showed better agreement than those in the other orientation. In engineering, physical realisations of perfect periodic structures are unusual; hence it is necessary to investigate the effect of variation in the beam properties. For practical purposes it was not possible to measure a truss-beam with more than three bays because there would not have been sufficient signal to noise ratio on beams after the third bay. This also meant that it was not feasible to measure a truss beam with longer beams which would have increased the importance of propagation losses. For these reasons, numerical experiments on a five-bay truss are considered where the beams are the same length as used in the isolated L- and T-junctions, and an assessment is made of the effect of uncertainty in the material properties.

This chapter only considers Euler-Bernoulli theory as it is only FEM, SEA and ASEA models that are being compared.

The material properties, dimensions and mode counts for the beams are given in section 2.3.

7.2 Investigation into the effect of junction and boundary conditions with the L-junction

In section 4.6.2 it was shown using an L-junction that in-plane vibration occurs due to bending wave motion. However, the in-plane vibration was sufficiently low that it was still possible to quantify the longitudinal wave energy above the fundamental longitudinal mode. Section 7.2.1 shows the effect of pinning the junction so that only Type A bending waves are generated (B model) which is compared with the BL model. Section 7.2.2 complements section 4.6.2 by showing the vibration level differences for the BL model with different boundary conditions.

In this section, energy level differences involving longitudinal wave energy are shown below the fundamental longitudinal mode to

7.2.1 Comparison of B and BL models

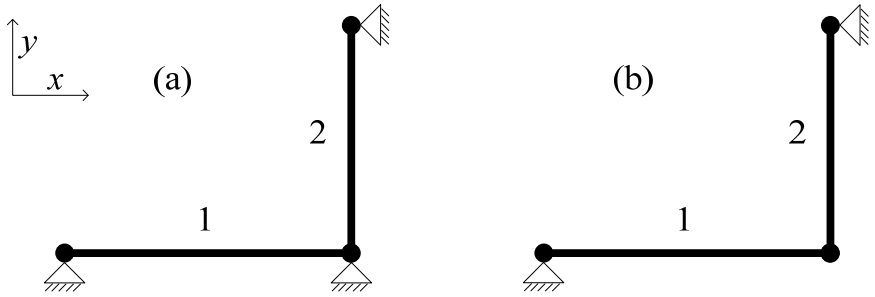

Figure 7.1 Sketch of isolated L-junction with (a) B model and (b) BL model

This section compares the results of isolated beam junctions with B model and BL model. Take the L-junction shown in Figure 7.1 as example. The natural mode counts of the isolated beams 1.3 m and 1.0 m with free-free boundary condition are given in Figure 2.5. The fundamental longitudinal mode on the single free-pinned beam occurs in the 500 Hz one-third octave band.

Figure 7.2 and Figure 7.3 show the energy level differences calculated from the ratio of source subsystem energy to receiving subsystem energy. On all figures, SEA/ASEA predictions with Euler-Bernoulli beam group velocity are compared against the results from the FEM model using Euler-Bernoulli beam element.

Figure 7.2 (a) allows comparison of E_{B1}/E_{B2} for the B and BL models. Between 10 Hz and 500 Hz the bending mode count is sufficiently low (approximately one mode per band) that there are large fluctuations in the FEM data; however, both SEA and ASEA give a good estimate of the mean value over this low-frequency range. Above 500 Hz there are at least one bending mode in each one third octave band; good agreements exist between FEM, SEA and ASEA in either the B or BL models. Above 500 Hz, the energy level difference for the BL model is larger than that with the B model because less power is transmitted to bending subsystem B2 when longitudinal waves are generated at the junction. Note that for this directly connected receiver subsystem there is no advantage in using ASEA instead of SEA because indirect coupling is negligible and the propagation losses are small.

Figure 7.2 (b) shows E_{B1}/E_{L1} and Figure 7.2 (c) shows E_{B1}/E_{L2} with excitation of bending modes in beam 1 and receiving subsystems which consider the longitudinal mode energy. There are no local longitudinal modes (free-free) below 500 Hz. For this

reason there are large differences between FEM and SEA/ASEA below 500 Hz in Figure 7.2 (b) and Figure 7.2 (c). This confirms that it is not appropriate to calculate longitudinal wave energy levels from FEM below the fundamental longitudinal mode. Between 500 Hz and 2.5 kHz SEA and ASEA still give a reasonable estimate of the mean value from FEM although there are only a few longitudinal modes in this frequency range.

In Figure 7.2 (b) there is closer agreement between FEM and ASEA than with SEA above 1.25 kHz. However, in Figure 7.2 (c) there is no significant difference between SEA and ASEA.

Figure 7.3 (a) shows E_{L1}/E_{B1}, Figure 7.3 (b) shows E_{L1}/E_{B2} and Figure 7.3 (c) shows E_{L1}/E_{L2} with excitation of longitudinal modes in beam 1 and receiving subsystems which consider either bending or longitudinal energy. Above the fundamental longitudinal mode, FEM shows agreements both with ASEA and SEA.

In conclusion, only small improvements are gained by using ASEA on a small system such as an L-junction at high-frequencies. This example has highlighted the problems in validating the BL model below the fundamental longitudinal mode. Above the frequency at which successive one-third octave bands have at least one local mode on each beam subsystem, there is good agreement between FEM and statistical models based on SEA or ASEA.

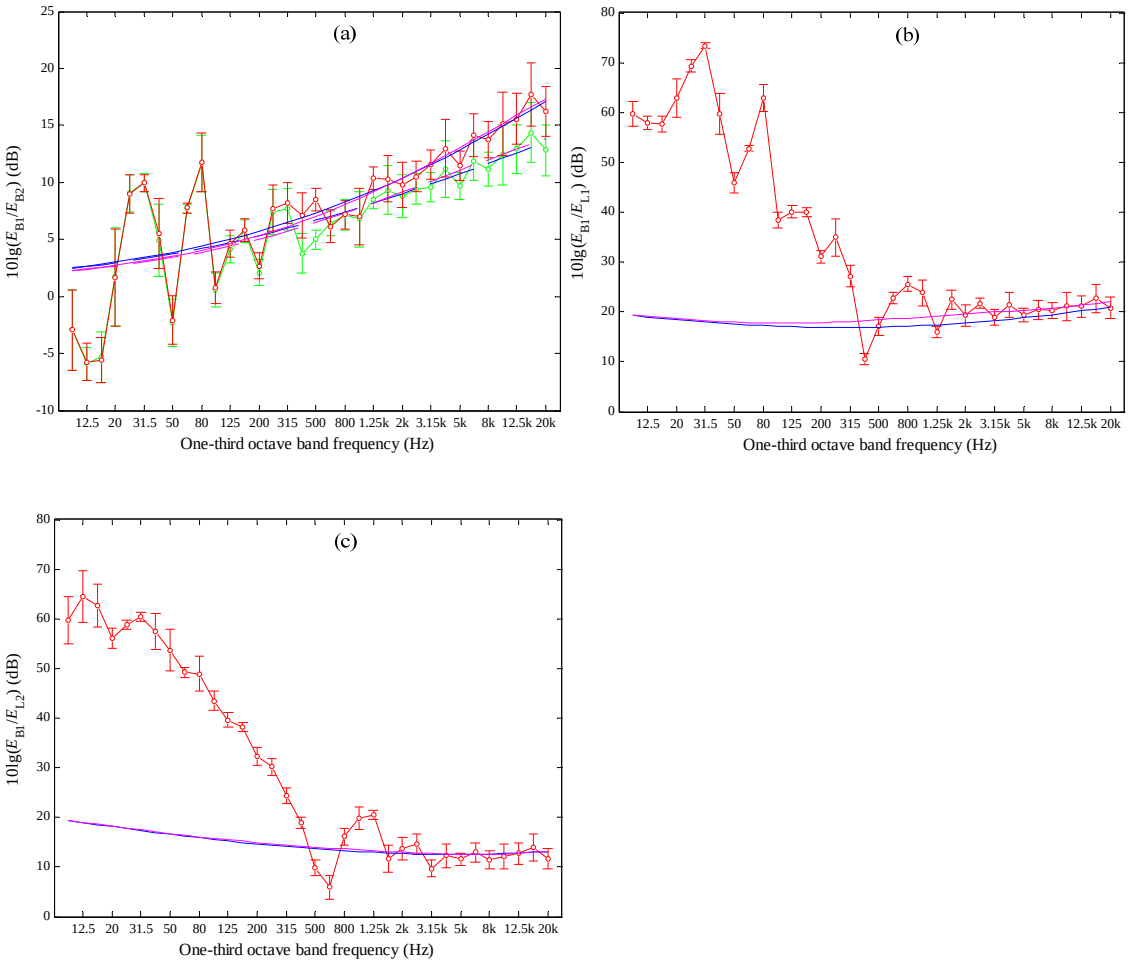

Figure 7.2 Vibration transmission on L-junction (BL model - Source subsystem: B1). ——○——, FEM with B model; ——○——, FEM with BL model; - - - - - -, SEA with B model; ———, SEA with BL model; - - - - - -, ASEA with B model; ———, ASEA with BL model. Results from FEM are shown with 95% confidence intervals.

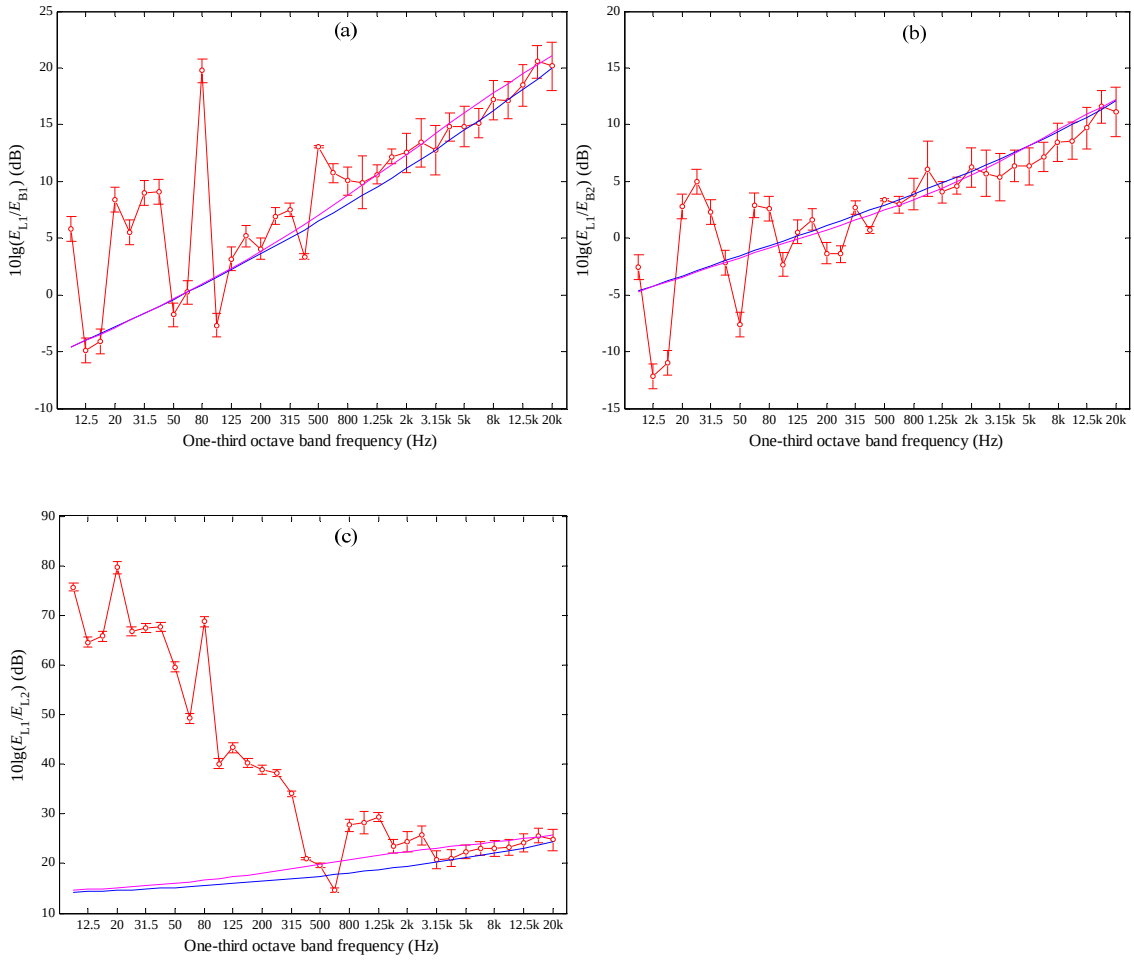

Figure 7.3 Vibration transmission on L-junction (BL model - Source subsystem: L1). —o—, FEM with BL model; ——, SEA with BL model; ——, ASEA with BL model. Results from FEM are shown with 95% confidence intervals.

7.2.2 Comparison of pinned and free boundary conditions with the BL model

In the section 7.2.1 it is concluded that good agreements between the FEM simulation and SEA/ASEA prediction would only occur above the band where the first longitudinal fundamental mode frequency exist, although the in-plane motion can be induced below the fundamental mode frequency due to bending motion. Referring back to the results in section 4.6.2, one might ask how the induced in-plane motion affects the out-of-plane response of beam structures when bending and longitudinal wave couple to each other. So in this section FEM is used to compare L-junctions with pinned and free ends alongside SEA and ASEA predictions.

From Figure 2.5 and Figure 2.6 it is shown that the fundamental longitudinal mode frequency occurs in the 500 Hz one-third octave band for the free-pinned beam and the 1k Hz band for the free-free beam.

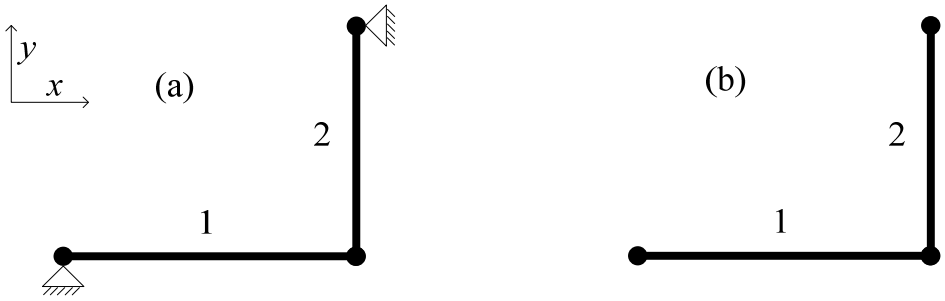

Figure 7.4 Sketch of isolated L-junction of BL model with (a) pinned ends and (b) free ends

Figure 7.5 (a), (b) and (c) shows the energy level difference with Type A bending excitation on beam 1, and Figure 7.6 (a), (b) and (c) shows the energy level difference with longitudinal excitation on beam 1.

In Figure 7.5 (a), from 10 Hz to 500 Hz the two FEM curves fluctuate around the SEA and ASEA curves but they have different peaks and troughs because the global modes are different due to the different boundary conditions. For receiving subsystems L1 and L2, Figure 7.6 (b) and (c)), FEM simulation with free ends gives much higher vibration levels than that with pinned ends below the fundamental longitudinal mode at 1000 Hz. This is due to greater in-plane motion that is generated with free ends as seen in the comparison of impedances on Figure 4.9 and Figure 4.10. Similarly, with longitudinal wave excitation on beam 1 shown in Figure 7.6, FEM simulation with free ends still provides higher vibration level than that of pinned ends below the fundamental longitudinal mode frequency. The main concern is that below the fundamental longitudinal mode, FEM sometimes shows closer agreement with SEA and ASEA for beams with free ends than with pinned ends. In an experimental study (rather than numerical studies as in this chapter) the fundamental longitudinal mode frequency for complex beams might not be known or measurable and this might lead to an incorrect conclusion when compared against SEA or ASEA.

The induced in-plane motion due to bending wave motion below the fundamental longitudinal mode frequency affects the FEM estimate of longitudinal wave energy;

hence it is not appropriate to use this estimate below the fundamental longitudinal mode. In purely experimental studies on complex beams it might be difficult to estimate the fundamental longitudinal mode; hence care always needs to be taken if measuring in-plane motion and attributing it to longitudinal wave energy.

It is concluded that FEM, SEA and ASEA show good agreement as long as there is at least one local mode in both the source and receiving subsystems.

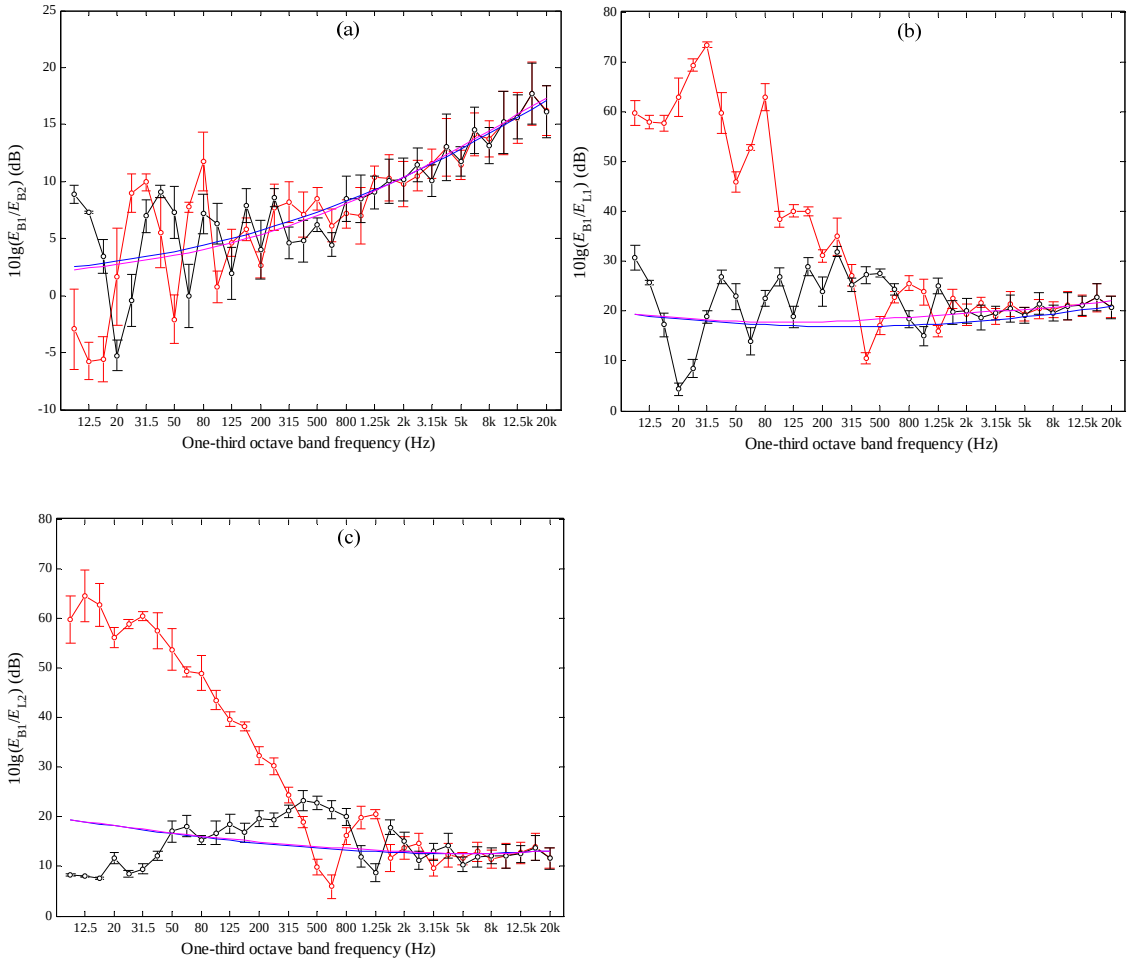

Figure 7.5 Vibration transmission on L-junction with different boundary condition (BL model - Source subsystem: B1). —○—, FEM with BL model of free end; —○—, FEM with BL model of pinned end; ——, SEA with BL model; ——, ASEA with BL model. Results from FEM are shown with 95% confidence intervals.

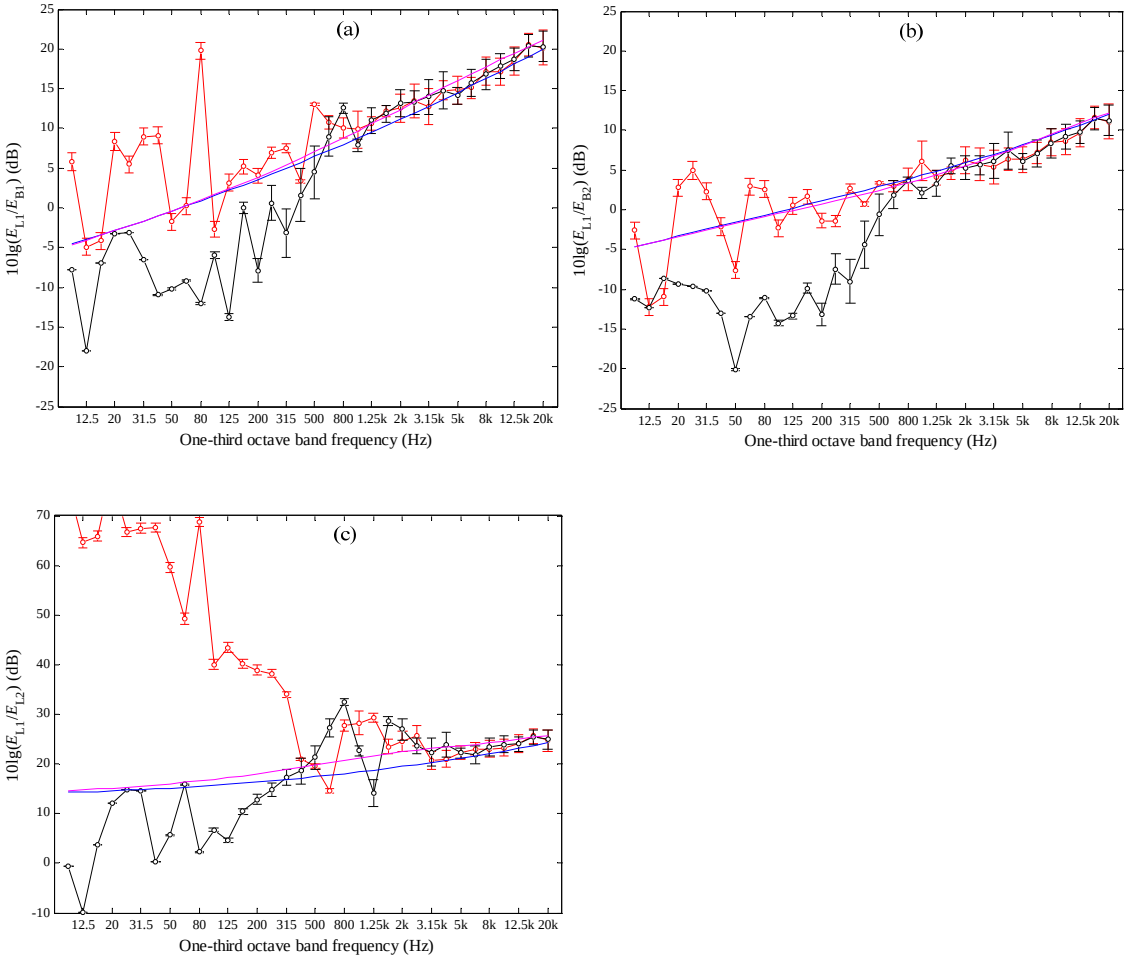

Figure 7.6 Vibration transmission on L-junction with different boundary condition (BL model - Source subsystem: L1). —○—, FEM with BL model of free end; —○—, FEM with BL model of pinned end; ——, SEA with BL model; ——, ASEA with BL model. Results from FEM are shown with 95% confidence intervals.

7.3 Investigation into zero transmission coefficients predicted with wave theory

7.3.1 BL model for T- and X-junctions

Transmission coefficients are zero between certain subsystems in the derivations of BL and BT models for T- and X- junctions as they are symmetric structures. Hence in the FEM simulation these perfectly symmetrical structures have an extremely low level response. To verify the existence of zero transmission coefficients, uncertainties in the Young's modulus are introduced, so that the structures are no longer perfectly symmetrical in terms of their material properties (although they remain symmetrical in

terms of their dimensions). In this section two different FEM models are considered: one model ("uniform material") using the same Young's modulus value for all beams and another model ("random material") where uncertainty is introduced using the Monte Carlo technique to generate an ensemble of ten junctions with different Young's modulus. These values are generated randomly from a normal distribution $N(\mu, \sigma)$ which is a reasonable assumption for material properties. The mean Young's modulus corresponds to the value in Table 2.3 and the standard deviation is calculated assuming μ/σ=0.3. In general, when μ/σ<0.3 it is possible to avoid bias due to extreme values in the distribution [89].

T- and X-junctions are considered as indicated in Figure 7.7. Pinned boundary conditions are used for the ends of the beams because from sections 4.6.2 and 7.2.2 it was shown that in-plane vibration due to bending waves is lower with pinned ends compared to free ends. For T123-junction, beams 1 and 3 are the same length. For T124-junction, beams 2 and 4 are the same length. For X-junction, beams 1 and 3 are the same length, and beams 2 and 4 are the same length.

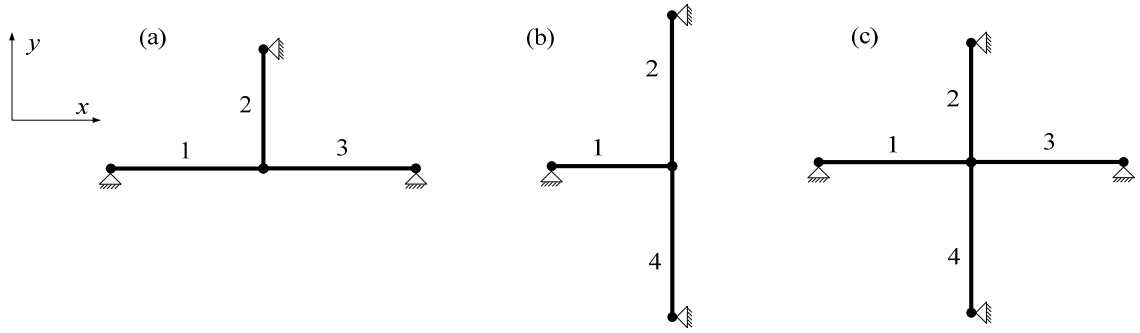

Figure 7.7 Beam junctions with pinned ends: (a) T123-junction, (b) T124-junction, (c) X-junction.

Referring back to section 2.3 the first longitudinal mode on the free-pinned beam occurs in the 500 Hz one-third octave band for 1.3 m and the 630 Hz one-third octave band for 1.0 m. So in this section the results with longitudinal motion in either source subsystem or receiving subsystem are only shown from 500 Hz to 20 kHz, while energy level differences for Type A bending waves are shown from 10 Hz to 20 kHz.

7.3.1.1 T123-junction

For the T123-junction, consideration is given to the assumption in the derivation that τ_{L1L2} is zero.

The energy level differences with Type A bending wave excitation are shown on Figure 7.8 for which there is good agreement between FEM (uniform material), SEA and ASEA indicating that the wave theory transmission coefficients are correct.

The energy level differences for longitudinal wave excitation are shown on Figure 7.9 and this allows greater insight into whether it is correct that τ_{L1L2} is zero. For E_{L1}/E_{L2} in Figure 7.9 (d), FEM with uniform material has an energy level difference >150dB from 10 Hz to 20 kHz. This indicates that τ_{L1L2} being zero is likely to be the correct assumption for transmission between L1 and L2 in the wave theory derivation (section 2.5.2.2). However, in Figure 7.9 (d) FEM (random material) is similar to ASEA and significantly lower (≈100dB) than FEM (uniform material) although the energy level difference is still relatively high at ≈43 dB. In section 2.5.2.2 the derivation for semi-infinite beams assumes structural symmetry such that Type A bending waves on beams 1 and 3 will have the same magnitude but travel in opposite directions with a phase difference of π between them causing zero displacement in the *y*-direction at the junction. Therefore beam 2 has bending wave motion but no longitudinal wave motion. The result corresponding to FEM (uniform material) represents an extreme example because beams 1 and 3 are identical in length, cross-section and material properties and therefore the bending waves that are transmitted onto beams 1 and 3 not only have a phase difference of π between them when they leave the junction but also form standing waves (modes) on these beams which reinforces this condition at the junction.

With FEM (random material), the energy level difference is lower because the T123-junction is not perfectly symmetrical when uncertainty is introduced into the material properties of all the beams. Hence, strictly speaking, the assumption in the wave theory derivation that beam 2 has no longitudinal wave motion is no longer true. In addition, beams 1 and 3 are no longer identical and therefore the modal displacement on beams 1 and 3 is no longer identical. However, it could be claimed that the ensemble average value of the Young's modulus (i.e. the mean value) is the same for beams 1 and 3, and therefore it is appropriate to use the wave theory derivation in section 2.5.2.2. Another

reason that FEM (random material) shows good agreement with ASEA is because there are a number of other transmission paths that result in longitudinal wave motion on beam 2; the most direct paths are L1-B1-L2, and L1-B3-L2 but there are many other longer paths which are possible.

The above finding is important because for real structures there will always be some uncertainty in the material properties and dimensions such that there will be longitudinal wave motion on beam 2. However, the energy level on beam 2 is ≈50 dB below the source subsystem and for most practical noise control problems it will not be critical to estimate the longitudinal wave energy on beam 2. It is therefore noteworthy that E_{L1}/E_{B1}, E_{L1}/E_{B2}, E_{L1}/E_{B3}, E_{L1}/E_{L3} show negligible difference between FEM (uniform material) and FEM (random material) and confirm that the wave theory derivation is appropriate.

This investigation also gives an opportunity to assess whether there is a problem with strong coupling when longitudinal waves are excited on L1 as the source subsystem and the receiving subsystem is L3.

Transmission coefficient $\tau_{L1L3} > 0.7$ above 2 kHz. For this reason one might consider that strong coupling exists between L1 and L3 which could be problematic for SEA but not ASEA.

ASEA involves ray tracing and therefore ignores phase effects but there is no sign that this adversely affects the prediction, as can be seen by the good agreement between FEM and ASEA.

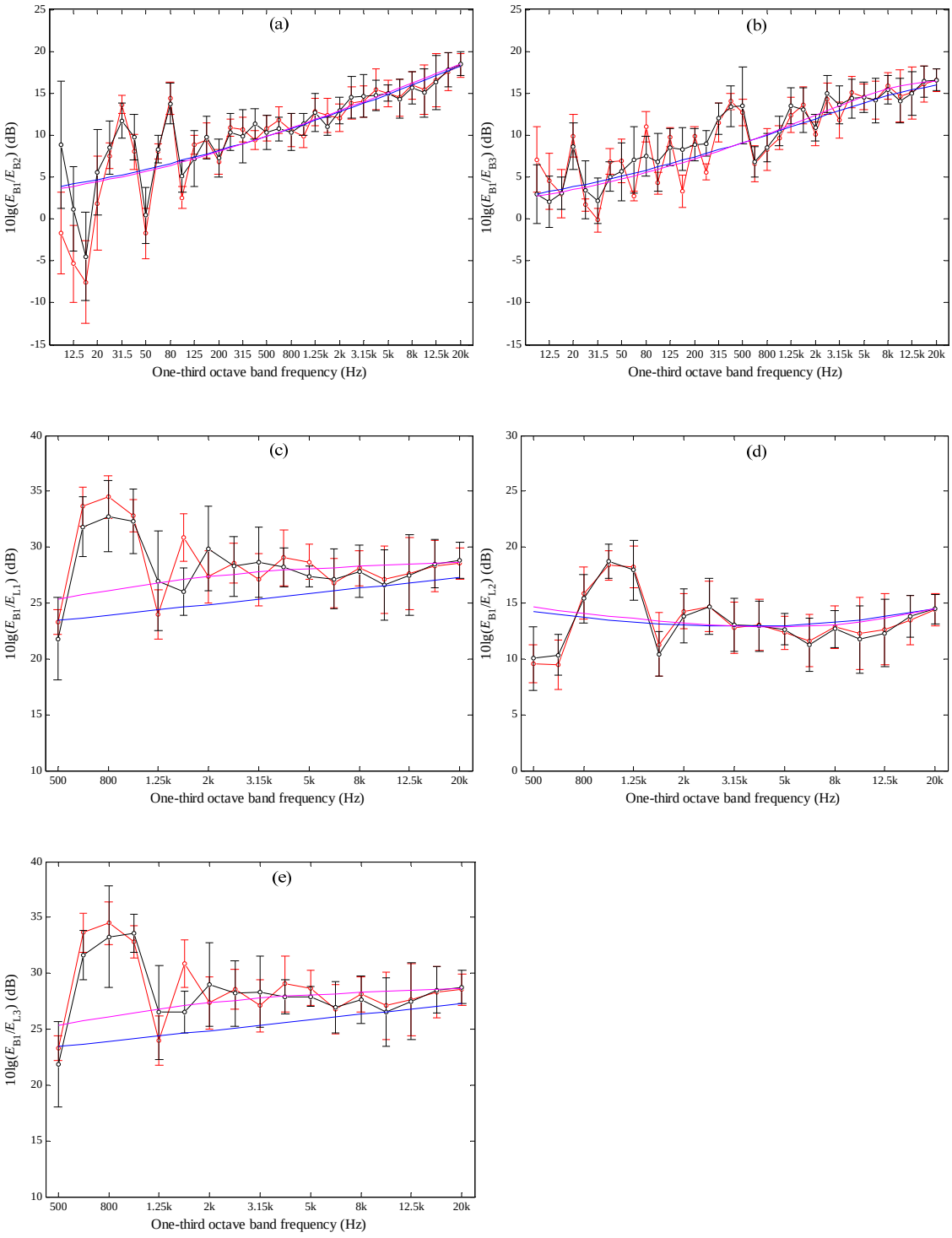

Figure 7.8 Vibration transmission on T123-junction (BL model - Source subsystem: B1). —○—, FEM with uniform material; —○—, FEM with random material; ——, SEA (Euler-Bernoulli group velocity); ——, ASEA (Euler-Bernoulli group velocity). Results from FEM are shown with 95% confidence intervals.

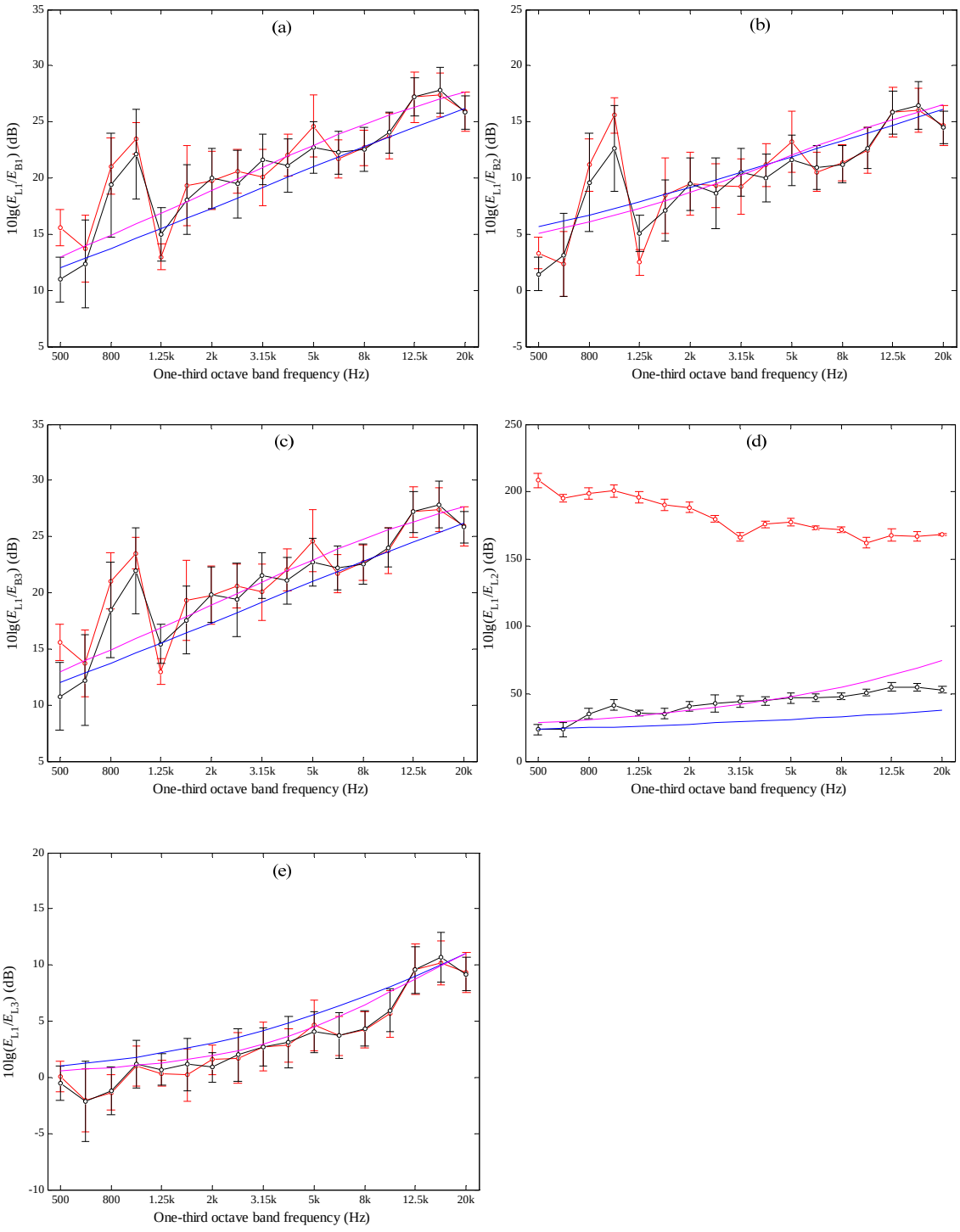

Figure 7.9 Vibration transmission on T123-junction (BL model - Source subsystem: L1). —○—, FEM with uniform material; —○—, FEM with random material; ——, SEA (Euler-Bernoulli group velocity); ——, ASEA (Euler-Bernoulli group velocity). Results from FEM are shown with 95% confidence intervals.

7.3.1.2 T124-junction

For the T124-junction, consideration is given to the assumption in the derivation (section 2.5.3) that τ_{B1L1}, τ_{L1L2} , τ_{L1B1} and τ_{L1L4} are zero.

The results from the T124-junction are shown with Type A bending wave excitation on Figure 7.10 and longitudinal wave excitation on Figure 7.11. The energy level differences shown in Figure 7.10 (c) and Figure 7.11 (a), (d) and (e) indicate that FEM (uniform material) values are much higher (>150dB) than FEM (random material) and that FEM (random material) is close to ASEA. Hence the conclusions and analysis for T123-junction also apply to T124-junction.

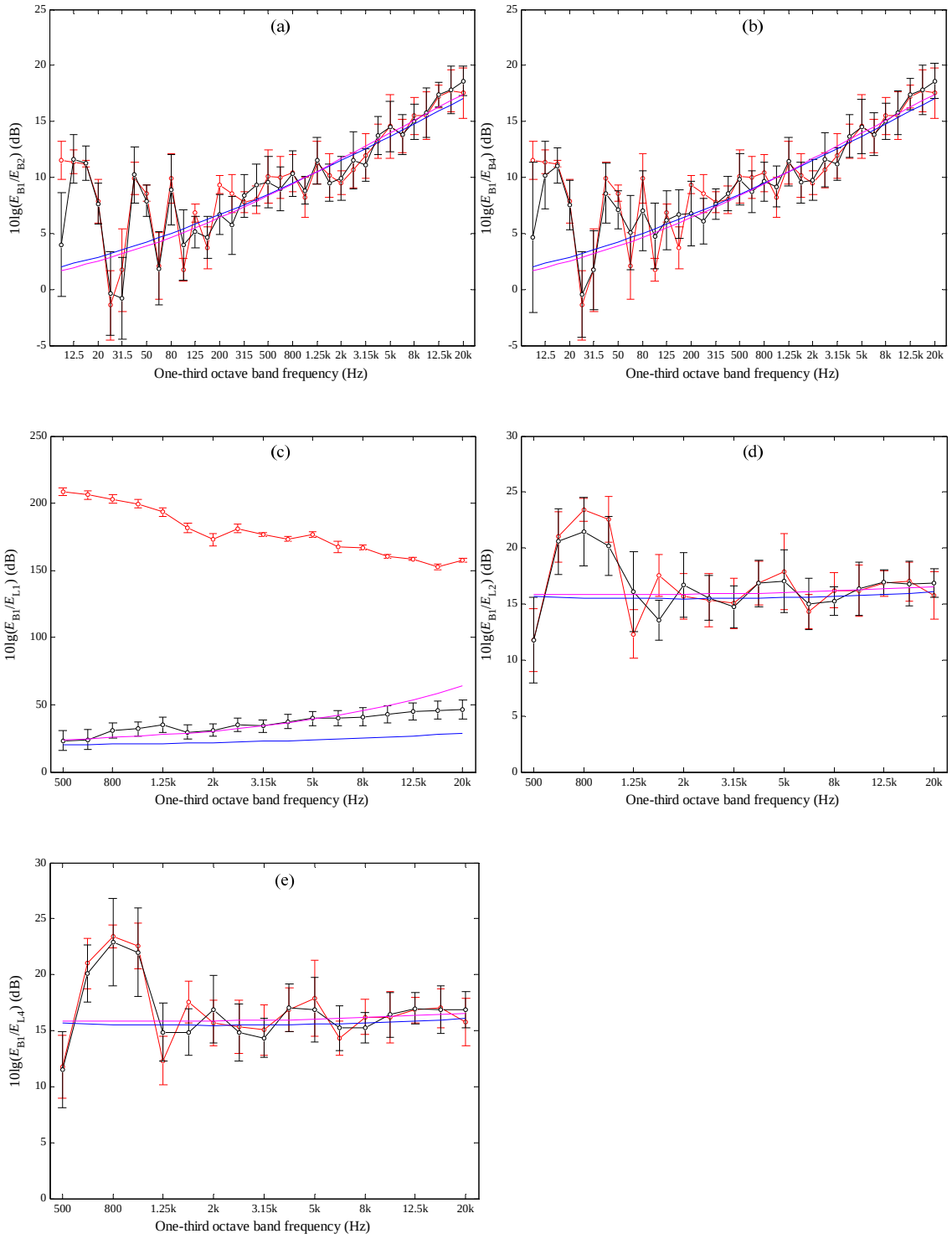

Figure 7.10 Vibration transmission on T124-junction (BL model - Source subsystem: B1). —○—, FEM with uniform material; —○—, FEM with random material; ——, SEA (Euler-Bernoulli group velocity); ——, ASEA (Euler-Bernoulli group velocity). Results from FEM are shown with 95% confidence intervals.

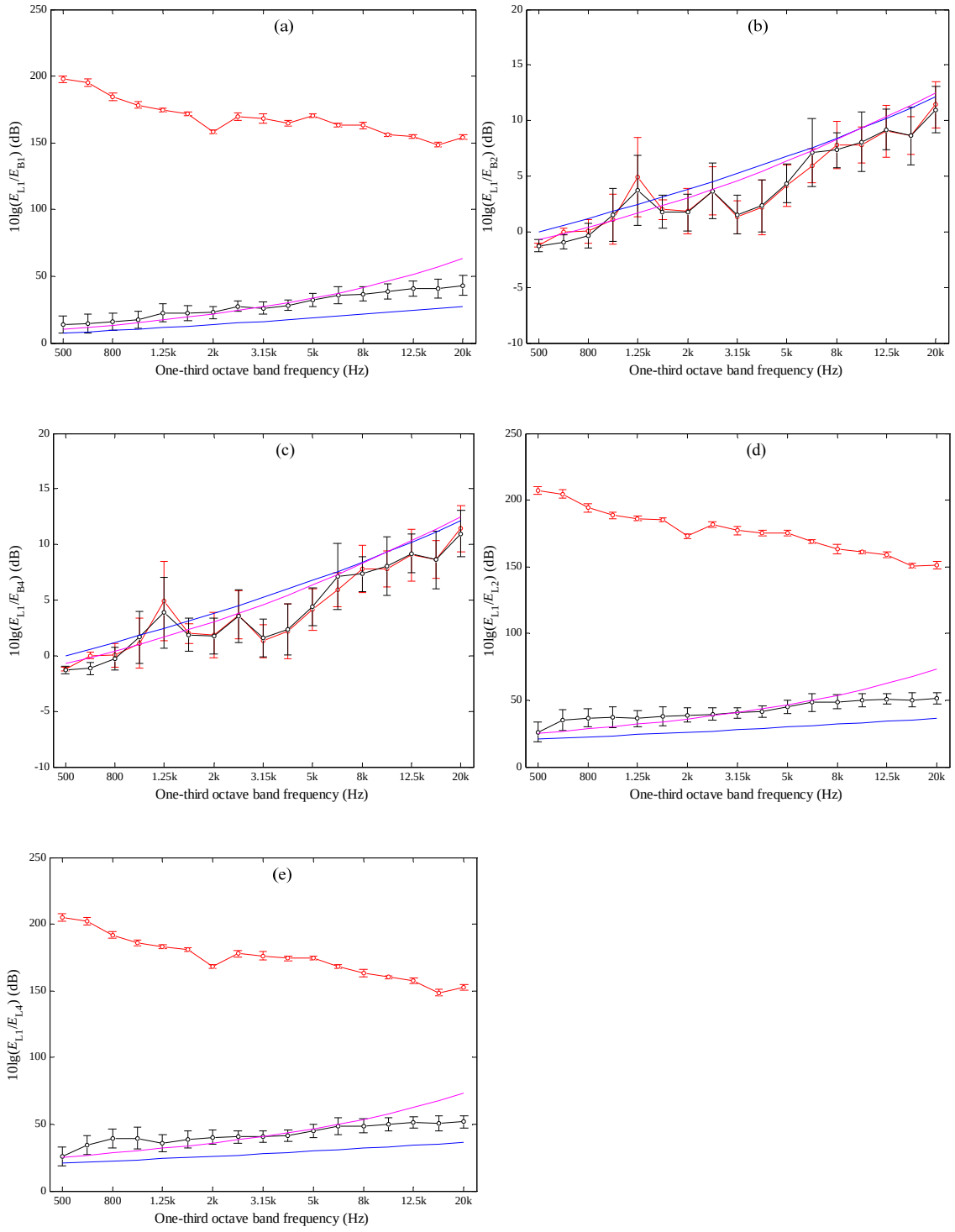

Figure 7.11 Vibration transmission on T124-junction (BL model - Source subsystem: L1). —o—, FEM with uniform material; —o—, FEM with random material; ——, SEA (Euler-Bernoulli group velocity); ——, ASEA (Euler-Bernoulli group velocity). Results from FEM are shown with 95% confidence intervals.

7.3.1.3 X-junction

For the X-junction, consideration is given to the assumption in the derivation (section 2.5.1) that τ_{B1L1}, τ_{B1L3}, τ_{L1B1} ,$\tau_{L1B3,}$ τ_{L1L2} and τ_{L1L4} are zero.

The results from the X-junction are shown with Type A bending wave excitation on Figure 7.12 and longitudinal wave excitation on Figure 7.13.

The energy level differences shown in Figure 7.12 (d), (f) and Figure 7.13 (a), (c), (e), and (g) are much higher (>150 dB) than FEM (uniform material). However FEM (random material) is close to ASEA. Hence the conclusions and analysis for T123-junction also apply to the X-junction.

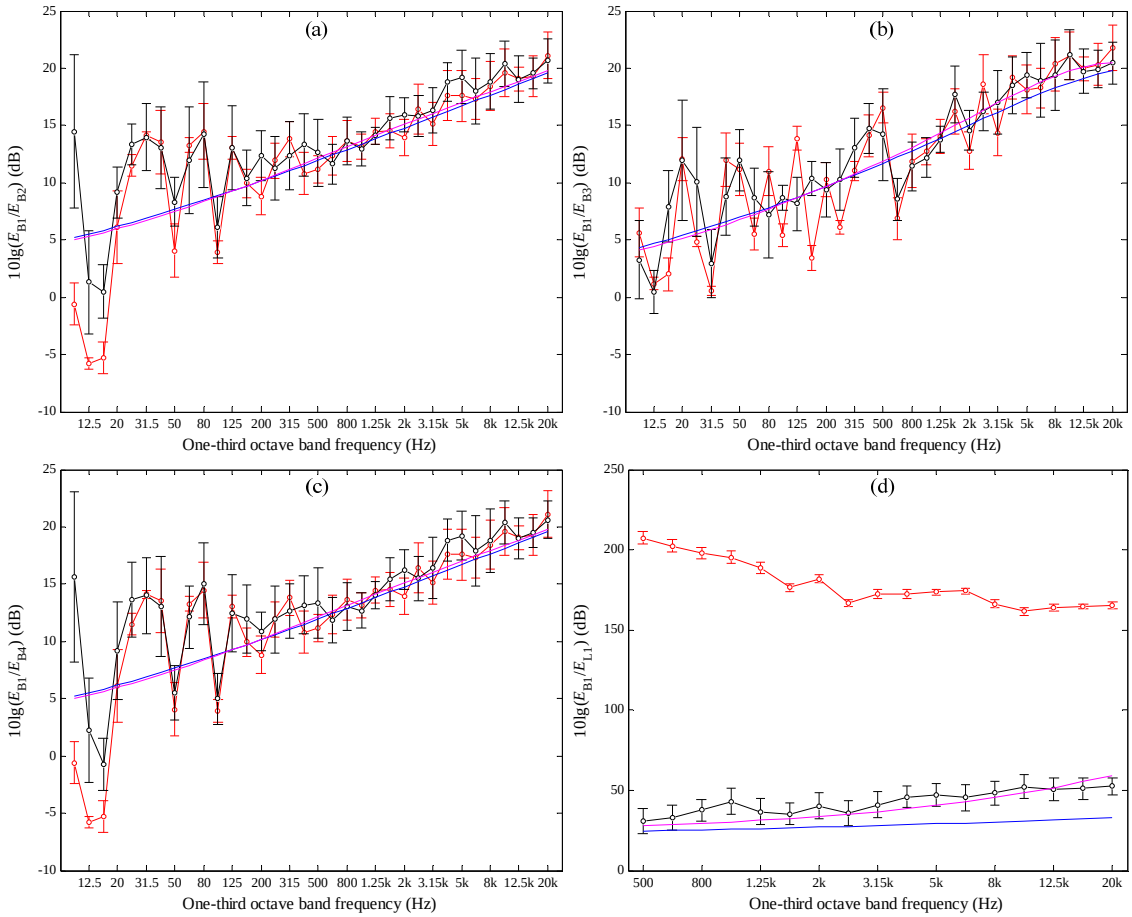

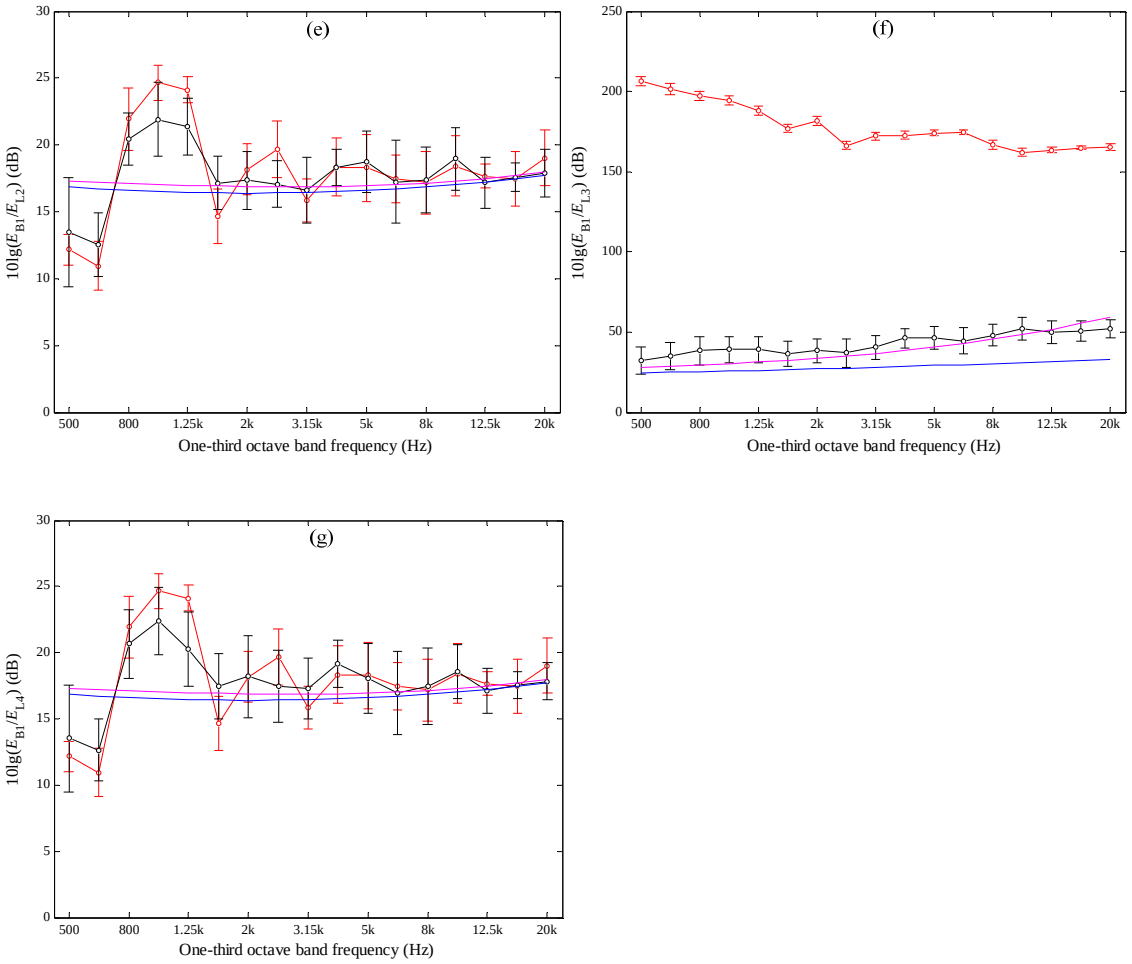

Figure 7.12 Vibration transmission on X-junction (BL model - Source subsystem: B1). —○—, FEM with uniform material; —○—, FEM with random material; ——, SEA (Euler-Bernoulli group velocity); ——, ASEA (Euler-Bernoulli group velocity). Results from FEM are shown with 95% confidence intervals.

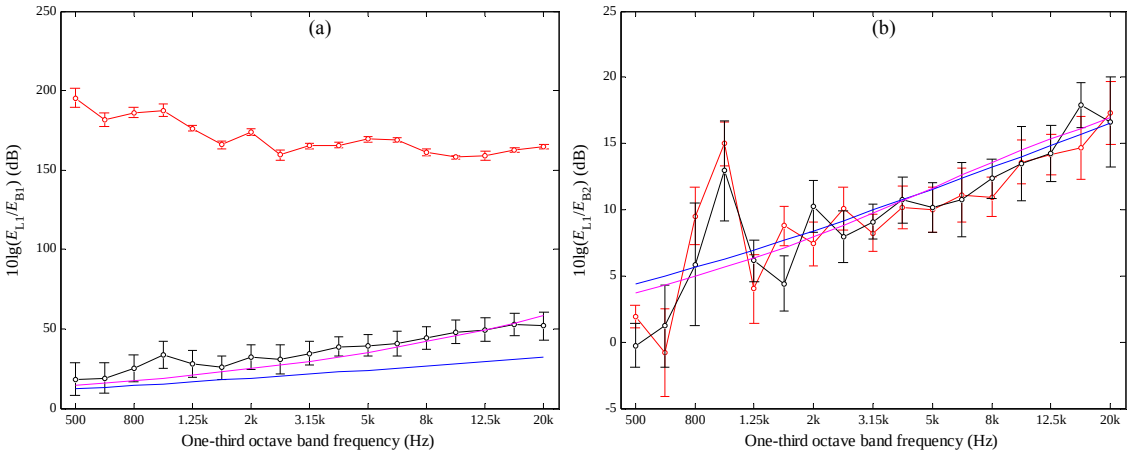

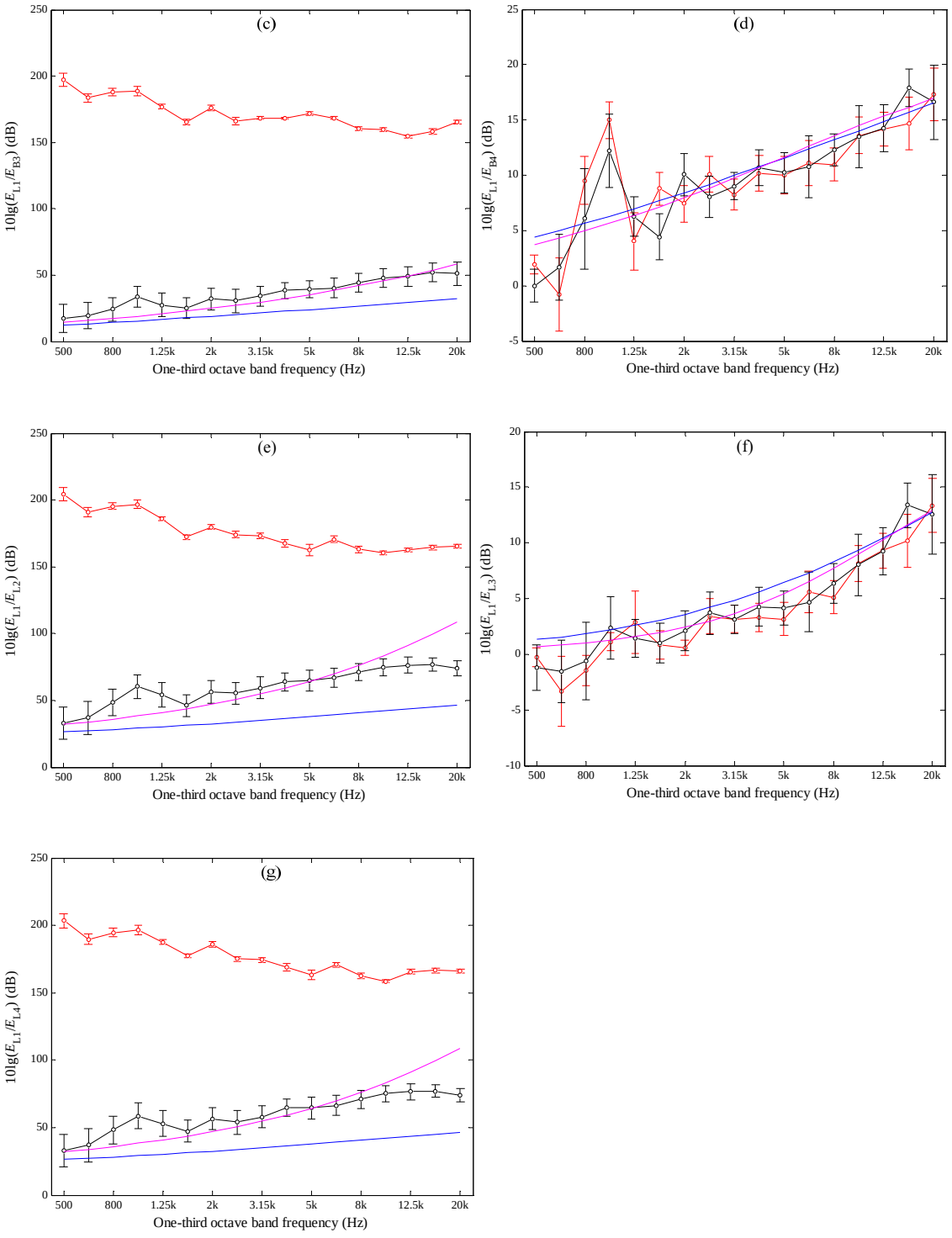

Figure 7.13 Vibration transmission on X-junction (BL model - Source subsystem: L1). —○—, FEM with uniform material; —○—, FEM with random material; ——, SEA (Euler-Bernoulli group velocity); ——, ASEA (Euler-Bernoulli group velocity). Results from FEM are shown with 95% confidence intervals.

7.3.2 BT model for T- and X-junctions

Referring back to section 2.3 on the free-pinned beam, the first torsional mode is in the 200 Hz one-third octave band, and the first Type B bending mode is in the 20 Hz one-third octave band for 1.3 m. Hence in this section the results with torsional motion in either the source subsystem or receiving subsystem are only shown from 200 Hz to 20 kHz, while energy level differences of Type B bending motions to Type B bending motions are shown from 20 Hz to 20 kHz.

7.3.2.1 T123-junction

For the T123-junction, consideration is given to the assumption in the derivation (section 2.6.2) that τ_{T1T2} is zero.

The results from the T123-junction with Type B bending wave excitation on Figure 7.14 and torsional wave excitation are shown on Figure 7.15. In general there is closest agreement between FEM (uniform and random material) and ASEA rather than with SEA. However, Figure 7.15 (d) shows that FEM (uniform material) values are much higher (>150dB) compared to FEM (random material) and that FEM (random material) is close to ASEA. Therefore, for the same reasons given in section 7.3.1 for T123-junction with the BL model, it can be concluded that the wave theory derivation is correct.

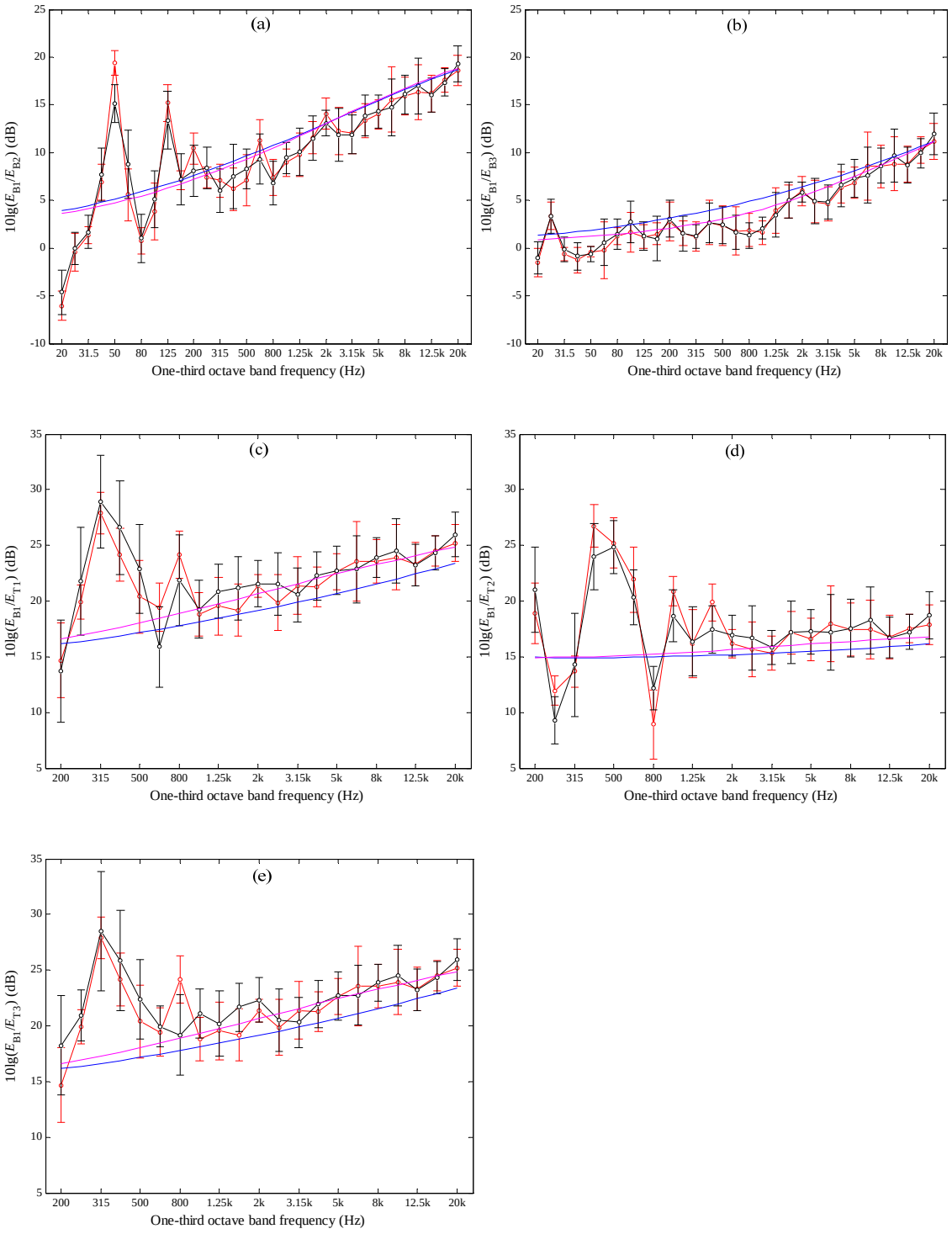

Figure 7.14 Vibration transmission on T123-junction (BT model - Source subsystem: B1). —○—, FEM with uniform material; —○—, FEM with random material; ——, SEA (Euler-Bernoulli group velocity); ——, ASEA (Euler-Bernoulli group velocity). Results from FEM are shown with 95% confidence intervals.

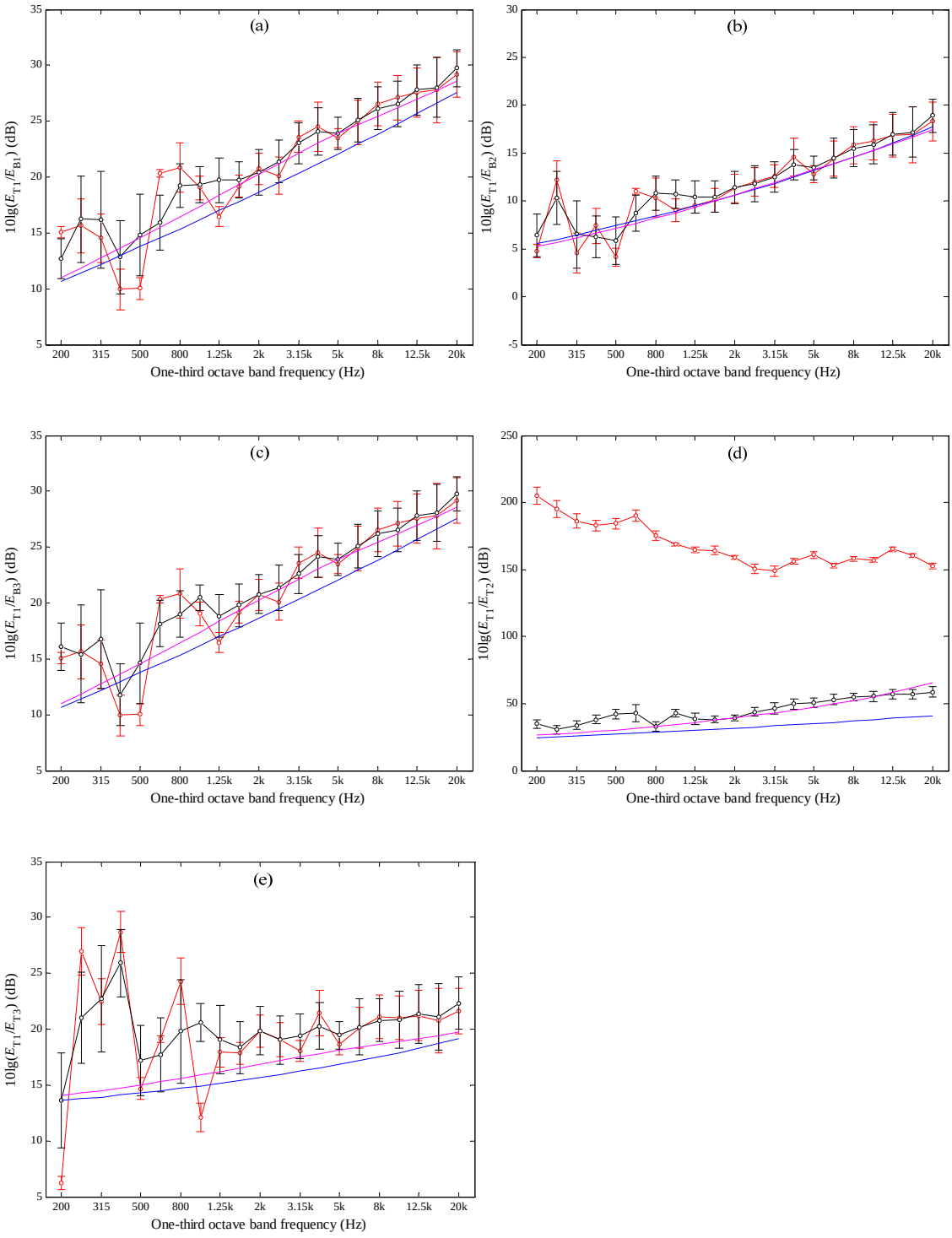

Figure 7.15 Vibration transmission on T123-junction (BT model - Source subsystem: T1). —○—, FEM with uniform material; —○—, FEM with random material; ——, SEA (Euler-Bernoulli group velocity); ——, ASEA (Euler-Bernoulli group velocity). Results from FEM are shown with 95% confidence intervals.

7.3.2.2 T124-junction

For the T124-junction, consideration is given to the assumption in the derivation (section 2.6.3) that τ_{B1T1}, τ_{T1T2} , τ_{T1B1} and τ_{T1T4} are zero.

The results from the T124-junction are shown with Type B bending wave excitation on Figure 7.16 and torsional wave excitation on Figure 7.17. The conclusion is the same as for T123-junction, that ASEA shows closer agreement than SEA with FEM and that the zero transmission coefficients are correct in the wave theory derivation.

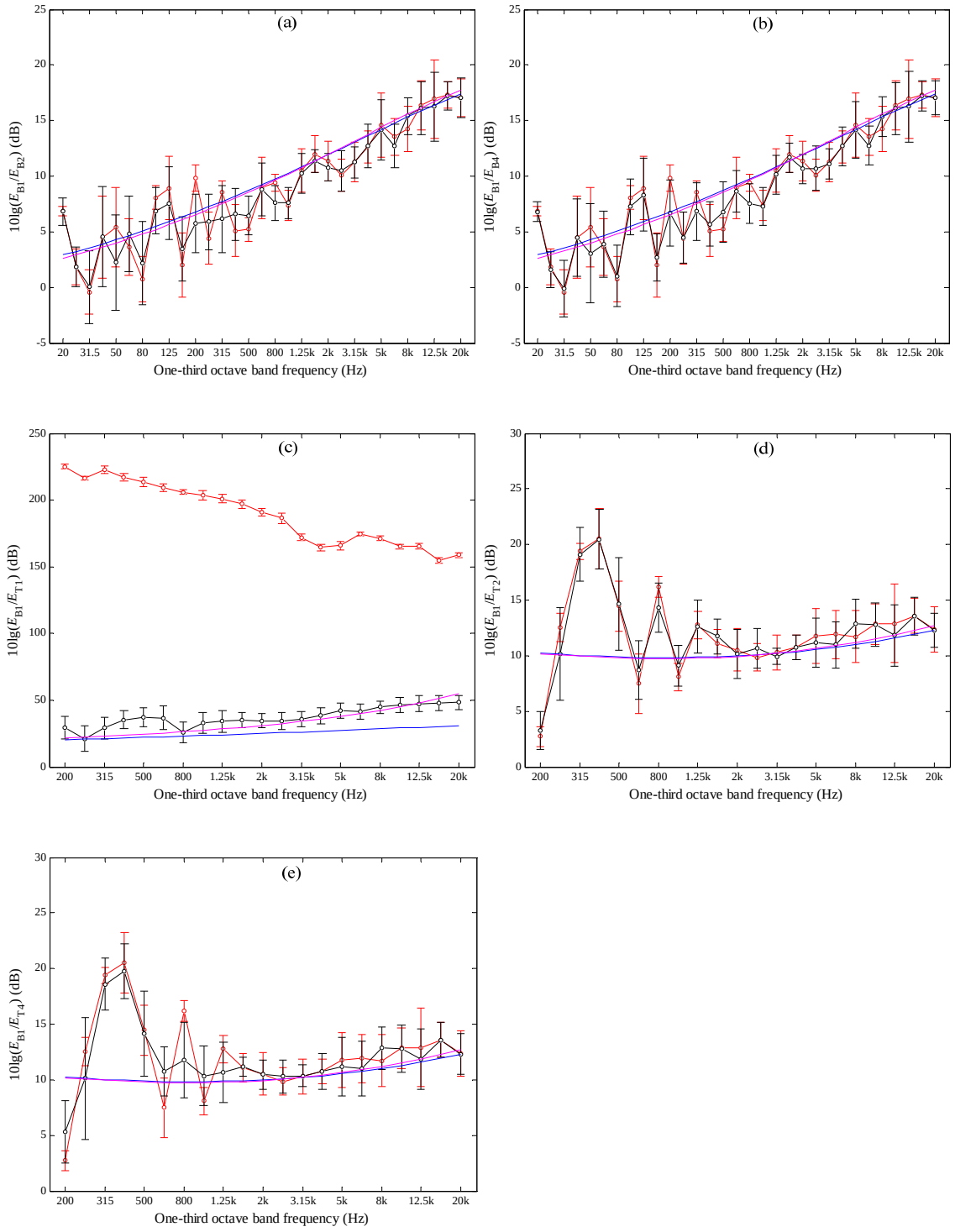

Figure 7.16 Vibration transmission onT124-junction (BT model - Source subsystem: B1). —○—, FEM with uniform material; —○—, FEM with random material; ——, SEA (Euler-Bernoulli group velocity); ——, ASEA (Euler-Bernoulli group velocity). Results from FEM are shown with 95% confidence intervals.

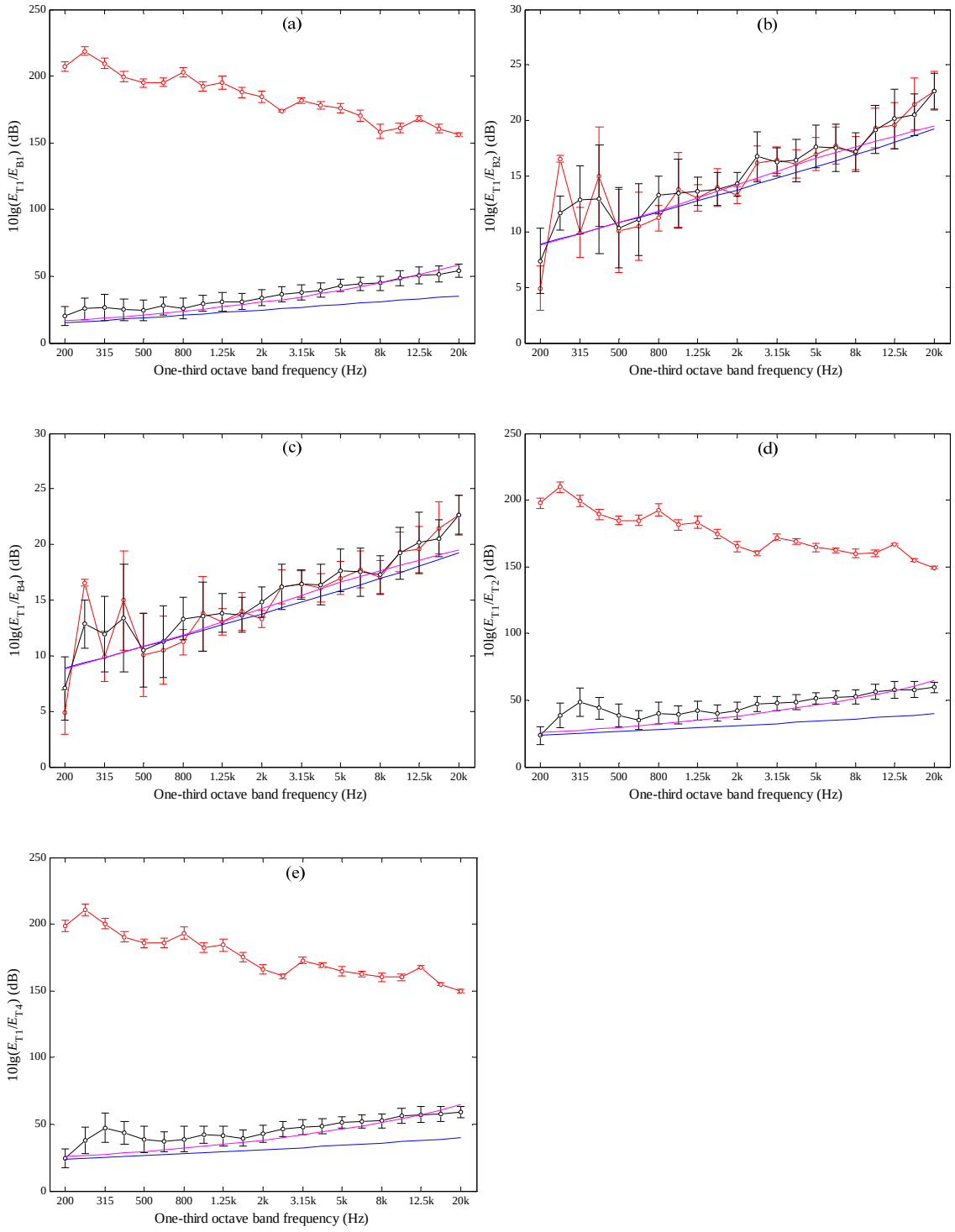

Figure 7.17 Vibration transmission onT124-junction (BT model - Source subsystem: T1). —○—, FEM with uniform material; —○—, FEM with random material; ——, SEA (Euler-Bernoulli group velocity); ——, ASEA (Euler-Bernoulli group velocity). Results from FEM are shown with 95% confidence intervals.

7.3.2.3 X-junction

For the X-junction, consideration is given to the assumption in the derivation (section 2.6.1) that τ_{B1T1}, τ_{B1T3}, τ_{T1B1} ,$\tau_{T1B3,}$ τ_{T1T2} and τ_{T1T4} are zero.

The results from the X-junction are shown with Type B bending wave excitation on Figure 7.18 and torsional wave excitation on Figure 7.19. The agreement indicates that the conclusions and analysis for T123-junction also applies to the X-junction.

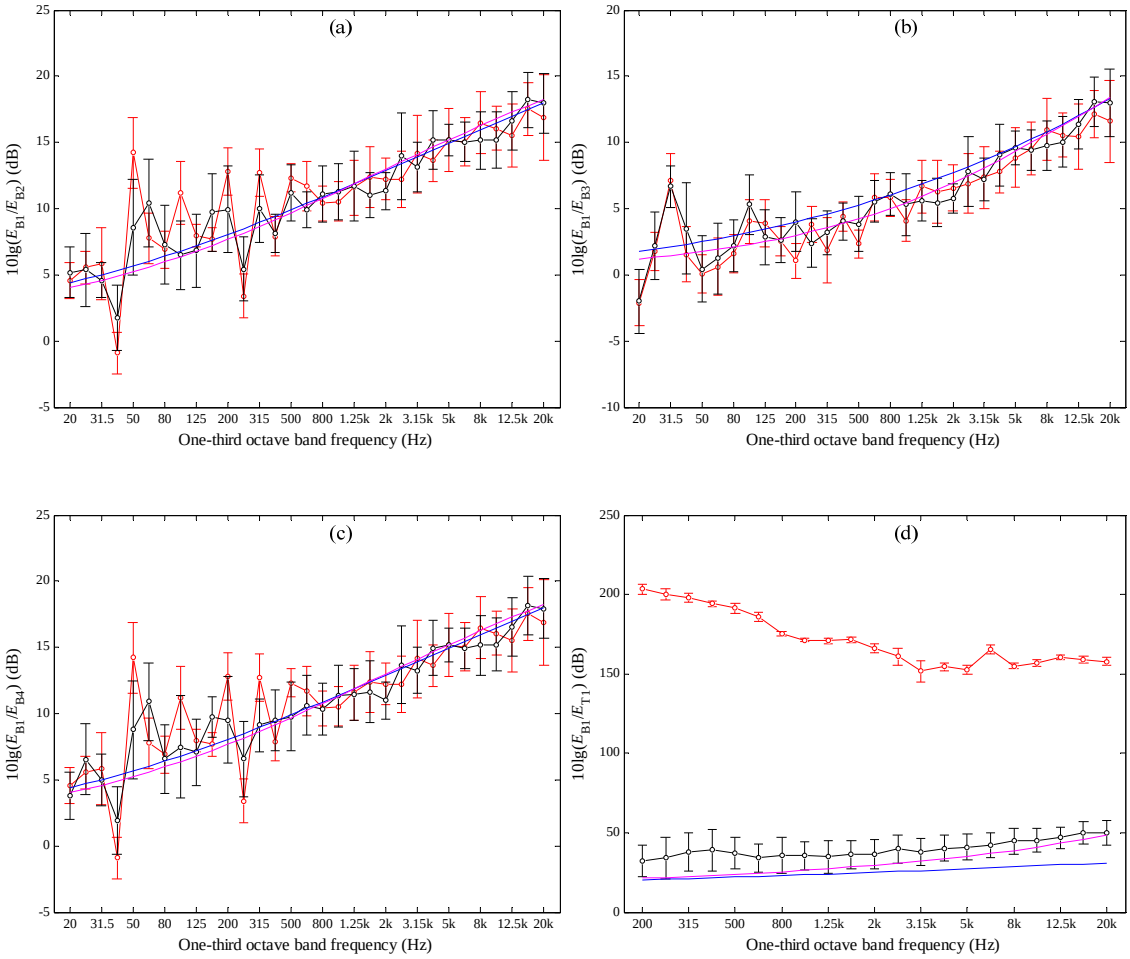

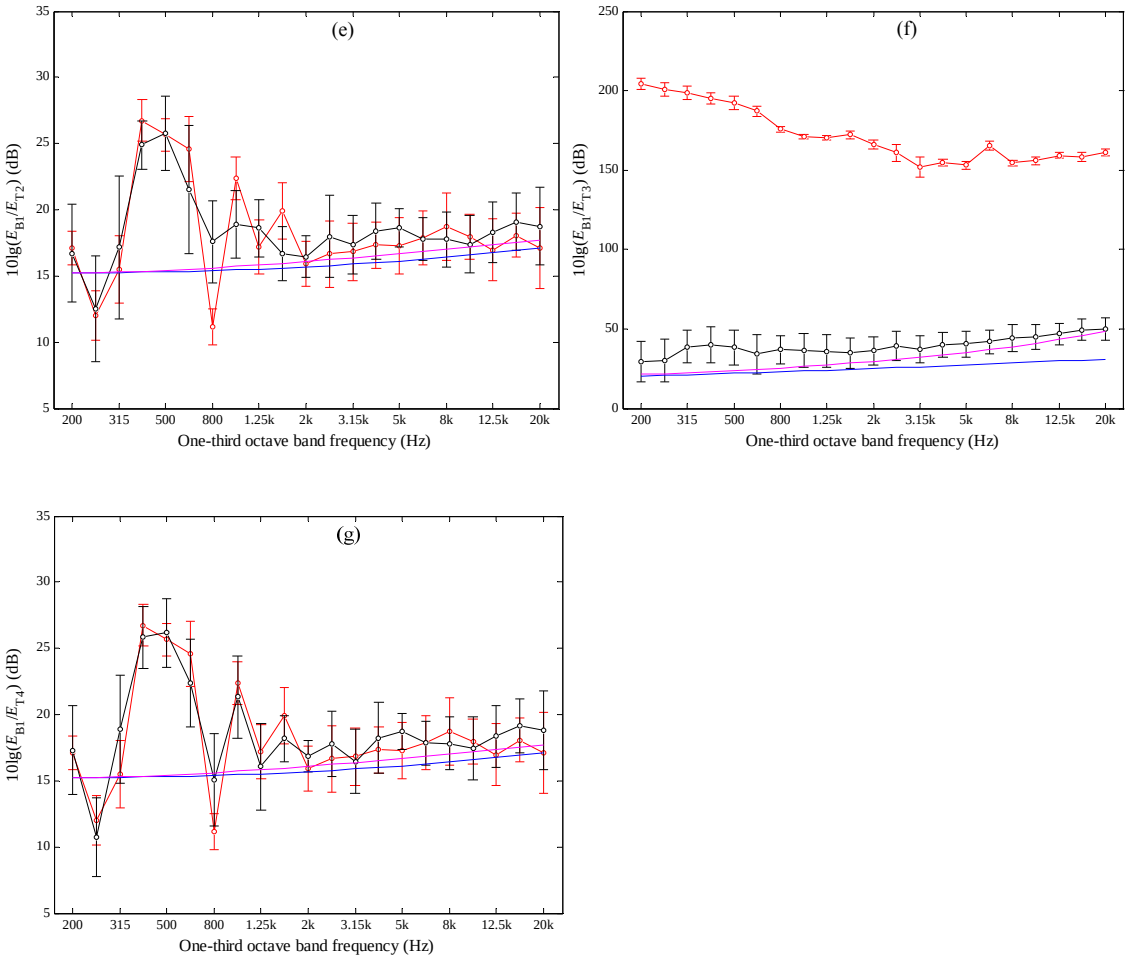

Figure 7.18 Vibration transmission on X-junction (BT model - Source subsystem: B1). —○—, FEM with uniform material; —○—, FEM with random material; ——, SEA (Euler-Bernoulli group velocity); ——, ASEA (Euler-Bernoulli group velocity). Results from FEM are shown with 95% confidence intervals.

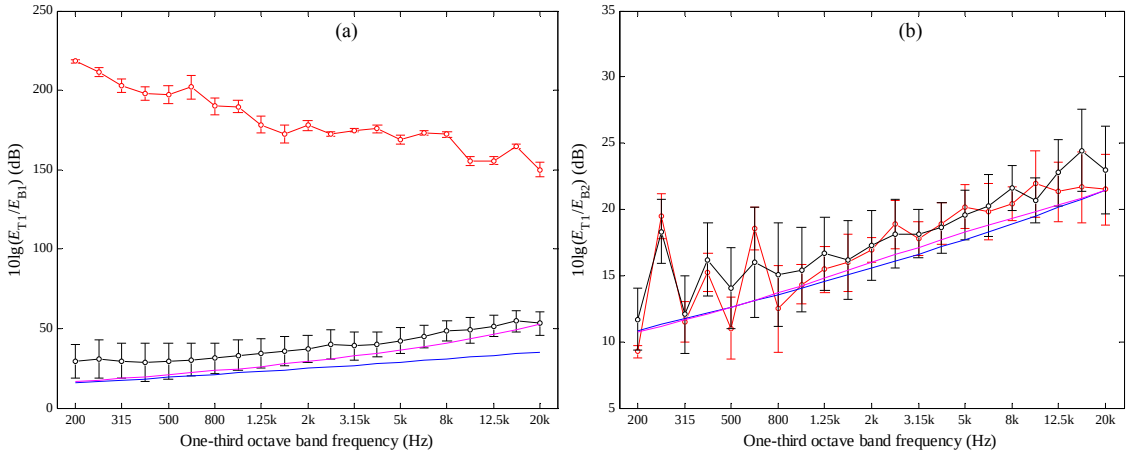

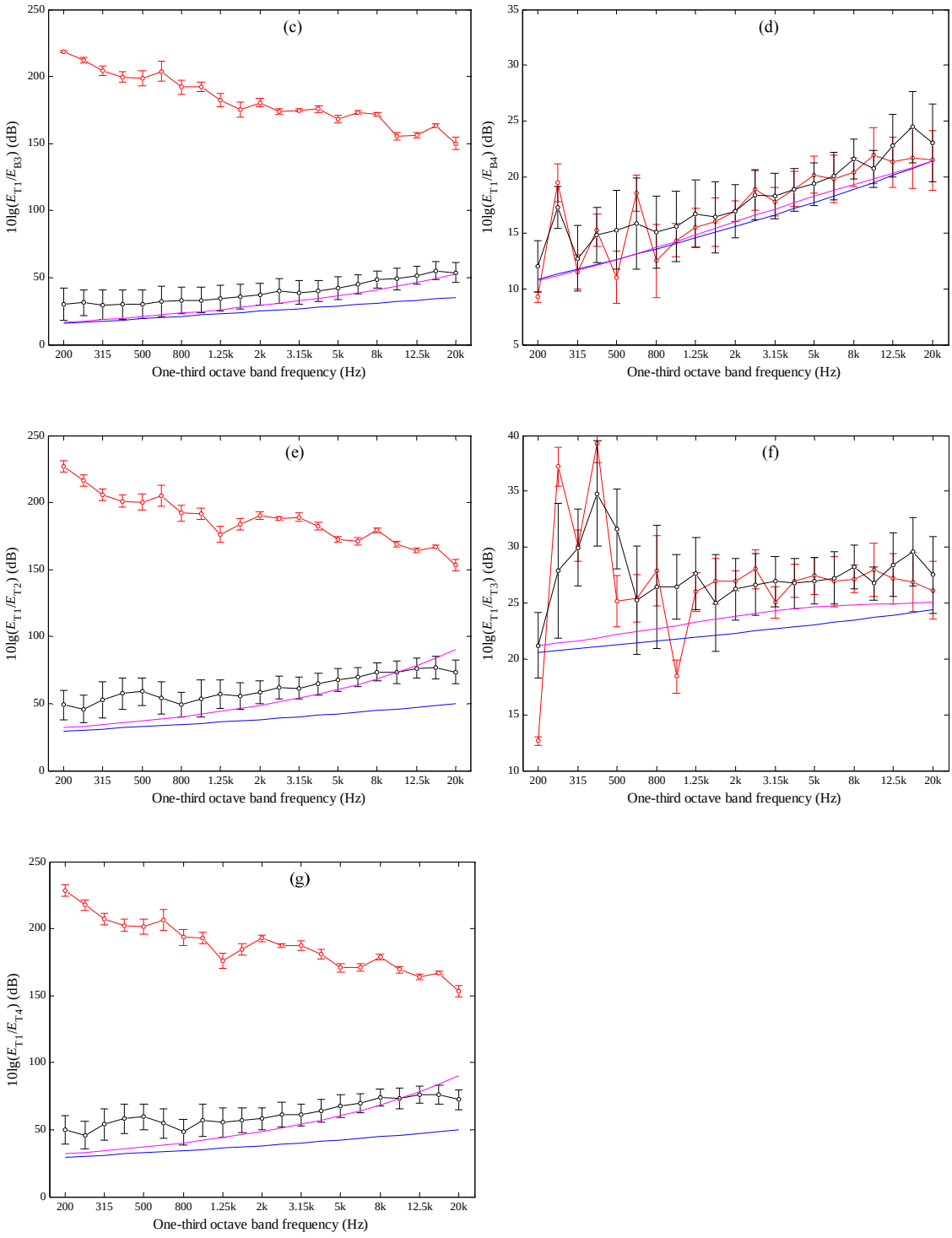

Figure 7.19 Vibration transmission on X-junction (BT model - Source subsystem: T1). —○—, FEM with uniform material; —○—, FEM with random material; ——, SEA (Euler-Bernoulli group velocity); ——, ASEA (Euler-Bernoulli group velocity). Results from FEM are shown with 95% confidence intervals.

7.4 Investigation into perfect and imperfectly periodic frameworks of beams

The five-bay truss shown in Figure 7.20 is investigated in this section considering the B model, BL model and BT model. The beam lengths for beams 1, 4, 7, 10, 13 and 16 are 1.0 m and the others are 1.3 m. The material is the same as described in section 2.3.

To assess the application of ASEA to a truss beam where the individual beams have low propagation losses, the B model is assessed with a lower internal loss factor.

FEM simulations (Euler-Bernoulli elements) on the truss beam are carried out with random material (i.e. an imperfect periodic structure) and with uniform material (i.e. a perfect periodic structure). These are both compared with SEA and ASEA predictions that use Euler-Bernoulli beam group velocity. Due to structural symmetry results are only shown for beams 2, 4, 5, 7, 8, 10, 11, 13, 14, 16.

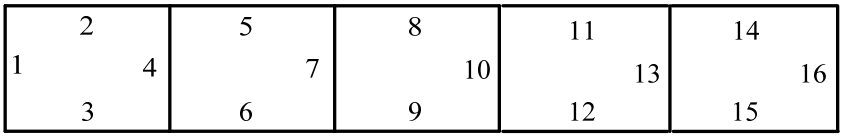

Figure 7.20 Five-bay truss.

7.4.1 Bending wave transmission (B model) for the five-bay truss beam

7.4.1.1 High internal losses (ILF=0.06)

Figure 7.21 the results for the B model of the five-bay truss with excitation of Type A bending waves on beam 1 where all beams have an ILF of 0.06.

Figure 7.21 (a) shows close agreement between FEM, SEA and ASEA for the subsystem B2 that is adjacent to the source (this also occurred with the isolated L- and T-junctions).

For Figure 7.21 (b) to (j) below 800 Hz ASEA gives lower energy level differences than SEA which indicates the existence of tunneling mechanisms. In general, FEM (random material) shows closer agreement with ASEA than FEM (uniform material). This is likely to be due to the fact that ASEA is not intended for perfectly periodic structures

where phase effects might be important, but (like SEA) it is suited to predicting the ensemble average response for similar subsystems.

Above 800 Hz ASEA results for the five-bay truss show significantly higher energy level differences than SEA in subsystems that are not directly connected to the source subsystem (see Figure 7.21 (b) to (j)). This indicates high propagation losses. Above 800 Hz, Figure 7.21 (b) and (c) show close agreement between FEM and ASEA. However, Figure 7.21 (d) to (j) above 800 Hz show that FEM (uniform and random material properties) no longer agrees with ASEA (or SEA) when there are three or more structural junctions between the source and receiving beam. This lack of agreement increases as the beam becomes increasingly distant from the source subsystem. This implies that high propagation losses no longer occur on beams that are at least three structural junctions away from the source beams. In chapter 6 this was not seen with bending excitation for the BL and BT models of the three-bay truss. However referring back to section 6.7.2 for longitudinal excitation on the three-bay truss, FEM was also significantly lower than ASEA and SEA on the beam that was furthest from the source subsystem (i.e. subsystem L10).

This problem is unlikely to be an error due to numerical accuracy in the Abaqus FEM model because in section 7.3 energy level differences were predicted that were >150dB. The fact that energy level differences from FEM are much lower than both SEA and ASEA might imply that the response of the distant subsystems is due to global modes rather than local modes. In sections 7.4.2 and 7.4.3 the BL and BT models will be investigated to see whether the same phenomenon occurs.

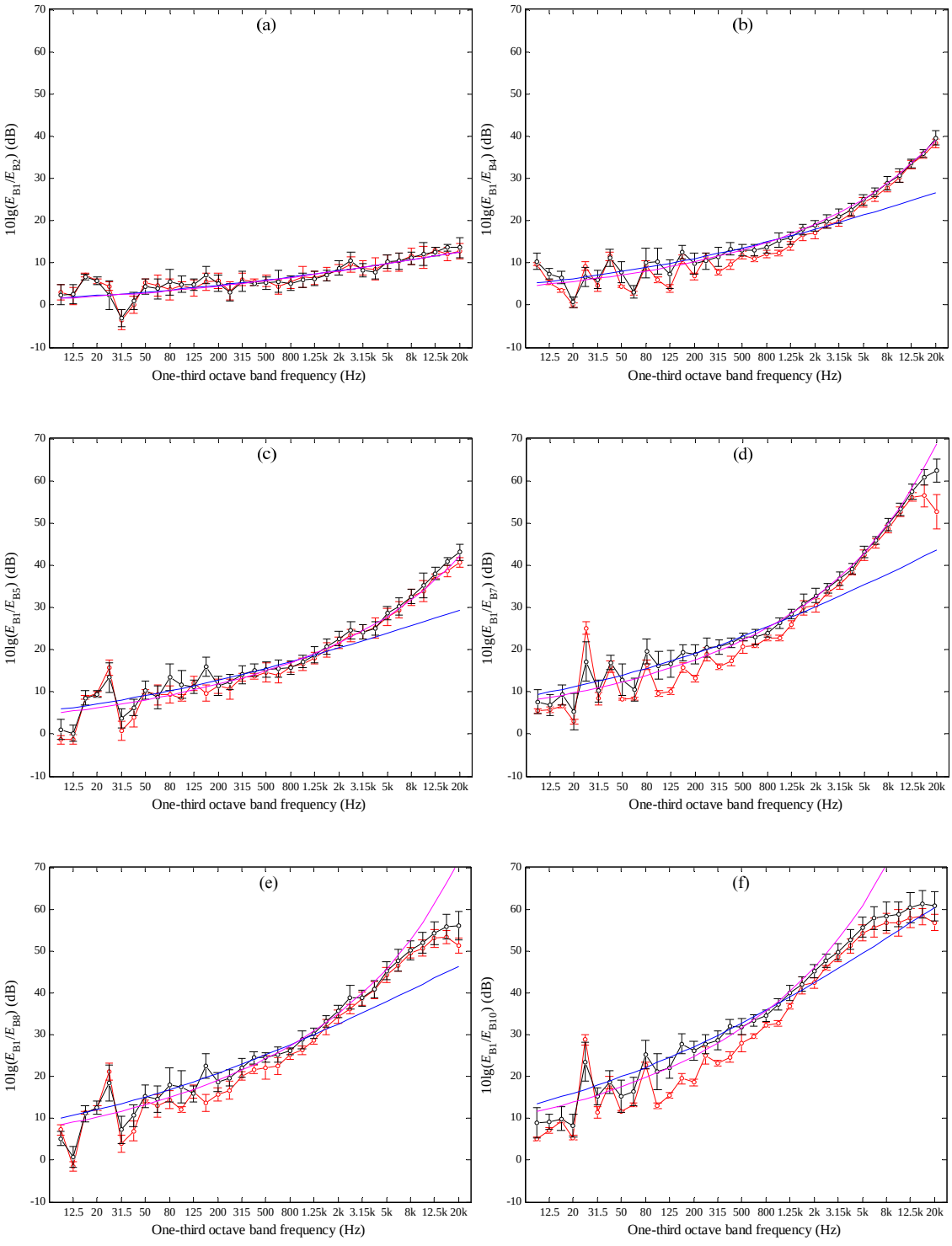
(a)
(b)
(c)
(d)
(e)
(f)
10lg(E_{B1}/E_{B2}) (dB)
10lg(E_{B1}/E_{B4}) (dB)
10lg(E_{B1}/E_{B5}) (dB)
10lg(E_{B1}/E_{B7}) (dB)
10lg(E_{B1}/E_{B8}) (dB)
10lg(E_{B1}/E_{B10}) (dB)
70
60
50
40
30
20
10
0
-10
12.5 20 31.5 50 80 125 200 315 500 800 1.25k 2k 3.15k 5k 8k 12.5k 20k
One-third octave band frequency (Hz)

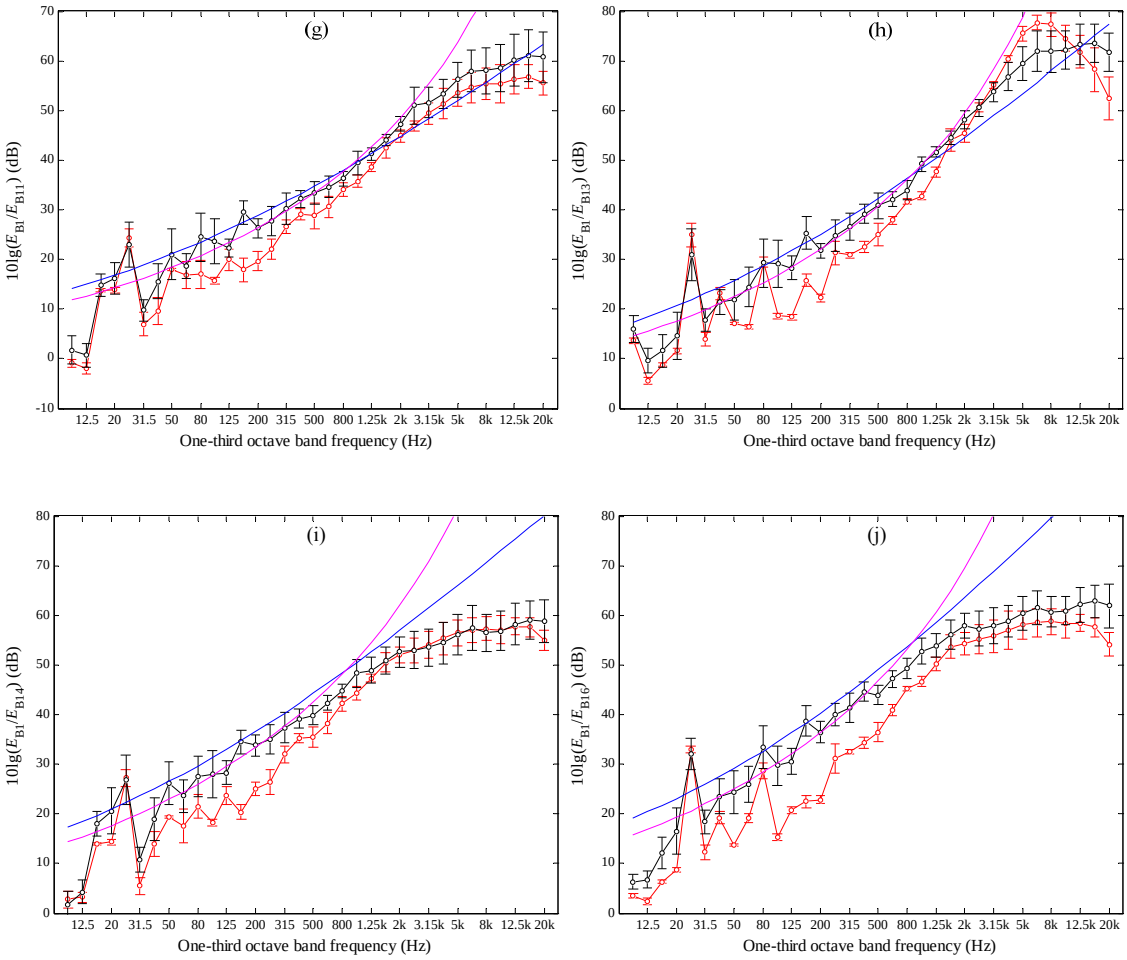

Figure 7.21 Vibration transmission on the five-bay truss beam of B model, ILF=0.06. —○—, FEM with uniform material; —○—, FEM with random material; ——, SEA (Euler-Bernoulli group velocity); ——, ASEA (Euler-Bernoulli group velocity). Results from FEM are shown with 95% confidence intervals.

7.4.1.2 Low internal losses (ILF=0.01)

In Figure 7.22 the results are shown for the B model of the five-bay truss with excitation of Type A bending waves on beam 1 where all beams have an ILF of 0.01.

Figure 7.22 (a) shows close agreement between FEM, SEA and ASEA for subsystem B2 that is adjacent to the source. In contrast to section 7.4.1.1 where the beams had an ILF of 0.06 and propagation losses were significant above 800Hz, Figure 7.22 (b) to (j) show no evidence of propagation losses but evidence of tunneling appears across the entire frequency range. In general, for beams that are not directly connected to the source subsystem, FEM (random material) shows closer agreement with ASEA than FEM (uniform material); FEM (uniform material) appears to have increased indirect

coupling (i.e. tunneling) due to the fact that all beams have exactly the same length and material properties.

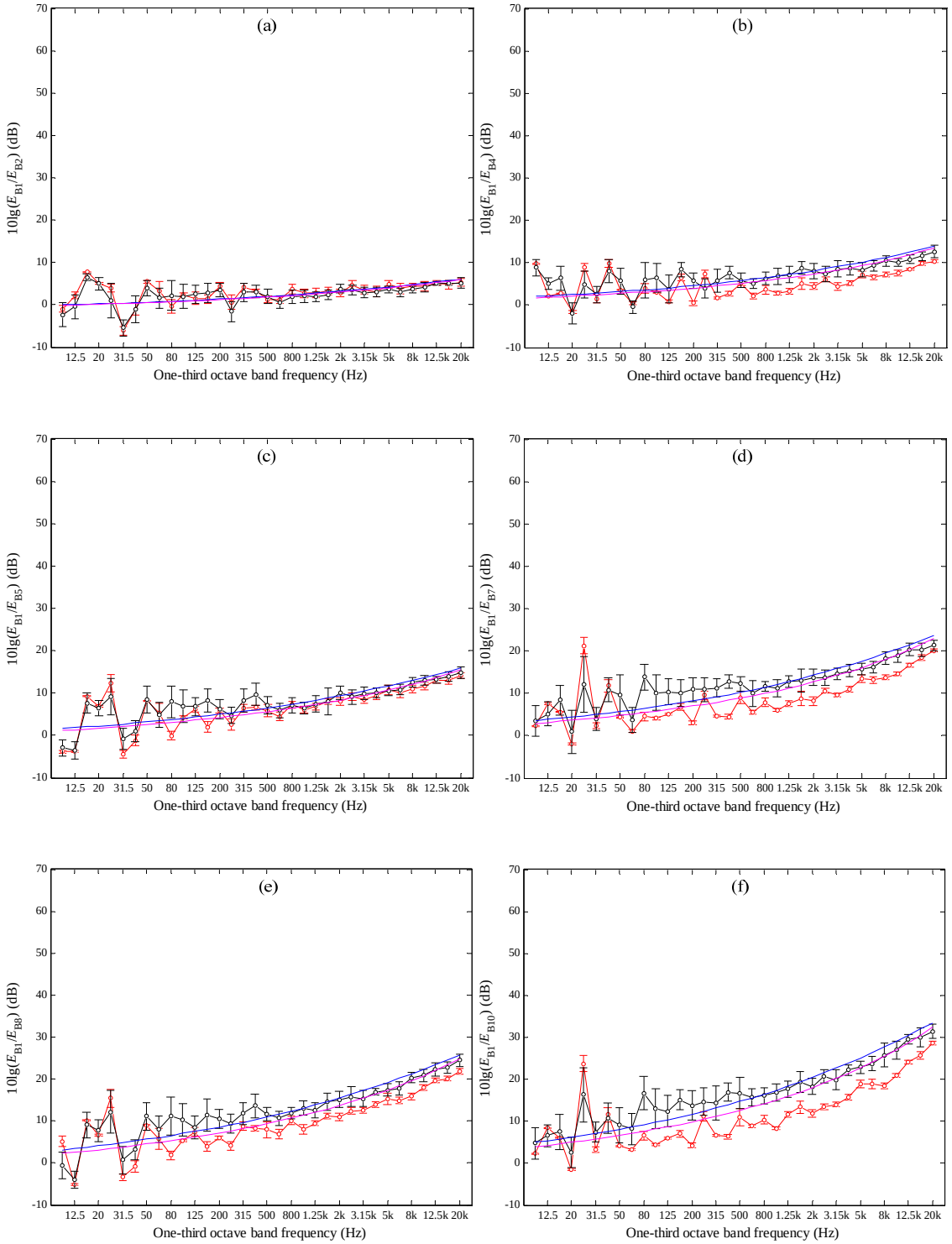

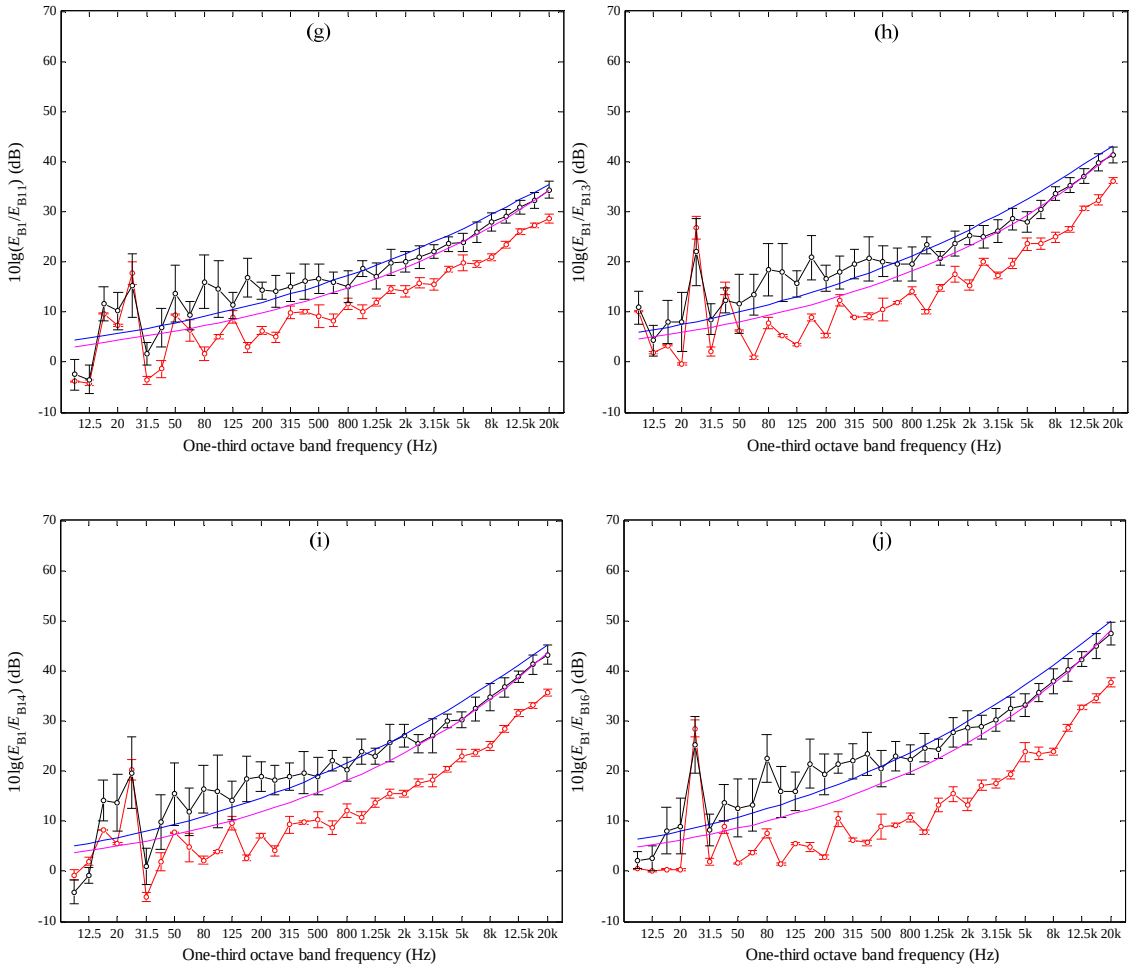

Figure 7.22 Vibration transmission on five bay truss of B model with reduced damping, ILF=0.01. —○—, FEM with uniform material; —○—, FEM with random material; ——, SEA (Euler-Bernoulli group velocity); ——, ASEA (Euler-Bernoulli group velocity). Results from FEM are shown with 95% confidence intervals.

7.4.2 Bending and longitudinal wave transmission (BL model) for the five-bay truss beam (ILF=0.06)

In this section, Type A bending waves or longitudinal waves are excited on the source subsystem of the five-bay truss.

Considering the isolated beam with pinned-pinned boundary (Figure 2.4) the fundamental longitudinal mode frequency is in the 1 kHz one-third octave band, and the fundamental Type A bending mode is in the 25 Hz band. So the energy level differences for BL model of the truss are shown from 10 Hz to 20 kHz for bending waves on the

source and receiving subsystem and from 1 kHz to 20 kHz for longitudinal waves on either the source or receiving subsystem.

Figure 7.23 shows the results for the BL model of the five-bay truss with excitation of Type A bending waves on beam 1. Figure 7.24 shows results for the BL model of the five-bay truss with excitation of Type A bending waves on beam 1.

In Figure 7.23 (b) to (j) below 8k Hz ASEA gives lower energy level differences than SEA which indicates the existence of tunneling mechanisms. In general, FEM (random material and uniform material) shows close agreement with ASEA.

In Figure 7.23 (b) to (j) above 8k Hz ASEA for the five-bay truss shows significantly higher energy level differences than SEA in subsystems that are not directly connected to the source subsystem. This indicates high propagation losses and these are adequately predicted by ASEA above 8 kHz (see Figure 7.23 (b), (c) and (d) show close agreement between FEM and ASEA). However, Figure 7.23 (e) to (j) above 8 kHz shows that FEM (uniform and random material properties) no longer agrees with ASEA (or SEA). This implies that high propagation losses no longer occur on subsystems that are at least three structural junctions away from the source subsystem.

The same general trends can be seen when (a) bending waves are excited on the source subsystem and the receiving subsystem represents longitudinal wave energy – see Figure 7.23 (k) to (u), and (b) when longitudinal waves are excited on the source subsystem – see Figure 7.24.

Compared with B model of the five-bay truss, ASEA shows closer agreement with FEM (uniform or random material) over a wider frequency range from 10 Hz to 8 kHz (e.g. Figure 7.23 (j)). It can therefore be concluded that the generation of longitudinal waves at the junctions increases the indirect coupling below 8 kHz. This indicates that ASEA can give good estimates when there is tunneling but can give poor estimates when the propagation losses become very high.

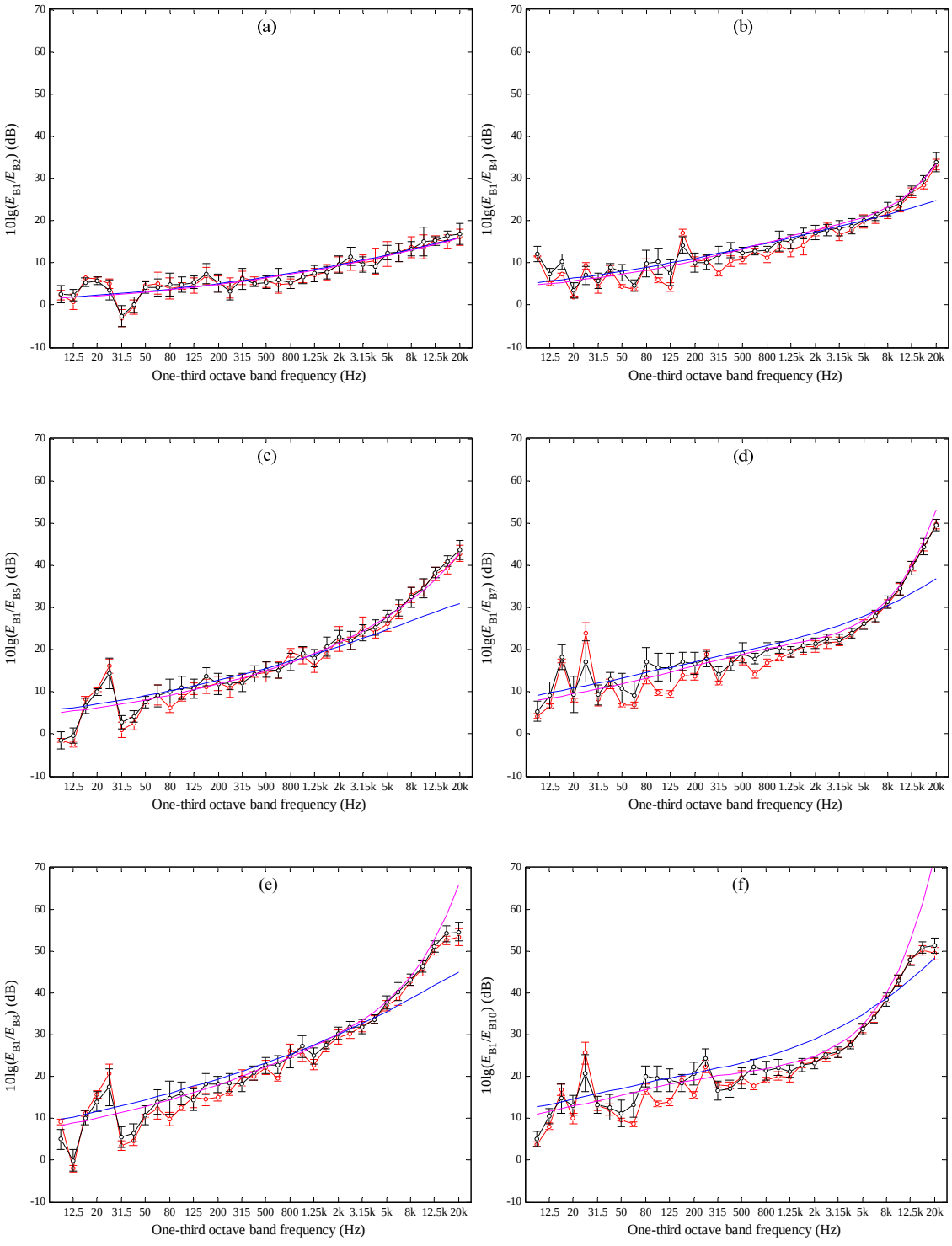
(a)
(b)
(c)
(d)
(e)
(f)
10lg(E_B1/E_B2) (dB)
10lg(E_B1/E_B4) (dB)
10lg(E_B1/E_B5) (dB)
10lg(E_B1/E_B7) (dB)
10lg(E_B1/E_B8) (dB)
10lg(E_B1/E_B10) (dB)
70
60
50
40
30
20
10
0
-10
12.5 20 31.5 50 80 125 200 315 500 800 1.25k 2k 3.15k 5k 8k 12.5k 20k
One-third octave band frequency (Hz)

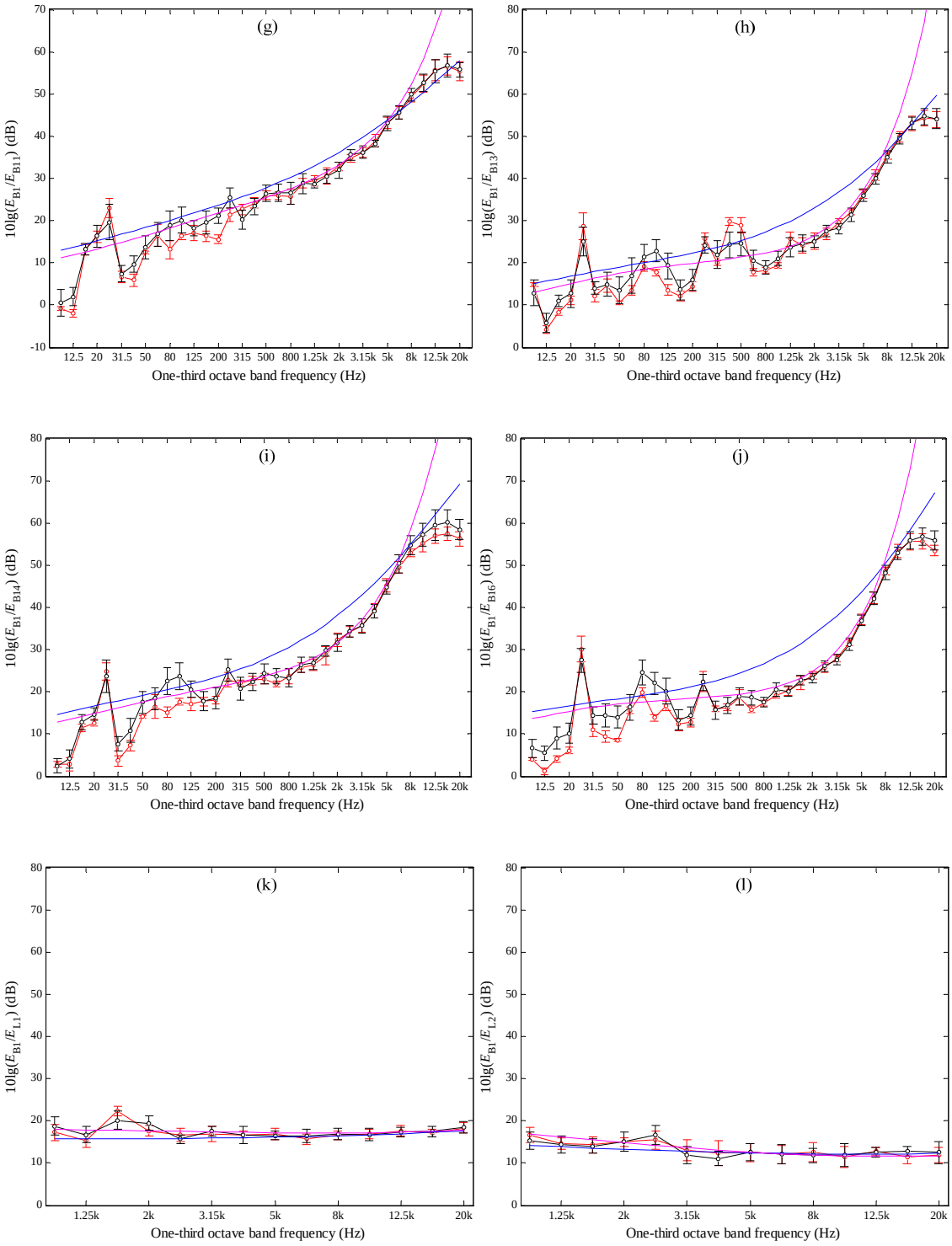
(g)
(h)
(i)
(j)
(k)
(l)
$10\lg(E_{B1}/E_{B11})$ (dB)
$10\lg(E_{B1}/E_{B13})$ (dB)
$10\lg(E_{B1}/E_{B14})$ (dB)
$10\lg(E_{B1}/E_{B16})$ (dB)
$10\lg(E_{B1}/E_{L1})$ (dB)
$10\lg(E_{B1}/E_{L2})$ (dB)
One-third octave band frequency (Hz)
12.5 20 31.5 50 80 125 200 315 500 800 1.25k 2k 3.15k 5k 8k 12.5k 20k
1.25k 2k 3.15k 5k 8k 12.5k 20k

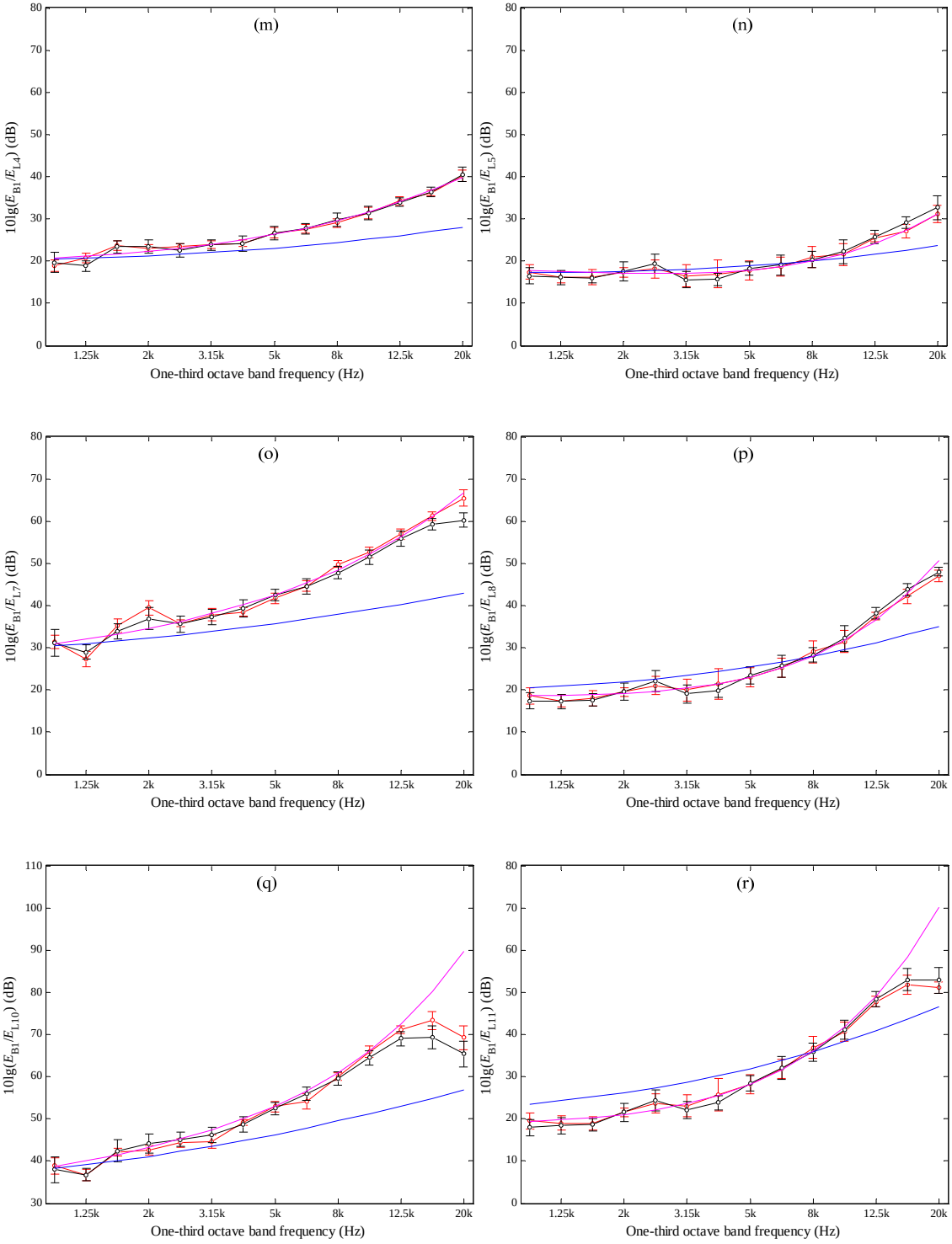
(m)
(n)
(o)
(p)
(q)
(r)
$10\lg(E_{B1}/E_{L4})$ (dB)
$10\lg(E_{B1}/E_{L5})$ (dB)
$10\lg(E_{B1}/E_{L7})$ (dB)
$10\lg(E_{B1}/E_{L8})$ (dB)
$10\lg(E_{B1}/E_{L10})$ (dB)
$10\lg(E_{B1}/E_{L11})$ (dB)
One-third octave band frequency (Hz)
1.25k
2k
3.15k
5k
8k
12.5k
20k

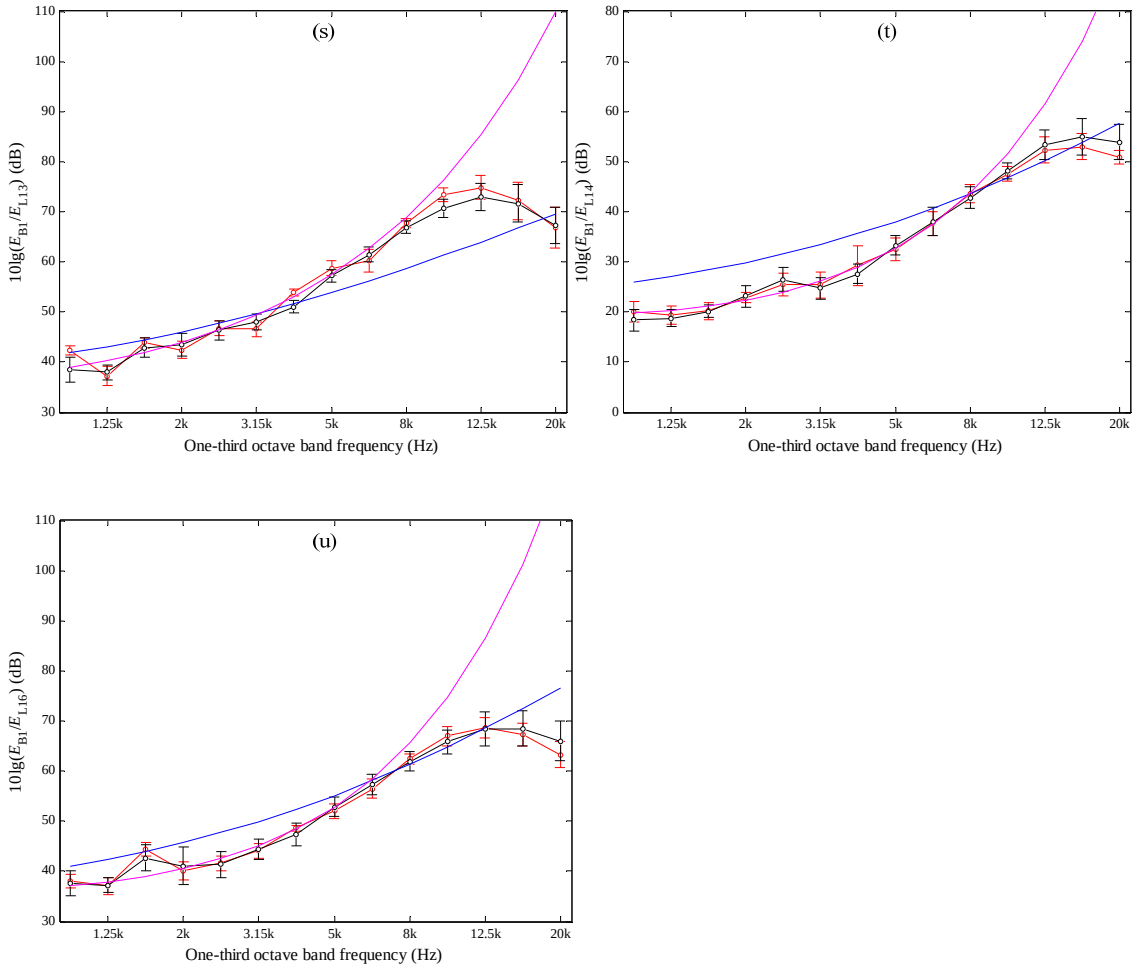

Figure 7.23 Type A bending wave transmission on the five-bay truss (BL model - Source subsystem: B1). —○—, FEM with uniform material; —○—, FEM with random material; ——, SEA (Euler-Bernoulli group velocity); ——, ASEA (Euler-Bernoulli group velocity). Results from FEM are shown with 95% confidence intervals.

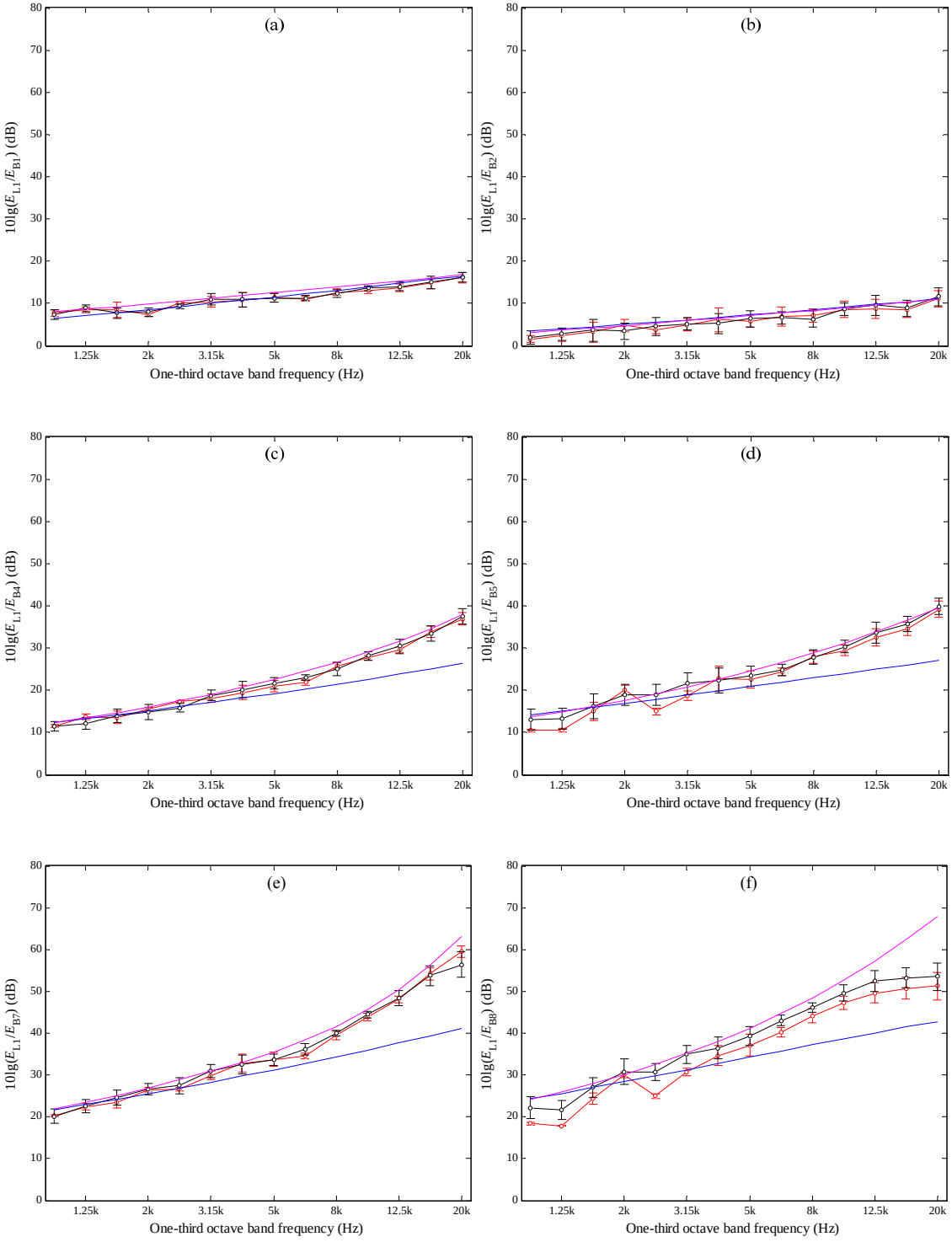
(a)
(b)
(c)
(d)
(e)
(f)
10lg(E_L1/E_B1) (dB)
10lg(E_L1/E_B2) (dB)
10lg(E_L1/E_B4) (dB)
10lg(E_L1/E_B5) (dB)
10lg(E_L1/E_B7) (dB)
10lg(E_L1/E_B8) (dB)
0
10
20
30
40
50
60
70
80
1.25k
2k
3.15k
5k
8k
12.5k
20k
One-third octave band frequency (Hz)

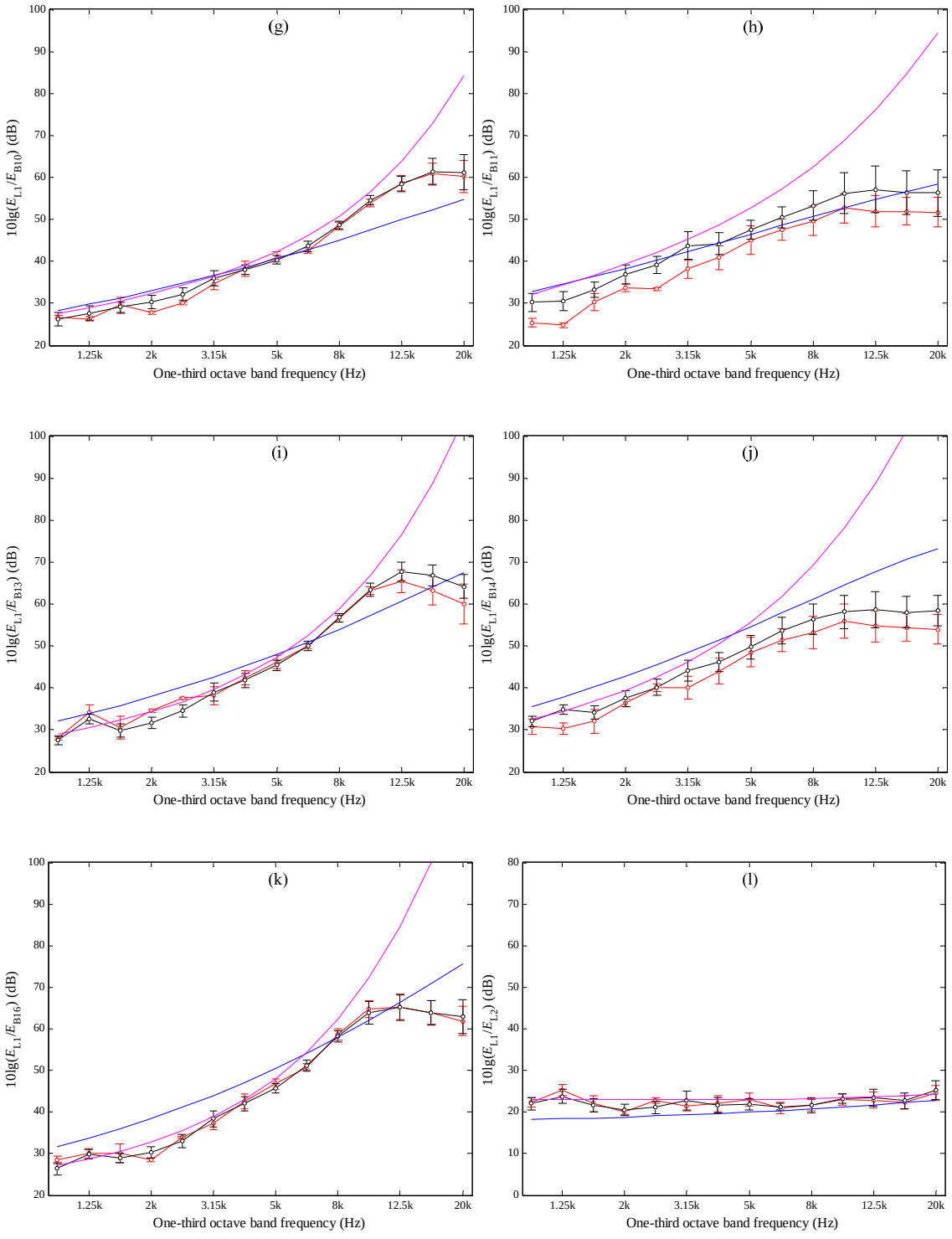
(g)
(h)
(i)
(j)
(k)
(l)
One-third octave band frequency (Hz)
1.25k
2k
3.15k
5k
8k
12.5k
20k

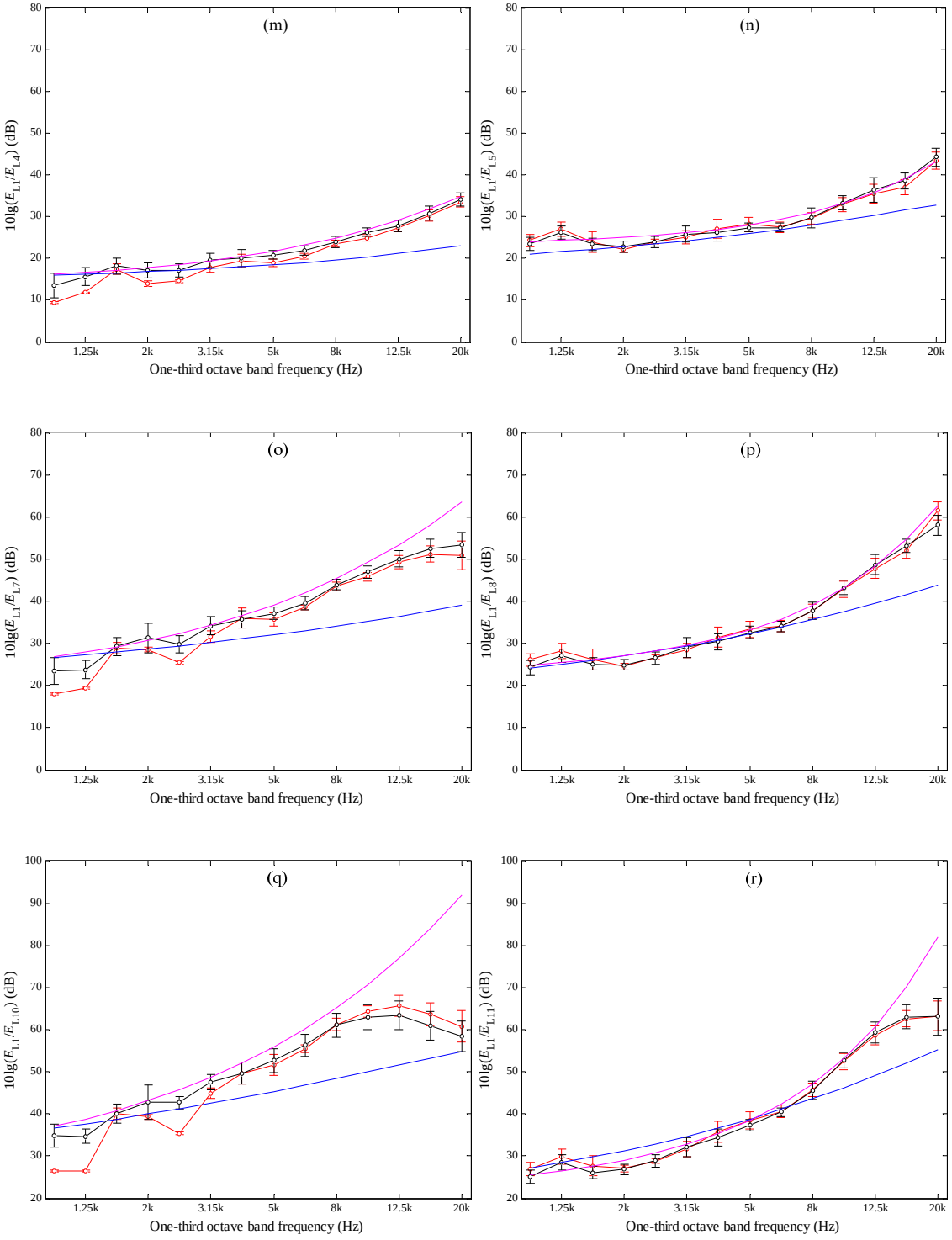
(m)
(n)
(o)
(p)
(q)
(r)
$10\lg(E_{L1}/E_{L4})$ (dB)
$10\lg(E_{L1}/E_{L5})$ (dB)
$10\lg(E_{L1}/E_{L7})$ (dB)
$10\lg(E_{L1}/E_{L8})$ (dB)
$10\lg(E_{L1}/E_{L10})$ (dB)
$10\lg(E_{L1}/E_{L11})$ (dB)
One-third octave band frequency (Hz)
1.25k
2k
3.15k
5k
8k
12.5k
20k

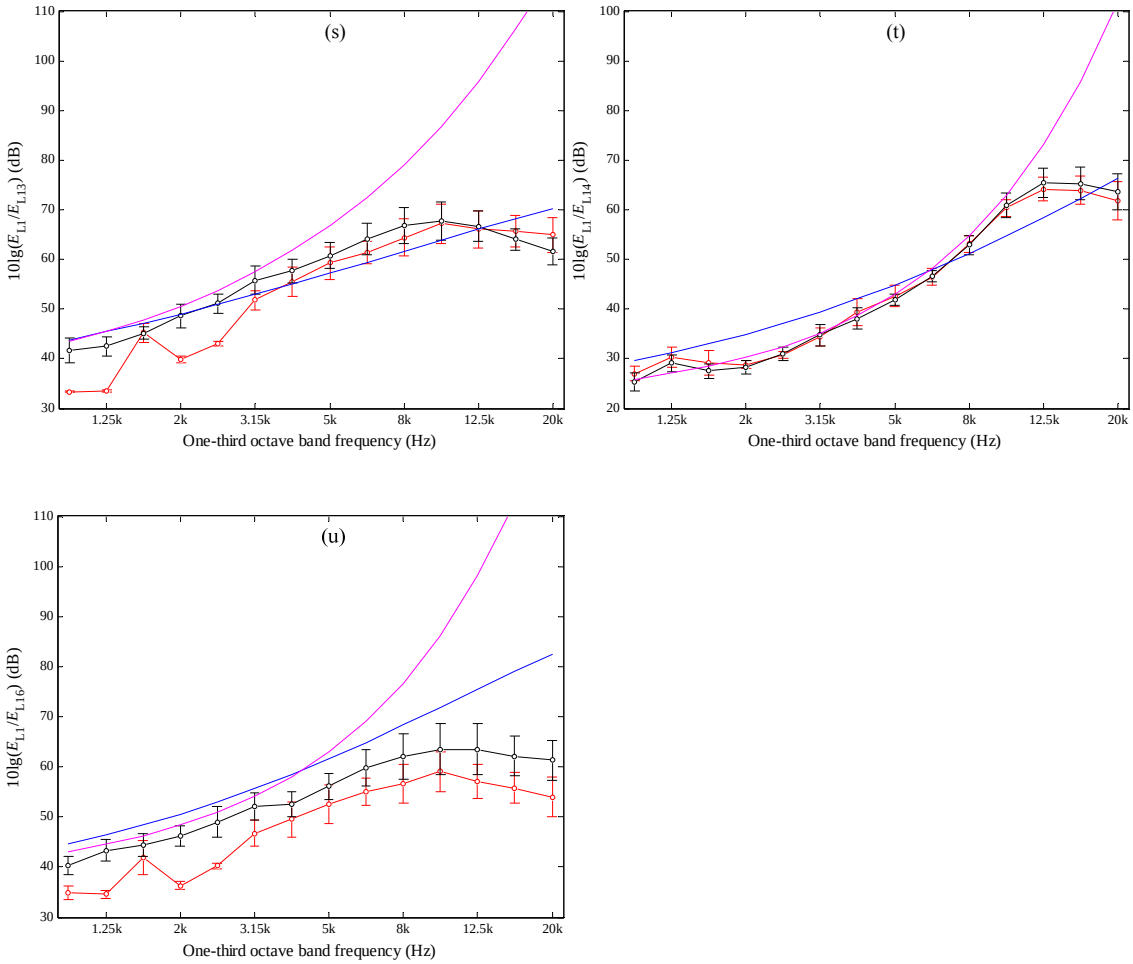

Figure 7.24 Longitudinal wave transmission on the five-bay truss (BL model - Source subsystem: L1). —o— , FEM with uniform material; —o— , FEM with random material; ——, SEA (Euler-Bernoulli group velocity); ——, ASEA (Euler-Bernoulli group velocity). Results from FEM are shown with 95% confidence intervals.

7.4.3 Bending and torsional wave transmission (BT model) for the five-bay truss beam (ILF=0.06)

In this section, Type B bending waves or torsional wave is excited on the source subsystem of the five-bay truss.

Considering the isolated beam with pinned-pinned boundary (Figure 2.9) the fundamental torsional mode frequency is in the 4 kHz one-third octave band, and the fundamental Type B bending mode is in the 20 Hz band. So the energy level differences for BT model of the truss are shown from 10 Hz to 20 kHz for bending waves on the

source and receiving subsystem and from 400 Hz to 20 kHz for torsional waves on either the source or receiving subsystem.

Figure 7.25 shows the results for the BT model of the five-bay truss with excitation of Type B bending waves on beam 1. Figure 7.26 shows the results for the BT model of the five-bay truss with excitation of torsional waves on beam 1.

For the BT model Figure 7.25 (a), (k) and (l) and Figure 7.26 (a), (b) and (l) show the energy level difference between source subsystems B1 or T1 and receiving subsystems B1, T1, B2, or T2. These results show close agreement between FEM, SEA and ASEA for these physically connected subsystems.

For Figure 7.25 (b), (m) and (n) and Figure 7.26 (c), (m) and (n), FEM, SEA and ASEA show close agreement with each other below 5 kHz but above ≈5 kHz the difference between SEA and ASEA indicates that there are high propagation losses.

For Figure 7.25 (c)-(j), and (o)-(u) and Figure 7.26 (d)-(k) and (o)-(u) the difference between SEA and ASEA indicates the presence of tunneling mechanisms below ≈4 kHz and high propagation losses above ≈4 kHz. The general trend is the same as that in sections 7.4.1and 7.4.2 i.e. ASEA gives good estimates when there is tunneling but for receiving beams that are at least three structural junctions away from the source beams the ASEA estimate for high propagation losses does not correspond with FEM predictions.

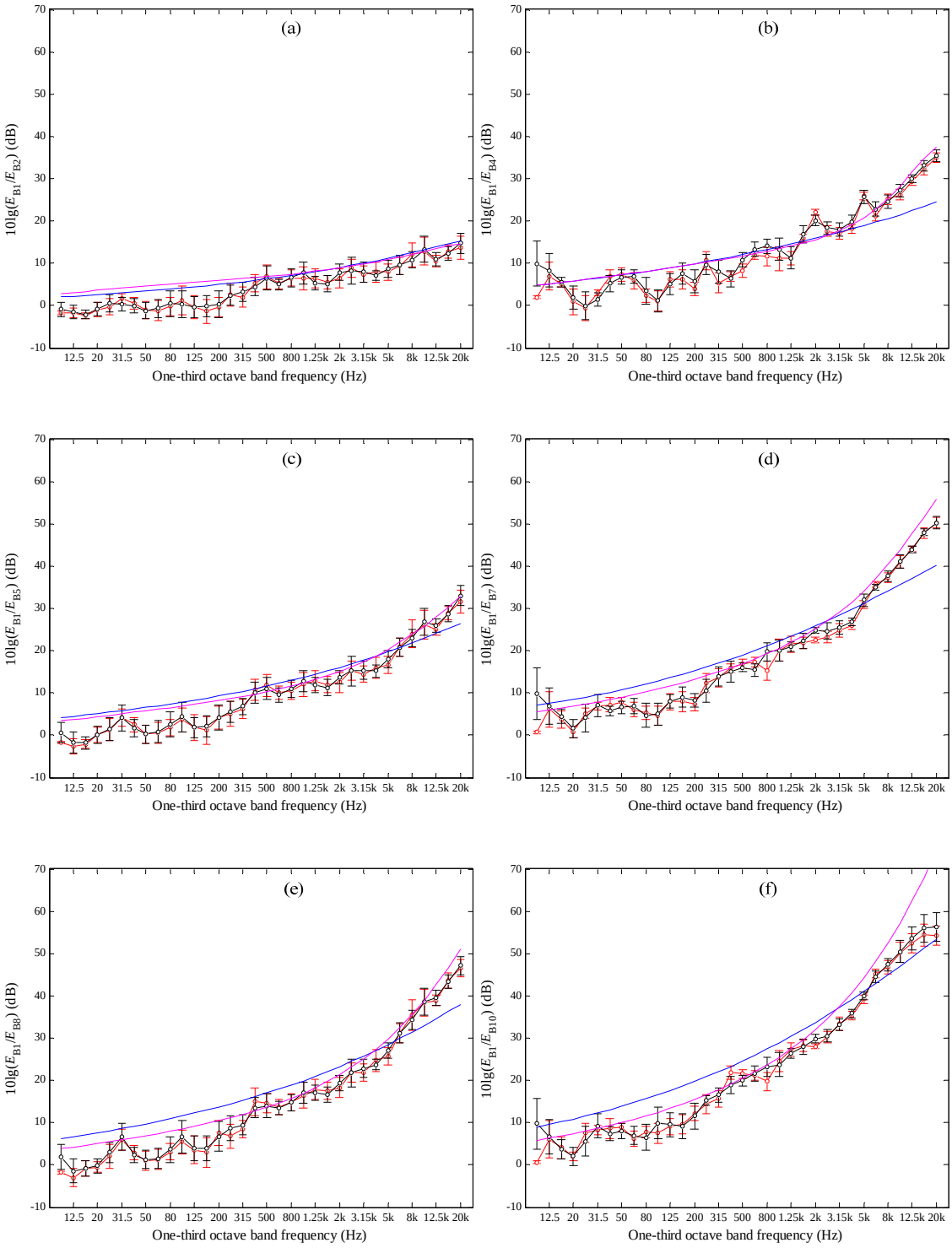
(a)
(b)
(c)
(d)
(e)
(f)
10lg(E_{B1}/E_{B2}) (dB)
10lg(E_{B1}/E_{B4}) (dB)
10lg(E_{B1}/E_{B5}) (dB)
10lg(E_{B1}/E_{B7}) (dB)
10lg(E_{B1}/E_{B8}) (dB)
10lg(E_{B1}/E_{B10}) (dB)
70
60
50
40
30
20
10
0
-10
12.5 20 31.5 50 80 125 200 315 500 800 1.25k 2k 3.15k 5k 8k 12.5k 20k
One-third octave band frequency (Hz)

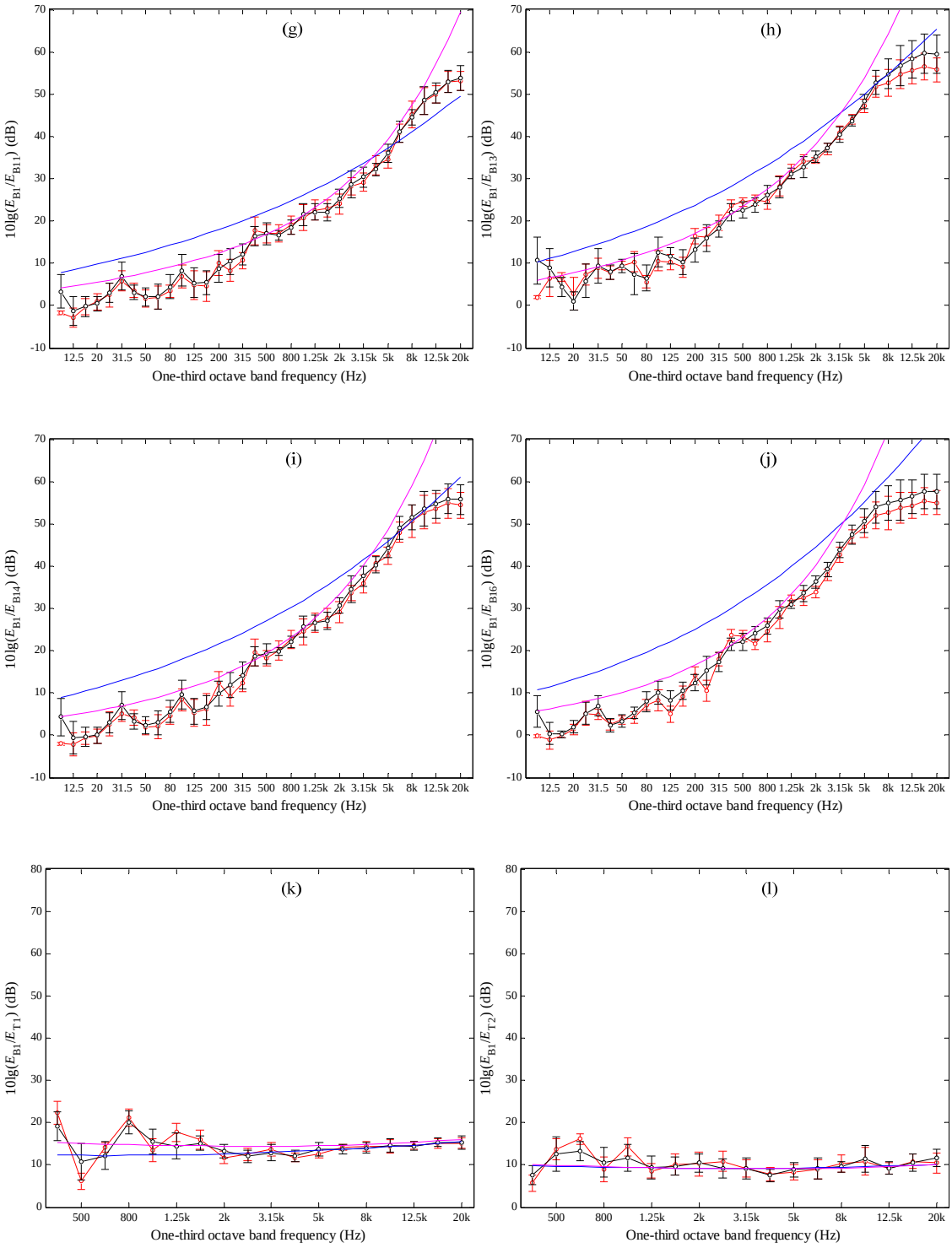
(g)
(h)
(i)
(j)
(k)
(l)
$10\lg(E_{B1}/E_{B11})$ (dB)
$10\lg(E_{B1}/E_{B13})$ (dB)
$10\lg(E_{B1}/E_{B14})$ (dB)
$10\lg(E_{B1}/E_{B16})$ (dB)
$10\lg(E_{B1}/E_{T1})$ (dB)
$10\lg(E_{B1}/E_{T2})$ (dB)
One-third octave band frequency (Hz)
12.5 20 31.5 50 80 125 200 315 500 800 1.25k 2k 3.15k 5k 8k 12.5k 20k
500 800 1.25k 2k 3.15k 5k 8k 12.5k 20k

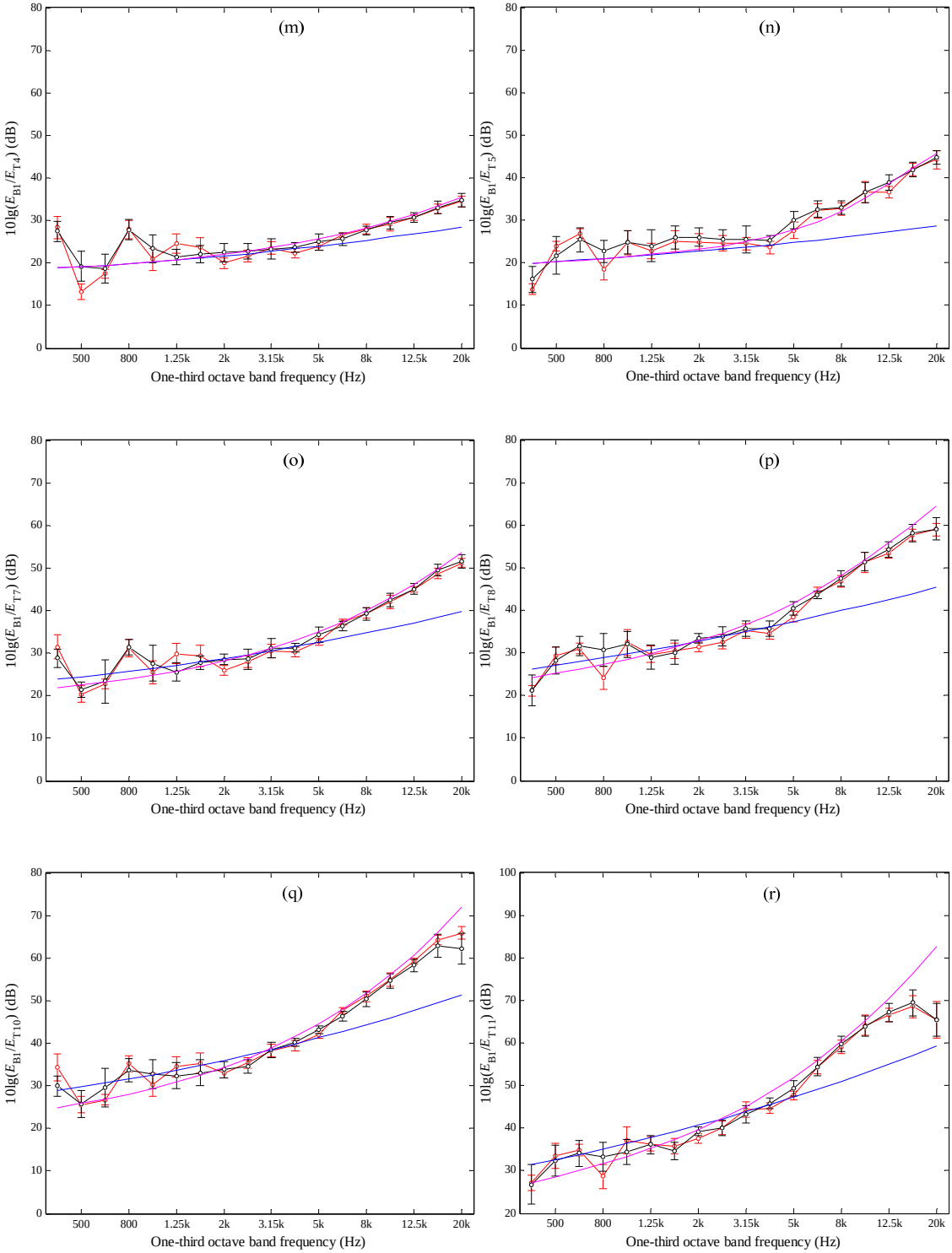
(m)
(n)
(o)
(p)
(q)
(r)
$10\lg(E_{B1}/E_{T4})$ (dB)
$10\lg(E_{B1}/E_{T5})$ (dB)
$10\lg(E_{B1}/E_{T7})$ (dB)
$10\lg(E_{B1}/E_{T8})$ (dB)
$10\lg(E_{B1}/E_{T10})$ (dB)
$10\lg(E_{B1}/E_{T11})$ (dB)
One-third octave band frequency (Hz)
500
800
1.25k
2k
3.15k
5k
8k
12.5k
20k

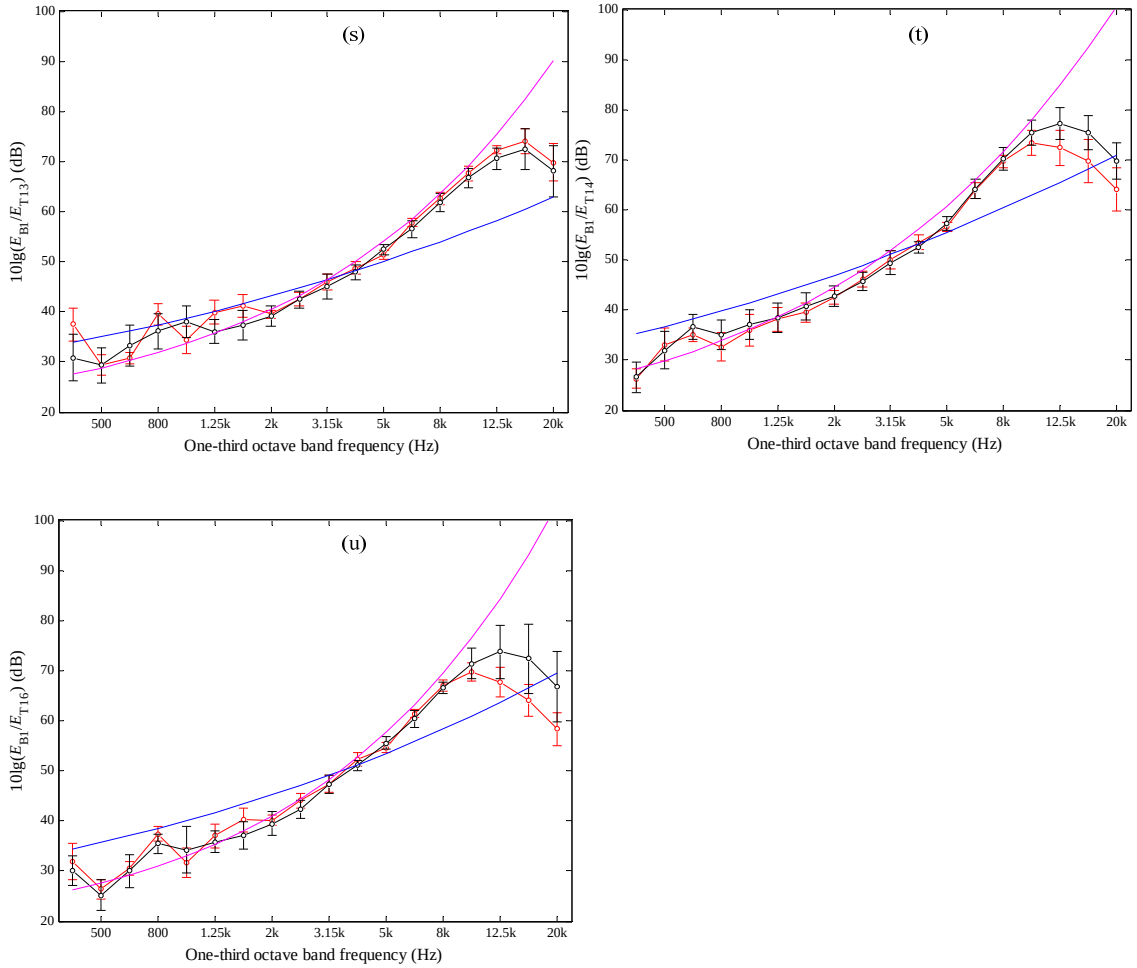

Figure 7.25 Type B bending wave transmission on the five-bay truss (BT model - Source subsystem: B1). —○—, FEM with uniform material; —○—, FEM with random material; ——, SEA (Euler-Bernoulli group velocity); ——, ASEA (Euler-Bernoulli group velocity). Results from FEM are shown with 95% confidence intervals.

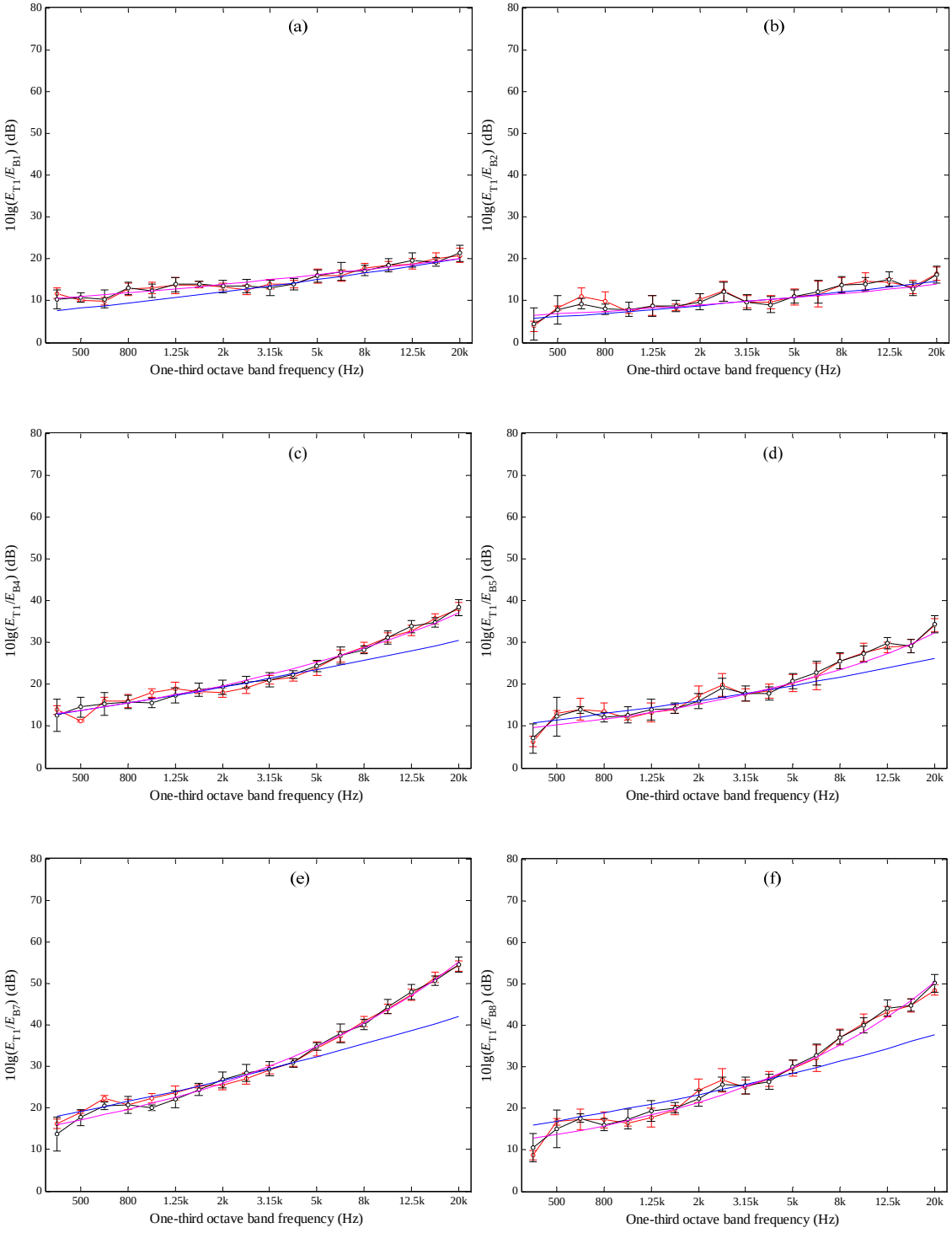
(a)
(b)
(c)
(d)
(e)
(f)
$10\lg(E_{T1}/E_{B1})$ (dB)
$10\lg(E_{T1}/E_{B2})$ (dB)
$10\lg(E_{T1}/E_{B4})$ (dB)
$10\lg(E_{T1}/E_{B5})$ (dB)
$10\lg(E_{T1}/E_{B7})$ (dB)
$10\lg(E_{T1}/E_{B8})$ (dB)
0
10
20
30
40
50
60
70
80
500
800
1.25k
2k
3.15k
5k
8k
12.5k
20k
One-third octave band frequency (Hz)

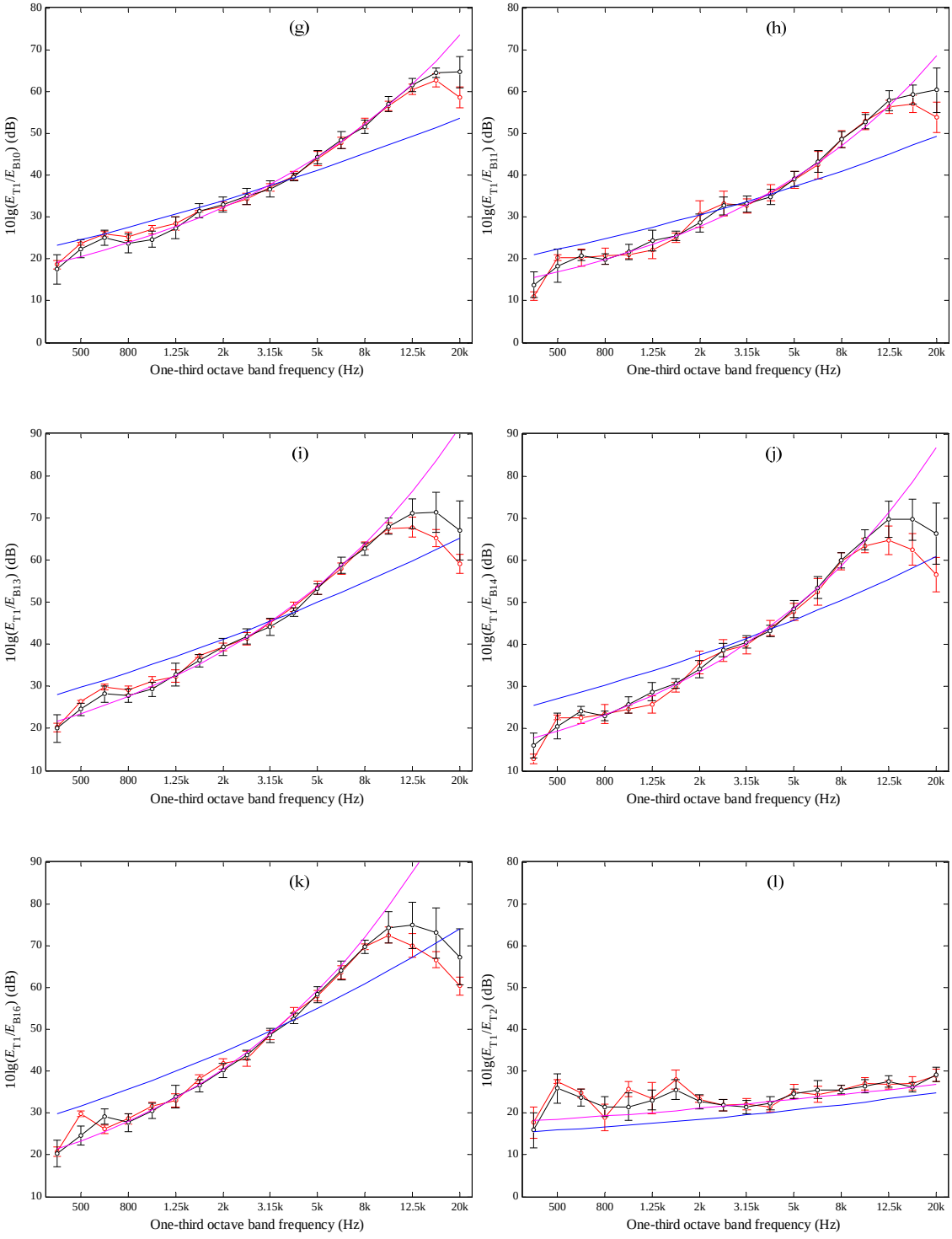
(g)
(h)
(i)
(j)
(k)
(l)
One-third octave band frequency (Hz)
500
800
1.25k
2k
3.15k
5k
8k
12.5k
20k

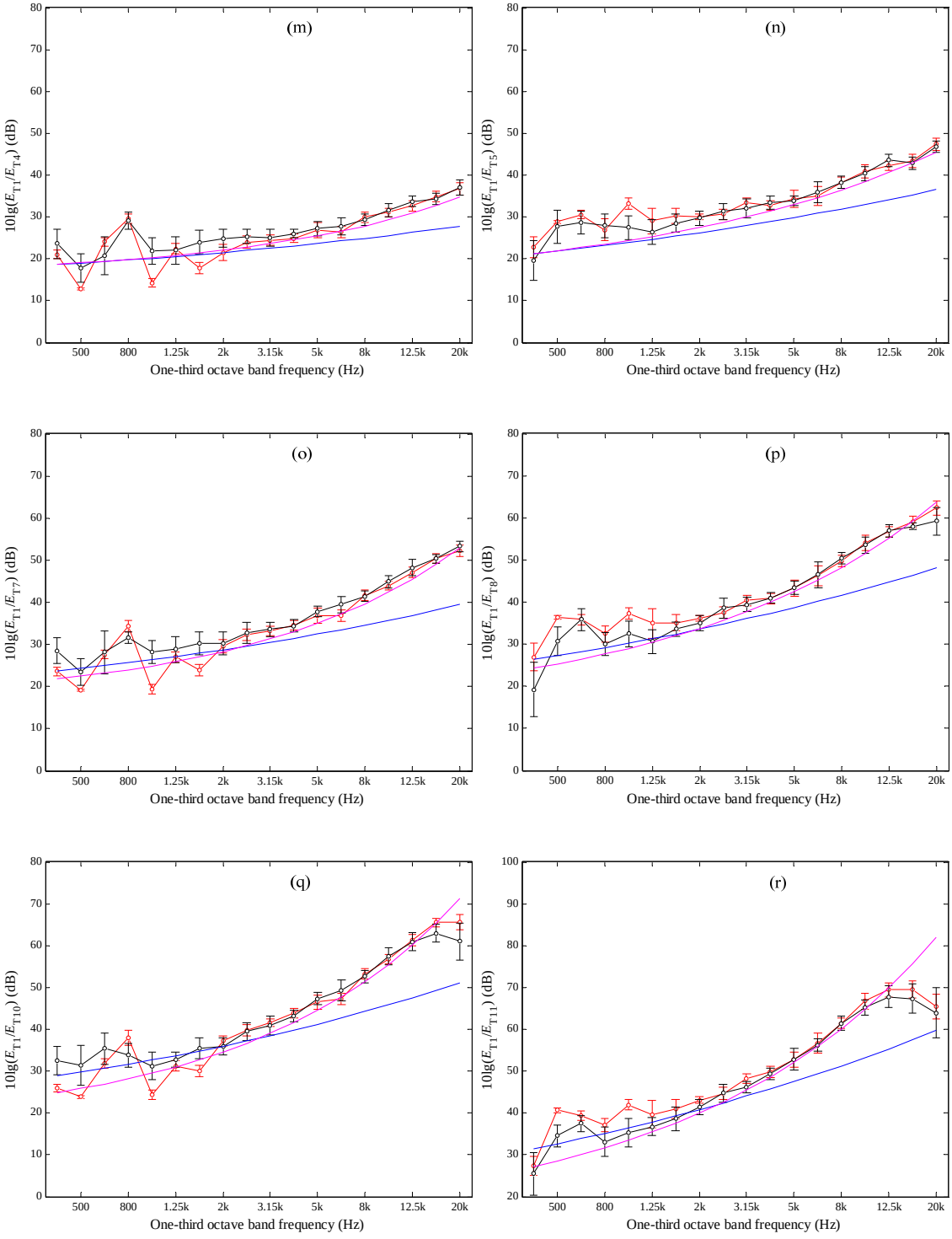
(m)
(n)
(o)
(p)
(q)
(r)
$10\lg(E_{T1}/E_{T4})$ (dB)
$10\lg(E_{T1}/E_{T5})$ (dB)
$10\lg(E_{T1}/E_{T7})$ (dB)
$10\lg(E_{T1}/E_{T8})$ (dB)
$10\lg(E_{T1}/E_{T10})$ (dB)
$10\lg(E_{T1}/E_{T11})$ (dB)
One-third octave band frequency (Hz)
500
800
1.25k
2k
3.15k
5k
8k
12.5k
20k

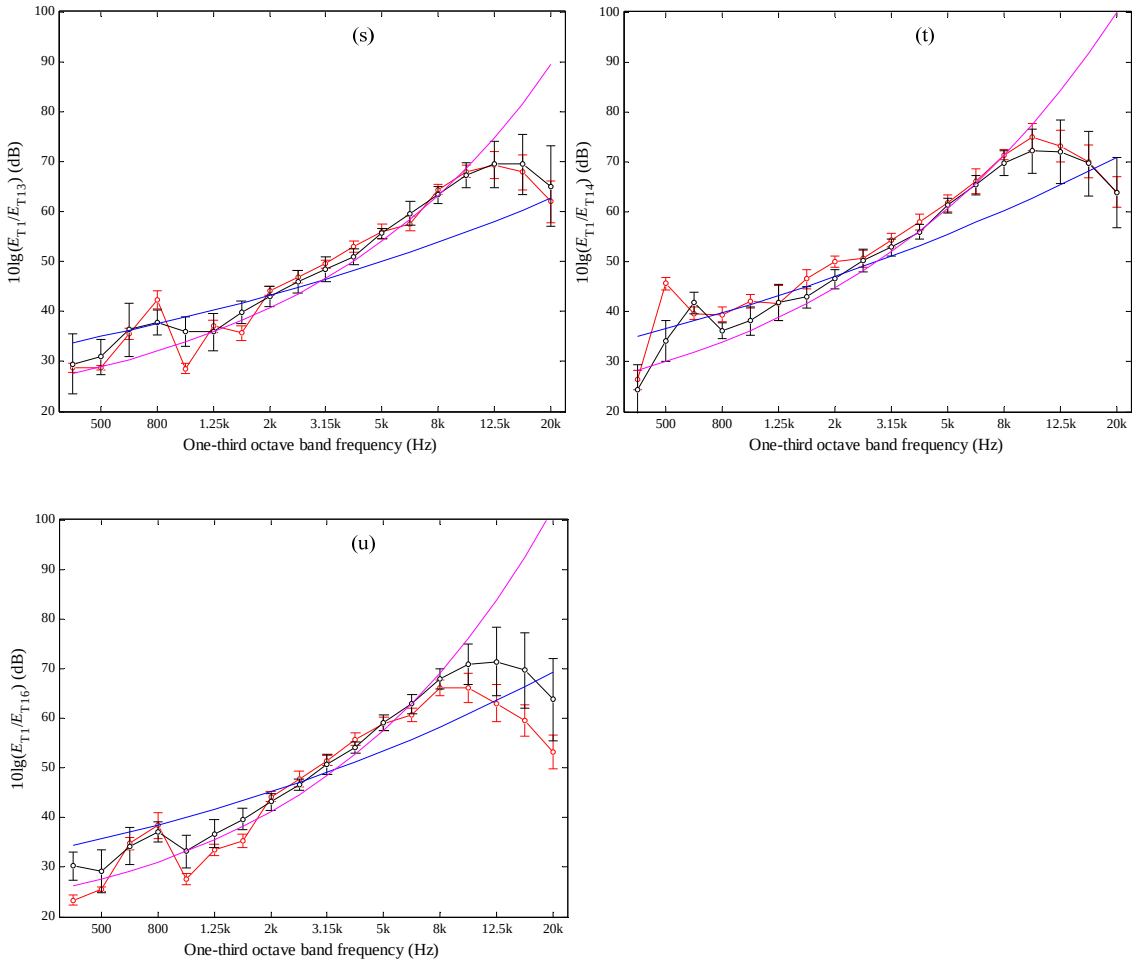

Figure 7.26 Torsional wave transmission on the five-bay truss (BT model - Source subsystem: T1). —○—, FEM with uniform material; —○—, FEM with random material; ——, SEA (Euler-Bernoulli group velocity); ——, ASEA (Euler-Bernoulli group velocity). Results from FEM are shown with 95% confidence intervals.

7.5 Summary

The investigation into the effect of junction and boundary conditions on an L-junction showed that (a) in-plane motion due to bending wave motion below the fundamental longitudinal mode varies significantly depending on the boundary conditions hence it is not appropriate to calculate longitudinal wave energy levels from FEM below the fundamental longitudinal mode and (b) below the fundamental longitudinal mode there is negligible difference between the B and BL models.

The investigation into the transmission coefficients of zero in the wave theory derivations for BL and BT models of T- and X-junctions from Chapter 2 showed that

when the energy level difference between subsystems *i* and *j* corresponded to a non-zero transmission coefficient between *i* and *j* (e.g. E_{B1}/E_{B2} when $\tau_{B1B2}\neq 0$) then FEM results assuming uniform and random material properties gave nominally the same result and there was closest agreement between FEM, SEA and ASEA although in some cases ASEA showed closer agreement than SEA. When the energy level difference between subsystems *i* and *j* directly corresponded to a transmission coefficient of zero between *i* and *j*, it was found that ASEA was closest to FEM (random material) rather than FEM (uniform material). The reason for this is that FEM (uniform material) represents an extreme example because the co-linear beams are identical in length, cross-section and material properties and therefore the bending waves on these beams not only have a phase difference of π between them when they leave the junction but they also form standing waves (modes) on these beams which reinforces this condition at the junction.

With the five-bay truss beam it was found that ASEA shows close agreement with FEM when there is tunneling. When ASEA predicts high propagation losses at high frequencies, ASEA and FEM show close agreement on receiving beams that are less than three structural junctions away from the source beam. However FEM does not agree with ASEA at high frequencies when ASEA predicts high propagation losses on receiving beams that are at least three structural junctions away from the source beam.

8. Conclusions

This thesis has investigated the prediction of vibration transmission using FEM, SEA and ASEA on frameworks of beams that support multiple wave types due to wave conversion at the junctions. To assess the validity of these models at high frequencies where Timoshenko beam theory is valid for bending wave motion, an assessment has been made into whether coupling loss factors can be calculated using Timoshenko (rather than Euler-Bernoulli) group velocity and wave transmission coefficients predicted using Euler-Bernoulli theory. Comparison with measurements on Perspex beams and FEM using Euler-Bernoulli and Timoshenko elements have been carried out to gain insight into the validity of this approach when there are low mode counts, low modal overlap, multiple wave types, different bending wave theories, propagation losses and indirect coupling.

In Chapter 2, the bending wave group velocity was derived for Timoshenko theory considering both rotatory inertia and shear deformation. This made it possible to assess a proposal made in this thesis to incorporate Timoshenko theory into SEA and ASEA by changing over from Euler-Bernoulli to Timoshenko group velocity when calculating the coupling loss factors whilst using the transmission coefficients derived assuming Euler-Bernoulli beams. These transmission coefficients were determined for B, BL and BT models for L-, T- and X-junctions of semi-infinite beams assuming a rigid, massless junction and where only the co-linear beams on T- and X-junctions have identical material properties and cross-sectional dimensions. This provided a consistent set of full derivations that were not previously available in the literature.

Chapter 3 described how SEA and ASEA were implemented to predict vibration transmission across frameworks of beams. Implementation of ASEA for frameworks of beams with multiple wave types satisfied the first aim of the thesis and to the author's knowledge this is the first time this has been done.

Chapter 4 described the finite element models. Calculations of mesh errors for beams supporting bending, longitudinal or torsional wave motion showed that the element size was sufficient for Type A and Type B bending waves when the element size is $< \lambda_B/10$

.

Chapter 5 described the experimental work. This thesis required analysis up to 20 kHz; hence it was necessary to quantify the material properties of Perspex over this wide frequency range. This indicated that a frequency-independent Young's modulus could be used but that the internal loss factor was frequency-dependent. Laser vibrometry was used to measure out-of-plane velocity on the coupled beams in order to avoid errors due to mass loading at high frequencies.

Chapter 6 compared measurements, FEM, SEA and ASEA on an isolated L-junction of beams, a rectangular beam frame and a three-bay truss beam. The rectangular beam framework was designed with relatively long beams to introduce high propagation losses. The three-bay truss beam was designed with relatively short beams so that tunneling mechanisms were more important than high propagation losses.

The second aim of the thesis was to identify the local mode requirements in terms of mode counts and modal overlap factors such that SEA and/or ASEA give reasonable estimates of the dynamic response on frameworks of beams that support multiple wave types. In general it was found that there are large fluctuations in the energy level differences when (a) there is only one local mode in each frequency band in either the source or the receiving beam and (b) there are intermediate frequency bands with no local modes on the source and receiving beams. When consecutive frequency bands have at least one local mode on the source or receiving beams the fluctuations are significantly reduced. When each beam supports at least two local modes for each wave type in the frequency band of interest and the modal overlap factor is at least 0.1, FEM and measurement data tend to have average values which form smooth curves such as those predicted with SEA and ASEA.

The third aim was to investigate whether SEA and ASEA models could incorporate both Euler-Bernoulli and Timoshenko theory by changing over from Euler-Bernoulli to Timoshenko group velocity when calculating the coupling loss factors, and to identify a suitable crossover frequency. It was found that when Timoshenko and Euler-Bernoulli group velocities differed by ≥26%, measurements using bending wave excitation showed closest agreement with FEM using Euler-Bernoulli elements when longitudinal waves were generated at the junction, but closest agreement with FEM using Timoshenko elements when torsional waves were generated at the junction. It would have been expected to be Timoshenko elements in both cases; for this reason clearer

conclusions were sought through comparison of FEM, SEA and ASEA. The results showed that when the difference between Timoshenko and Euler-Bernoulli group velocities was ≥26% there were significant differences between FEM models using Euler-Bernoulli and Timoshenko elements. For receiving subsystems that were not directly coupled to the source subsystem, FEM using Euler-Bernoulli and Timoshenko elements showed closest agreement with ASEA (rather than SEA) using Euler-Bernoulli and Timoshenko group velocities respectively. One reason for this is that wave conversion and propagation losses become more important for more distant subsystems; hence there were clear differences between SEA and ASEA. The agreement between FEM and ASEA indicates that it is a reasonable assumption that phase effects can be ignored in the ray tracing approach used with ASEA. This is particularly noteworthy for the three-bay truss which essentially forms a finite perfectly periodic construction for which phase effects were more likely to have been important. ASEA results for the L-junctions and the rectangular beam frame demonstrated that unlike SEA it was able to incorporate high propagation losses.

Chapter 7 built on the validation of FEM, SEA and ASEA by using parametric studies with these models. Varying the junction and boundary conditions on an L-junction showed that in-plane motion due to bending wave motion below the fundamental longitudinal mode varied significantly depending on the boundary conditions hence it is not appropriate to calculate longitudinal wave energy levels from FEM below the fundamental longitudinal mode. This also showed that below the fundamental longitudinal mode there is negligible difference between the B and BL models.

With the five-bay truss beam it was found that ASEA shows close agreement with FEM when there is significant indirect coupling. When ASEA predicts high propagation losses at high frequencies, ASEA and FEM show close agreement on receiving beams that are less than three structural junctions away from the source beam. The findings from chapters 6 and 7 on the rectangular beam frame, the three-bay truss and the five-bay truss addressed the fourth aim of the thesis. These results showed that ASEA generally provides more accurate predictions than SEA by accounting for propagation losses and/or tunnelling (i.e. indirect coupling). However, there are indications from the five-bay truss beams that ASEA may no longer be accurate in predicting the response

on beams that are at least three structural junctions away from the source beam, particularly when ASEA predicts high propagation losses on the receiving beam.

8.1 Future work

Heron [2] only validated ASEA on a series of co-linear rods which resulted in high propagation losses. Results in Chapter 7 indicate a lack of agreement between FEM and ASEA where there are high propagation losses on the five-bay truss beam. To investigate whether there is a problem with Abaqus modelling propagation losses it would be worthwhile creating a series of beams connected at L-junctions.

In chapter 7 it was seen that high propagation losses in the high-frequency range on the five-bay truss beam were not predicted by ASEA; hence it would be worth pursuing an alternative prediction model, possibly based on global modes.

Appendix 1. Derivation of the wave motion equation of Timoshenko beam

The two differential equations about force and moment on a Timoshenko beam element are

$$\frac{GA}{\kappa}(\frac{\partial \xi}{\partial x}-\theta)+EI\frac{\partial^2 \theta}{\partial x^2}-\rho I\frac{\partial^2 \theta}{\partial t^2}=0 \tag{A1}$$

$$\frac{GA}{\kappa}(\frac{\partial^2 \xi}{\partial x^2}-\frac{\partial \theta}{\partial x})-\rho A\frac{\partial^2 \xi}{\partial t^2}=0 \tag{A2}$$

To solve the general wave motion, we have to eliminate the variable θ. From equation A2 one can obtain

$$\frac{\partial \theta}{\partial x}=\frac{\partial^2 \xi}{\partial x^2}-\frac{\rho\kappa}{G}\frac{\partial^2 \xi}{\partial t^2} \tag{A3}$$

$$\frac{\partial^2 \theta}{\partial x^2}=\frac{\partial^3 \xi}{\partial x^3}-\frac{\rho\kappa}{G}\frac{\partial^3 \xi}{\partial t^2 \partial x} \tag{A4}$$

$$\frac{\partial^3 \theta}{\partial x \partial t^2}=\frac{\partial^4 \xi}{\partial x^2 \partial t^2}-\frac{\rho\kappa}{G}\frac{\partial^4 \xi}{\partial t^4} \tag{A5}$$

Inserting (A4) into (A1) gives the following equation

$$\frac{GA}{\kappa}(\frac{\partial \xi}{\partial x}-\theta)+EI(\frac{\partial^3 \xi}{\partial x^3}-\frac{\rho\kappa}{G}\frac{\partial^3 \xi}{\partial t^2 \partial x})-\rho I\frac{\partial^2 \theta}{\partial t^2}=0 \tag{A6}$$

Calculate the differential to *x* of this equation, we have

$$\frac{GA}{\kappa}(\frac{\partial^2 \xi}{\partial x^2}-\frac{\partial \theta}{\partial x})+EI(\frac{\partial^4 \xi}{\partial x^4}-\frac{\rho\kappa}{G}\frac{\partial^4 \xi}{\partial t^2 \partial^2 x})-\rho I\frac{\partial^3 \theta}{\partial t^2 \partial x}=0 \tag{A7}$$

Applying (A3) and (A5) to (A7) yields the general four order differential wave motion equation of Timoshenko beam

$$EI\frac{\partial^4 \xi}{\partial x^4}+\rho A\frac{\partial^2 \xi}{\partial t^2}-\rho I(1+\frac{E\kappa}{G})\frac{\partial^4 \xi}{\partial x^2 \partial t^2}+\frac{\rho^2 I\kappa}{G}\frac{\partial^4 \xi}{\partial t^4}=0 \tag{A8}$$

References

[1] Lyons, R. H. (1975). Statistical Energy Analysis of dynamical systems. MIT Press, Cambridge, Mass. (1975). ISBN: 0-262-12071-2.

[2] Heron, K. H. (1994). Advanced statistical energy analysis. *Philosophical Transactions of the Royal Society of London A: Mathematical, Physical and Engineering Sciences*, *346*(1681), 501-510.

[3] Yin, J., & Hopkins, C. (2013). Prediction of high-frequency vibration transmission across coupled, periodic ribbed plates by incorporating tunnelling mechanisms. *The Journal of the Acoustical Society of America*, *133*(4), 2069-2081.

[4] Cremer, L. (1953). Calculation of sound propagation in structures. *Acta Acustica united with Acustica*, *3*(5), 317-335.

[5] Cremer, L., Heckl, M., & Ungar, E. E. Structure-borne sound, 1973. *Heidelbrg: Springer-Verlag, Berlin, New York*.

[6] Heckl, M., & Petersson, B. A. T. (2005). *Structure-Borne Sound: Structural Vibrations and Sound Radiation at Audio Frequencies*. Springer.

[7] Lyapunov, V. (1967). Vibration isolation of articulated joints. *Soviet Physics Acoustics-USSR*, *13*(2), 201.

[8] Wang, T. M., & Kinsman, T. A. (1971). Vibrations of frame structures according to the Timoshenko theory. *Journal of Sound and Vibration*, *14*(2), 215-227.

[9] Rosenhouse, G., Ertel, H., & Mechel, F. P. (1981). Theoretical and experimental investigations of structure borne sound transmission through a’’T’’joint in a finite system. *The Journal of the Acoustical Society of America*,*70*(2), 492-499.

[10] Mace, B. R. (1984). Wave reflection and transmission in beams. *Journal of Sound and Vibration*, *97*(2), 237-246.

[11] Moore, J. A. (1990). Vibration transmission through frame or beam junctions.*The Journal of the Acoustical Society of America*, *88*(6), 2766-2776.

[12] Horner, J. L., & White, R. G. (1990). Prediction of vibrational power transmission through jointed beams. *International Journal of Mechanical Sciences*, *32*(3), 215-223.

[13] Horner, J. L., & White, R. G. (1991). Prediction of vibrational power transmission through bends and joints in beam-like structures. *Journal of Sound and Vibration*, *147*(1), 87-103.

[14] Leung, R. C. N., & Pinnington, R. J. (1990). Wave propagation through right-angled joints with compliance-flexural incident wave. *Journal of Sound and Vibration*, *142*(1), 31-48.

[15] Leung, R. C. N., & Pinnington, R. J. (1992). Wave propagation through right-angled joints with compliance: longitudinal incidence wave. *Journal of Sound and Vibration*, *153*(2), 223-237.

[16] Szwerc, R. P., Burroughs, C. B., Hambric, S. A., & McDevitt, T. E. (2000). Power flow in coupled bending and longitudinal waves in beams. *The Journal of the Acoustical Society of America*, *107*(6), 3186-3195.

[17] Ouisse, M., & Guyader, J. L. (2003). Vibration sensitive behaviour of a connecting angle. Case of coupled beams and plates. *Journal of Sound and Vibration*, *267*(4), 809-850.

[18] Song, J. H., & Hong, S. Y. (2007). Development of non-conservative joints in beam networks for vibration energy flow analysis. *Shock and Vibration*, *14*(1), 15-28.

[19] Mei, C., & Mace, B. R. (2005). Wave reflection and transmission in Timoshenko beams and wave analysis of Timoshenko beam structures. *Journal of Vibration and Acoustics*, *127*(4), 382-394.

[20] Mei, C. (2008). Wave analysis of in-plane vibrations of H-and T-shaped planar frame structures. *Journal of Vibration and Acoustics*, *130*(6), 061004.

[21] Mei, C. (2010). In-plane vibrations of classical planar frame structures—an exact wave-based analytical solution. *Journal of Vibration and Control*, *16*(9), 1265-1285.

[22] Mei, C. (2013). Wave vibration control of L-shaped and portal planar frames. *Journal of Vibration and Acoustics*, *135*(5), 051022.

[23] Mei, C. (2013, November). Vibration control of H-shaped planar frames based on the classical Euler-Bernoulli and the advanced Timoshenko bending theories. In *ASME 2013 International Mechanical Engineering Congress and Exposition* (pp. V04BT04A060-V04BT04A060). American Society of Mechanical Engineers.

[24] Lee, J. P., & Kolsky, H. (1972). The generation of stress pulses at the junction of two noncollinear rods. *Journal of Applied Mechanics*, *39*(3), 809-813.

[25] Atkins, K. J., & Hunter, S. C. (1975). The propagation of longitudinal elastic waves around right-angled corners in rods of square cross-section. *The Quarterly Journal of Mechanics and Applied Mathematics*, *28*(2), 245-260.

[26] Yong, K. H., & Atkins, K. J. (1982). Generation of elastic stress waves at a corner junction of square rods. *Journal of Sound and Vibration*, *84*(3), 431-441.

[27] Yong, K. H., & Atkins, K. J. (1983). Generation of elastic stress waves at a T-junction of square rods. *Journal of Sound and Vibration*, *88*(4), 431-436.

[28] Desmond, T. P. (1981). Theoretical and experimental investigation of stress waves at a junction of three bars. *Journal of Applied Mechanics*, *48*(1), 148-154.

[29] Farag, N. H., & Pan, J. (1996). Dynamic response and power flow in two-dimensional coupled beam structures under in-plane loading. *The Journal of the Acoustical Society of America*, *99*(5), 2930-2937.

[30] Beshara, M., & Keane, A. J. (1997). Vibrational energy flows in beam networks with compliant and dissipative joints. *Journal of Sound and Vibration*, *203*(2), 321-339.

[31] Heckl, M. A. (1964). Investigations on the vibrations of grillages and other simple beam structures. *The Journal of the Acoustical Society of America*,*36*(7), 1335-1343.

[32] Sablik, M. J. (1982). Coupling loss factors at a beam L-joint revisited. *The Journal of the Acoustical Society of America*, *72*(4), 1285-1288.

[33] Chi, R. M. (1989). Asymptotic Modal Analysis of Structure Borne Noise in Cross Beams. *Journal of Vibration and Acoustics*, *111*(4), 472-479.

[34] Tso, Y. K., & Norwood, C. J. (1995). Vibratory power transmission through three-dimensional beam junctions. *Journal of Sound and Vibration*, *185*(4), 595-607.

[35] Kurtze, G., Tamm, K., & Vogel, S. (1955). Modellversuche zur Biegewellendämmung an Ecken. *Acta Acustica united with Acustica*, *5*(4), 223-233.

[36] Hinsch, H. (1960). Verkettete medumische Impedanzen zur Messung der Körpersdudldämmung an edcen-und kreuzförmigen Stoβ-Stellen (Modellversudie). *Acta Acustica united with Acustica*, *10*(Supplement 1), 287-294.

[37] Rosenhouse, G., Ertel, H., & Mechel, F. P. (1981). Theoretical and experimental investigations of structureborne sound transmission through a’’T’’joint in a finite system. *The Journal of the Acoustical Society of America*,*70*(2), 492-499.

[38] Gibbs, B. M., & Tattersall, J. D. (1987). Vibrational energy transmission and mode conversion at a corner-junction of square section rods. *Journal of Vibration and Acoustics*, *109*(4), 348-355.

[39] Doyle, J. F., & Kamle, S. (1985). An experimental study of the reflection and transmission of flexural waves at discontinuities. *Journal of Applied Mechanics*,*52*(3), 669-673.

[40] Doyle, J. F., & Kamle, S. (1987). An experimental study of the reflection and transmission of flexural waves at an arbitrary T-joint. *Journal of Applied Mechanics*, *54*(1), 136-140.

[41] Troshin, A. G., & Sanderson, M. A. (1997). Structural energy flow propagation in a T-shaped beam: an evaluation of an intensity and a component mobility approach. *Acta Acustica united with Acustica*, *83*(3), 489-505.

[42] Troshin, A. G., & Sanderson, M. A. (1998). Structural energy flow in a resiliently coupled T-shaped beam by wave intensity and Mobility Approaches. *Acta Acustica united with Acustica*, *84*(5), 860-869.

[43] Feng, L., Liu, M., & Nilsson, A. (2001). Experimental study of structure-borne sound transmission loss of mechanical joints. *The Journal of the Acoustical Society of America*, *110*(3), 1391-1397.

[44] Gautier, F., Moulet, M. H., & Pascal, J. C. (2006). Reflection, transmission and coupling of longitudinal and flexural waves at beam junctions. Part I: measurement methods. *Acta Acustica united with Acustica*, *92*(6), 982-997.

[45] Moulet, M. H., & Gautier, F. (2007). Reflection, transmission and coupling of longitudinal and flexural waves at beam junctions. Part II: experimental and theoretical results. *Acta Acustica united with Acustica*, *93*(1), 37-47.

[46] Muggleton, J. M., Waters, T. P., Mace, B. R., & Zhang, B. (2007). Approaches to estimating the reflection and transmission coefficients of discontinuities in waveguides from measured data. *Journal of Sound and Vibration*, *307*(1), 280-294.

[47] Mead, D. J. (1970). Free wave propagation in periodically supported, infinite beams. *Journal of Sound and Vibration*, *11*(2), 181-197.

[48] Mead, D. J., & Yaman, Y. (1991). The response of infinite periodic beams to point harmonic forces: a flexural wave analysis. *Journal of Sound and Vibration*,*144*(3), 507-529.

[49] Wen, J., Yu, D., Wang, G., & Wen, X. (2008). Directional propagation characteristics of flexural wave in two-dimensional periodic grid-like structures. *Journal of Physics D: Applied Physics*, *41*(13), 135505.

[50] Langley, R. S. (1996). The response of two-dimensional periodic structures to point harmonic forcing. *Journal of Sound and Vibration*, *197*(4), 447-469.

[51] Xiao, Y., Mace, B. R., & Wen, X. (2014). Wave propagation in periodic truss beams with members of different materials. *The 16th International Congress on Sound and Vibration, Cairo, Egypt*.

[52] Phani, A. S., Woodhouse, J., & Fleck, N. A. (2006). Wave propagation in two-dimensional periodic lattices. *The Journal of the Acoustical Society of America, 119*(4), 1995-2005.

[53] Uhrig, R. (1966). The transfer matrix method seen as one method of structural analysis among others. *Journal of Sound and Vibration, 4*(2), 136-148.

[54] Yun, Y., & Mak, C. M. (2009). A study of coupled flexural-longitudinal wave motion in a periodic dual-beam structure with transverse connection. *The Journal of the Acoustical Society of America, 126*(1), 114-121.

[55] Yun, Y., & Mak, C. M. (2011). Experimental study of coupled vibration in a finite periodic dual-layered structure with transverse connection. *Applied Acoustics,72*(5), 287-296.

[56] Langley, R. S. (1990). Analysis of power flow in beams and frameworks using the direct-dynamic stiffness method. *Journal of Sound and Vibration, 136*(3), 439-452.

[57] Shankar, K., & Keane, A. J. (1995). Energy flow predictions in a structure of rigidly joined beams using receptance theory. *Journal of Sound and Vibration,185*(5), 867-890.

[58] Sablik, M. J., Beissner, R. E., Silvus, H. S., & Miller, M. L. (1985). Statistical energy analysis, structural resonances, and beam networks. *The Journal of the Acoustical Society of America, 77*(3), 1038-1045.

[59] Lyon, R. H., & DEJONG, R. (1995). Theory and application of statistical energy analysis (Butterworth-Heinemann, MA, USA).

[60] Fahy, F. J., & Mohammed, A. D. (1992). A study of uncertainty in applications of SEA to coupled beam and plate systems, part I: computational experiments. *Journal of Sound and Vibration, 158*(1), 45-67.

[61] Hopkins, C. (2007). *Sound insulation*. Butterworth-Heinemann, Imprint of Elsevier, Oxford, ISBN: 978-0-7506-6526-1.

[62] Davies, H. G., Wahab, M. A., & Khandoker, S. I. (1981). Ensemble averages of power flow in randomly excited coupled beams. *The Journal of the Acoustical Society of America, 69*(S1), S87-S87.

[63] Craik, R. J., & Galbrun, L. (2005). Vibration transmission through a frame typical of timber-framed buildings. *Journal of Sound and Vibration*, *281*(3), 763-782.

[64] Lyon, R. H. (2014). *Theory and application of statistical energy analysis*. Elsevier. Second edition.

[65] Mace, B. R. (1994). On the statistical energy analysis hypothesis of coupling power proportionality and some implications of its failure. *Journal of Sound and Vibration*, *178*(1), 95-112.

[66] Bercin, A. N. (1996). An assessment of the effects of in-plane vibrations on the energy flow between coupled plates. *Journal of Sound and Vibration*, *191*(5), 661-680.

[67] Mace, B. R. (2005). Statistical energy analysis: coupling loss factors, indirect coupling and system modes. *Journal of Sound and Vibration*, *279*(1), 141-170.

[68] You, J., Meng, G., & Li, H. G. (2011). Random energy flow analysis of coupled beam structures and its correlation with SEA. *Archive of Applied Mechanics*,*81*(1), 37-50.

[69] Langley, R. S. (1990). A derivation of the coupling loss factors used in statistical energy analysis. *Journal of Sound and Vibration*, *141*(2), 207-219.

[70] Wilson, D., & Hopkins, C. (2015). Analysis of bending wave transmission using beam tracing with advanced statistical energy analysis for periodic box-like structures affected by spatial filtering. *Journal of Sound and Vibration*, *341*, 138-161.

[71] Ziekiewicz, O. C. (1971). The finite element method in engineering science. McGraw-Hill Inc.,US. ISBN: 0070941386.

[72] Dhatt, G., Lefrançois, E., & Touzot, G. (2012). *Finite element method*. John Wiley & Sons.

[73] Fahy, F., & Walker, J. (Eds.). (2004). *Advanced applications in acoustics, noise and vibration*. CRC Press.

[74] Timoshenko, S. P., & Goodier, J. N. (1970). Theory of Elasticity. Third edition. McGraw-Hill Book Company.

[75] Timoshenko, S., & Young, D. H. *Vibration Problems in Engineering, 1974 John Wiley & Sons*. ISBN 0-471-87315-2.

[76] Cowper, G. R. (1966). The shear coefficient in Timoshenko's beam theory. *Journal of Applied Mechanics*, *33*(2), 335-340.

[77] Han, S. M., Benaroya, H., & Wei, T. (1999). Dynamics of transversely vibrating beams using four engineering theories. *Journal of Sound and Vibration*, *225*(5), 935-988.

[78] Diaz-de-Anda, A., Flores, J., Gutiérrez, L., Méndez-Sánchez, R. A., Monsivais, G., & Morales, A. (2012). Experimental study of the Timoshenko beam theory predictions. *Journal of Sound and Vibration*, *331*(26), 5732-5744.

[79] Stephen, N. G., & Puchegger, S. (2006). On the valid frequency range of Timoshenko beam theory. *Journal of Sound and Vibration*, *297*(3), 1082-1087.

[80] Bhashyam, G. R., & Prathap, G. (1981). The second frequency spectrum of Timoshenko beams. *Journal of Sound and Vibration*, *76*(3), 407-420.

[81] Craik, R. J. (1996). *Sound transmission through buildings: using statistical energy analysis*. Gower Publishing Company.

[82] Inman, D. J., & Singh, R. C. (2001). *Engineering vibration* (Vol. 3). Upper Saddle River: Prentice Hall.

[83] Abaqus user's manual v6.12.

[84] Hopkins, C. (2000). *Structure-borne sound transmission between coupled plates* (Doctoral dissertation, Heriot-Watt University).

[85] ISO/PAS 16940:2004 Glass in building – Glazing and airborne sound insulation – Measurement of the mechanical impedance of laminated glass. International Organization for Standardization.

[86] Pritz, T. (2001). Loss factor peak of viscoelastic materials: magnitude to width relations. *Journal of sound and vibration*, *246*(2), 265-280.

[87] Cortés, F., & Elejabarrieta, M. J. (2006). Modelling viscoelastic materials whose storage modulus is constant with frequency. *International journal of solids and structures*, *43*(25), 7721-7726.

[88] Fahy, F. J. (1970). Energy flow between oscillators: special case of point excitation. *Journal of Sound and Vibration*, *11*(4), 481-483.

[89] Keane, A. J., & Manohar, C. S. (1993). Energy flow variability in a pair of coupled stochastic rods. *Journal of Sound and Vibration*, *168*(2), 253-284.